FEDERAL UNIVERSITY OF ITAJUBA - UNIFEI
GRADUATE PROGRAM IN ELECTRICAL ENGINEERING

Dynamic State Estimation of Electrical Power Systems - Unified Solution in the Complex Domain

Eduardo Marcel Resende

Itajubá, June 14th, 2026

FEDERAL UNIVERSITY OF ITAJUBA - UNIFEI
GRADUATE PROGRAM IN ELECTRICAL ENGINEERING

Eduardo Marcel Resende

Dynamic State Estimation of Electrical Power Systems - Unified Solution in the Complex Domain

Thesis proposal submitted to the Graduate Program in Electrical Engineering as part of the requirements for obtaining the title of Doctor of Science in Electrical Engineering.

Concentration Area: Methods for Analysis, Planning and Operation of Electrical Systems

Supervisor: Prof. Dr. Robson Celso Pires
Co-supervisor: Prof. Dr. Zulmar Soares Machado Junior

June 14th, 2026
Itajubá

Eduardo Marcel Resende

Dynamic State Estimation of Electrical Power Systems - Unified Solution in the Complex Domain

Thesis proposal submitted to the Graduate Program in Electrical Engineering as part of the requirements for obtaining the title of Doctor of Science in Electrical Engineering.

Prof. Dr. Robson Celso Pires
Supervisor

Prof. Dr. Zulmar Soares Machado Junior
Co-supervisor

Prof. Dr. Benedito Donizeti Bonatto

Prof. Dr. Antônio José Alves Simões Costa

Prof. Dr. Lamine Mili

Prof. Dr. Marcos Netto

June 14th, 2026
Itajubá

Acknowledgements

To Prof. Dr. Robson Pires for all the knowledge shared, for his constant effort to foster new ideas that enrich research, and for all his support during the supervision of this work.

To Prof. Dr. Zulmar Soares Machado Junior for all his contributions and support during my academic journey.

To Prof. Dr. Marcos Netto, who kindly provided enriching information for this work.

To Prof. Dr. Benedito Donizeti Bonatto, Prof. Dr. Antônio José Alves Simões Costa (UFSC), and Prof. Dr. Lamine Mili (Virginia Tech) for agreeing to serve on my defense committee and for their considerable contributions to the work.

To CAPES (Coordenação de Aperfeiçoamento de Pessoal de Nível Superior) for the scholarship and financial aid that enabled me to dedicate myself full-time to writing this work.

To UNIFEI for providing the infrastructure and technical knowledge that were essential to completing this work.

To my parents and siblings for always believing in me and encouraging me to follow an academic path.

"Creativity is seeing what others see and thinking what no one else has ever thought. "

(Albert Einstein)

Abstract

For decades, the numerical solution of network analysis applications has invariably occurred in the real number domain. However, the phasor nature of electrical quantities allows these problems to be formulated directly in the complex domain. This thesis proposes a comprehensive framework for Dynamic State Estimation (DSE) in complex-conjugate coordinates, leveraging Wirtinger calculus to linearize functions involving complex and conjugate variables. The algebraic-differential modeling of network dynamics is presented, incorporating classical and two-axis synchronous machine models with voltage and speed regulators. The work evaluates the Extended Kalman Filter (EKF) and the Unscented Kalman Filter (UKF) in complex-conjugate coordinates, introducing structural optimizations such as the Decoupled EKF (D-EKF) to mitigate the computational burden of augmented complex statistics. Furthermore, robust versions of these algorithms are developed to handle gross errors, bad leverage points, and communication failures, ensuring high reliability in adverse operational scenarios. The methodology also integrates real-time frequency estimation, which is critical for the operational security of low-inertia systems. Numerical simulations conducted on the IEEE 3-bus system for detailed validation, followed by scalability analyses on the IEEE 39-bus, IEEE 118-bus, and a 340-bus equivalent of the Brazilian Interconnected Power System (SIN-340), demonstrate that while the D-EKF significantly reduces execution times, making complex-domain linearization-based filters computationally viable, the complex-domain UKF achieves superior computational performance in large-scale systems.

Keywords: Dynamic state estimation; Complex-conjugate coordinates; Wirtinger Calculus; Decoupled Extended Kalman Filter; Unscented Kalman Filter; Robust estimation; Computational efficiency.

List of Figures

Figure 1 – Flowchart for CV-SHGM-EKF. 59
Figure 2 – Flowchart for CV-SHGM-UKF. 61
Figure 3 – Changing of power system frequency. 64
Figure 4 – Frequency response control with different timescales. 65
Figure 5 – System frequency. 65
Figure 6 – Primary frequency response. 66
Figure 7 – 3-bus test system. 70
Figure 8 – Dynamic State Estimation: 3-bus system - Scenario 1. 77
Figure 9 – Dynamic State Estimation: 3-bus system - Scenario 2. 80
Figure 10 – Dynamic State Estimation: 3-bus system - Scenario 3. 83
Figure 11 – Frequency of generators and center of inertia over time. 84
Figure 12 – Estimation of f_{COI} - Scenario 2. 85
Figure 13 – Estimation of f_{COI} - Scenario 3. 86
Figure 14 – Dynamic State Estimation for 39-bus system - Generator 8. 88
Figure 15 – Dynamic State Estimation for 39-bus system - Generator 8 - Loss of communication at bus 17. 89
Figure 16 – MSE for all estimated measurements - Communication loss at bus 17. . 90
Figure 17 – Mean squared error (MSE) per state variable for the 39-bus case considering non-robust filters. 91
Figure 18 – Mean squared error (MSE) per state variable for the 39-bus case considering robust filters. 92
Figure 19 – Frequency of generators and center of inertia over time - IEEE - 39 bus. 94
Figure 20 – Estimation of f_{COI} - Communication loss at bus 17. 94
Figure 21 – Computational time ratio between complex-domain and real-domain formulations. 98
Figure 22 – Contour plot of scalar real function of complex variable. 118

List of Tables

Table 1 – Classical Model: Comparison between the formulations in the real and complex domain 27
Table 2 – Conversion of variables for the two-axis model 30
Table 3 – Two-Axis Model: Comparison between algebraic equations in the real and complex domain 36
Table 4 – Two-Axis Model: Comparison between differential equations in the real and complex domain 37
Table 5 – Two-Axis Model: Constants used in the complex-domain formulation . . 38
Table 6 – Line data for 3-bus test system 70
Table 7 – Bus data for 3-bus test system 70
Table 8 – Bus report for 3-bus test system 71
Table 9 – Branch report for 3-bus test system 71
Table 10 – Machine data for 3-bus test system 72
Table 11 – Converted machine data for 3-bus test system 72
Table 12 – Initial operating conditions - 3-bus test system 73
Table 13 – Computational performance comparison (two-axis model). 96

List of abbreviations and acronyms

ACEKF	Augmented Complex-Valued Extended Kalman Filter
CKF	Cubature Kalman Filter
COI	Center of Inertia
CV	Complex-Valued
D-EKF	Decoupled Extended Kalman Filter
DER	Distributed Energy Resources
DSE	Dynamic State Estimator
EKF	Extended Kalman Filter
EnKF	Ensemble Kalman Filter
ERCOT	Electric Reliability Council of Texas
FACTS	Flexible AC Transmission System
FASE	Forecasting-Aided State Estimation
HVDC	High-Voltage Direct Current
IEEE	Institute of Electrical and Electronics Engineers
IRLS	Iteratively Reweighted Least Squares
KF	Kalman Filter
LAV	Least Absolute Value
LP	Leverage Point
NERC	North American Electric Reliability Corporation
PF	Particle Filter
PFR	Primary Frequency Response
PMU	Phasor Measurement Unit
PSSE	Power System Simulator for Engineering
PV	Photovoltaic
ROCOF	Rate of Change of Frequency
RV	Real-Valued
SCADA	Supervisory Control and Data Acquisition
SG	Synchronous Generator
SHGM	Schweppe-type Huber Generalized Maximum-likelihood

SIN	Brazilian Interconnected Power System
SSE	Static State Estimator
UKF	Unscented Kalman Filter
WLS	Weighted Least Squares

List of symbols

$(\ \bar{\cdot}\ )$	Denotes a variable represented in the complex-domain formulation
$\lceil\ \cdot\ \rceil$	Denotes the entire part
$(\ \cdot\ )_{k\|k-1}$	Denotes the state *a priori*
$(\ \cdot\ )_{k\|k}$	Denotes the state *a posteriori*
$(\ \cdot\ )^*$	Denotes the complex conjugate
$(\ \cdot\ )^H$	Denotes the transposed conjugate, i.e., the Hermitian operator
$(\ \cdot\ )^T$	Denotes the transposed
$(\ \cdot\ )^\dagger$	Denotes the pseudo-inverse of Moore-Penrose
$\|\ \cdot\ \|_\infty$	Infinite norm
$\mathbb{E}\{\ \cdot\ \}$	Denotes the mathematical expectation
$\mathfrak{I}(\ \cdot\ )$	Denotes the imaginary part
$\mathfrak{R}(\ \cdot\ )$	Denotes the real part
$sign(\ \cdot\ )$	Denotes the sign

Contents

1 INTRODUCTION . . . 14
1.1 Motivation . . . 14
1.1.1 Real-time Control and Monitoring Centers for Transmission Systems . . . 14
1.2 Dynamic State Estimator: Literature Review . . . 16
1.3 Network Analysis Applications in the Complex Domain . . . 18
1.3.1 General Objective . . . 20
1.3.2 Specific Objectives . . . 20
1.4 Thesis Contributions . . . 21
1.5 Thesis Organization . . . 23
1.6 Notation Definitions . . . 23

2 ALGEBRAIC-DIFFERENTIAL MODEL OF SYNCHRONOUS MACHINES IN THE COMPLEX DOMAIN . . . 24
2.1 Classical Model . . . 24
2.2 Two-Axis Model . . . 28

3 FORMULATION OF KALMAN FILTERS IN THE COMPLEX DOMAIN . . . 39
3.1 Complex-Valued Extended Kalman Filter (CV-EKF) . . . 39
3.1.1 Decoupled Complex-Valued Extended Kalman Filter (CV-D-EKF) . . . 43
3.2 Complex-Valued Unscented Kalman Filter (CV-UKF) . . . 50
3.3 Robustification of Kalman Filters . . . 53
3.3.1 Complex-Valued Schweppe-type Huber Generalized Maximum-likelihood Extended Kalman Filter (CV-SHGM-EKF) . . . 54
3.3.2 Complex-Valued Schweppe-type Huber Generalized Maximum-likelihood Unscented Kalman Filter (CV-SHGM-UKF) . . . 59

4 FREQUENCY ESTIMATION . . . 62
4.1 Power System Frequency Control . . . 63
4.2 Frequency Response . . . 64
4.3 The Estimations of Center of Inertia Frequency, ROCOF, and the Disturbance's Size (MW) . . . 66
4.3.1 Center of Inertia Frequency ($\mathbf{f_{COI}}$) . . . 66
4.3.2 Rate of Change of Frequency (ROCOF) . . . 67
4.3.3 Disturbance's Size - ΔP_{dist} (MW) . . . 67

5 NUMERICAL RESULTS 69
5.1 3-bus Test System 70
5.1.1 Preliminary Calculations 71
5.1.2 Construction of Kalman Filters 73
5.1.3 Dynamic State Estimation - 3-bus Test System 74
5.1.3.1 Scenario 1: Absence of Communication Failures and Gross Errors 74
5.1.3.2 Scenario 2: Loss of Communication Link of the PMU of Bus 1 77
5.1.3.3 Scenario 3: Impulse in the $\bar{S}_2$ 80
5.1.3.4 Scenario 4: Center of Inertia Frequency Estimation 83
5.2 IEEE 39-Bus Test System 86
5.3 Computational Performance Analysis 95

6 GENERAL CONCLUSIONS 100
6.1 Future Works 101
6.2 Publications 102

BIBLIOGRAPHY 104

APPENDIX 114

APPENDIX A – ANALYSIS OF COMPLEX FUNCTIONS AND VARIABLES 115
A.1 Differentiability of Complex Functions 115
A.2 Wirtinger Calculus or *CR-Calculus* 116

APPENDIX B – DERIVATIVES AND JACOBIAN MATRICES FOR THE DYNAMIC STATE ESTIMATOR FORMULATED IN THE COMPLEX DOMAIN 120
B.1 Classical Model 120
B.2 Two-Axis Model 121

1 Introduction

1.1 Motivation

In recent decades, the increasing demand for electrical energy has fueled the search for more reliable and efficient energy generation, transmission, and distribution systems. Enhancing real-time monitoring of electrical power systems is crucial for the continuous and safe supply of energy to various applications, e.g., industrial, commercial, and residential.

However, ensuring the reliable real-time operation of these systems is a complex challenge, especially given the ongoing transformations in the electrical grid. The existence of Distributed Energy Resources (DERs), FACTS (Flexible AC Transmission Systems) devices, responsive loads, and microgrids introduces uncertainty into the dynamic characteristics of electrical power systems [1].

In addition to these factors, the increasing adoption of power electronics implies faster system response to disturbances, requiring a control and monitoring infrastructure capable of operating at the same speed. In this scenario, protection functions based on conventional characteristics, such as high fault currents, may not be the most appropriate [2, 3]. This transition requires constant updating of real-time operation and monitoring applications for electrical systems.

Another relevant point is that the modern wide-area measurement systems are transitioning to obtaining synchronized phasor measurements via PMUs (Phasor Measurement Units) [4, 5]. In contrast to SCADA (Supervisory Control and Data Acquisition) measurements, PMU measurements are obtained at a high sampling rate, providing vital information such as the local frequency and the Rate of Change of Frequency (ROCOF) [6]. Such particularities enable more reliable, robust real-time monitoring of transient phenomena. However, the effective use of these measurements requires estimation frameworks that can integrate high-rate data with dynamic system models.

1.1.1 Real-time Control and Monitoring Centers for Transmission Systems

Currently, in operational control centers, the monitoring and operation of electrical power systems are typically carried out using static state estimators [7]. Fred Schweppe introduced the concept of a state estimator in 1970 [8], and since then, it has been widely developed and refined in the academic literature. The primary method applied in these estimators is the *Weighted Least Squares* (WLS), which minimizes the error between the actual and estimated measurements [9].

These static applications use measurements from the SCADA system as the primary source of information. The premise of static estimation is that the system operates in a steady state, allowing the algebraic states of the network to be estimated, such as the magnitude and angle of the bus voltage. In exceptional cases, it is also possible to calculate the position of transformer taps and the firing angle of converters. However, given the increasing dynamism of the power grid due to the increase in FACTS devices and distributed networks, estimates based on steady-state operation are not the best alternatives for monitoring and controlling the power grid [10].

The measurement rate in a SCADA system varies depending on the type of data acquisition. Traditional SCADA systems typically sample measurements only once per interval greater than 1 second, providing a steady-state view of the power system's behavior [11]. In contrast, PMUs offer higher sampling frequencies, typically 30-60 samples per second, thereby enabling more accurate and dynamic power grid monitoring [12].

These different sampling rates are critical to accurate state estimation in power systems, as measurement errors may lead to misleading economic dispatch decisions, faulty contingency analyses, and other important calculations [13]. Integrating data from both low-sampling-rate SCADA systems and high-sampling-rate PMUs through multi-sensor multi-rate data fusion techniques can increase the reliability and efficiency of power system operation, especially during transient events [14]. In this context, hybrid measurement-based estimation approaches have demonstrated improved numerical conditioning and enhanced robustness when combining conventional SCADA data with synchronized phasor measurements [15, 16].

Static estimators must be able to identify and suppress erroneous measurements that often result from failures in measurement equipment or errors in model parameterization. In the literature, the term robust estimator [17, 18, 19] is used to describe estimators capable of handling gross errors, even in measurements classified as leverage points. This concept is important throughout this thesis and is discussed in Chapter 3.

The points raised summarize some of the main aspects of the traditional methodology for monitoring and control in operational centers. However, as the network's dynamism increases, it becomes necessary to use tools that can operate within transient time windows. In addition, improving the traditional state estimation methodology is required to enable operators to make more assertive, proactive decisions in control centers. In this context, the dynamic state estimator is an essential application for the future of control centers and remote monitoring of electrical systems.

1.2 Dynamic State Estimator: Literature Review

The dynamic state estimator (DSE) has emerged as a powerful tool to meet the operational need for real-time monitoring of increasingly fast functionalities and controls. Although it was initially proposed in the 1970s [20, 21], much of the progress in the academic literature has occurred in recent decades. This type of estimator allows monitoring operational oscillations and estimating dynamic parameters, such as machine speed and transient voltages. In addition, it is also possible to identify unknown control variables and detect operational anomalies [22].

The structure of a DSE seeks to encompass all the dynamic particularities of a power system, including parameter and control variability. In this context, the time derivatives of a set of algebraic and differential equations describe the network's dynamics. For synchronous machines, these equations represent the electromagnetic and electromechanical processes associated with their respective controls [23]. In addition, DSE allows modeling generators with voltage and speed regulators and turbine models, capturing slow dynamics for more accurate system monitoring compared to static methods [22]. Understanding the process and control complexities of synchronous machines is crucial to devising a practical dynamic state estimator capable of overcoming the challenges of those power systems.

Today, as renewable energy sources are increasingly integrated into the electrical system, grid inertia is decreasing, potentially compromising frequency stability. Despite this, system inertia is not yet routinely monitored or predicted in real time in most operational control centers. This aspect is relevant when evaluating the impact of integrating these renewable resources asynchronously into the grid. In this sense, the dynamic estimator can estimate the frequency of the buses, ROCOF (Rate of Change of Frequency), and the frequency of the center of inertia (COI - Center of Inertia) of the system [22].

In addition, dynamic state estimators primarily use synchronized phasor measurements. PMUs provide accurate, highly synchronized measurements at sampling rates of 30-60 samples per second. The increased sampling rate enables detailed capture of the system's inherent oscillations and transients, providing more accurate and dynamic modeling of electrical system behavior. The scope of the measuring instruments of a DSE also covers smart meters [24] and micro PMUs [25].

In this context, dynamic state estimation—historically rooted in the Forecasting-Aided State Estimation (FASE) framework [26]—has evolved to exploit synchronized measurements better. While traditional FASE-type estimators were initially developed for slow-sampled SCADA data, modern formulations leverage PMU data to provide improved numerical robustness and enhanced tracking of electromechanical dynamics [27]. More recently, the literature has provided a comprehensive overview of these dynamic

techniques, encompassing both phasor- and Kalman-filter-based approaches, and has outlined the ongoing challenges in the field [28, 29].

Typically, engineers implement DSEs based on the Kalman filter algorithm, which uses a series of time-observed data, along with noise and other imprecision, to estimate the states of a dynamic system [30]. In this context, the DSE has two classes of algorithms: algorithms with and without linearizations. In the first class, expansions in the Taylor series are made to circumvent the nonlinearity of the evaluated functions. In contrast, for the second class, sampling points are chosen to be propagated by the nonlinear model, promoting the estimation of the posterior state [1].

In this scenario, the EKF (Extended Kalman Filter) is the main linearization-based algorithm used for the DSE. Academic literature presents several applications of this filter. Fan and Wehbe demonstrate the application of the EKF for estimating states and parameters by decoupling measurements [31]. In [32], the authors report using parallel computing to optimize the filter's computational cost. In this context, the comparative study in [33] shows that the EKF achieves faster execution time than its peers, the UKF (Unscented Kalman Filter), PF (Particle Filter), and EnKF (Ensemble Kalman Filter). However, this type of algorithm has some limitations because it is sensitive to the accuracy of the system model, the initial conditions, and the nature of the noise present in the measurements. The performance of the EKF can be significantly impaired, especially when there is a high nonlinear relationship in the evaluated model, that is, when it is impossible to neglect higher-order terms of the Taylor series expansion [30].

On the other hand, UKF is an alternative method that addresses the drawbacks of linearization. This algorithm uses the propagation of sigma points, a set of sample points. The nonlinear model determines the mean and covariance of these samples using a procedure called the unscented transformation [34]. For example, Qi *et al.* [35] show an improved version of the UKF to deal with numerical instability. In [36], the authors demonstrate the applicability of the UKF for distribution systems. Despite compensating for the EKF's weaknesses and avoiding linearizations, the Unscented Kalman filter may have its computational performance compromised by sigma-point propagation, depending on the process's scale.

Another aspect to consider during implementation is the network monitoring structural hierarchy. In this context, centralized or decentralized structures are the traditional hierarchical framework of dynamic state estimators. The centralized form indicates that a central system processes all measurements or observations. Thus, a global view of the system forms the basis for all operational decisions [1]. However, this methodology requires knowledge of all system parameters and controls and relies on centralized communication, which, in turn, is vulnerable to failures, potentially compromising the estimation process.

In this context, several applications of centralized DSE have been reported in the

academic literature. In [37], the performance of the EKF algorithm with unknown input data is demonstrated using PMU measurements, while in [38], the authors demonstrate superior performance and robustness with the UKF algorithm. On the other hand, Paul *et al.* [39] evaluate the vulnerabilities of centralized estimation under interruptions and communication delays in a DSE.

On the other hand, in the decentralized approach, measurements are processed locally in different nodes or agents of the system. This type of implementation can be helpful when centralized communication is difficult, costly, or vulnerable. In addition, it is only necessary to know the parameters and controls locally, thereby improving computational efficiency during implementation. However, the lack of local redundancy, as found in telemetry systems, can compromise the quality of the estimation and monitoring processes [1].

Researchers study this type of estimator for applications with unknown input variables [40], transmission lines [41], renewable energy [42, 43], protection [3, 44], among others. In [45], the authors show estimates with non-Gaussian noise using *Particle Filtering* (PF) and process outliers based on the measurement history. However, this decentralized methodology is complex in terms of data communication and coordination, which creates security risks, such as cyberattacks.

In addition to the aspects raised, implementing an effective and reliable dynamic state estimator requires improving the tool's robustness against gross errors in measurements, parameters, or estimates [46]. In [47], the authors present the implementation of the Extended Kalman Filter (EKF) with robustness against errors originating from measurement processes (*Observation outliers*) and against errors related to the state prediction model (*Innovation outliers*). Analogously, the Unscented Kalman filter based on the *Generalized Maximum-Likelihood* approach [48] is capable of dealing with unknown statistics of the noises involved in the estimation processes [49], and also with unknown input variables [50].

1.3 Network Analysis Applications in the Complex Domain

Given the initial considerations addressed, it is essential to emphasize that, since the beginning (approximately seven decades), the numerical solution of network analysis applications has invariably occurred in the real number domain; power flow and state estimation applications stand out among others. However, such a procedure is not natural, since the solution of alternating current (AC) networks is performed in the frequency domain, that is, via the voltage- and current-phasor system introduced by Steinmetz [51].

In this context, researchers have begun developing power-flow applications in the complex domain in recent years. Pires *et al.* [52] report the efficiency of these applications

in solving the power flow of ill-conditioned systems, in addition to explaining the exact solution of the problem based on the property of the Hessian matrix of the load flow [53]. This formulation has recently been extended to include FACTS devices by incorporating direct current networks and HVDC links [54]. The numerical migration of power flow applications has led to mathematical simplification in implementation, while providing more efficient results and computational gains.

The academic literature also illustrates applications of state estimation in complex-conjugate coordinates. These estimators use the *Wirtinger Calculus* [55] to enable the numerical analysis of the problem. The classical static state estimator WLS (*Weighted Least Squares*) in the complex number domain stands out for its ease of implementation [56], its efficiency in processing gross errors and zero injections [57], and has also been studied for applications in distribution systems [58].

In addition to the classic formulation (WLS), Pires *et al.* [59] proposed the robust static estimation SHGM (*Schweppe-type Huber Generalized Maximum-likelihood*) in this new numerical domain based on the theory expressed in [60] and [18]. Such estimators demonstrate efficiency against gross errors, including leverage points. Furthermore, implementation within the complex-domain framework becomes more advantageous as the inclusion of synchronized phasor measurements increases.

However, given the global trend towards hybrid networks, dynamic state estimation is a necessary evolution for the future of network analysis applications present in control centers [1]. The presence of distributed energy resources, FACTS devices, responsive loads, and microgrids implies that electrical networks exhibit diverse dynamics; therefore, the applicability of various remote monitoring methodologies must be studied. In this context, dynamic estimation in the complex-conjugate coordinate system has not yet been developed. Considering the demonstrated flexibility and efficiency of network applications formulated in the complex domain, dynamic estimation in complex-conjugate coordinates is a promising avenue for investigation.

Signal processing studies apply the EKF and UKF algorithms in this new numerical domain. In [61], the authors present the equations of the primary Kalman filters for complex-valued signals. Mandic *et al.* [62] demonstrate the use of the *Augmented Complex-Valued Extended Kalman Filter* (ACEKF) for neural networks. Conversely, the authors in [63] propose a generalization of the Unscented Kalman Filter algorithm to deal with statistical particularities of complex signals, including non-circular and improper complex signals [64, 65].

1.3.1 General Objective

The general objective of this thesis is to develop, formulate, and validate a dynamic state estimation framework for electrical power systems in complex-conjugate coordinates. The proposed framework exploits the phasor nature of electrical quantities to provide a mathematically consistent alternative to conventional real-valued formulations. It assesses its accuracy, robustness, and computational scalability under both normal and adverse measurement conditions.

1.3.2 Specific Objectives

To achieve this general objective, the following specific objectives are pursued:

1. To formulate algebraic-differential models of synchronous machines directly in complex-conjugate coordinates, including both the classical model and the ninth-order two-axis model equipped with excitation and turbine-governor controls.

2. To derive state-transition and measurement models in the complex domain using Wirtinger calculus, allowing nonlinear functions involving complex variables and their conjugates to be handled consistently.

3. To extend the Extended Kalman Filter (EKF) and the Unscented Kalman Filter (UKF) to the complex-domain DSE problem. These two algorithms are selected because they represent complementary classes of Kalman-filter-based estimators: the EKF is a computationally efficient linearization-based method widely used in power system DSE, whereas the UKF is a derivative-free alternative that better handles nonlinear transformations at the cost of propagating sigma points.

4. To propose a Decoupled Complex-Valued EKF (CV-D-EKF) that exploits the structural symmetry of the augmented complex formulation to reduce redundant operations, especially in the covariance propagation and update stages.

5. To extend SHGM-based robust dynamic state estimation to the complex domain, enabling the proposed estimators to handle gross errors, communication failures, observation outliers, innovation outliers, and bad leverage points.

6. To evaluate the use of the proposed DSE framework for frequency-security applications, including the estimation of the center-of-inertia frequency, ROCOF, and disturbance-size indicators as byproducts of the estimated dynamic states.

7. To validate the proposed formulations through numerical simulations on the IEEE 3-bus, IEEE 39-bus, IEEE 118-bus, and a 340-bus equivalent of the Brazilian Interconnected Power System (SIN), hereafter referred to as the SIN-340 system,

comparing real-valued and complex-valued implementations in terms of accuracy, robustness, computational cost, and scalability.

1.4 Thesis Contributions

Dynamic state estimation methods reported in the power systems literature are traditionally formulated in the real-valued numerical domain. Although this representation is well established, it does not directly exploit the phasor nature of voltages and currents, which are inherently complex-valued quantities. Previous complex-domain formulations in power systems have been mainly restricted to static applications, such as power flow and static state estimation. Therefore, a complete dynamic state estimation framework in complex-conjugate coordinates, including dynamic modeling, Kalman filtering, robust estimation, computational analysis, and frequency-security assessment, has not yet been fully established.

To address this gap, this thesis develops a complex-valued DSE framework for electrical power systems. The main and original contributions are summarized as follows:

1. **Formulation of dynamic models in complex-conjugate coordinates.** This thesis develops the algebraic-differential models of synchronous machines directly in the complex domain, including the classical model and the ninth-order two-axis model with excitation and turbine-governor controls. This formulation provides a phasor-native representation of the dynamic estimation problem and enables the use of Wirtinger calculus for functions involving complex variables and their conjugates.

2. **Extension of EKF and UKF algorithms to complex-valued DSE.** The Extended Kalman Filter and the Unscented Kalman Filter are extended to the complex-domain formulation. These algorithms were selected because they represent two complementary estimation strategies: the EKF is a widely used linearization-based estimator with relatively low computational cost, whereas the UKF is a derivative-free alternative that better handles nonlinear transformations but requires sigma-point propagation. This comparison allows the advantages and limitations of the complex-domain formulation to be assessed for both estimator classes.

3. **Proposal of the Decoupled Complex-Valued EKF.** A Decoupled Complex-Valued EKF (CV-D-EKF) is proposed to reduce the computational burden of the standard augmented CV-EKF. The method exploits the mirror symmetry of the complex-conjugate formulation to avoid redundant operations without introducing additional approximations. Numerical results show execution-time reductions of up to 68% compared with the full augmented CV-EKF, making linearization-based complex-domain estimation computationally viable for large-scale systems. Its main

limitation is that, even after decoupling, complex-valued covariance propagation may still be more demanding than in the real-valued EKF.

4. **Demonstration of the computational cross-over of complex-valued UKF estimators.** For sigma-point-based estimators, the complex-domain formulation reduces the effective state dimension and, consequently, the number of propagated sigma points and nonlinear function evaluations. In large-scale systems, this dimensional reduction outweighs the overhead of complex arithmetic. In the SIN-340 system, the complex-valued UKF achieved execution times approximately 29% lower than the real-valued UKF. However, the non-robust UKF is more sensitive to bad data and measurement inconsistencies, indicating that robustification is required for adverse operating conditions.

5. **Extension of SHGM-based robust filtering to the complex domain.** This thesis extends the SHGM-based robust EKF and UKF formulations to complex-valued dynamic state estimation. The proposed robust estimators use projection statistics and IRLS-based weighting to reduce the influence of gross errors, communication failures, observation outliers, innovation outliers, and bad leverage points. The main advantage is improved reliability in the presence of corrupted PMU data, while the main drawback is the additional computational effort required by the robust weighting procedure.

6. **Frequency-security indicators as byproducts of DSE.** The proposed framework also enables the estimation of center-of-inertia frequency, ROCOF, and indicators of disturbance size directly from the estimated dynamic states, without requiring a dedicated frequency-estimation module. This contribution connects dynamic state estimation with real-time frequency monitoring, which is particularly relevant for wide-area monitoring, under-frequency load shedding, and fast corrective control in low-inertia power systems.

7. **Comprehensive validation on benchmark and large-scale systems.** The proposed methods are validated on the IEEE 3-bus, IEEE 39-bus, IEEE 118-bus, and SIN-340 systems. The results show that the complex domain is not automatically superior for all estimators; its advantages depend on the estimator structure. For EKF-based methods, decoupling is necessary to reduce computational burden, whereas for UKF-based methods, dimensionality reduction yields clear scalability gains in large-scale systems. For adverse measurement conditions, SHGM-based robustification is essential to preserve estimation accuracy.

Overall, this thesis shows when and how complex-conjugate coordinates can be advantageous for dynamic state estimation in power systems. The main contribution

is therefore not only the use of complex arithmetic, but the development of estimator structures that exploit the benefits of the complex domain while explicitly addressing its computational and robustness limitations.

1.5 Thesis Organization

This thesis is organized as follows. Chapter 2 presents the algebraic-differential modeling of synchronous machines in the complex domain, including the classical and two-axis models, and establishes the mathematical basis for the proposed phasor-based dynamic representation. Chapter 3 develops the complex-valued Kalman filtering framework, including the EKF, UKF, Decoupled EKF, and their robust SHGM-based versions. Chapter 4 discusses frequency estimation and shows how center-of-inertia frequency, ROCOF, and disturbance-size indicators can be obtained from the dynamic state estimator. Chapter 5 presents the numerical results, beginning with the IEEE 3-bus system for detailed validation and then extending the analysis to the IEEE 39-bus, IEEE 118-bus, and SIN-340 bus systems to assess robustness and computational scalability. Finally, Chapter 6 summarizes the main conclusions of the thesis and outlines possible directions for future research.

1.6 Notation Definitions

In this thesis, vectors are denoted by lowercase bold Roman letters (e.g., $\boldsymbol{y}$) or lowercase bold Greek letters (e.g., $\boldsymbol{\psi}$).

On the other hand, matrices are denoted with Roman letters (e.g., $\boldsymbol{Y}$) or Greek letters (e.g., $\boldsymbol{\Psi}$) in uppercase bold letters.

Vectors, by definition, are column vectors unless transposition is indicated.

$$\boldsymbol{y} = \begin{bmatrix} y_1 \\ y_2 \\ y_3 \\ \vdots \end{bmatrix}, \qquad \boldsymbol{y}^T = [y_1, y_2, y_3, \dots].$$

2 Algebraic-Differential Model of Synchronous Machines in the Complex Domain

This chapter presents the algebraic-differential model of synchronous machines formulated in the complex domain. This modeling is the first step in developing a dynamic state estimator in the complex-conjugate coordinate system. This work evaluates two synchronous machine models, the classical model and the two-axis model [66]. The proposed formulation aims to reduce the number of state and control variables. Furthermore, it satisfies the differentiability criteria of functions of complex variables proposed by Cauchy-Riemann [55], through the Wirtinger calculus or *CR-Calculus* [67]. The Appendix A briefly explains the holomorphism of complex variable functions.

2.1 Classical Model

Synchronous machines are vital for the creation and operation of electrical power systems that generate most of the world's electricity. It is essential to understand the dynamic behavior of synchronous machines to control these systems effectively. The classical model of a synchronous machine provides a simplified representation of the electromagnetic and mechanical phenomena within the machine [68].

The representation of the classical model of a synchronous machine is a set of differential equations expressed in the equations (2.1) and (2.2) [66].

$$\frac{d\delta}{dt} = \omega - \omega_s, \tag{2.1}$$

$$\frac{d\omega}{dt} = \frac{\omega_s}{2 \cdot H} \cdot \left(T_M - T_e - D \cdot (\omega - \omega_s)\right). \tag{2.2}$$

where δ, ω, T_M, and T_e are the angle of the internal voltage of the machine, the angular speed of the rotor, the mechanical torque, and the electrical torque of each synchronous machine, respectively. The constant H represents the inertia of each machine, and the coefficient D represents the mechanical damping. The synchronous angular velocity of the rotor is expressed by ω_s.

The electrical power is defined as

$$P_e = \omega \cdot T_e. \tag{2.3}$$

As ω remains close to the synchronous speed $\omega_s = 1$ [pu], the approximation $T_e \approx P_e$ is usually adopted in (2.2).

The equation (2.4) expresses the internal voltage, and the (2.5) expresses each synchronous machine's electrical power.

$$\bar{E}_i = E_i \angle \delta_i = \bar{V}_i + \left(R_{a_i} + j \cdot X'_{d_i}\right) \cdot \bar{I}_i, \tag{2.4}$$

$$\begin{aligned} P_{e_i} &= \Re\{\bar{E}_i \cdot \bar{I}_i^*\} = \Re\{\bar{E}_i \cdot \left(\bar{Y}^{red} \cdot \bar{E}_i\right)^*\} \\ &= E_i^2 \cdot G_{ii}^{red} + \sum_{j=1}^{n} E_i \cdot E_j \cdot \left|\bar{Y}_{ij}^{red}\right| \cdot cos\left(\delta_{ij} - \varphi_{ij}\right), \end{aligned} \tag{2.5}$$

where $\bar{E}$ and $\bar{I}$ represent the excitation voltage and current phasors; $\bar{V}$ represents the terminal voltage phasor; R_a and X'_d represent the armature resistance and direct-axis transient reactance; G_{ii}^{red} and $\left|\bar{Y}_{ij}^{red}\right|$ represent the absolute value of the elements of the conductance and admittance matrices originating from the reduction of the passive network via the Kron's reduction method; φ represents the angular value of the element of the reduced admittance matrix, respectively [68].

To begin modeling in the complex-conjugate coordinate system, equation (2.6) expresses a complex variable $\bar{\alpha}$.

$$\bar{\alpha} = \delta + j \cdot (\omega - \omega_s) = \delta + j \cdot \Delta\omega. \tag{2.6}$$

This formulation aims to simplify the proposed problem by grouping the real variables in pairs. During the model's development, several types of complex variables were tested, including phasors, trigonometric functions, and nonlinear functions. However, grouping real variables in rectangular coordinates was the most straightforward way. This approach easily generalizes to all models evaluated in this study.

Although the variable $\bar{\alpha}$ has no direct physical meaning—since it combines rotor angle and speed deviation—it provides a convenient mathematical representation within the complex-conjugate framework. By grouping δ and $\Delta\omega$ into a single complex state, the swing equations are expressed compactly, enabling the direct application of Wirtinger calculus for linearization-based methods such as the Extended Kalman Filter (EKF). This guarantees analytical Jacobian derivation in the complex domain while preserving the consistency of the unified formulation. Then, deriving (2.6) in time, results:

$$\bar{f}_1 = \frac{d\bar{\alpha}}{dt} = \frac{d\delta}{dt} + j \cdot \frac{d\omega}{dt}. \tag{2.7}$$

Now, considering δ and $\Delta\omega$ expressed as a function of $\bar{\alpha}$:

$$\delta = (\bar{\alpha} + \bar{\alpha}^*) \cdot 0.5, \tag{2.8}$$

$$\Delta\omega = j \cdot (\bar{\alpha}^* - \bar{\alpha}) \cdot 0.5, \tag{2.9}$$

and substituting (2.8) and (2.9) into (2.1) and (2.2), the equation (2.7) becomes:

$$\begin{aligned} \bar{f}_1 = \frac{d\bar{\alpha}}{dt} = & \overbrace{-0.5 \cdot \left(\frac{D \cdot \omega_s}{2 \cdot H} + j\right)}^{\bar{\mathcal{A}}_1} \cdot \bar{\alpha} + 0.5 \cdot \left(\frac{D \cdot \omega_s}{2 \cdot H} + j\right) \cdot \bar{\alpha}^* \\ & + \underbrace{j \cdot \frac{\omega_s}{2 \cdot H}}_{\bar{\mathcal{A}}_2} \cdot T_M - j \cdot \frac{\omega_s}{2 \cdot H} \cdot P_e, \end{aligned} \tag{2.10}$$

in compact form:

$$\bar{f}_1 = \frac{d\bar{\alpha}}{dt} = \bar{\mathcal{A}}_1 \cdot \bar{\alpha} - \bar{\mathcal{A}}_1 \cdot \bar{\alpha}^* + \bar{\mathcal{A}}_2 \cdot T_M - \bar{\mathcal{A}}_2 \cdot P_e. \tag{2.11}$$

The electrical power, in turn, is calculated as a byproduct of the apparent power,

$$\bar{S}_{e_i} = \bar{E}_i \cdot \bar{I}_i^* = \bar{E}_i \cdot \left(\bar{Y}^{red} \cdot \bar{E}_i\right)^*, \tag{2.12}$$

$$P_{e_i} = 0.5 \cdot \left(\bar{S}_{e_i} + \bar{S}_{e_i}^*\right). \tag{2.13}$$

Replacing (2.13) in (2.11) results in the dynamic equation formulated in the complex domain for the classical model of a synchronous machine:

$$\bar{f}_1 = \frac{d\bar{\alpha}}{dt} = \bar{\mathcal{A}}_1 \cdot \bar{\alpha} - \bar{\mathcal{A}}_1 \cdot \bar{\alpha}^* - 0.5 \cdot \bar{\mathcal{A}}_2 \cdot \bar{S}_e - 0.5 \cdot \bar{\mathcal{A}}_2 \cdot \bar{S}_e^* + \bar{\mathcal{A}}_2 \cdot T_M. \tag{2.14}$$

In this initial model, there are no speed or turbine governors, and therefore, the mechanical torque is constant, making the previous equation dependent solely on complex variables.

This work will present formulations based on Jacobian matrices for constructing a dynamic state estimator. Thus, in the Appendix B, the derivatives for assembling each Jacobian matrix are shown based on the formulation detailed in this chapter.

Summarizing the presented formulation, Table 1 compares the formulations of the algebraic-differential model in the domain of real and complex numbers.

Table 1 – Classical Model: Comparison between the formulations in the real and complex domain

Differential equations		
Real Domain	**Complex Domain**	**Constants**
$\frac{d\delta}{dt} = \omega - \omega_s$ $\frac{d\omega}{dt} = \frac{\omega_s}{2 \cdot H} \cdot (T_M - P_e - D \cdot (\omega - \omega_s))$	$\frac{d\bar{\alpha}}{dt} = \bar{\mathcal{A}}_1 \cdot \bar{\alpha} - \bar{\mathcal{A}}_1 \cdot \bar{\alpha}^* - 0.5 \cdot \bar{\mathcal{A}}_2 \cdot \bar{S}_e - 0.5 \cdot \bar{\mathcal{A}}_2 \cdot \bar{S}_e^* + \bar{\mathcal{A}}_2 \cdot T_M$	$\bar{\mathcal{A}}_1 = -0.5 \cdot \left(\frac{D \cdot \omega_s}{2 \cdot H} + j\right)$ $\bar{\mathcal{A}}_2 = j \cdot \frac{\omega_s}{2 \cdot H}$
Algebraic equations		
Real Domain	**Complex Domain**	
$P_{e_i} = \Re\{\bar{E}_i \cdot \bar{I}_i^*\} = \Re\{\bar{E}_i \cdot \left(\bar{Y}^{red} \cdot \bar{E}_i\right)^*\}$	$\bar{S}_{e_i} = \bar{E}_i \cdot \bar{I}_i^* = \bar{E}_i \cdot \left(\bar{Y}^{red} \cdot \bar{E}_i\right)^*$	

2.2 Two-Axis Model

The two-axis model, also known as the d-q model, is widely used to analyze the dynamic characteristics of synchronous machines. It is a model that uses mathematical representations to convert the equations of the three-phase system into a rotating coordinate system. This, in turn, simplifies the analysis of the dynamic phenomena and their interrelation. This model uses the Park transformation, which converts the current, voltage, and magnetic flux variables of a three-phase system into direct (d) and quadrature (q) axis components [68].

Thus, consider the 9^{th} order two-axis model expressed by the differential equations (2.15)-(2.23) [69]. This model implements the IEEE DC1A voltage regulator [70] and the TGOV1 turbine speed regulator [71].

$$\frac{d\delta}{dt} = \omega - \omega_s, \tag{2.15}$$

$$\frac{d\omega}{dt} = \frac{\omega_s}{2 \cdot H} \cdot \left(T_M - T_e - D \cdot (\omega - \omega_s)\right), \tag{2.16}$$

$$\frac{dE_q^{'}}{dt} = \frac{1}{\tau_{d_0}^{'}} \cdot \left[-E_q^{'} - \left(X_d - X_d^{'}\right) \cdot I_d + E_{fd}\right], \tag{2.17}$$

$$\frac{dE_d^{'}}{dt} = \frac{1}{\tau_{q_0}^{'}} \cdot \left[-E_d^{'} + \left(X_q - X_q^{'}\right) \cdot I_q\right], \tag{2.18}$$

$$\frac{dE_{fd}}{dt} = \frac{1}{T_E} \cdot \left[-\left(K_E + \underbrace{S_E\left(E_{fd}\right)}_{U_x}\right) \cdot E_{fd} + V_R\right], \tag{2.19}$$

$$\frac{dV_R}{dt} = \frac{1}{T_A} \cdot \left[-V_R + K_A \cdot (V_{ref} - V_F - V)\right], \tag{2.20}$$

$$\frac{dV_F}{dt} = \frac{1}{T_F} \cdot \left[-V_F + \frac{K_F}{T_E} \cdot V_R - \frac{K_F}{T_E} \cdot \left(K_E + S_E\left(E_{fd}\right)\right) \cdot E_{fd}\right], \tag{2.21}$$

$$\frac{dT_M}{dt} = \frac{1}{T_{CH}} \cdot \left(-T_M + P_{SV}\right), \tag{2.22}$$

$$\frac{dP_{SV}}{dt} = \frac{1}{T_{SV}} \cdot \left[-P_{SV} + P_C - \frac{1}{R_D \cdot \omega_s} \cdot (\omega - \omega_s)\right]. \tag{2.23}$$

In the previous expressions, $\tau_{d_0}^{'}$ and $\tau_{q_0}^{'}$ represent the direct and quadrature axis time constants; T_E, T_F, T_A, T_{CH} and T_{SV} are time constants related to the regulators; K_E, K_F, K_A are the regulator gains; $S_E\left(E_{fd}\right) = U_x = A_{ex} \cdot e^{\left(B_{ex} \cdot E_{fd}\right)}$ is a voltage saturation

function with constants A_{ex} and B_{ex}; V_{ref} and P_C are known input variables; $E_d^{'}$, $E_q^{'}$, E_{fd}, and V represent the direct-axis and quadrature transient voltages, the field voltage, and the terminal voltage magnitude of the machine; V_R and V_F are the step-down outputs of the amplifier and the stabilizing transformer; T_M and P_{SV} are the mechanical torque and the steam valve position; R_D is the amount of speed regulation; X_d, $X_d^{'}$, X_q and $X_q^{'}$ represent the steady-state and transient reactances of the direct and quadrature axes; I_d and I_q represent the direct and quadrature axis currents, respectively [69].

On the other hand, equations (2.24)-(2.29) show the algebraic variables of this model.

$$V_d = V \cdot \sin\left(\delta - \theta\right), \tag{2.24}$$

$$V_q = V \cdot \cos\left(\delta - \theta\right), \tag{2.25}$$

$$I_d = \frac{E_q^{'} - V_q}{X_d^{'}}, \tag{2.26}$$

$$I_q = \frac{V_d - E_d^{'}}{X_q^{'}}, \tag{2.27}$$

$$P_e = V_d \cdot I_d + V_q \cdot I_q, \tag{2.28}$$

$$Q_e = -V_d \cdot I_q + V_q \cdot I_d, \tag{2.29}$$

where V_d and V_q represent the direct and quadrature axis voltage; θ the terminal voltage angle of the machine; P_e and Q_e the active and reactive power generated, respectively.

To begin the migration of the two-axis model to the complex domain, consider the variable conversion shown in Table 2. The idea behind the formulation is to pair the state variables of the conventional model to form a new complex variable. However, since this model has an odd number of state variables, the variable $\bar{\gamma}$ now depends exclusively on the field voltage (E_{fd}).

Consider initially the terminal-voltage expression for each machine in (2.30) [69].

$$\bar{V} = V\angle\theta = \left[\left(E_d^{'} + j \cdot E_q^{'}\right) + \left(X_q^{'} - X_d^{'}\right) \cdot I_q - j \cdot X_d^{'} \cdot \left(I_d + j \cdot I_q\right)\right] \cdot e^{j \cdot \left(\delta - \frac{\pi}{2}\right)}. \tag{2.30}$$

The conversion of algebraic variables (2.24)-(2.29) for the domain of complex numbers begins with the joining of the direct and quadrature axis voltages. Rewriting δ as a function of $\bar{\alpha}$ as proposed in Table 2 and substituting in the expressions (2.24) and (2.25),

Table 2 – Conversion of variables for the two-axis model

Real → Complex	**Complex → Real**
$\bar{\alpha} = \delta + j \cdot \Delta\omega$	$\delta = 0.5 \cdot (\bar{\alpha} + \bar{\alpha}^*)$ $\Delta\omega = j \cdot 0.5 \cdot (\bar{\alpha}^* - \bar{\alpha})$
$\bar{\beta} = E'_q + j \cdot E'_d$	$E'_q = 0.5 \cdot \left(\bar{\beta} + \bar{\beta}^*\right)$ $E'_d = j \cdot 0.5 \cdot \left(\bar{\beta}^* - \bar{\beta}\right)$
$\bar{\gamma} = E_{fd}$	$E_{fd} = 0.5 \cdot (\bar{\gamma} + \bar{\gamma}^*)$
$\bar{\lambda} = V_R + j \cdot V_F$	$V_R = 0.5 \cdot \left(\bar{\lambda} + \bar{\lambda}^*\right)$ $V_F = j \cdot 0.5 \cdot \left(\bar{\lambda}^* - \bar{\lambda}\right)$
$\bar{\mu} = T_M + j \cdot P_{SV}$	$T_M = 0.5 \cdot (\bar{\mu} + \bar{\mu}^*)$ $P_{SV} = j \cdot 0.5 \cdot (\bar{\mu}^* - \bar{\mu})$

one arrives at the expression (2.31).

$$\bar{V}_{qd} = V_q + j \cdot V_d = V \cdot e^{j \cdot (\delta - \theta)} = V \cdot e^{j \cdot (0.5 \cdot (\bar{\alpha} + \bar{\alpha}^*) - \theta)}, \tag{2.31}$$

or:

$$V_q = 0.5 \cdot \left(\bar{V}_{qd} + \bar{V}^*_{qd}\right), \tag{2.32}$$

$$V_d = j \cdot 0.5 \cdot \left(\bar{V}^*_{qd} - \bar{V}_{qd}\right). \tag{2.33}$$

Considering E'_d and E'_q as a function of $\bar{\beta}$, according to Table 2 and replacing (2.32) and (2.33) in (2.27) and (2.26), one gets the expressions:

$$I_d = \frac{0.5}{X'_d} \cdot \left(\bar{\beta} + \bar{\beta}^* - \bar{V}_{qd} - \bar{V}^*_{qd}\right), \tag{2.34}$$

$$I_q = \frac{j \cdot 0.5}{X'_q} \cdot \left(\bar{\beta} - \bar{\beta}^* + \bar{V}^*_{qd} - \bar{V}_{qd}\right). \tag{2.35}$$

This way, the expression for $\bar{I}_{qd} = I_q + j \cdot I_d$ will be:

$$\bar{I}_{qd} = \underbrace{j \cdot 0.5 \cdot \left(\frac{1}{X'_q} + \frac{1}{X'_d}\right)}_{\bar{\mathcal{K}}_1} \cdot \left(\bar{\beta} - \bar{V}_{qd}\right) + \underbrace{j \cdot 0.5 \cdot \left(\frac{-1}{X'_q} + \frac{1}{X'_d}\right)}_{\bar{\mathcal{K}}_2} \cdot \left(\bar{\beta}^* - \bar{V}^*_{qd}\right). \tag{2.36}$$

Rewriting in a compact form,

$$\bar{I}_{qd} = \bar{\mathcal{K}}_1 \cdot \bar{\beta} + \bar{\mathcal{K}}_2 \cdot \bar{\beta}^* - \bar{\mathcal{K}}_1 \cdot \bar{V}_{qd} - \bar{\mathcal{K}}_2 \cdot \bar{V}^*_{qd}. \tag{2.37}$$

Similarly, (2.38) express $\bar{I}^*_{qd}$.

$$\bar{I}^*_{qd} = -\bar{\mathcal{K}}_2 \cdot \bar{\beta} - \bar{\mathcal{K}}_1 \cdot \bar{\beta}^* + \bar{\mathcal{K}}_2 \cdot \bar{V}_{qd} + \bar{\mathcal{K}}_1 \cdot \bar{V}^*_{qd}. \tag{2.38}$$

Thus, equations (2.39) and (2.40) present the direct and quadrature axis currents, respectively.

$$I_d = j \cdot 0.5 \cdot \left(\bar{I}^*_{qd} - \bar{I}_{qd}\right), \tag{2.39}$$

$$I_q = 0.5 \cdot \left(\bar{I}_{qd} + \bar{I}^*_{qd}\right). \tag{2.40}$$

Finally, the terminal voltage of each machine expressed in (2.30) becomes:

$$\begin{aligned}
\bar{V} = V\angle\theta &= \left[j \cdot \bar{\beta}^* + \left(X'_q - X'_d\right) \cdot 0.5 \cdot \left(\bar{I}_{qd} + \bar{I}^*_{qd}\right) + X'_d \cdot \bar{I}^*_{qd}\right] \cdot e^{j\cdot\left(0.5(\bar{\alpha}+\bar{\alpha}^*)-\frac{\pi}{2}\right)} \\
&= \left[j \cdot \bar{\beta}^* + 0.5 \cdot \left(X'_q - X'_d\right) \cdot \bar{I}_{qd} + 0.5 \cdot \left(X'_q + X'_d\right) \cdot \bar{I}^*_{qd}\right] \cdot e^{j\cdot\left(0.5(\bar{\alpha}+\bar{\alpha}^*)-\frac{\pi}{2}\right)} \\
&= \left[\bar{\beta}^* - \underbrace{j \cdot 0.5 \cdot \left(X'_q - X'_d\right)}_{\bar{\mathcal{K}}_3} \cdot \bar{I}_{qd} - \underbrace{j \cdot 0.5 \cdot \left(X'_q + X'_d\right)}_{\bar{\mathcal{K}}_4} \cdot \bar{I}^*_{qd}\right] \cdot e^{j\cdot(0.5(\bar{\alpha}+\bar{\alpha}^*))} \\
&= \left[\bar{\beta}^* - \bar{\mathcal{K}}_3 \cdot \bar{I}_{qd} - \bar{\mathcal{K}}_4 \cdot \bar{I}^*_{qd}\right] \cdot e^{j\cdot(0.5(\bar{\alpha}+\bar{\alpha}^*))}.
\end{aligned} \tag{2.41}$$

On the other hand, equations (2.42) and (2.43) represent the complex and complex-conjugate electrical powers, respectively.

$$\begin{aligned}
\bar{S}_e &= \bar{V}^*_{qd} \cdot \bar{I}_{qd} = (V_q - j \cdot V_d) \cdot (I_q + j \cdot I_d) \\
&= (V_d \cdot I_d + V_q \cdot I_q) + j \cdot (-V_d \cdot I_q + V_q \cdot I_d), \\
&= P_e + j \cdot Q_e,
\end{aligned} \tag{2.42}$$

$$\begin{aligned}
\bar{S}^*_e &= \bar{V}_{qd} \cdot \bar{I}^*_{qd} = (V_q + j \cdot V_d) \cdot (I_q - j \cdot I_d), \\
&= (V_d \cdot I_d + V_q \cdot I_q) - j \cdot (-V_d \cdot I_q + V_q \cdot I_d)
\end{aligned}$$

$$= P_e - j \cdot Q_e. \tag{2.43}$$

The conversion of the differential equations (2.15)-(2.23) can be done in a manner analogous to the classical model by following the Table 2 for variable conversion. The equation of $d\bar{\alpha}/dt$ is expressed by (2.10). Assuming the approximation $T_e \approx P_e$ introduced in (2.3) and rewriting the mechanical torque as a function of $\bar{\mu}$ and $\bar{\mu}^*$ and the active power as a function of S_e, one has:

$$\bar{f}_1 = \frac{d\bar{\alpha}}{dt} = \bar{\mathcal{A}}_1 \cdot \bar{\alpha} - \bar{\mathcal{A}}_1 \cdot \bar{\alpha}^* + \bar{\mathcal{A}}_2 \cdot \bar{\mu} + \bar{\mathcal{A}}_2 \cdot \bar{\mu}^* - \bar{\mathcal{A}}_2 \cdot \bar{S}_e - \bar{\mathcal{A}}_2 \cdot \bar{S}_e^*, \tag{2.44}$$

where $\bar{\mathcal{A}}_1 = -0.5 \cdot \left(\frac{D \cdot \omega_s}{2 \cdot H} + j\right)$ and $\bar{\mathcal{A}}_2 = j \cdot 0.5 \cdot \frac{\omega_s}{2 \cdot H}$.

Then, the second differential equation in the complex-conjugate domain, $d\bar{\beta}/dt$, will be expressed by (2.45).

$$\bar{f}_2 = \frac{d\bar{\beta}}{dt} = \frac{dE_q^{'}}{dt} + j \cdot \frac{dE_d^{'}}{dt}, \tag{2.45}$$

Replacing (2.39) and (2.40) in (2.17) and (2.18), the (2.45) becomes:

$$\begin{aligned} \bar{f}_2 = {} & \frac{1}{\tau_{d_0}^{'}} \cdot \left[-0.5 \cdot \left(\bar{\beta} + \bar{\beta}^*\right) - \left(X_d - X_d^{'}\right) \cdot j \cdot 0.5 \cdot \left(\bar{I}_{qd}^* - \bar{I}_{qd}\right) + 0.5 \cdot (\bar{\gamma} + \bar{\gamma}^*)\right] \\ & + \frac{j}{\tau_{q_0}^{'}} \cdot \left[-j \cdot 0.5 \cdot \left(\bar{\beta}^* - \bar{\beta}\right) - \left(X_q - X_q^{'}\right) \cdot 0.5 \cdot (\bar{I}_{qd} + \bar{I}_{qd}^*)\right]. \end{aligned} \tag{2.46}$$

Rearranging the terms,

$$\begin{aligned} \bar{f}_2 = {} & \overbrace{-0.5 \cdot \left(\frac{1}{\tau_{d_0}^{'}} + \frac{1}{\tau_{q_0}^{'}}\right)}^{\bar{\mathcal{B}}_1} \cdot \bar{\beta} + \overbrace{0.5 \cdot \left(-\frac{1}{\tau_{d_0}^{'}} + \frac{1}{\tau_{q_0}^{'}}\right)}^{\bar{\mathcal{B}}_2} \cdot \bar{\beta}^* + \overbrace{\frac{0.5}{\tau_{d_0}^{'}}}^{\bar{\mathcal{B}}_3} \cdot \bar{\gamma} + \frac{0.5}{\tau_{d_0}^{'}} \cdot \bar{\gamma}^* \\ & + \underbrace{j \cdot 0.5 \cdot \left[\frac{\left(X_d - X_d^{'}\right)}{\tau_{d_0}^{'}} + \frac{\left(X_q - X_q^{'}\right)}{\tau_{q_0}^{'}}\right]}_{\bar{\mathcal{B}}_4} \cdot \bar{I}_{qd} + \underbrace{j \cdot 0.5 \cdot \left[-\frac{\left(X_d - X_d^{'}\right)}{\tau_{d_0}^{'}} + \frac{\left(X_q - X_q^{'}\right)}{\tau_{q_0}^{'}}\right]}_{\bar{\mathcal{B}}_5} \cdot \bar{I}_{qd}^*, \end{aligned} \tag{2.47}$$

in a simplified form results,

$$\bar{f}_2 = \bar{\mathcal{B}}_1 \cdot \bar{\beta} + \bar{\mathcal{B}}_2 \cdot \bar{\beta}^* + \bar{\mathcal{B}}_3 \cdot \bar{\gamma} + \bar{\mathcal{B}}_3 \cdot \bar{\gamma}^* + \bar{\mathcal{B}}_4 \cdot \bar{I}_{qd} + \bar{\mathcal{B}}_5 \cdot \bar{I}_{qd}^*. \tag{2.48}$$

In sequence, (2.49) presents the third differential equation $d\bar{\gamma}/dt$.

$$\bar{f}_3 = \frac{d\bar{\gamma}}{dt} = \frac{dE_{fd}}{dt}. \tag{2.49}$$

Making the variable substitutions according to Table 2 and substituting in (2.19), it follows that,

$$\bar{f}_3 = \frac{1}{T_E} \cdot \left[-\left(K_E + U_x\right) \cdot 0.5 \cdot \left(\bar{\gamma} + \bar{\gamma}^*\right) + 0.5 \cdot \left(\bar{\lambda} + \bar{\lambda}^*\right) \right], \tag{2.50}$$

which, simplifying, comes,

$$\begin{aligned} \bar{f}_3 = & \underbrace{\left(-\frac{0.5 \cdot K_E}{T_E}\right)}_{\bar{\mathcal{C}}_1} \cdot \bar{\gamma} + \left(-\frac{0.5 \cdot K_E}{T_E}\right) \bar{\gamma}^* + \underbrace{\left(-\frac{0.5}{T_E}\right)}_{\bar{\mathcal{C}}_2} \cdot U_x \cdot \bar{\gamma} + \left(-\frac{0.5}{T_E}\right) \cdot U_x \cdot \bar{\gamma}^* \\ & + \frac{0.5}{T_E} \cdot \bar{\lambda} + \frac{0.5}{T_E} \cdot \bar{\lambda}^*. \end{aligned} \tag{2.51}$$

Written in a compact form, results:

$$\bar{f}_3 = \bar{\mathcal{C}}_1 \cdot \bar{\gamma} + \bar{\mathcal{C}}_1 \cdot \bar{\gamma}^* + \bar{\mathcal{C}}_2 \cdot U_x \cdot \bar{\gamma} + \bar{\mathcal{C}}_2 \cdot U_x \cdot \bar{\gamma}^* - \bar{\mathcal{C}}_2 \cdot \bar{\lambda} - \bar{\mathcal{C}}_2 \cdot \bar{\lambda}^*, \tag{2.52}$$

where U_x is a saturation function of the field voltage [69], given by:

$$U_x = A_{ex} \cdot e^{B_{ex} \cdot E_{fd}} = A_{ex} \cdot e^{B_{ex} \cdot 0.5 \cdot (\bar{\gamma} + \bar{\gamma}^*)}. \tag{2.53}$$

Next, equation (2.54) evidences the fourth differential equation $d\bar{\lambda}/dt$ in the complex domain.

$$\bar{f}_4 = \frac{d\bar{\lambda}}{dt} = \frac{dV_R}{dt} + j \cdot \frac{dV_F}{dt}. \tag{2.54}$$

Rewriting V_R and V_F in terms of $\bar{\lambda}$ and E_{fd} in terms of $\bar{\gamma}$ in the equations (2.20) and (2.21), the equation (2.54) results in (2.55).

$$\begin{aligned} \bar{f}_4 = & \frac{1}{T_A} \cdot \left[-0.5 \cdot \left(\bar{\lambda} + \bar{\lambda}^*\right) + K_A \cdot \left(V_{ref} - j \cdot 0.5 \cdot \left(\bar{\lambda}^* - \bar{\lambda}\right) - V\right) \right] \\ & + \frac{j}{T_F} \cdot \left[-j \cdot 0.5 \cdot \left(\bar{\lambda}^* - \bar{\lambda}\right) + \frac{K_F}{T_E} \cdot 0.5 \cdot \left(\bar{\lambda} + \bar{\lambda}^*\right) - \frac{K_F}{T_E} \cdot \left(K_E + U_x\right) \cdot 0.5 \cdot \left(\bar{\gamma} + \bar{\gamma}^*\right) \right]. \end{aligned} \tag{2.55}$$

After algebraic simplification of the terms, it leads to

$$\begin{aligned}\bar{f}_4 = &\underbrace{\left(-j\cdot 0.5\cdot\left(\frac{K_E\cdot K_F}{T_E\cdot T_F}\right)\right)}_{\bar{\mathcal{D}}_1}\cdot\bar{\gamma} + \left(-j\cdot 0.5\cdot\left(\frac{K_E\cdot K_F}{T_E\cdot T_F}\right)\right)\cdot\bar{\gamma}^* \\ &+\underbrace{\left(-j\cdot 0.5\cdot\left(\frac{K_F}{T_E\cdot T_F}\right)\right)}_{\bar{\mathcal{D}}_2}\cdot U_x\cdot\bar{\gamma} + \left(-j\cdot 0.5\cdot\left(\frac{K_E\cdot K_F}{T_E\cdot T_F}\right)\right)\cdot U_x\cdot\bar{\gamma}^* \\ &+\underbrace{0.5\cdot\left[\left(-\frac{1}{T_A}+j\cdot\frac{K_F}{T_E\cdot T_F}\right)+\left(-\frac{1}{T_F}+j\cdot\frac{K_A}{T_A}\right)\right]}_{\bar{\mathcal{D}}_3}\cdot\bar{\lambda} \\ &+\underbrace{0.5\cdot\left[\left(-\frac{1}{T_A}+j\cdot\frac{K_F}{T_E\cdot T_F}\right)-\left(-\frac{1}{T_F}+j\cdot\frac{K_A}{T_A}\right)\right]}_{\bar{\mathcal{D}}_4}\cdot\bar{\lambda}^* + \underbrace{\left(-\frac{K_A}{T_A}\right)}_{\bar{\mathcal{D}}_5}\cdot V + \frac{K_A}{T_A}\cdot V_{ref}.\end{aligned} \tag{2.56}$$

Thus, the fourth differential equation of the model in complex-conjugate coordinates will be:

$$\begin{aligned}\bar{f}_4 = &\bar{\mathcal{D}}_1\cdot\bar{\gamma} + \bar{\mathcal{D}}_1\cdot\bar{\gamma}^* + \bar{\mathcal{D}}_2\cdot U_x\cdot\bar{\gamma} + \bar{\mathcal{D}}_2\cdot U_x\cdot\bar{\gamma}^* + \bar{\mathcal{D}}_3\cdot\bar{\lambda} + \bar{\mathcal{D}}_4\cdot\bar{\lambda}^* + \bar{\mathcal{D}}_5\cdot V \\ &-\bar{\mathcal{D}}_5\cdot V_{ref},\end{aligned} \tag{2.57}$$

where V_{ref} is a known input variable [69] and V is the magnitude of the terminal voltage of the machine. Equation (2.58) expresses the voltage magnitude of each machine.

$$V = \sqrt{\bar{V}_{qd}\cdot\bar{V}_{qd}^*}. \tag{2.58}$$

Finally, equation (2.59) shows the two-axis model's fifth and final differential equation in the complex domain.

$$\bar{f}_5 = \frac{d\bar{\mu}}{dt} = \frac{dT_M}{dt} + j\cdot\frac{dP_{SV}}{dt}. \tag{2.59}$$

Replacing (2.22) and (2.23) with complex variables, results:

$$\begin{aligned}\bar{f}_5 = &\frac{1}{T_{CH}}\cdot\left[-0.5\cdot(\bar{\mu}+\bar{\mu}^*) + j\cdot 0.5\cdot(\bar{\mu}^*-\bar{\mu})\right] \\ &+\frac{j}{T_{SV}}\cdot\left[-j\cdot 0.5\cdot(\bar{\mu}^*-\bar{\mu}) + P_C - \frac{1}{R_D\cdot\omega_s}\cdot j\cdot 0.5\cdot(\bar{\alpha}^*-\bar{\alpha})\right].\end{aligned} \tag{2.60}$$

Rearranging the equation, it follows that,

$$\bar{f}_5 = \underbrace{\left(\frac{0.5}{T_{SV}\cdot R_D\cdot \omega_s}\right)}_{\bar{\varepsilon}_1}\cdot\bar{\alpha} + \left(\frac{-0.5}{T_{SV}\cdot R_D\cdot \omega_s}\right)\cdot\bar{\alpha}^* + \underbrace{0.5\cdot\left[-\left(\frac{1}{T_{CH}}+\frac{1}{T_{SV}}\right) - j\cdot\frac{1}{T_{CH}}\right]}_{\bar{\varepsilon}_2}\cdot\bar{\mu}$$
$$+ \underbrace{0.5\cdot\left[-\left(\frac{1}{T_{CH}}-\frac{1}{T_{SV}}\right) + j\cdot\frac{1}{T_{CH}}\right]}_{\bar{\varepsilon}_3}\cdot\bar{\mu}^* + \underbrace{\frac{j}{T_{SV}}}_{\bar{\varepsilon}_4}\cdot P_C. \tag{2.61}$$

Therefore, equation (2.62) is the last differential equation in the complex domain.

$$\bar{f}_5 = \bar{\mathcal{E}}_1\cdot\bar{\alpha} - \bar{\mathcal{E}}_1\cdot\bar{\alpha}^* + \bar{\mathcal{E}}_2\cdot\bar{\mu} + \bar{\mathcal{E}}_3\cdot\bar{\mu}^* + \bar{\mathcal{E}}_4\cdot P_C, \tag{2.62}$$

where P_C is a known input variable [69].

The resulting set of complex-domain algebraic-differential equations provides a unified framework for representing the dynamics of synchronous machines. By reformulating the real-valued *d-q* model into complex-conjugate coordinates, the non-analytic nature of power system functions is effectively managed. This provides the necessary mathematical foundation for the Jacobian derivations presented in Appendix B and the robust estimation strategies detailed in the subsequent chapter. In summary, Tables 3, 4, and 5 show the comparison between the algebraic-differential models formulated in the domain of real and complex numbers.

Table 3 – Two-Axis Model: Comparison between algebraic equations in the real and complex domain

Real domain	**Complex domain**	**Constants**
$\bar{V} = V\angle\theta$ $\bar{V} = \left[\left(E_d^{'} + j \cdot E_q^{'}\right) + \left(X_q^{'} - X_d^{'}\right) \cdot I_q - j \cdot X_d^{'} \cdot (I_d + j \cdot I_q)\right] \cdot e^{j \cdot \left(\delta - \frac{\pi}{2}\right)}$	$\bar{V} = \left[\bar{\beta}^* - \bar{\mathcal{K}}_3 \cdot \bar{I}_{qd} - \bar{\mathcal{K}}_4 \cdot \bar{I}_{qd}^*\right] \cdot e^{j \cdot (0.5(\bar{\alpha} + \bar{\alpha}^*))}$	$\bar{\mathcal{K}}_3 = j \cdot 0.5 \cdot \left(X_q^{'} - X_d^{'}\right)$ $\bar{\mathcal{K}}_4 = j \cdot 0.5 \cdot \left(X_q^{'} + X_d^{'}\right)$
$V_d = V \cdot \sin(\delta - \theta)$ $V_q = V \cdot \cos(\delta - \theta)$	$\bar{V}_{qd} = V_q + j \cdot V_d = V \cdot e^{j \cdot (0.5 \cdot (\bar{\alpha} + \bar{\alpha}^*) - \theta)}$ $\bar{V}_{qd}^* = V_q - j \cdot V_d = V \cdot e^{-j \cdot (0.5 \cdot (\bar{\alpha} + \bar{\alpha}^*) - \theta)}$	
$I_d = \dfrac{E_q^{'} - V_q}{X_d^{'}}$ $I_q = \dfrac{V_d - E_d^{'}}{X_q^{'}}$	$\bar{I}_{qd} = I_q + j \cdot I_d$ $\bar{I}_{qd} = \bar{\mathcal{K}}_1 \cdot \bar{\beta} + \bar{\mathcal{K}}_2 \cdot \bar{\beta}^* - \bar{\mathcal{K}}_1 \cdot \bar{V}_{qd} - \bar{\mathcal{K}}_2 \cdot \bar{V}_{qd}^*$ $\bar{I}_{qd}^* = -\bar{\mathcal{K}}_2 \cdot \bar{\beta} - \bar{\mathcal{K}}_1 \cdot \bar{\beta}^* + \bar{\mathcal{K}}_2 \cdot \bar{V}_{qd} + \bar{\mathcal{K}}_1 \cdot \bar{V}_{qd}^*$	$\bar{\mathcal{K}}_1 = j \cdot 0.5 \cdot \left(\dfrac{1}{X_q^{'}} + \dfrac{1}{X_d^{'}}\right)$ $\bar{\mathcal{K}}_2 = j \cdot 0.5 \cdot \left(\dfrac{-1}{X_q^{'}} + \dfrac{1}{X_d^{'}}\right)$
$P_e = V_d \cdot I_d + V_q \cdot I_q$ $Q_e = -V_d \cdot I_q + V_q \cdot I_d$	$\bar{S}_e = \bar{V}_{qd}^* \cdot \bar{I}_{qd}$ $\bar{S}_e^* = \bar{V}_{qd} \cdot \bar{I}_{qd}^*$	

Table 4 – Two-Axis Model: Comparison between differential equations in the real and complex domain

Real domain	**Complex domain**
$\frac{d\delta}{dt} = \omega - \omega_s$ $\frac{d\omega}{dt} = \frac{\omega_s}{2 \cdot H} \cdot (T_M - P_e - D \cdot (\omega - \omega_s))$	$\frac{d\bar{\alpha}}{dt} = \bar{\mathcal{A}}_1 \cdot \bar{\alpha} - \bar{\mathcal{A}}_1 \cdot \bar{\alpha}^* + \bar{\mathcal{A}}_2 \cdot \bar{\mu} + \bar{\mathcal{A}}_2 \cdot \bar{\mu}^* - \bar{\mathcal{A}}_2 \cdot \bar{S}_e - \bar{\mathcal{A}}_2 \cdot \bar{S}_e^*$
$\frac{dE_q^{'}}{dt} = \frac{1}{\tau_{d_0}^{'}} \cdot \left[-E_q^{'} - \left(X_d - X_d^{'}\right) \cdot I_d + E_{fd}\right]$ $\frac{dE_d^{'}}{dt} = \frac{1}{\tau_{q_0}^{'}} \cdot \left[-E_d^{'} - \left(X_q - X_q^{'}\right) \cdot I_q\right]$	$\frac{d\bar{\beta}}{dt} = \bar{\mathcal{B}}_1 \cdot \bar{\beta} + \bar{\mathcal{B}}_2 \cdot \bar{\beta}^* + \bar{\mathcal{B}}_3 \cdot \bar{\gamma} + \bar{\mathcal{B}}_3 \cdot \bar{\gamma}^* + \bar{\mathcal{B}}_4 \cdot \bar{I}_{qd} + \bar{\mathcal{B}}_5 \cdot \bar{I}_{qd}^*$
$\frac{dE_{fd}}{dt} = \frac{1}{T_E} \cdot \left[-\left(K_E + \underbrace{S_E\left(E_{fd}\right)}_{U_x}\right) \cdot E_{fd} + V_R\right]$	$\frac{d\bar{\gamma}}{dt} = \bar{\mathcal{C}}_1 \cdot \bar{\gamma} + \bar{\mathcal{C}}_1 \cdot \bar{\gamma}^* + \bar{\mathcal{C}}_2 \cdot U_x \cdot \bar{\gamma} + \bar{\mathcal{C}}_2 \cdot U_x \cdot \bar{\gamma}^* - \bar{\mathcal{C}}_2 \cdot \bar{\lambda} - \bar{\mathcal{C}}_2 \cdot \bar{\lambda}^*$
$\frac{dV_R}{dt} = \frac{1}{T_A} \cdot [-V_R + K_A \cdot (V_{ref} - V_F - V)]$ $\frac{dV_F}{dt} = \frac{1}{T_F} \cdot \left[-V_F + \frac{K_F}{T_E} \cdot V_R - \frac{K_F}{T_E} \cdot (K_E + S_E\left(E_{fd}\right)) \cdot E_{fd}\right]$	$\frac{d\bar{\lambda}}{dt} = \bar{\mathcal{D}}_1 \cdot \bar{\gamma} + \bar{\mathcal{D}}_1 \cdot \bar{\gamma}^* + \bar{\mathcal{D}}_2 \cdot U_x \cdot \bar{\gamma} + \bar{\mathcal{D}}_2 \cdot U_x \cdot \bar{\gamma}^* + \bar{\mathcal{D}}_3 \cdot \bar{\lambda} + \bar{\mathcal{D}}_4 \cdot \bar{\lambda}^* + \bar{\mathcal{D}}_5 \cdot V - \bar{\mathcal{D}}_5 \cdot V_{ref}$
$\frac{dT_M}{dt} = \frac{1}{T_{CH}} \left(-T_M + P_{SV}\right)$ $\frac{dP_{SV}}{dt} = \frac{1}{T_{SV}} \left[-P_{SV} + P_C - \frac{1}{R_D \cdot \omega_s} \cdot (\omega - \omega_s)\right]$	$\frac{d\bar{\mu}}{dt} = \bar{\mathcal{E}}_1 \cdot \bar{\alpha} - \bar{\mathcal{E}}_1 \cdot \bar{\alpha}^* + \bar{\mathcal{E}}_2 \cdot \bar{\mu} + \bar{\mathcal{E}}_3 \cdot \bar{\mu}^* + \bar{\mathcal{E}}_4 \cdot P_C$

Table 5 – Two-Axis Model: Constants used in the complex-domain formulation

Equation	**Constants**		
$\bar{f}_1$	$\bar{\mathcal{A}}_1 = -0.5 \cdot \left(\frac{D \cdot \omega_s}{2 \cdot H} + j\right)$	$\bar{\mathcal{A}}_2 = j \cdot 0.5 \cdot \frac{\omega_s}{2 \cdot H}$	
$\bar{f}_2$	$\bar{\mathcal{B}}_1 = -0.5 \cdot \left(\frac{1}{\tau'_{d_0}} + \frac{1}{\tau'_{q_0}}\right)$	$\bar{\mathcal{B}}_2 = 0.5 \cdot \left(-\frac{1}{\tau'_{d_0}} + \frac{1}{\tau'_{q_0}}\right)$	$\bar{\mathcal{B}}_3 = \frac{0.5}{\tau'_{d_0}}$
	$\bar{\mathcal{B}}_4 = j \cdot 0.5 \cdot \left[\frac{X_d - X'_d}{\tau'_{d_0}} + \frac{X_q - X'_q}{\tau'_{q_0}}\right]$	$\bar{\mathcal{B}}_5 = j \cdot 0.5 \cdot \left[-\frac{X_d - X'_d}{\tau'_{d_0}} + \frac{X_q - X'_q}{\tau'_{q_0}}\right]$	
$\bar{f}_3$	$\bar{\mathcal{C}}_1 = -\frac{0.5 \cdot K_E}{T_E}$	$\bar{\mathcal{C}}_2 = -\frac{0.5}{T_E}$	
$\bar{f}_4$	$\bar{\mathcal{D}}_1 = -j \cdot 0.5 \cdot \frac{K_E \cdot K_F}{T_E \cdot T_F}$	$\bar{\mathcal{D}}_2 = -j \cdot 0.5 \cdot \frac{K_F}{T_E \cdot T_F}$	
	$\bar{\mathcal{D}}_3 = 0.5 \cdot \left(-\frac{1}{T_A} + j \cdot \frac{K_F}{T_E \cdot T_F}\right) + 0.5 \cdot \left(-\frac{1}{T_F} + j \cdot \frac{K_A}{T_A}\right)$	$\bar{\mathcal{D}}_4 = 0.5 \cdot \left(-\frac{1}{T_A} + j \cdot \frac{K_F}{T_E \cdot T_F}\right) - 0.5 \cdot \left(-\frac{1}{T_F} + j \cdot \frac{K_A}{T_A}\right)$	$\bar{\mathcal{D}}_5 = -\frac{K_A}{T_A}$
$\bar{f}_5$	$\bar{\mathcal{E}}_1 = \frac{0.5}{T_{SV} \cdot R_D \cdot \omega_s}$	$\bar{\mathcal{E}}_2 = -0.5 \cdot \left(\frac{1}{T_{CH}} + \frac{1}{T_{SV}}\right) - 0.5 \cdot j \cdot \frac{1}{T_{CH}}$	
	$\bar{\mathcal{E}}_3 = -0.5 \cdot \left(\frac{1}{T_{CH}} - \frac{1}{T_{SV}}\right) + 0.5 \cdot j \cdot \frac{1}{T_{CH}}$	$\bar{\mathcal{E}}_4 = \frac{j}{T_{SV}}$	

3 Formulation of Kalman Filters in the Complex Domain

This chapter presents the theoretical foundation and formulation of Kalman filter algorithms commonly used for state estimation, extending these concepts to the complex domain. Initially, this chapter presents the structures of the Extended Kalman Filter (EKF) and the Unscented Kalman Filter (UKF) in this new numerical domain. Mandic and Goh [72] proposed the theory of these structures based on complex signal processing algorithms. Next, this chapter presents the robust versions of the EKF and UKF algorithms in complex-conjugate coordinates, based on the theory presented in [47] and [48].

3.1 Complex-Valued Extended Kalman Filter (CV-EKF)

The Extended Kalman filter (EKF) is widely used to study state dynamics in nonlinear systems. Its application in these systems is crucial given the complex and dynamic nature of the components and processes involved in electrical power systems.

In this context, equations (3.1) and (3.2) illustrate the algebraic-differential model that represents the dynamics of an electrical system over time [66].

$$\frac{d\bar{x}\left(t\right)}{dt} = \bar{f}\left(\bar{x}(t), \bar{u}(t), \bar{w}(t)\right), \tag{3.1}$$

$$\bar{y}\left(t\right) = \bar{h}\left(\bar{x}\left(t\right), \bar{v}\left(t\right)\right), \tag{3.2}$$

or, in discretized form,

$$\bar{\boldsymbol{x}}_{k} = \bar{\boldsymbol{f}}_{k-1}\left(\bar{\boldsymbol{x}}_{k-1}, \bar{\boldsymbol{u}}_{k-1}, \bar{\boldsymbol{w}}_{k-1}\right), \tag{3.3}$$

$$\bar{\boldsymbol{y}}_{k} = \bar{\boldsymbol{h}}_{k}\left(\bar{\boldsymbol{x}}_{k}, \bar{\boldsymbol{v}}_{k}\right), \tag{3.4}$$

where,

- $\bar{\boldsymbol{x}}_{k}$: $n \times 1$ vector of state variables
- $\bar{\boldsymbol{y}}_{k}$: $m \times 1$ vector of output variables (measurements)
- $\bar{\boldsymbol{f}}_{k}$ and $\bar{\boldsymbol{h}}_{k}$: $n \times 1$ and $m \times 1$ vectors of nonlinear functions

- $\bar{\boldsymbol{u}}_k$: $\mathfrak{p} \times 1$ vector of known inputs
- $\bar{\boldsymbol{v}}_k$ and $\bar{\boldsymbol{w}}_k$: $m \times 1$ and $n \times 1$ white Gaussian noises with zero mean and known covariance matrices, $\bar{\boldsymbol{R}}_k$ and $\bar{\boldsymbol{Q}}_k$, respectively.

The EKF extends the classical Kalman filter to nonlinear systems by linearizing the equations around the current operating point using a Taylor series. In the domain of complex numbers, this expansion is made possible by using the Wirtinger Calculus or *CR-Calculus* [55], which enables the analysis of functions of complex variables, as detailed in the Appendix A.

Thus, consider the vector of state variables $\bar{\boldsymbol{x}}_k$, composed of complex and conjugate variables,

$$\bar{\boldsymbol{x}}_k = \begin{bmatrix} \bar{x}_{1_k} \\ \vdots \\ \bar{x}_{n_k} \\ \bar{x}^*_{1_k} \\ \vdots \\ \bar{x}^*_{n_k} \end{bmatrix}, \qquad \bar{\boldsymbol{x}}_k \in \mathbb{C}^{2n \times 1}, \tag{3.5}$$

where,

$$\bar{x}_{i_k} = a_{i_k} + j \cdot b_{i_k}, \qquad \bar{x}^*_{i_k} = a_{i_k} - j \cdot b_{i_k}, \qquad i = 1, 2, 3, \ldots n, \tag{3.6}$$

with a_i and $b_i \in \mathbb{R}$. The nonlinear functions in complex conjugate coordinates are:

$$\bar{\boldsymbol{f}}_{k-1}\left(\bar{\boldsymbol{x}}_{k-1}, \bar{\boldsymbol{u}}_{k-1}, \bar{\boldsymbol{w}}_{k-1}\right) = \begin{bmatrix} \bar{f}_{1_{k-1}} \\ \vdots \\ \bar{f}_{n_{k-1}} \\ \bar{f}^*_{1_{k-1}} \\ \vdots \\ \bar{f}^*_{n_{k-1}} \end{bmatrix}, \qquad \bar{\boldsymbol{h}}_k\left(\bar{\boldsymbol{x}}_k, \bar{\boldsymbol{v}}_k\right) = \begin{bmatrix} \bar{h}_{1_k} \\ \vdots \\ \bar{h}_{m_k} \\ \bar{h}^*_{1_k} \\ \vdots \\ \bar{h}^*_{m_k} \end{bmatrix}. \tag{3.7}$$

Applying a first-order Taylor series expansion around the estimate $\bar{\boldsymbol{x}}_{k-1} = \hat{\bar{\boldsymbol{x}}}_{k-1|k-1}$, where $\hat{\bar{\boldsymbol{x}}}_{k-1|k-1}$ denotes the *a posteriori* state estimate at time $k-1$, (3.3) can be rewritten

as (3.8) [73].

$$\begin{aligned}\bar{\boldsymbol{x}}_k &= \bar{\boldsymbol{f}}_{k-1}\left(\hat{\bar{\boldsymbol{x}}}_{k-1|k-1}, \bar{\boldsymbol{u}}_{k-1}\right) + \underbrace{\left.\frac{\partial \bar{\boldsymbol{f}}_{k-1}}{\partial \bar{\boldsymbol{x}}}\right|_{\hat{\bar{\boldsymbol{x}}}_{k-1|k-1}}}_{\bar{\boldsymbol{F}}_{k-1}} \cdot \left(\bar{\boldsymbol{x}}_{k-1} - \hat{\bar{\boldsymbol{x}}}_{k-1|k-1}\right) + \underbrace{\left.\frac{\partial \bar{\boldsymbol{f}}_{k-1}}{\partial \bar{\boldsymbol{w}}}\right|_{\hat{\bar{\boldsymbol{x}}}_{k-1|k-1}}}_{\bar{\boldsymbol{L}}_{k-1}} \cdot \bar{\boldsymbol{w}}_{k-1} \\ &= \bar{\boldsymbol{F}}_{k-1} \cdot \bar{\boldsymbol{x}}_{k-1} + \underbrace{\left[\bar{\boldsymbol{f}}_{k-1}\left(\hat{\bar{\boldsymbol{x}}}_{k-1|k-1}, \bar{\boldsymbol{u}}_{k-1}\right) - \bar{\boldsymbol{F}}_{k-1} \cdot \hat{\bar{\boldsymbol{x}}}_{k-1|k-1}\right]}_{\tilde{\bar{\boldsymbol{r}}}_{k-1}} + \underbrace{\bar{\boldsymbol{L}}_{k-1} \cdot \bar{\boldsymbol{w}}_{k-1}}_{\tilde{\bar{\boldsymbol{w}}}_{k-1}} \\ &= \bar{\boldsymbol{F}}_{k-1} \cdot \bar{\boldsymbol{x}}_{k-1} + \tilde{\bar{\boldsymbol{r}}}_{k-1} + \tilde{\bar{\boldsymbol{w}}}_{k-1}. \end{aligned} \tag{3.8}$$

Repeating the Taylor series expansion process for the discovery (3.4), around the point $\bar{\boldsymbol{x}}_k = \hat{\bar{\boldsymbol{x}}}_{k|k-1}$, results:

$$\begin{aligned}\bar{\boldsymbol{y}}_k &= \bar{\boldsymbol{h}}_k\left(\hat{\bar{\boldsymbol{x}}}_{k|k-1}\right) + \underbrace{\left.\frac{\partial \bar{\boldsymbol{h}}_k}{\partial \bar{\boldsymbol{x}}}\right|_{\hat{\bar{\boldsymbol{x}}}_{k|k-1}}}_{\bar{\boldsymbol{H}}_k} \cdot \left(\bar{\boldsymbol{x}}_k - \hat{\bar{\boldsymbol{x}}}_{k|k-1}\right) + \underbrace{\left.\frac{\partial \bar{\boldsymbol{h}}_k}{\partial \bar{\boldsymbol{v}}}\right|_{\hat{\bar{\boldsymbol{x}}}_{k|k-1}}}_{\bar{\boldsymbol{V}}_k} \cdot \bar{\boldsymbol{v}}_k \\ &= \bar{\boldsymbol{H}}_k \cdot \bar{\boldsymbol{x}}_k + \underbrace{\left[\bar{\boldsymbol{h}}_k\left(\hat{\bar{\boldsymbol{x}}}_{k|k-1}\right) - \bar{\boldsymbol{H}}_k \cdot \hat{\bar{\boldsymbol{x}}}_{k|k-1}\right]}_{\hat{\bar{\boldsymbol{r}}}_{y_k}} + \underbrace{\bar{\boldsymbol{V}}_k \cdot \bar{\boldsymbol{v}}_k}_{\tilde{\bar{\boldsymbol{v}}}_k} \\ &= \bar{\boldsymbol{H}}_k \cdot \bar{\boldsymbol{x}}_k + \tilde{\bar{\boldsymbol{r}}}_{y_k} + \tilde{\bar{\boldsymbol{v}}}_k. \end{aligned} \tag{3.9}$$

The matrices $\bar{\boldsymbol{F}}_{k-1}$, $\bar{\boldsymbol{L}}_{k-1}$, $\bar{\boldsymbol{H}}_k$, $\bar{\boldsymbol{V}}_k$ are Jacobian matrices of the linearization process. In the domain of complex numbers, Jacobian matrices have a mirroring property between the submatrices corresponding to the partitions of the diagonals of the Jacobian matrix [55]. This property simplifies the modeling of the problem in complex-conjugate coordinates. In practice, the upper partitions of the Jacobian matrix are calculated, and the others are the complex conjugate of these partitions. Equations (3.10) and (3.11) demonstrate this property.

$$\bar{\boldsymbol{F}}_{k-1} = \begin{bmatrix} \dfrac{\partial \bar{\boldsymbol{f}}\left(\bar{\boldsymbol{x}}_{k-1}\right)}{\partial \bar{\boldsymbol{x}}_{k-1}} & \dfrac{\partial \bar{\boldsymbol{f}}\left(\bar{\boldsymbol{x}}_{k-1}\right)}{\partial \bar{\boldsymbol{x}}^*_{k-1}} \\ \dfrac{\partial \bar{\boldsymbol{f}}^*\left(\bar{\boldsymbol{x}}_{k-1}\right)}{\partial \bar{\boldsymbol{x}}_{k-1}} & \dfrac{\partial \bar{\boldsymbol{f}}^*\left(\bar{\boldsymbol{x}}_{k-1}\right)}{\partial \bar{\boldsymbol{x}}^*_{k-1}} \end{bmatrix} = \begin{bmatrix} \bar{\boldsymbol{F}}_{1_{k-1}} & \bar{\boldsymbol{F}}_{2_{k-1}} \\ \bar{\boldsymbol{F}}^*_{2_{k-1}} & \bar{\boldsymbol{F}}^*_{1_{k-1}} \end{bmatrix}, \tag{3.10}$$

$$\bar{\boldsymbol{H}}_{k} = \begin{bmatrix} \dfrac{\partial \bar{\boldsymbol{h}}\left(\bar{\boldsymbol{x}}_{k}\right)}{\partial \bar{\boldsymbol{x}}_{k}} & \dfrac{\partial \bar{\boldsymbol{h}}\left(\bar{\boldsymbol{x}}_{k}\right)}{\partial \bar{\boldsymbol{x}}^{*}_{k}} \\ \dfrac{\partial \bar{\boldsymbol{h}}^{*}\left(\bar{\boldsymbol{x}}_{k}\right)}{\partial \bar{\boldsymbol{x}}_{k}} & \dfrac{\partial \bar{\boldsymbol{h}}^{*}\left(\bar{\boldsymbol{x}}_{k}\right)}{\partial \bar{\boldsymbol{x}}^{*}_{k}} \end{bmatrix} = \begin{bmatrix} \bar{\boldsymbol{H}}_{1_{k}} & \bar{\boldsymbol{H}}_{2_{k}} \\ \bar{\boldsymbol{H}}^{*}_{2_{k}} & \bar{\boldsymbol{H}}^{*}_{1_{k}} \end{bmatrix}. \tag{3.11}$$

After linearizations shown in the equations (3.8) and (3.9), traditional Kalman filter equations are applied to estimate the states. Finally, the Extended Kalman Filter in the complex domain is summarized by the following equations [72].

- Initialize the filter:

$$\hat{\bar{\boldsymbol{x}}}_{0|0} = \mathbb{E}\{\bar{\boldsymbol{x}}_{0}\}, \tag{3.12}$$

$$\bar{\boldsymbol{P}}_{0|0} = \mathbb{E}\left\{\left(\bar{\boldsymbol{x}}_{0} - \mathbb{E}\left\{\bar{\boldsymbol{x}}_{0}\right\}\right) \cdot \left(\bar{\boldsymbol{x}}_{0} - \mathbb{E}\left\{\bar{\boldsymbol{x}}_{0}\right\}\right)^{H}\right\}, \tag{3.13}$$

  where $\bar{\boldsymbol{P}}_{0|0}$ is the covariance matrix *a priori* of estimation error.

- Prediction: State update and calculation of the estimation error matrix $\left(\bar{\boldsymbol{P}}_{k|k-1}\right)$

$$\bar{\boldsymbol{F}}_{k-1} = \left.\frac{\partial \bar{\boldsymbol{f}}_{k-1}}{\partial \bar{\boldsymbol{x}}}\right|_{\hat{\bar{\boldsymbol{x}}}_{k-1|k-1}}, \tag{3.14}$$

$$\bar{\boldsymbol{L}}_{k-1} = \left.\frac{\partial \bar{\boldsymbol{f}}_{k-1}}{\partial \bar{\boldsymbol{w}}}\right|_{\hat{\bar{\boldsymbol{x}}}_{k-1|k-1}}, \tag{3.15}$$

$$\hat{\bar{\boldsymbol{x}}}_{k|k-1} = \bar{\boldsymbol{f}}\left(\hat{\bar{\boldsymbol{x}}}_{k-1|k-1}\right), \tag{3.16}$$

$$\bar{\boldsymbol{P}}_{k|k-1} = \bar{\boldsymbol{F}}_{k-1} \cdot \bar{\boldsymbol{P}}_{k-1|k-1} \cdot \bar{\boldsymbol{F}}^{H}_{k-1} + \bar{\boldsymbol{L}}_{k-1} \cdot \bar{\boldsymbol{Q}}_{k-1} \cdot \bar{\boldsymbol{L}}^{H}_{k-1}, \tag{3.17}$$

- Filtering: Update of estimated measurements $\left(\bar{\boldsymbol{h}}\left(\hat{\bar{\boldsymbol{x}}}_{k|k-1}\right)\right)$, the estimated state variables $\left(\hat{\bar{\boldsymbol{x}}}_{k|k}\right)$ and the estimation covariance error matrix $\left(\bar{\boldsymbol{P}}_{k|k}\right)$

$$\bar{\boldsymbol{H}}_{k} = \left.\frac{\partial \bar{\boldsymbol{h}}_{k}}{\partial \bar{\boldsymbol{x}}}\right|_{\hat{\bar{\boldsymbol{x}}}_{k|k-1}}, \tag{3.18}$$

$$\bar{\boldsymbol{V}}_{k} = \left.\frac{\partial \bar{\boldsymbol{h}}_{k}}{\partial \bar{\boldsymbol{v}}}\right|_{\hat{\bar{\boldsymbol{x}}}_{k|k-1}}, \tag{3.19}$$

$$\bar{\boldsymbol{G}}_{k} = \bar{\boldsymbol{P}}_{k|k-1} \cdot \bar{\boldsymbol{H}}_{k}^{H} \cdot \left(\bar{\boldsymbol{H}}_{k} \cdot \bar{\boldsymbol{P}}_{k|k-1} \cdot \bar{\boldsymbol{H}}_{k}^{H} + \bar{\boldsymbol{V}}_{k} \cdot \bar{\boldsymbol{R}}_{k} \cdot \bar{\boldsymbol{V}}_{k}^{H} \right)^{-1}, \tag{3.20}$$

$$\hat{\bar{\boldsymbol{x}}}_{k|k} = \hat{\bar{\boldsymbol{x}}}_{k|k-1} + \bar{\boldsymbol{G}}_{k} \cdot \left(\bar{\boldsymbol{y}}_{k} - \bar{\boldsymbol{h}} \left(\hat{\bar{\boldsymbol{x}}}_{k|k-1} \right) \right), \tag{3.21}$$

$$\bar{\boldsymbol{P}}_{k|k} = \left(\boldsymbol{I} - \bar{\boldsymbol{G}}_{k} \cdot \bar{\boldsymbol{H}}_{k} \right) \cdot \bar{\boldsymbol{P}}_{k|k-1}, \tag{3.22}$$

where $\bar{\boldsymbol{G}}$ is known as the gain of Kalman.

Although EKF performs well for processes with Gaussian noise, linearization promotes errors in the estimation process. In addition, this method requires superior computational performance because it uses iterative Jacobian matrices. In some cases, calculating the Jacobian matrices may not be possible, making this method unfeasible [30].

The framework proposed by Mandic and Goh [72] utilizes augmented complex statistics to generalize filtering algorithms for improper complex signals. Within this context, the augmented covariance matrices for the state ($\bar{\boldsymbol{P}}$), process noise ($\bar{\boldsymbol{Q}}$), and measurement noise ($\bar{\boldsymbol{R}}$) are composed of both conventional covariance and pseudo-covariance partitions. The latter are essential to characterize the statistical coupling between the complex variables and their conjugates.

In this work, based on empirical characterizations of PMU data [74], the process ($\bar{\boldsymbol{Q}}$) and measurement ($\bar{\boldsymbol{R}}$) noise processes are modeled as proper (circular) complex random variables. Consequently, the pseudo-covariance partitions of these noise covariance matrices are assumed to vanish, which simplifies the modeling of the uncertainty sources affecting the system.

However, for the Extended Kalman Filter (EKF) implementation, the augmented state-space formulation remains a structural requirement. Given that power system dynamic and algebraic equations are inherently non-analytic, the linearization process necessitates the application of Wirtinger calculus. This mathematical framework treats the state and its conjugate as independent variables to define the complex Jacobian matrices. Even under the assumption of circular noise, the non-analytic nature of the system functions induces a deterministic coupling between the errors of the state and its conjugate during the prediction step. Therefore, to ensure mathematical consistency with the analytical derivatives and numerical stability, the EKF maintains an augmented state-covariance structure ($\bar{\boldsymbol{P}}$) that preserves its pseudo-covariance partition throughout the estimation process.

3.1.1 Decoupled Complex-Valued Extended Kalman Filter (CV-D-EKF)

This section presents an alternative formulation of the Extended Kalman Filter in the complex domain, aiming to reduce the dimension of the matrices involved in the

algorithm while preserving estimator consistency.

In many practical implementations, the Jacobian matrices $\bar{\boldsymbol{L}}_{k-1}$ and $\bar{\boldsymbol{V}}_{k-1}$ are assumed to be identity matrices, which corresponds to modeling the process and measurement noises as additive terms. This assumption is commonly employed to reduce computational complexity and does not compromise the estimation performance when additive noise models are appropriate. Under this hypothesis, the prediction covariance matrix in (3.17) can be rewritten as:

$$\bar{\boldsymbol{P}}^{-}_{k|k-1} = \bar{\boldsymbol{F}}_{k-1}\bar{\boldsymbol{P}}_{k-1|k-1}\bar{\boldsymbol{F}}^{H}_{k-1} + \bar{\boldsymbol{Q}}_{k-1}. \tag{3.23}$$

In widely linear filtering, covariance and Jacobian matrices naturally appear in augmented form, since an accurate second-order statistical description of complex signals requires jointly accounting for both the variables and their conjugates [72]. In the CV-EKF, this augmented form arises from applying Wirtinger calculus during linearization, yielding mirrored block structures in which the lower partitions are conjugate counterparts of the upper ones. Exploiting this property, the prediction stage requires explicit computation only of the upper Jacobian blocks, $\bar{\boldsymbol{F}}_1$ and $\bar{\boldsymbol{F}}_2$, while the remaining partitions are implicitly determined. Here, the subscripts "1" and "2" are used solely to identify the upper-left and upper-right matrix partitions, respectively. Consequently, block operations involve submatrices whose dimensions are one-quarter of those of the full augmented matrices, providing substantial computational savings, particularly in large-scale systems.

Partitioning the previous matrices leads to

$$\bar{\boldsymbol{P}}_{k-1|k-1} = \begin{bmatrix} \bar{\boldsymbol{P}}_{1_{k-1|k-1}} & \bar{\boldsymbol{P}}_{2_{k-1|k-1}} \\ \bar{\boldsymbol{P}}^{*}_{2_{k-1|k-1}} & \bar{\boldsymbol{P}}^{*}_{1_{k-1|k-1}} \end{bmatrix}, \qquad \bar{\boldsymbol{Q}}_{k-1} = \begin{bmatrix} \bar{\boldsymbol{Q}}_{1_{k-1}} & \bar{\boldsymbol{Q}}_{2_{k-1}} \\ \bar{\boldsymbol{Q}}^{*}_{2_{k-1}} & \bar{\boldsymbol{Q}}^{*}_{1_{k-1}} \end{bmatrix}, \tag{3.24}$$

$$\bar{\boldsymbol{F}}_{k-1} = \begin{bmatrix} \bar{\boldsymbol{F}}_{1_{k-1}} & \bar{\boldsymbol{F}}_{2_{k-1}} \\ \bar{\boldsymbol{F}}^{*}_{2_{k-1}} & \bar{\boldsymbol{F}}^{*}_{1_{k-1}} \end{bmatrix}, \qquad \bar{\boldsymbol{F}}^{H}_{k-1} = \begin{bmatrix} \bar{\boldsymbol{F}}^{H}_{1_{k-1}} & \bar{\boldsymbol{F}}^{T}_{2_{k-1}} \\ \bar{\boldsymbol{F}}^{H}_{2_{k-1}} & \bar{\boldsymbol{F}}^{T}_{1_{k-1}} \end{bmatrix}. \tag{3.25}$$

where

$$\bar{\boldsymbol{P}}_{k-1|k-1},\ \bar{\boldsymbol{Q}}_{k-1},\ \bar{\boldsymbol{F}}_{k-1},\ \bar{\boldsymbol{F}}^{H}_{k-1} \in \mathbb{C}^{2n\times 2n},$$

and each submatrix

$$\bar{\boldsymbol{P}}_1,\ \bar{\boldsymbol{P}}_2,\ \bar{\boldsymbol{Q}}_1,\ \bar{\boldsymbol{Q}}_2,\ \bar{\boldsymbol{F}}_1,\ \bar{\boldsymbol{F}}_2 \in \mathbb{C}^{n\times n}.$$

After matrix multiplication, (3.23) will be of the form,

$$\bar{\boldsymbol{P}}_{k|k-1} = \begin{bmatrix} \bar{\boldsymbol{P}}_{1_{k|k-1}} & \bar{\boldsymbol{P}}_{2_{k|k-1}} \\ \bar{\boldsymbol{P}}^{*}_{2_{k|k-1}} & \bar{\boldsymbol{P}}^{*}_{1_{k|k-1}} \end{bmatrix}, \tag{3.26}$$

where,

$$\begin{aligned} \bar{\boldsymbol{P}}_{1_{k|k-1}} &= \left(\bar{\boldsymbol{F}}_{1_{k-1}} \cdot \bar{\boldsymbol{P}}_{1_{k-1|k-1}} + \bar{\boldsymbol{F}}_{2_{k-1}} \cdot \bar{\boldsymbol{P}}^{*}_{2_{k-1|k-1}}\right) \cdot \bar{\boldsymbol{F}}^{H}_{1_{k-1}} \\ &+ \left(\bar{\boldsymbol{F}}_{1_{k-1}} \cdot \bar{\boldsymbol{P}}_{2_{k-1|k-1}} + \bar{\boldsymbol{F}}_{2_{k-1}} \cdot \bar{\boldsymbol{P}}^{*}_{1_{k-1|k-1}}\right) \cdot \bar{\boldsymbol{F}}^{H}_{2_{k-1}} + \bar{\boldsymbol{Q}}_{1_{k-1}}, \end{aligned} \tag{3.27}$$

$$\begin{aligned} \bar{\boldsymbol{P}}_{2_{k|k-1}} &= \left(\bar{\boldsymbol{F}}_{1_{k-1}} \cdot \bar{\boldsymbol{P}}_{1_{k-1|k-1}} + \bar{\boldsymbol{F}}_{2_{k-1}} \cdot \bar{\boldsymbol{P}}^{*}_{2_{k-1|k-1}}\right) \cdot \bar{\boldsymbol{F}}^{T}_{2_{k-1}} \\ &+ \left(\bar{\boldsymbol{F}}_{1_{k-1}} \cdot \bar{\boldsymbol{P}}_{2_{k-1|k-1}} + \bar{\boldsymbol{F}}_{2_{k-1}} \cdot \bar{\boldsymbol{P}}^{*}_{1_{k-1|k-1}}\right) \cdot \bar{\boldsymbol{F}}^{T}_{1_{k-1}} + \bar{\boldsymbol{Q}}_{2_{k-1}}. \end{aligned} \tag{3.28}$$

Similarly, in the correction stage of the estimator, consider the expression for the Kalman gain (3.20) rewritten as:

$$\bar{\boldsymbol{G}}_{k} = \bar{\boldsymbol{U}}_{k} \cdot \bar{\boldsymbol{T}}^{-1}_{k}, \tag{3.29}$$

where,

$$\bar{\boldsymbol{U}}_{k} = \bar{\boldsymbol{P}}_{k|k-1} \cdot \bar{\boldsymbol{H}}^{H}_{k}, \tag{3.30}$$

$$\bar{\boldsymbol{T}}_{k} = \bar{\boldsymbol{H}}_{k} \cdot \bar{\boldsymbol{U}}_{k} + \bar{\boldsymbol{R}}_{k}, \tag{3.31}$$

$$\bar{\boldsymbol{U}}_{k} = \begin{bmatrix} \bar{\boldsymbol{U}}_{1_{k}} & \bar{\boldsymbol{U}}_{2_{k}} \\ \bar{\boldsymbol{U}}^{*}_{2_{k}} & \bar{\boldsymbol{U}}^{*}_{1_{k}} \end{bmatrix}, \qquad \bar{\boldsymbol{T}}_{k} = \begin{bmatrix} \bar{\boldsymbol{T}}_{1_{k}} & \bar{\boldsymbol{T}}_{2_{k}} \\ \bar{\boldsymbol{T}}^{*}_{2_{k}} & \bar{\boldsymbol{T}}^{*}_{1_{k}} \end{bmatrix}, \tag{3.32}$$

$$\bar{\boldsymbol{H}}_{k-1} = \begin{bmatrix} \bar{\boldsymbol{H}}_{1_{k}} & \bar{\boldsymbol{H}}_{2_{k}} \\ \bar{\boldsymbol{H}}^{*}_{2_{k}} & \bar{\boldsymbol{H}}^{*}_{1_{k}} \end{bmatrix}, \qquad \bar{\boldsymbol{H}}^{H}_{k-1} = \begin{bmatrix} \bar{\boldsymbol{H}}^{H}_{1_{k}} & \bar{\boldsymbol{H}}^{T}_{2_{k}} \\ \bar{\boldsymbol{H}}^{H}_{2_{k}} & \bar{\boldsymbol{H}}^{T}_{1_{k}} \end{bmatrix}, \tag{3.33}$$

$$\bar{\boldsymbol{R}}_{k} = \begin{bmatrix} \bar{\boldsymbol{R}}_{1_k} & \bar{\boldsymbol{R}}_{2_k} \\ \bar{\boldsymbol{R}}^{*}_{2_k} & \bar{\boldsymbol{R}}^{*}_{1_k} \end{bmatrix}. \tag{3.34}$$

where the submatrices of $\bar{\boldsymbol{U}}_{k}$ are of dimension $(n \times m)$, the partitions of $\bar{\boldsymbol{H}}_{k}$ are of dimension $(m \times n)$, and the submatrices of $\bar{\boldsymbol{T}}_{k}$ and $\bar{\boldsymbol{R}}_{k}$ are of dimension $(m \times m)$.

Putting (3.30) and (3.31) in block form, yields the submatrices

$$\bar{\boldsymbol{U}}_{1_k} = \bar{\boldsymbol{P}}_{1_{k|k-1}} \cdot \bar{\boldsymbol{H}}^{H}_{1_k} + \bar{\boldsymbol{P}}_{2_{k|k-1}} \cdot \bar{\boldsymbol{H}}^{H}_{2_k}, \tag{3.35}$$

$$\bar{\boldsymbol{U}}_{2_k} = \bar{\boldsymbol{P}}_{1_{k|k-1}} \cdot \bar{\boldsymbol{H}}^{T}_{2_k} + \bar{\boldsymbol{P}}_{2_{k|k-1}} \cdot \bar{\boldsymbol{H}}^{T}_{1_k}, \tag{3.36}$$

$$\bar{\boldsymbol{T}}_{1_k} = \bar{\boldsymbol{H}}_{1_k} \cdot \bar{\boldsymbol{U}}_{1_k} + \bar{\boldsymbol{H}}_{2_k} \cdot \bar{\boldsymbol{U}}^{*}_{2_k} + \bar{\boldsymbol{R}}_{1_k}, \tag{3.37}$$

$$\bar{\boldsymbol{T}}_{2_k} = \bar{\boldsymbol{H}}_{1_k} \cdot \bar{\boldsymbol{U}}_{2_k} + \bar{\boldsymbol{H}}_{2_k} \cdot \bar{\boldsymbol{U}}^{*}_{1_k} + \bar{\boldsymbol{R}}_{2_k}. \tag{3.38}$$

Due to the linearization process of the EKF, the state vector of the dynamic estimator in the complex domain has redundant equations, since the problem is solved for both the complex part and its conjugate. It aims to meet the Cauchy-Riemann criterion for the analyticity of functions of complex variables. Thus, the updated state vector in (3.21) will be an augmented vector, with complex and conjugate parts, and can be rewritten as (3.39), considering $\Delta\hat{\bar{\boldsymbol{x}}}_{k|k} = \hat{\bar{\boldsymbol{x}}}_{k|k} - \hat{\bar{\boldsymbol{x}}}_{k|k-1}$ and $\Delta\bar{\boldsymbol{y}}_{k} = \bar{\boldsymbol{y}}_{k} - \bar{\boldsymbol{h}}\left(\hat{\bar{\boldsymbol{x}}}_{k|k-1}\right)$.

$$\begin{bmatrix} \Delta\hat{\bar{\boldsymbol{x}}}_{k|k} \\ \left(\Delta\hat{\bar{\boldsymbol{x}}}_{k|k}\right)^{*} \end{bmatrix} = \bar{\boldsymbol{U}}_{k} \cdot \bar{\boldsymbol{T}}^{-1}_{k} \cdot \begin{bmatrix} \Delta\hat{\bar{\boldsymbol{y}}}_{k} \\ \left(\Delta\hat{\bar{\boldsymbol{y}}}_{k}\right)^{*} \end{bmatrix}. \tag{3.39}$$

Instead of explicitly computing $\bar{\boldsymbol{T}}^{-1}_{k}$, the correction step is performed by first solving the linear system

$$\begin{bmatrix} \bar{\boldsymbol{T}}_{1_k} & \bar{\boldsymbol{T}}_{2_k} \\ \bar{\boldsymbol{T}}^{*}_{2_k} & \bar{\boldsymbol{T}}^{*}_{1_k} \end{bmatrix} \cdot \begin{bmatrix} \tilde{\bar{\boldsymbol{b}}}_{1_k} \\ \tilde{\bar{\boldsymbol{b}}}_{2_k} \end{bmatrix} = \begin{bmatrix} \Delta\hat{\bar{\boldsymbol{y}}}_{k} \\ \left(\Delta\hat{\bar{\boldsymbol{y}}}_{k}\right)^{*} \end{bmatrix}. \tag{3.40}$$

Expanding (3.40) yields the block equations

$$\bar{\boldsymbol{T}}_{1_k} \cdot \tilde{\tilde{\boldsymbol{b}}}_{1_k} + \bar{\boldsymbol{T}}_{2_k} \cdot \tilde{\tilde{\boldsymbol{b}}}_{2_k} = \Delta\hat{\tilde{\boldsymbol{y}}}_k, \tag{3.41}$$

$$\bar{\boldsymbol{T}}^*_{2_k} \cdot \tilde{\tilde{\boldsymbol{b}}}_{1_k} + \bar{\boldsymbol{T}}^*_{1_k} \cdot \tilde{\tilde{\boldsymbol{b}}}_{2_k} = \left(\Delta\hat{\tilde{\boldsymbol{y}}}_k\right)^*. \tag{3.42}$$

Solving (3.42) for $\tilde{\tilde{\boldsymbol{b}}}_{2_k}$ gives

$$\tilde{\tilde{\boldsymbol{b}}}_{2_k} = \left(\bar{\boldsymbol{T}}^*_{1_k}\right)^{-1} \cdot \left(\left(\Delta\hat{\tilde{\boldsymbol{y}}}_k\right)^* - \bar{\boldsymbol{T}}^*_{2_k} \cdot \tilde{\tilde{\boldsymbol{b}}}_{1_k}\right). \tag{3.43}$$

Substituting (3.43) into (3.41) leads to

$$\left(\bar{\boldsymbol{T}}_{1_k} - \bar{\boldsymbol{T}}_{2_k} \cdot \left(\bar{\boldsymbol{T}}^*_{1_k}\right)^{-1} \cdot \bar{\boldsymbol{T}}^*_{2_k}\right) \cdot \tilde{\tilde{\boldsymbol{b}}}_{1_k} = \Delta\hat{\tilde{\boldsymbol{y}}}_k - \bar{\boldsymbol{T}}_{2_k} \cdot \left(\bar{\boldsymbol{T}}^*_{1_k}\right)^{-1} \cdot \left(\Delta\hat{\tilde{\boldsymbol{y}}}_k\right)^*. \tag{3.44}$$

Defining the Schur complement of $\bar{\boldsymbol{T}}^*_{1_k}$ as

$$\mathbb{SC}\left(\bar{\boldsymbol{T}}^*_{1_k}\right) = \bar{\boldsymbol{T}}_{1_k} - \bar{\boldsymbol{T}}_{2_k} \cdot \left(\bar{\boldsymbol{T}}^*_{1_k}\right)^{-1} \cdot \bar{\boldsymbol{T}}^*_{2_k}, \tag{3.45}$$

the first solution vector is obtained as

$$\tilde{\tilde{\boldsymbol{b}}}_{1_k} = \left(\mathbb{SC}\left(\bar{\boldsymbol{T}}^*_{1_k}\right)\right)^{-1} \cdot \left(\Delta\hat{\tilde{\boldsymbol{y}}}_k - \bar{\boldsymbol{T}}_{2_k} \cdot \left(\bar{\boldsymbol{T}}^*_{1_k}\right)^{-1} \cdot \left(\Delta\hat{\tilde{\boldsymbol{y}}}_k\right)^*\right). \tag{3.46}$$

Finally, $\tilde{\tilde{\boldsymbol{b}}}_{2_k}$ follows by back-substitution into (3.43). The solution vectors $\tilde{\tilde{\boldsymbol{b}}}_{1_k}$ and $\tilde{\tilde{\boldsymbol{b}}}_{2_k}$ are then employed to obtain the state increment without explicitly forming the Kalman gain matrix, resulting in

$$\Delta\hat{\tilde{\boldsymbol{x}}}_{k|k} = \bar{\boldsymbol{U}}_{1_k} \cdot \tilde{\tilde{\boldsymbol{b}}}_{1_k} + \bar{\boldsymbol{U}}_{2_k} \cdot \tilde{\tilde{\boldsymbol{b}}}_{2_k}. \tag{3.47}$$

Therefore, the updated state estimate becomes

$$\hat{\tilde{\boldsymbol{x}}}_{k|k} = \hat{\tilde{\boldsymbol{x}}}_{k|k-1} + \Delta\hat{\tilde{\boldsymbol{x}}}_{k|k}. \tag{3.48}$$

Similarly, the covariance update can be written without explicitly forming the

Kalman gain matrix. From the standard EKF correction in augmented form (3.22),

$$\bar{\boldsymbol{P}}_{k|k} = \bar{\boldsymbol{P}}_{k|k-1} - \bar{\boldsymbol{G}}_k \cdot \bar{\boldsymbol{U}}_k^H, \tag{3.49}$$

and using $\bar{\boldsymbol{G}}_k = \bar{\boldsymbol{U}}_k \cdot \bar{\boldsymbol{T}}_k^{-1}$, one obtains

$$\bar{\boldsymbol{P}}_{k|k} = \bar{\boldsymbol{P}}_{k|k-1} - \bar{\boldsymbol{U}}_k \cdot \bar{\boldsymbol{T}}_k^{-1} \cdot \bar{\boldsymbol{U}}_k^H. \tag{3.50}$$

Instead of explicitly computing $\bar{\boldsymbol{T}}_k^{-1}$, the product $\bar{\boldsymbol{T}}_k^{-1} \cdot \bar{\boldsymbol{U}}_k^H$ is obtained by solving linear system in (3.51). Using the mirrored structure in (3.32), define the auxiliary matrix $\bar{\boldsymbol{B}}_k$ as the solution of

$$\bar{\boldsymbol{T}}_k \cdot \bar{\boldsymbol{B}}_k = \bar{\boldsymbol{U}}_k^H. \tag{3.51}$$

It is worth noting that $\bar{\boldsymbol{B}}_k$ is equivalent to the Hermitian of the Kalman gain matrix, since $\bar{\boldsymbol{T}}_k = \bar{\boldsymbol{T}}_k^H$ and $\bar{\boldsymbol{B}}_k = \bar{\boldsymbol{T}}_k^{-1} \cdot \bar{\boldsymbol{U}}_k^H = \bar{\boldsymbol{G}}_k^H$. In partitioned form, (3.51) can be written as

$$\begin{bmatrix} \bar{\boldsymbol{T}}_{1_k} & \bar{\boldsymbol{T}}_{2_k} \\ \bar{\boldsymbol{T}}_{2_k}^* & \bar{\boldsymbol{T}}_{1_k}^* \end{bmatrix} \cdot \begin{bmatrix} \bar{\boldsymbol{B}}_{1_k} & \bar{\boldsymbol{B}}_{2_k} \\ \bar{\boldsymbol{B}}_{2_k}^* & \bar{\boldsymbol{B}}_{1_k}^* \end{bmatrix} = \begin{bmatrix} \bar{\boldsymbol{U}}_{1_k}^H & \bar{\boldsymbol{U}}_{2_k}^T \\ \bar{\boldsymbol{U}}_{2_k}^H & \bar{\boldsymbol{U}}_{1_k}^T \end{bmatrix}. \tag{3.52}$$

Since $\bar{\boldsymbol{B}}_k$ preserves the augmented mirrored structure, only the upper partitions $\bar{\boldsymbol{B}}_{1_k}$ and $\bar{\boldsymbol{B}}_{2_k}$ are required to update the covariance in (3.50). To compute these quantities without explicitly forming $\bar{\boldsymbol{T}}_k^{-1}$, the block system in (3.52) is solved for the first column partition as

$$\bar{\boldsymbol{T}}_k \cdot \begin{bmatrix} \bar{\boldsymbol{B}}_{1_k} \\ \bar{\boldsymbol{B}}_{2_k}^* \end{bmatrix} = \begin{bmatrix} \bar{\boldsymbol{U}}_{1_k}^H \\ \bar{\boldsymbol{U}}_{2_k}^H \end{bmatrix}. \tag{3.53}$$

Following the same procedure adopted to compute $\tilde{\bar{\boldsymbol{b}}}_{1_k}$ and $\tilde{\bar{\boldsymbol{b}}}_{2_k}$, the solution in

(3.53) is obtained via the Schur complement of $\bar{\boldsymbol{T}}^{*}_{1_k}$. Define

$$\bar{\boldsymbol{B}}_{1_k} = \left(\mathbb{SC}\left(\bar{\boldsymbol{T}}^{*}_{1_k}\right)\right)^{-1} \cdot \left(\bar{\boldsymbol{U}}^{H}_{1_k} - \bar{\boldsymbol{T}}_{2_k} \cdot \left(\bar{\boldsymbol{T}}^{*}_{1_k}\right)^{-1} \cdot \bar{\boldsymbol{U}}^{H}_{2_k}\right), \tag{3.54}$$

$$\bar{\boldsymbol{B}}^{*}_{2_k} = \left(\bar{\boldsymbol{T}}^{*}_{1_k}\right)^{-1} \cdot \left(\bar{\boldsymbol{U}}^{H}_{2_k} - \bar{\boldsymbol{T}}^{*}_{2_k} \cdot \bar{\boldsymbol{B}}_{1_k}\right). \tag{3.55}$$

After obtaining $\bar{\boldsymbol{B}}_{1_k}$ and $\bar{\boldsymbol{B}}_{2_k}$, the covariance correction in (3.50) can be performed using only the upper partitions,

$$\bar{\boldsymbol{P}}_{1_{k|k}} = \bar{\boldsymbol{P}}_{1_{k|k-1}} - \bar{\boldsymbol{U}}_{1_k} \cdot \bar{\boldsymbol{B}}_{1_k} - \bar{\boldsymbol{U}}_{2_k} \cdot \bar{\boldsymbol{B}}^{*}_{2_k}, \tag{3.56}$$

$$\bar{\boldsymbol{P}}_{2_{k|k}} = \bar{\boldsymbol{P}}_{2_{k|k-1}} - \bar{\boldsymbol{U}}_{1_k} \cdot \bar{\boldsymbol{B}}_{2_k} - \bar{\boldsymbol{U}}_{2_k} \cdot \bar{\boldsymbol{B}}^{*}_{1_k}. \tag{3.57}$$

This strategy ensures strict algebraic equivalence with the full augmented EKF update while bypassing the explicit construction of the high-dimensional gain matrix $\bar{\boldsymbol{G}}_k$. By operating exclusively on the upper partitions, the method reduces computational overhead and enhances numerical stability, which are critical requirements for large-scale power system applications. It is fundamental to underscore that this decoupling introduces no numerical approximations; instead, it leverages the structural mirror properties inherent to widely linear formulations. Consequently, the estimator preserves the statistical consistency and convergence dynamics of the standard augmented EKF, effectively transforming structural redundancy into significant performance gains.

Algorithm 1 details the implementation of the proposed D-EKF. The structure maintains the classic Kalman filter prediction–correction cycle but optimizes it by manipulating only the independent blocks of the covariance matrix. By exploiting the symmetry properties of the augmented formalism, the algorithm avoids redundant operations involving conjugate components. This results in a computationally agile execution without sacrificing state estimation accuracy.

Algorithm 1 Decoupled Complex-Valued EKF (CV-D-EKF)

Require: $\hat{\bar{\boldsymbol{x}}}_{k-1|k-1}$, $\bar{\boldsymbol{P}}_{k-1|k-1}$, $\bar{\boldsymbol{Q}}_{k-1}$, $\bar{\boldsymbol{R}}_{k}$, $\bar{\boldsymbol{y}}_{k}$, $\bar{\boldsymbol{h}}(\cdot)$, $\bar{\boldsymbol{f}}(\cdot)$

Ensure: $\hat{\bar{\boldsymbol{x}}}_{k|k}$, $\bar{\boldsymbol{P}}_{k|k}$

$\hat{\bar{\boldsymbol{x}}}_{k|k-1} \leftarrow \bar{\boldsymbol{f}}(\hat{\bar{\boldsymbol{x}}}_{k-1|k-1})$

Compute the partitions of $\bar{\boldsymbol{F}}_{k-1} \rightarrow \bar{\boldsymbol{F}}_{1_{k-1}}, \bar{\boldsymbol{F}}_{2_{k-1}}$

Compute $\bar{\boldsymbol{P}}_{1_{k|k-1}}$ and $\bar{\boldsymbol{P}}_{2_{k|k-1}}$ using (3.27) and (3.28)

$\hat{\bar{\boldsymbol{y}}}_{k} \leftarrow \bar{\boldsymbol{h}}(\hat{\bar{\boldsymbol{x}}}_{k|k-1})$

$\Delta\bar{\boldsymbol{y}}_{k} \leftarrow \bar{\boldsymbol{y}}_{k} - \hat{\bar{\boldsymbol{y}}}_{k}$

Compute the partitions of $\bar{\boldsymbol{H}}_{k} \rightarrow \bar{\boldsymbol{H}}_{1_k}, \bar{\boldsymbol{H}}_{2_k}$

Compute the partitions of $\bar{\boldsymbol{R}}_{k} \rightarrow \bar{\boldsymbol{R}}_{1_k}, \bar{\boldsymbol{R}}_{2_k}$

Compute $\bar{\boldsymbol{U}}_{k} = \bar{\boldsymbol{P}}_{k|k-1} \cdot \bar{\boldsymbol{H}}_{k}^{H}$ (upper blocks)

$\bar{\boldsymbol{U}}_{1_k} \leftarrow \bar{\boldsymbol{P}}_{1_{k|k-1}} \cdot \bar{\boldsymbol{H}}_{1_k}^{H} + \bar{\boldsymbol{P}}_{2_{k|k-1}} \cdot \bar{\boldsymbol{H}}_{2_k}^{H}$

$\bar{\boldsymbol{U}}_{2_k} \leftarrow \bar{\boldsymbol{P}}_{1_{k|k-1}} \cdot \bar{\boldsymbol{H}}_{2_k}^{T} + \bar{\boldsymbol{P}}_{2_{k|k-1}} \cdot \bar{\boldsymbol{H}}_{1_k}^{T}$

Compute $\bar{\boldsymbol{T}}_{k} = \bar{\boldsymbol{H}}_{k} \cdot \bar{\boldsymbol{U}}_{k} + \bar{\boldsymbol{R}}_{k}$ (upper blocks)

$\bar{\boldsymbol{T}}_{1_k} \leftarrow \bar{\boldsymbol{H}}_{1_k} \cdot \bar{\boldsymbol{U}}_{1_k} + \bar{\boldsymbol{H}}_{2_k} \cdot \bar{\boldsymbol{U}}_{2_k}^{*} + \bar{\boldsymbol{R}}_{1_k}$

$\bar{\boldsymbol{T}}_{2_k} \leftarrow \bar{\boldsymbol{H}}_{1_k} \cdot \bar{\boldsymbol{U}}_{2_k} + \bar{\boldsymbol{H}}_{2_k} \cdot \bar{\boldsymbol{U}}_{1_k}^{*} + \bar{\boldsymbol{R}}_{2_k}$

Solve $\bar{\boldsymbol{T}}_{k} \cdot \begin{bmatrix} \tilde{\bar{\boldsymbol{b}}}_{1_k} \\ \tilde{\bar{\boldsymbol{b}}}_{2_k} \end{bmatrix} = \begin{bmatrix} \Delta\bar{\boldsymbol{y}}_{k} \\ \left(\Delta\bar{\boldsymbol{y}}_{k}\right)^{*} \end{bmatrix}$ using (3.46) and (3.43) to obtain $\tilde{\bar{\boldsymbol{b}}}_{1_k}, \tilde{\bar{\boldsymbol{b}}}_{2_k}$

$\Delta\hat{\bar{\boldsymbol{x}}}_{k|k} \leftarrow \bar{\boldsymbol{U}}_{1_k} \cdot \tilde{\bar{\boldsymbol{b}}}_{1_k} + \bar{\boldsymbol{U}}_{2_k} \cdot \tilde{\bar{\boldsymbol{b}}}_{2_k}$

$\hat{\bar{\boldsymbol{x}}}_{k|k} \leftarrow \hat{\bar{\boldsymbol{x}}}_{k|k-1} + \Delta\hat{\bar{\boldsymbol{x}}}_{k|k}$

Solve $\bar{\boldsymbol{T}}_{k} \cdot \bar{\boldsymbol{B}}_{k} = \bar{\boldsymbol{U}}_{k}^{H}$ using (3.54) and (3.55) to obtain $\bar{\boldsymbol{B}}_{1_k}, \bar{\boldsymbol{B}}_{2_k}^{*}$

$\bar{\boldsymbol{P}}_{1_{k|k}} \leftarrow \bar{\boldsymbol{P}}_{1_{k|k-1}} - \bar{\boldsymbol{U}}_{1_k} \cdot \bar{\boldsymbol{B}}_{1_k} - \bar{\boldsymbol{U}}_{2_k} \cdot \bar{\boldsymbol{B}}_{2_k}^{*}$

$\bar{\boldsymbol{P}}_{2_{k|k}} \leftarrow \bar{\boldsymbol{P}}_{2_{k|k-1}} - \bar{\boldsymbol{U}}_{1_k} \cdot \bar{\boldsymbol{B}}_{2_k} - \bar{\boldsymbol{U}}_{2_k} \cdot \bar{\boldsymbol{B}}_{1_k}^{*}$

3.2 Complex-Valued Unscented Kalman Filter (CV-UKF)

The Unscented Kalman Filter (UKF) has made a breakthrough in dynamic state estimation for electrical power systems, offering an efficient alternative to the linear KF and EKF. Designed to handle nonlinearity in different dynamic systems, the UKF uses an *unscented* transform that provides a more accurate approximation of the probability distributions associated with the system states [34].

The UKF overcomes the limitations of the EKF by not requiring the linearization of the system model, thus avoiding errors introduced by the linear approximation. Instead, the UKF employs a set of sigma points propagated through the system's nonlinear functions, capturing the mean and covariance of the state distributions with greater accuracy.

Thus, the steps of the Unscented Kalman filter for nonlinear functions dependent on complex variables are described below [72]:

- Initialize the filter:

$$\hat{\bar{\boldsymbol{x}}}_{0|0} = \mathbb{E}\{\bar{\boldsymbol{x}}_0\}, \tag{3.58}$$

$$\bar{\boldsymbol{P}}_{0|0} = \mathbb{E}\left\{\left(\bar{\boldsymbol{x}}_0 - \mathbb{E}\left\{\bar{\boldsymbol{x}}_0\right\}\right) \cdot \left(\bar{\boldsymbol{x}}_0 - \mathbb{E}\left\{\bar{\boldsymbol{x}}_0\right\}\right)^H\right\}. \tag{3.59}$$

- Calculate the sigma points $\tilde{\tilde{\boldsymbol{\mathfrak{x}}}}_i$ for $i = 1, \ldots, 4 \cdot p$:

$$\tilde{\tilde{\boldsymbol{\mathfrak{x}}}}_{0_{k-1}} = \hat{\bar{\boldsymbol{x}}}_{k-1|k-1}, \tag{3.60}$$

$$\tilde{\tilde{\boldsymbol{\mathfrak{x}}}}_{i_{k-1}} = \hat{\bar{\boldsymbol{x}}}_{k-1|k-1} \pm \left(\sqrt{(p+\zeta) \cdot \bar{\boldsymbol{P}}_{k-1|k-1}}\right)_i, \quad i = 1, \ldots, 4 \cdot p, \tag{3.61}$$

where:

p is the dimension of the status vector $\bar{\boldsymbol{x}}$,

$\zeta = \mathfrak{s}_\mathfrak{p}{}^2 \cdot (2 \cdot p + \kappa)$ is a scale parameter,

$\mathfrak{s}_\mathfrak{p}$ is the spread of the sigma points around the mean and is typically a small value, *e.g.* 10^{-3},

κ is a secondary scale parameter and is typically zero,

$\left(\sqrt{(p+\zeta) \cdot \bar{\boldsymbol{P}}_{k-1|k-1}}\right)_i$ is the i-th column of the square root of the matrix. Considering $\bar{\boldsymbol{P}}_{k-1|k-1} = \bar{\boldsymbol{L}}_{\boldsymbol{p}} \cdot \bar{\boldsymbol{L}}_{\boldsymbol{p}}^H$, then the expression becomes $\left(\sqrt{(p+\zeta)} \cdot \bar{\boldsymbol{L}}_{\boldsymbol{p}}\right)_i$, where $\bar{\boldsymbol{L}}_{\boldsymbol{p}}$ is the factor matrix of the Cholesky decomposition.

- Calculate the weights for the sigma points:

$$W_0^{(me)} = \frac{\zeta}{(2 \cdot p + \zeta)}, \tag{3.62}$$

$$W_0^{(co)} = \frac{\zeta}{(2 \cdot p + \zeta)} + \left(1 - \mathfrak{s}_\mathfrak{p}{}^2 + \mathfrak{p}_\mathfrak{d}\right), \tag{3.63}$$

$$W_i^{(me)} = W_i^{(co)} = \frac{\zeta}{2 \cdot (2 \cdot p + \zeta)}, \quad i = 1, \ldots, 4 \cdot p, \tag{3.64}$$

where $\mathfrak{p}_\mathfrak{d}$ is the parameter related to the prior knowledge of the distribution used (for the Gaussian distribution, $\mathfrak{p}_\mathfrak{d} = 2$ is the optimal value).

Generally, in the academic literature [48], [50], dynamic state estimators for electrical power systems consider, for computational simplification, the weights of the sigma

points equal to $\frac{1}{2 \cdot p}$, where p is the dimension of the state vector $\bar{\boldsymbol{x}}$. Although the original unscented transformation employs a central sigma point with a distinct weight [75], the simplified weighting strategy considered here has been shown to provide satisfactory accuracy in practical applications. Thus, in the results section, such simplification will be adopted.

- Prediction: Update of the state variables $\left(\hat{\bar{\boldsymbol{x}}}_{k|k-1}\right)$, the estimation error matrix $\left(\bar{\boldsymbol{P}}_{k|k-1}\right)$ and the estimated measurements $\left(\hat{\bar{\boldsymbol{y}}}_{k|k-1}\right)$

$$\tilde{\bar{\boldsymbol{\mathfrak{x}}}}_{i_{k|k-1}} = \bar{\boldsymbol{f}}\left(\tilde{\bar{\boldsymbol{\mathfrak{x}}}}_{i_{k-1|k-1}}\right), \tag{3.65}$$

$$\hat{\bar{\boldsymbol{x}}}_{k|k-1} = \sum_{i=0}^{4p} W_i^{(me)} \cdot \tilde{\bar{\boldsymbol{\mathfrak{x}}}}_{i_{k|k-1}}, \tag{3.66}$$

$$\bar{\boldsymbol{P}}_{k|k-1} = \sum_{i=0}^{4p} W_i^{(co)} \cdot \left(\tilde{\bar{\boldsymbol{\mathfrak{x}}}}_{i_{k|k-1}} - \hat{\bar{\boldsymbol{x}}}_{k|k-1}\right) \cdot \left(\tilde{\bar{\boldsymbol{\mathfrak{x}}}}_{i_{k|k-1}} - \hat{\bar{\boldsymbol{x}}}_{k|k-1}\right)^H + \bar{\boldsymbol{Q}}_k, \tag{3.67}$$

$$\tilde{\bar{\boldsymbol{y}}}_{i_{k|k-1}} = \bar{\boldsymbol{h}}\left(\tilde{\bar{\boldsymbol{\mathfrak{x}}}}_{i_{k-1|k-1}}\right), \tag{3.68}$$

$$\hat{\bar{\boldsymbol{y}}}_{k|k-1} = \sum_{i=0}^{4p} W_i^{(me)} \cdot \tilde{\bar{\boldsymbol{y}}}_{i_{k|k-1}}. \tag{3.69}$$

where $\tilde{\bar{\boldsymbol{y}}}_i$ is the vector of measurements originating from the propagation of sigma points and $\hat{\bar{\boldsymbol{y}}}$ is the vector of predicted measurements.

- Estimated State Update:

$$\bar{\boldsymbol{P}}_{\boldsymbol{y}_{k|k-1}} = \sum_{i=0}^{4p} W_i^{(co)} \cdot \left(\tilde{\bar{\boldsymbol{y}}}_{i_{k|k-1}} - \hat{\bar{\boldsymbol{y}}}_{k|k-1}\right) \cdot \left(\tilde{\bar{\boldsymbol{y}}}_{i_{k|k-1}} - \hat{\bar{\boldsymbol{y}}}_{k|k-1}\right)^H + \bar{\boldsymbol{R}}_k, \tag{3.70}$$

$$\bar{\boldsymbol{P}}_{\boldsymbol{xy}_{k|k-1}} = \sum_{i=0}^{4p} W_i^{(co)} \cdot \left(\tilde{\bar{\boldsymbol{\mathfrak{x}}}}_{i_{k|k-1}} - \hat{\bar{\boldsymbol{x}}}_{k|k-1}\right) \cdot \left(\tilde{\bar{\boldsymbol{y}}}_{i_{k|k-1}} - \hat{\bar{\boldsymbol{y}}}_{k|k-1}\right)^H, \tag{3.71}$$

$$\bar{\boldsymbol{G}}_k = \bar{\boldsymbol{P}}_{\boldsymbol{xy}_{k|k-1}} \cdot \left(\bar{\boldsymbol{P}}_{\boldsymbol{y}_{k|k-1}}\right)^{-1}, \tag{3.72}$$

$$\hat{\bar{\boldsymbol{x}}}_{k|k} = \hat{\bar{\boldsymbol{x}}}_{k|k-1} + \bar{\boldsymbol{G}}_k \cdot \left(\bar{\boldsymbol{y}}_k - \hat{\bar{\boldsymbol{y}}}_{k|k-1}\right), \tag{3.73}$$

$$\bar{\boldsymbol{P}}_{k|k} = \bar{\boldsymbol{P}}_{k|k-1} - \bar{\boldsymbol{G}}_k \cdot \bar{\boldsymbol{P}}_{\boldsymbol{y}_{k|k-1}} \cdot \bar{\boldsymbol{G}}_k^H, \tag{3.74}$$

where, $\bar{\boldsymbol{P}}_{\boldsymbol{y}}$, $\bar{\boldsymbol{P}}_{\boldsymbol{xy}}$ are the predicted measurement covariance and cross-covariance matrices, respectively. The Kalman gain is expressed by $\bar{\boldsymbol{G}}$.

In contrast to the EKF, the Unscented Kalman Filter (UKF) eliminates the need

for analytical linearization by propagating deterministic sigma points to estimate the posterior mean and covariance. Since the UKF does not rely on Jacobian matrices, the structural constraints imposed by Wirtinger calculus are not strictly applicable. This algorithmic flexibility enables the formulation of the UKF in a reduced complex-valued domain, provided specific statistical assumptions are met.

In this work, a *proper* (circular) approximation is assumed for the state variables, whereby the state pseudo-covariance is neglected. While the circularity of state transients is a simplifying assumption, this modeling choice is motivated by the circularity evidenced in typical PMU measurement noise [74], which justifies a similar treatment for the noise covariance matrices ($\bar{\boldsymbol{Q}}$ and $\bar{\boldsymbol{R}}$). By omitting the complex-conjugate components and neglecting the pseudo-covariance partitions, the problem dimensionality is reduced by half. This reduction significantly enhances computational efficiency, as the number of sigma points to be propagated through the non-linear system model is halved.

While this simplification assumes that the standard covariance matrix adequately captures the second-order statistics, it provides a computationally superior alternative for large-scale systems. The assessment of the performance trade-offs between this reduced (proper) formulation and a fully augmented (widely linear) UKF—which would be necessary for strictly improper signals—is relegated to future research.

3.3 Robustification of Kalman Filters

In power systems, accurate state estimation is crucial for the efficient, safe, and stable operation of electrical networks. The presence of gross errors, including leverage points, can significantly compromise the accuracy and reliability of these estimators. In this scenario, Gandhi and Mili [76] report three types of DSE's gross errors: observation, innovation, and structural errors. Observation errors can be associated with communication losses with PMUs, a lack of synchronization between phasors, or even saturation problems in the current or voltage transformers of the equipment. Innovation errors are often associated with incorrect generator modeling, inaccuracies in the prediction model, or even noise impulses in the process. Finally, structural errors are associated with parameter or system-topology errors.

The approach proposed in [47] and [48] aims to suppress *observation* and *innovation outliers*, even at leverage points, and this topic will extend the proposal to the domain of complex numbers. It is worth remembering that leverage points are measurements whose associated row vectors of the Jacobian matrix are *outliers* concerning the other elements of the factor space [77]. In estimating states in power systems, branches with reactance that are quite discrepant from the other branches, power flow measurements on this branch, or injection measurements at buses that affect them can create

leverage points. In addition, injection measurements in buses with high branch incidence can configure measurements as leverage points [78].

3.3.1 Complex-Valued Schweppe-type Huber Generalized Maximum-likelihood Extended Kalman Filter (CV-SHGM-EKF)

Consider that the predicted state variable vector $\hat{\bar{\boldsymbol{x}}}_{k|k-1}$ in (3.16) and the measurement vector $\bar{\boldsymbol{y}}_k$ in (3.4) are expressed by (3.75) and (3.76), considering their respective errors $\bar{\boldsymbol{e}}_k$ and $\bar{\boldsymbol{v}}_k$.

$$\hat{\bar{\boldsymbol{x}}}_{k|k-1} = \bar{\boldsymbol{x}}_k - \bar{\boldsymbol{e}}_k, \tag{3.75}$$

$$\bar{\boldsymbol{y}}_k = \bar{\boldsymbol{h}}\left(\bar{\boldsymbol{x}}_k\right) + \bar{\boldsymbol{v}}_k, \tag{3.76}$$

$$\mathbb{E}\left\{\bar{\boldsymbol{e}}_k \cdot \bar{\boldsymbol{e}}_k^H\right\} = \bar{\boldsymbol{P}}_{k|k-1}, \tag{3.77}$$

$$\mathbb{E}\left\{\bar{\boldsymbol{v}}_k \cdot \bar{\boldsymbol{v}}_k^H\right\} = \bar{\boldsymbol{R}}_k. \tag{3.78}$$

Rewriting (3.75) (3.76) in matrix form, leads to,

$$\begin{bmatrix} \hat{\bar{\boldsymbol{x}}}_{k|k-1} \\ \bar{\boldsymbol{y}}_k \end{bmatrix} = \begin{bmatrix} \bar{\boldsymbol{x}}_k \\ \bar{\boldsymbol{h}}\left(\bar{\boldsymbol{x}}_k\right) \end{bmatrix} + \begin{bmatrix} -\bar{\boldsymbol{e}}_k \\ \bar{\boldsymbol{v}}_k \end{bmatrix}, \tag{3.79}$$

or,

$$\tilde{\bar{\boldsymbol{z}}}_k = \tilde{\bar{\boldsymbol{h}}}\left(\bar{\boldsymbol{x}}_k\right) + \tilde{\bar{\boldsymbol{e}}}_k, \tag{3.80}$$

$$\mathbb{E}\left\{\tilde{\bar{\boldsymbol{e}}}_k \cdot \tilde{\bar{\boldsymbol{e}}}_k\right\} = \begin{bmatrix} \bar{\boldsymbol{P}}_{k|k-1} & \mathbf{0} \\ \mathbf{0} & \bar{\boldsymbol{R}}_k \end{bmatrix} = \bar{\boldsymbol{S}}_k \cdot \bar{\boldsymbol{S}}_k^H, \tag{3.81}$$

where $\bar{\boldsymbol{S}}$ is the Cholesky factor matrix and $\mathbf{0}$ is the null matrix. It is important to note that the covariance matrix is no longer diagonal since $\bar{\boldsymbol{P}}_{k|k-1}$ is a dense matrix.

As recommended in [47], the algorithm is robustified by calculating projection statistics indices for the augmented matrix $\bar{\boldsymbol{\Phi}}_k$ to prevent the whitening step from cor-

rupting the results.

$$\bar{\boldsymbol{\Phi}}_{k} = \begin{bmatrix} \hat{\bar{\boldsymbol{x}}}_{k-1|k-2} & \hat{\bar{\boldsymbol{x}}}_{k|k-1} \\ \bar{\boldsymbol{y}}_{k-1} - \bar{\boldsymbol{h}}\left(\hat{\bar{\boldsymbol{x}}}_{k-1|k-2}\right) & \bar{\boldsymbol{y}}_{k} - \bar{\boldsymbol{h}}\left(\hat{\bar{\boldsymbol{x}}}_{k|k-1}\right) \end{bmatrix}. \tag{3.82}$$

Stahel [79] and Donoho [80] initially proposed the calculation of projection statistics indices (PS_i), and recently the formulation was extended to the domain of complex numbers, according to equation (3.83) [59].

$$PS_i = \underset{\bar{\boldsymbol{\phi}}_u}{max} \left(\frac{|\bar{\boldsymbol{\phi}}_i^H \cdot \bar{\boldsymbol{\phi}}_u|}{\xi} \right), \tag{3.83}$$

for each i-th column $\left(\bar{\boldsymbol{\phi}}_i\right)$ of $\bar{\boldsymbol{\Phi}}_k$, $u = 1 \cdots (m+n)$ is varied.

The high robustness factor ξ is expressed by (3.84) [18].

$$\xi = 1.1926 \cdot lomed_i \left(lomed_{t \neq i} \left(|\bar{\boldsymbol{\phi}}_i^H \cdot \bar{\boldsymbol{\phi}}_u + \bar{\boldsymbol{\phi}}_t^H \cdot \bar{\boldsymbol{\phi}}_u| \right) \right), \tag{3.84}$$

being the constant 1.1926 needed to make this an approximately unbiased estimate of the scale when the error model is Gaussian [81]. The term *lomed* represents the lower median.

Prewhitening is then applied by multiplying the terms in (3.80) by $\bar{\boldsymbol{S}}^{-1}$, resulting in:

$$\bar{\boldsymbol{S}}_k^{-1} \cdot \tilde{\bar{\boldsymbol{z}}}_k = \bar{\boldsymbol{S}}_k^{-1} \cdot \tilde{\bar{\boldsymbol{h}}}\left(\bar{\boldsymbol{x}}_k\right) + \bar{\boldsymbol{S}}_k^{-1} \cdot \tilde{\bar{\boldsymbol{e}}}_k, \tag{3.85}$$

in compact form,

$$\bar{\boldsymbol{z}}_k = \bar{\boldsymbol{\pi}}\left(\bar{\boldsymbol{x}}_k\right) + \bar{\boldsymbol{\nu}}_k, \tag{3.86}$$

$$\begin{aligned} \mathbb{E}\left\{\bar{\boldsymbol{\nu}}_k \cdot \bar{\boldsymbol{\nu}}_k^H\right\} &= \mathbb{E}\left\{\bar{\boldsymbol{S}}_k^{-1} \cdot \tilde{\bar{\boldsymbol{e}}}_k \cdot \tilde{\bar{\boldsymbol{e}}}_k^H \cdot \left(\bar{\boldsymbol{S}}_k^{-1}\right)^H\right\} \\ &= \bar{\boldsymbol{S}}_k^{-1} \cdot \mathbb{E}\left\{\tilde{\bar{\boldsymbol{e}}}_k \cdot \tilde{\bar{\boldsymbol{e}}}_k^H\right\} \cdot \left(\bar{\boldsymbol{S}}_k^{-1}\right)^H \\ &= \bar{\boldsymbol{S}}_k^{-1} \cdot \bar{\boldsymbol{S}}_k \cdot \bar{\boldsymbol{S}}_k^H \cdot \left(\bar{\boldsymbol{S}}_k^{-1}\right)^H \\ &= \boldsymbol{I}. \end{aligned} \tag{3.87}$$

This formulation aims at reducing the problem to the system of equations in (3.86) from the prediction stage of the Extended Kalman filter. In addition, this framework processes state variables and measurements simultaneously, enabling the correction of erroneous variables arising from various types of failures, including inaccuracies in prediction models, communication losses, and synchronization issues between meters.

In this scenario, the SHGM estimator is used to solve the problem through the IRLS (Iteratively Reweighted Least Squares) algorithm. The IRLS algorithm uses the Huber objective function ($\rho\left(\bar{r}_s\right)$), which is convex over its domain, ensuring a global minimum. In that sense, equation (3.88) expresses the minimization of the objective function.

$$\mathcal{J}\left(\bar{\boldsymbol{x}}\right) = \sum_{i=1}^{2\cdot(m+n)} \varpi_i^2 \cdot \rho\left(\bar{r}_{s_i}\right), \tag{3.88}$$

where ϖ_i is the weight associated with each i-th value of the Huber function $\rho\left(\bar{r}_{s_i}\right)$, m is the number of occurrences, and n is the number of states evaluated.

The main characteristic of the objective function proposed by Huber derives from the statistical robustness of the LAV (Least Absolute Value) estimator and the statistical efficiency of the WLS estimator. Thus, the Huber objective function ensures statistical efficiency in the quadratic portion of the function. At the same time, in the interval tangent to the point onwards, its robustness is preserved, according to the investigation (3.89).

$$\rho\left(\bar{r}_{s_i}\right) = \begin{cases} \dfrac{\bar{r}_{s_i}^2}{2}, & \text{for } \left|\bar{r}_{s_i}\right| \leq \tau, \\ \\ \tau \cdot \left|\bar{r}_{s_i}\right| - \dfrac{\tau^2}{2}, & \text{for } \left|\bar{r}_{s_i}\right| > \tau. \end{cases} \tag{3.89}$$

The first derivative of the Huber cost function $\rho\left(\bar{r}_{s_i}\right)$ with respect to $\bar{r}_{s_i}$, denoted by $\psi\left(\bar{r}_{s_i}\right)$, corresponds to the influence function of the estimator, as shown in (3.90). This work adopts the threshold $\tau = 1.345$, which provides a statistical efficiency of approximately 95% under Gaussian noise conditions [82].

$$\psi\left(\bar{r}_{s_i}\right) = \begin{cases} \bar{r}_{s_i}, & \text{for } \left|\bar{r}_{s_i}\right| \leq \tau, \\ \\ \tau \cdot sign\left(\bar{r}_{s_i}\right), & \text{for } \left|\bar{r}_{s_i}\right| > \tau. \end{cases} \tag{3.90}$$

The i-th standardized residual ($\bar{r}_{s_i}$) can be expressed by the relation:

$$\bar{r}_{s_i} = \frac{\bar{r}_i}{s \cdot \varpi_i}, \tag{3.91}$$

where the i-th residual $\bar{r}_i = \bar{z}_i - \bar{\phi}_i\left(\hat{\bar{\boldsymbol{x}}}_k\right)$; the factor $s = 1.4826 \cdot b_m \cdot median_i\left(|\bar{r}_i|\right)$ is a scaling attribute of the robust estimator that depends on the correction factor b_m used to promote unbiasedness of the Gaussian distribution [18]. The equation (3.92) evidentiates the weight assigned to the measures identified as leverage points.

$$\varpi_i = min\left(1, \left(\frac{c_i}{PS_i}\right)^2\right), \tag{3.92}$$

where c_i is the cutoff value for detecting leverage points, i.e., the variable is considered a leverage point if $PS_i > c_i$. It is assumed $c_i = 1.5$ [76] for good statistical efficiency in the presence of leverage points.

The optimality condition corresponding to the objective function is met when $\nabla \mathcal{J}\left(\bar{\boldsymbol{x}}\right) = \mathbf{0}$, i.e.,

$$\sum_{i=1}^{m+n} \varpi_i^2 \cdot \left(\frac{\partial \bar{r}_{s_i}}{\partial \bar{x}_i}\right)^H \cdot \psi\left(\bar{r}_{s_i}\right) = \mathbf{0}. \tag{3.93}$$

The IRLS algorithm solves the equation (3.93) derived in the complex domain. Thus, multiplying and dividing $\psi\left(\bar{r}_{s_i}\right)$ by $\bar{r}_{s_i}$, in (3.93), yields:

$$\sum_{i=1}^{m+n} \varpi_i^2 \cdot \left(\frac{1}{s \cdot \varpi_i} \cdot \frac{\partial \bar{r}_i}{\partial \bar{x}_i}\right)^H \cdot \frac{\psi\left(\bar{r}_{s_i}\right)}{\left(\frac{\bar{r}_i}{s \cdot \varpi_i}\right)} \cdot \left(\frac{\bar{r}_i}{s \cdot \varpi_i}\right) = \mathbf{0}, \tag{3.94}$$

which rearranged (3.94), results in the following equality:

$$\sum_{i=1}^{m+n} \left(\frac{\partial \bar{r}_i}{\partial \bar{x}_i}\right)^H \cdot q\left(\bar{r}_{s_i}\right) \cdot \left(\frac{\bar{r}_i}{s^2}\right) = \mathbf{0}, \tag{3.95}$$

where $q\left(\bar{r}_{s_i}\right) = \dfrac{\psi\left(\bar{r}_{s_i}\right)}{\bar{r}_{s_i}}$ is the variable weight function of the SHGM estimator.

In matrix form the equation (3.95) in the complex domain becomes:

$$\bar{\boldsymbol{\Upsilon}}^H \cdot \bar{\mathbf{Q}}_{\mathbf{v}} \cdot \left(\bar{\boldsymbol{z}} - \bar{\boldsymbol{\pi}}\left(\bar{\boldsymbol{x}}\right)\right) = \mathbf{0}, \tag{3.96}$$

where

$$\bar{\boldsymbol{\Upsilon}} = \left.\frac{\partial \bar{\boldsymbol{\pi}}}{\partial \bar{\boldsymbol{x}}}\right|_{\bar{\boldsymbol{x}}=\hat{\bar{\boldsymbol{x}}}}, \tag{3.97}$$

$$\bar{\mathbf{Q}}_{\mathbf{v}} = diag\left(q\left(\bar{r}_{s_i}\right)\right). \tag{3.98}$$

The Taylor series expansion of $\bar{\boldsymbol{\pi}}\left(\bar{\boldsymbol{x}}\right)$ in $\hat{\bar{\boldsymbol{x}}}_{k|k}$ is:

$$\bar{\boldsymbol{\pi}}\left(\bar{\boldsymbol{x}}\right) \cong \bar{\boldsymbol{\pi}}\left(\bar{\boldsymbol{x}}_{k|k}^{(\vartheta)}\right) + \bar{\boldsymbol{\Upsilon}} \cdot \Delta\hat{\bar{\boldsymbol{x}}}_{k|k}^{(\vartheta+1)}, \tag{3.99}$$

which substituting in (3.96), leads to,

$$\bar{\boldsymbol{\Upsilon}}^{H} \cdot \bar{\mathbf{Q}}_{\mathbf{v}} \cdot \bar{\boldsymbol{\Upsilon}} \cdot \Delta\hat{\bar{\boldsymbol{x}}}_{k|k}^{(\vartheta+1)} = \bar{\boldsymbol{\Upsilon}}^{H} \cdot \bar{\mathbf{Q}}_{\mathbf{v}} \cdot \Delta\bar{\boldsymbol{z}}^{(\vartheta)}, \tag{3.100}$$

where $\Delta\hat{\bar{\boldsymbol{x}}}_{k|k}^{(\vartheta+1)} = \hat{\bar{\boldsymbol{x}}}_{k|k}^{(\vartheta+1)} - \hat{\bar{\boldsymbol{x}}}_{k|k}^{(\vartheta)}$ and $\Delta\bar{\boldsymbol{z}}^{(\vartheta)} = \bar{\boldsymbol{z}}^{(\vartheta)} - \bar{\boldsymbol{\pi}}\left(\hat{\bar{\boldsymbol{x}}}_{k|k}^{(\vartheta)}\right)$. On the other hand, it should be noted that the previous equation is equivalent to solving the redundant system of equations as follows:

$$\Delta\hat{\bar{\boldsymbol{x}}}_{k|k}^{(\vartheta+1)} = \overline{\boldsymbol{\Upsilon}}^{\dagger} \cdot \Delta\overline{\boldsymbol{z}}^{(\vartheta)}, \tag{3.101}$$

$$\overline{\boldsymbol{\Upsilon}} = \bar{\mathbf{Q}}_{\mathbf{v}}^{0.5} \cdot \bar{\boldsymbol{\Upsilon}}, \tag{3.102}$$

$$\Delta\overline{\boldsymbol{z}}^{(\vartheta)} = \bar{\mathbf{Q}}_{\mathbf{v}}^{0.5} \cdot \Delta\bar{\boldsymbol{z}}^{(\vartheta)}. \tag{3.103}$$

Finally, equations (3.101-3.103) represent the solution of a redundant system of equations, and the stopping criterion of the iterative process is expressed in the equation (3.104).

$$\left\|\Delta\hat{\bar{\boldsymbol{x}}}_{k|k}^{(v+1)}\right\|_{\infty} \leq 10^{-3}. \tag{3.104}$$

However, it is essential to emphasize that in this work, it was chosen to use the *weighted least squares with the minimum norm - lsqminnorm* algorithm [83]; that is, it minimizes not only the Euclidean norm of the problem: $\boldsymbol{A} \cdot \bar{\boldsymbol{x}} = \boldsymbol{b}$, but also the Euclidean norm of the solution vector $\bar{\boldsymbol{x}}$. This algorithm uses QR factorization and simultaneously seeks the solution with the minimum norm when solving systems of redundant linear algebraic equations. Another alternative to improve computational performance is the

application of fast Givens rotations in the complex domain, which do not perform the arithmetic operations of square root and division [84].

The flowchart in Figure 1 summarizes the steps for the CV-SHGM-EKF algorithm.

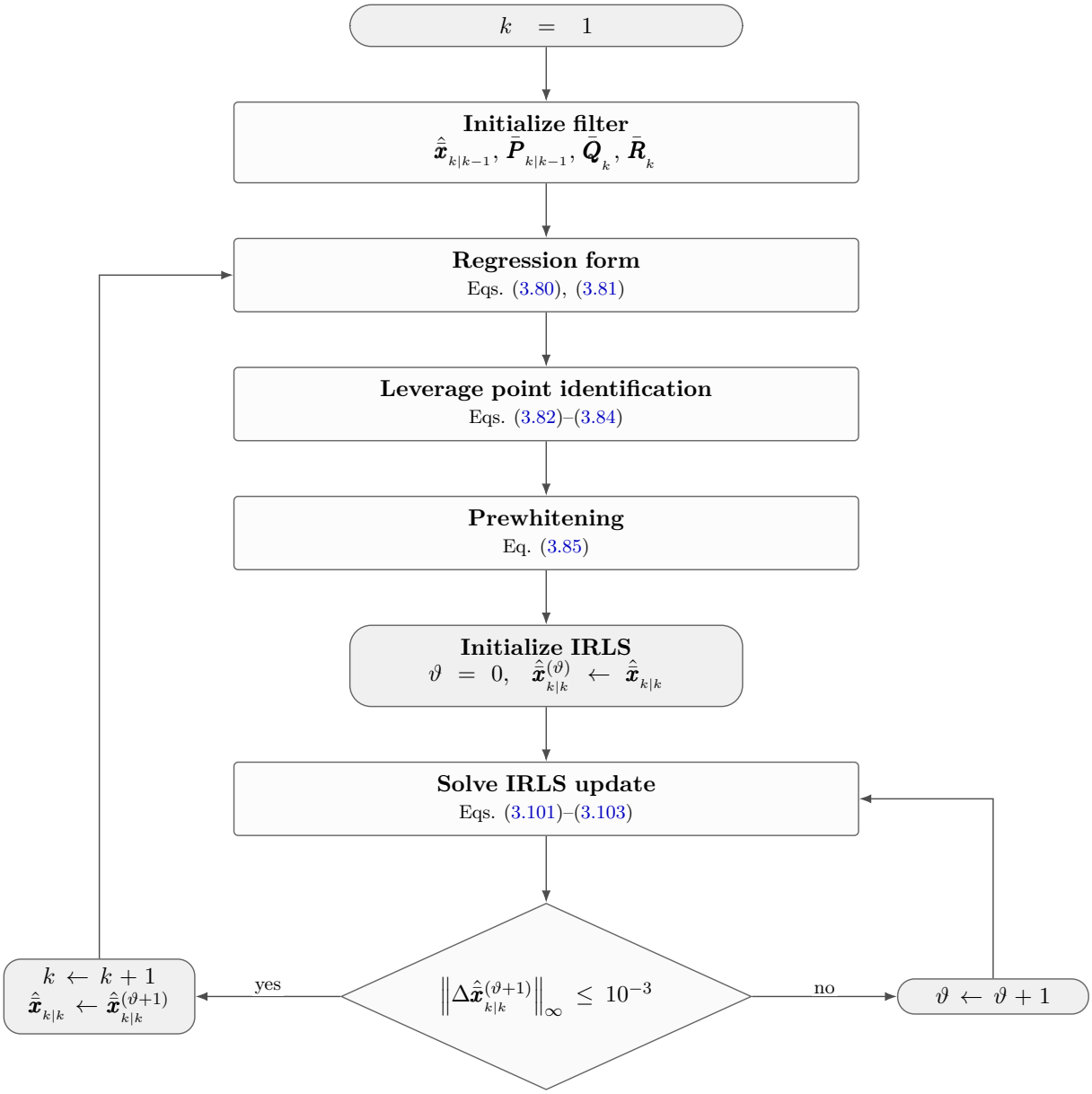


Figure 1 – Flowchart for CV-SHGM-EKF.

3.3.2 Complex-Valued Schweppe-type Huber Generalized Maximum-likelihood Unscented Kalman Filter (CV-SHGM-UKF)

Similar to the robust estimator based on the EKF, robustification of the UKF starts by assembling a system as a linear regression, grouping state variables and measurements. Thus, consider the equation (3.75) and the statistical linearization of (3.76) in (3.105)

[48, 50].

$$\bar{\boldsymbol{y}}_{k} = \bar{\boldsymbol{h}}\left(\hat{\bar{\boldsymbol{x}}}_{k|k-1}\right) + \tilde{\bar{\boldsymbol{H}}}_{k} \cdot \left(\bar{\boldsymbol{x}}_{k} - \hat{\bar{\boldsymbol{x}}}_{k|k-1}\right) + \bar{\boldsymbol{v}}_{k} + \bar{\boldsymbol{\epsilon}}_{k}. \tag{3.105}$$

It is essential to highlight that statistical linearization creates the matrix $\tilde{\bar{\boldsymbol{H}}}$ in (3.106) which is not a Jacobian matrix, with the process covariance expressed in (3.107) assuming the algebra of complex numbers [48, 85].

$$\tilde{\bar{\boldsymbol{H}}}_{k} = \left(\bar{\boldsymbol{P}}_{\boldsymbol{xy}_{k|k-1}}\right)^{H} \cdot \left(\bar{\boldsymbol{P}}_{k|k-1}\right)^{-1}, \tag{3.106}$$

$$\mathbb{E}\left\{\bar{\boldsymbol{\epsilon}} \cdot \bar{\boldsymbol{\epsilon}}^{H}\right\} = \bar{\boldsymbol{P}}_{\boldsymbol{y}_{k|k-1}} - \left(\bar{\boldsymbol{P}}_{\boldsymbol{xy}_{k|k-1}}\right)^{H} \cdot \left(\bar{\boldsymbol{P}}_{k|k-1}\right)^{-1} \cdot \bar{\boldsymbol{P}}_{\boldsymbol{xy}_{k|k-1}} = \tilde{\bar{\boldsymbol{R}}}_{k}. \tag{3.107}$$

Rewriting (3.75) and (3.105) in matrix form, it follows that,

$$\begin{bmatrix} \hat{\bar{\boldsymbol{x}}}_{k|k-1} \\ \bar{\boldsymbol{y}}_{k} - \bar{\boldsymbol{h}}\left(\hat{\bar{\boldsymbol{x}}}_{k|k-1}\right) + \tilde{\bar{\boldsymbol{H}}}_{k} \cdot \hat{\bar{\boldsymbol{x}}}_{k|k-1} \end{bmatrix} = \begin{bmatrix} \boldsymbol{I} \\ \tilde{\bar{\boldsymbol{H}}}_{k} \end{bmatrix} \cdot \bar{\boldsymbol{x}}_{k} + \begin{bmatrix} -\bar{\boldsymbol{e}}_{k} \\ \bar{\boldsymbol{v}}_{k} + \bar{\boldsymbol{\epsilon}}_{k} \end{bmatrix}. \tag{3.108}$$

Thus, regrouping the terms, the equation will be of the form (3.80), with the covariance matrix given by:

$$\mathbb{E}\left\{\tilde{\bar{\boldsymbol{e}}}_{k} \cdot \tilde{\bar{\boldsymbol{e}}}_{k}\right\} = \begin{bmatrix} \bar{\boldsymbol{P}}_{k|k-1} & \boldsymbol{0} \\ \boldsymbol{0} & \bar{\boldsymbol{R}}_{k} + \tilde{\bar{\boldsymbol{R}}}_{k} \end{bmatrix} = \bar{\boldsymbol{S}}_{k} \cdot \bar{\boldsymbol{S}}_{k}^{H}. \tag{3.109}$$

Analogously to CV-SHGM-EKF, the UKF robustness process follows the same line of reasoning, starting with the process of identifying leverage points (3.82)-(3.84) followed by the whitening process (3.85), arriving at the process of solving the system of equations through the IRLS algorithm (3.101)-(3.103). The step-by-step is shown in Figure 2.

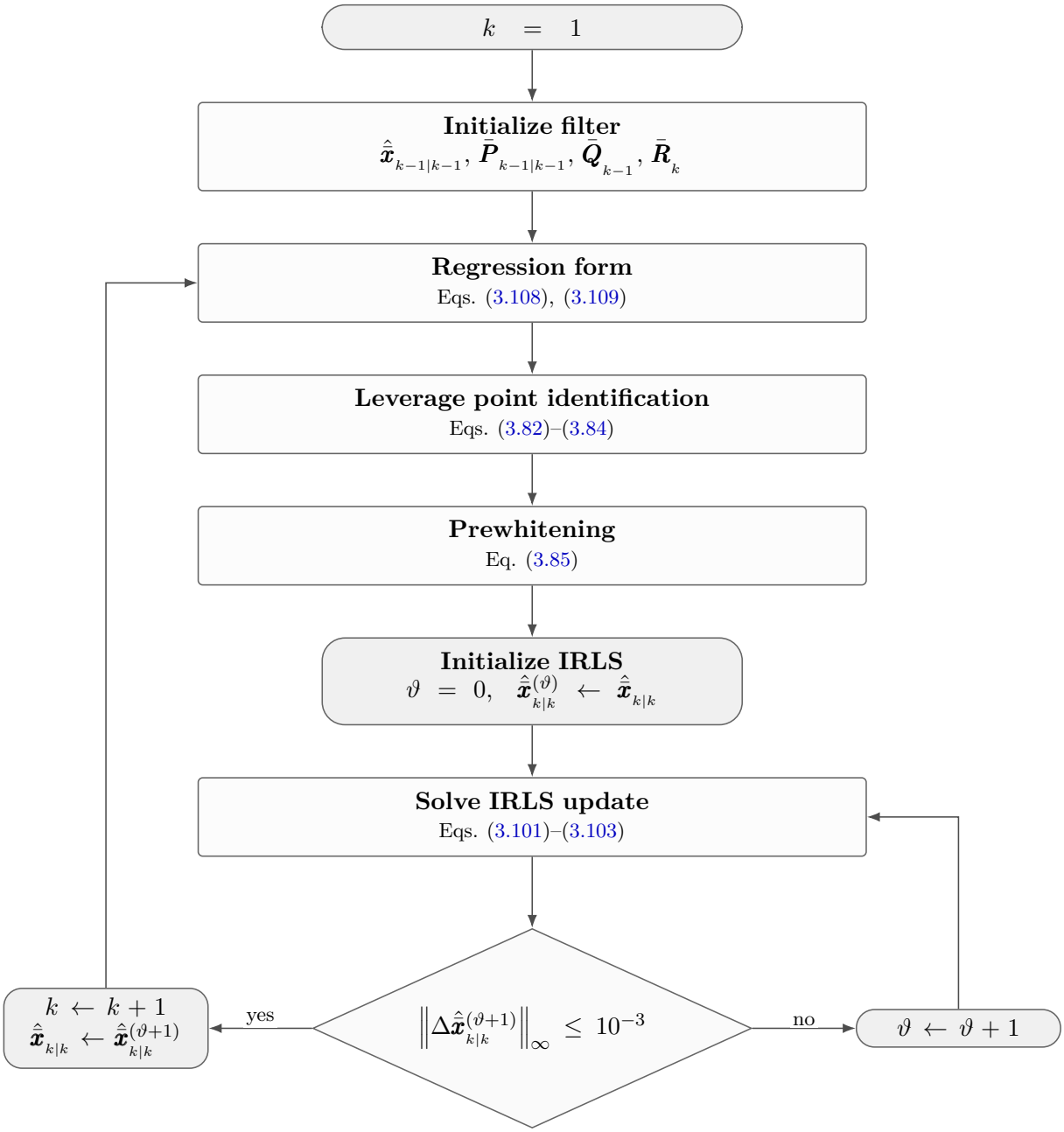


Figure 2 – Flowchart for CV-SHGM-UKF.

The modeling and estimation framework developed in Chapters 2 and 3 enables direct interpretation of frequency-control phenomena in the complex domain. In this context, Chapter 4 revisits classical frequency response concepts to provide a coherent bridge between physical frequency dynamics and the proposed complex-valued estimation framework.

4 Frequency Estimation

Over the past few years, the exponential growth in the number of renewable energy sources connected to the power grid worldwide has been remarkable. For instance, photovoltaics (PVs), wind, and energy storage are added to replace energy production from traditional synchronous generators (SGs). However, the power electronic converter used to interface the renewable energy sources with the power grid operates asynchronously. As a result, the intermittent nature of renewable energy, along with decreased power system inertia, raises concerns about frequency stability. Furthermore, voltage and frequency deviations occur more frequently when reverse power flow occurs under supply-demand imbalance in distributed power systems [86].

Recalling that the synchronous generator's inertia is defined as the ratio between its kinetic energy and its rated power [87], the system inertia tends to reduce significantly. Indeed, in response to a sudden loss of generation, the stored kinetic energy will automatically be extracted from the rotating synchronized machines on the interconnection, causing the machines to slow down and, consequently, the system frequency to decline.

On the other hand, system inertia has not traditionally been monitored or forecast in today's control room. Thus, system inertia should be included among the key attributes to assess the operational impact of non-synchronous machines on a power grid. So, if abundant wind or solar generation coincides with low load conditions, wholesale energy market prices could be low or even negative, forcing many synchronous generators offline for economic reasons and resulting in low system inertia.

This new scenario represents an excellent endeavor for maintaining system stability, as reduced inertia might otherwise trigger over-/under-frequency relays, load shedding, and exceptional protection goals [88, 87]. Indeed, the frequency measurements at different locations during electromechanical oscillations are usually distinct, so it isn't easy to take one of them as representative of the system-level frequency. To circumvent this difficulty, the center of inertia frequency (f_{COI}) has been proposed to represent the actual system frequency [89, 90]. Notice the f_{COI} is defined as the frequency using electric rotor speeds weighted by rotor inertia values.

Regarding this issue, the literature offers interesting approaches; e.g., in [87], a review of methods for power system inertia estimation is presented, and the impacts of converter-interfaced generations are nicely discussed. Equally, in [91], an estimation algorithm for calculating the ROCOF under low inertia power grids is proposed using filtering noises [92].

In the academic literature, the most in-depth investigation of the frequency re-

sponse impacts of variable renewable generation is found in [93, 94, 89, 95]; therefore, this work follows their recommendations. Specifically, a new approach is proposed to more accurately calculate the system's f_{COI} and ROCOF values. But to reach this goal, instead of using local frequency-based estimation [96], this chapter proposes extending the frequency estimation concept as a byproduct of the dynamic state estimator formulated in the complex domain.

4.1 Power System Frequency Control

The primary frequency control acts automatically and faster than secondary and tertiary control layers. Nevertheless, its dynamic response is fundamentally limited by the inertia of synchronous generators, which dictates the initial frequency evolution after a disturbance. Even so, primary control is indispensable for preserving system reliability following sudden generation losses. Fortunately, a growing number of studies on renewable integration have examined requirements for primary frequency control; in the near past, most focused only on secondary and tertiary frequency control [97]. When a frequency event occurs, depending on the types of synchronous generators, e.g., hydro, nuclear, and thermal, the rotational inertia constant ranges from 1.75 [s] to approximately 10 [s] [98]. Figure 3 shows the temporal changes in the power frequency. Meanwhile, Figure 4 shows the sequential actions of primary, secondary, and tertiary frequency control to restore system frequency following the sudden imbalance between generation and demand. Hence, based on the points A, B, and C shown in Figure 5, the following definitions should be made:

1. Pre-disturbance Frequency: Frequency at point A
2. Settling Frequency: Frequency at point B
3. Frequency Nadir: Frequency at point C, i.e., minimum value of frequency reached during the transient period.

Based on the preceding definitions, the industry measures frequency response by relating the size of the loss-of-generation event to the resulting change in system frequency once the system has stabilized (see Point B in Figure 5). This can be expressed as presented below [95].

$$\underbrace{Frequency\ Response}_{current\ practice} = \frac{Generation\ Lost\ (MW)}{f_{Point\ A} - f_{Point\ B}}, \tag{4.1}$$

$$\underbrace{Nadir\ Based}_{Frequency\ Response} = \frac{Generation\ Lost\ (MW)}{f_{Point\ A} - f_{Point\ C}}, \tag{4.2}$$

whereas *Nadir based frequency response* is evaluated through the equation (4.2).

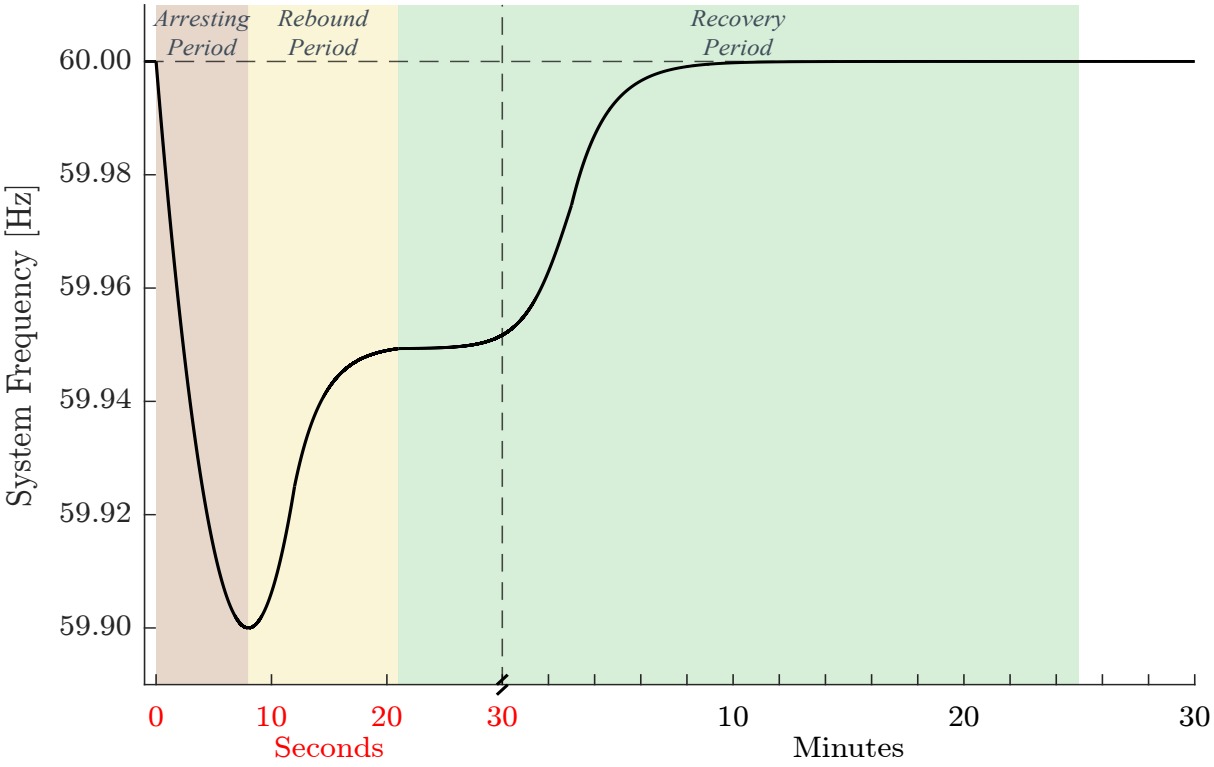


Figure 3 – Changing of power system frequency [95].

4.2 Frequency Response

Accordingly, the following questions concerning the frequency responses of variable renewable generation can be stated:

1. Will Lower System Inertia require increased reserves for primary frequency control?
2. May Displace Primary Frequency Control Reserves require procedures for ensuring adequate reserves for primary frequency control?
3. May the Location of Primary Frequency Control Reserves require consideration of transmission system limits and deliverability of primary frequency control actions?
4. Will Increased Requirements on the Adequacy of Secondary Frequency Control Reserves require better forecasting and improved operating practices?

The rapid ramping of variable renewable generation output is not considered a frequency response event comparable to the sudden loss of conventional generation. Still, rapid ramping represents an essential new operating challenge directly related to Impact 4. Nevertheless, an open question remains about the most effective Primary Frequency

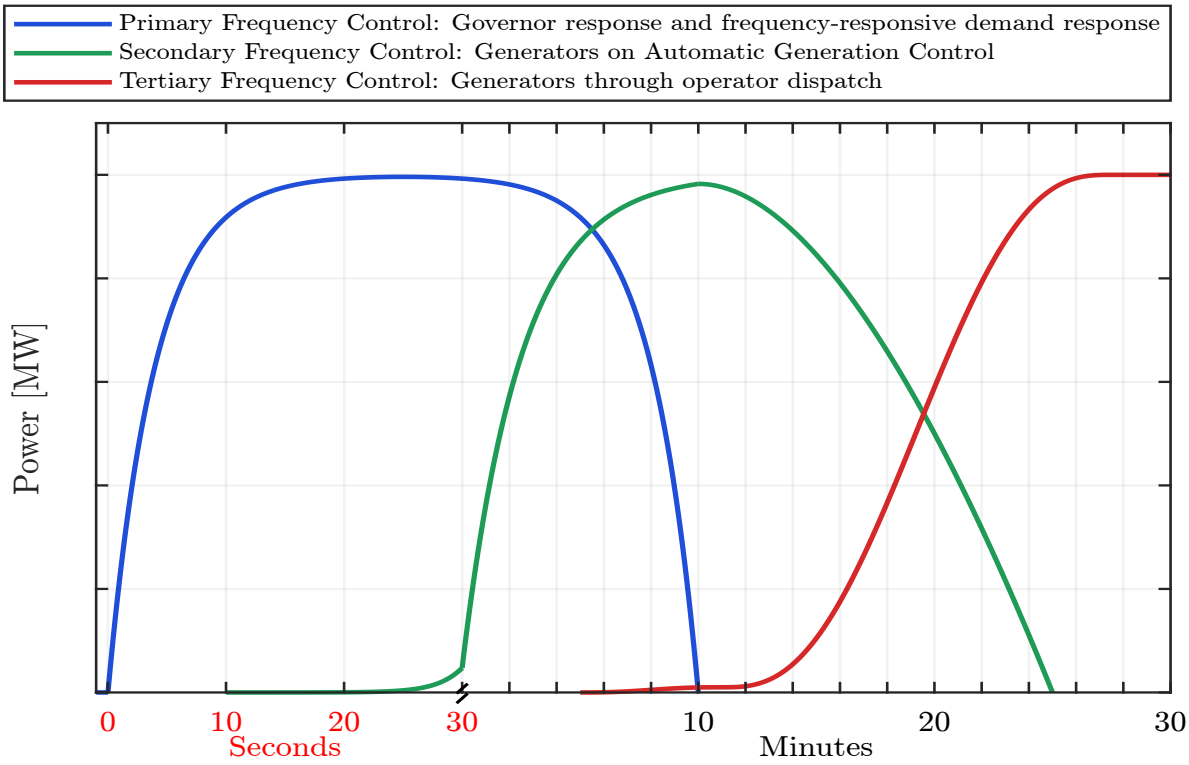


Figure 4 – Frequency response control with different timescales [95].

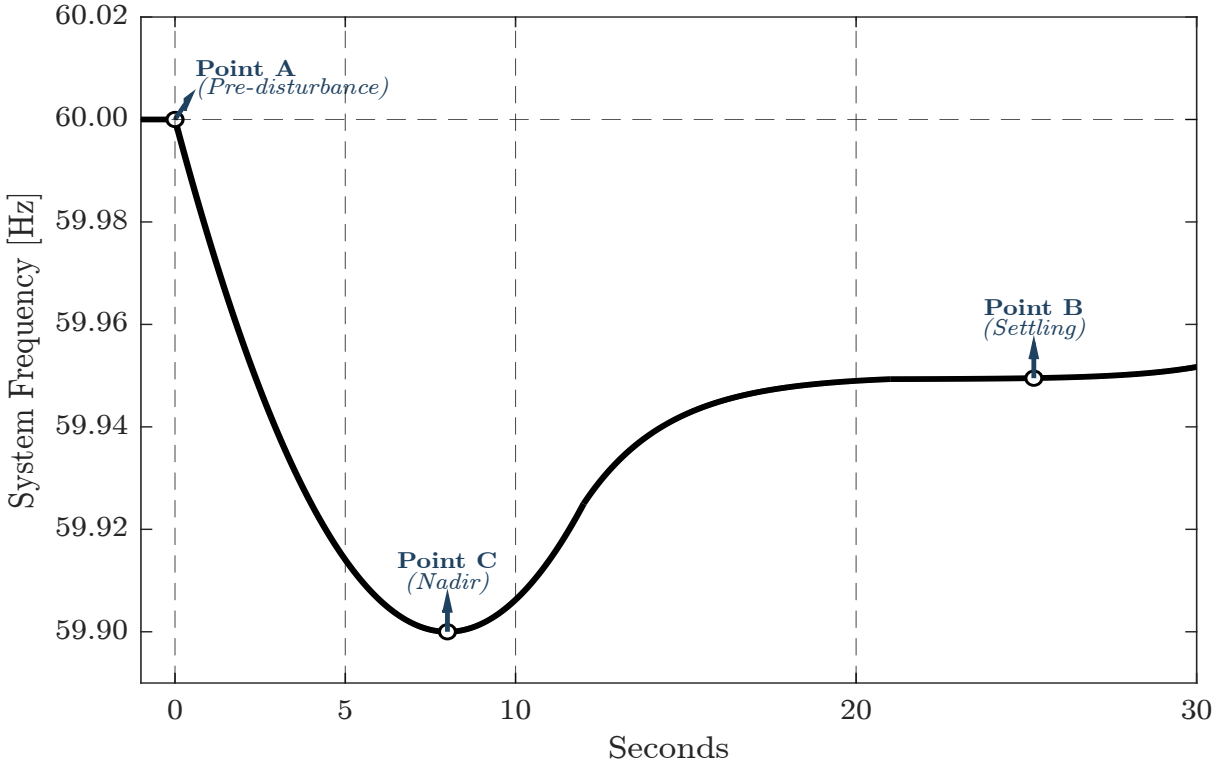


Figure 5 – System frequency [95].

Response (PFR) to adopt, as shown in Figure 6. Although system inertia has traditionally not been an explicit operational variable in many control rooms, it has become a key attribute for assessing the operational impact of nonsynchronous generation on modern power systems. Procuring a fixed-frequency response reserve is inefficient, as system inertia can vary widely over the course of a year. Hence, monitoring system inertia in real time and forecasting it for the coming hours is imperative. For instance, the performance investigated on the ERCOT system showed that the proposed method is promising for forecasting system inertia and Primary Frequency Response (PFR) 3 hours ahead, thus increasing real-time situation awareness as more renewables are integrated [99].

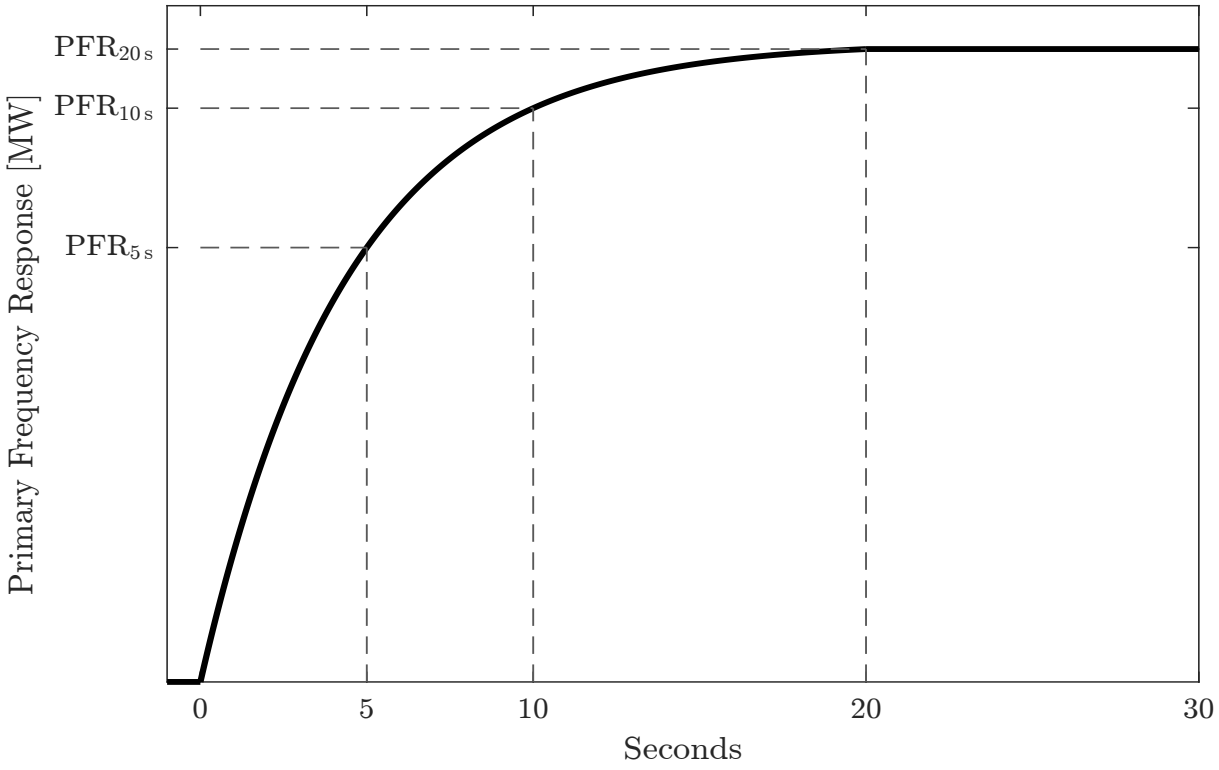


Figure 6 – Primary frequency response [95].

In short, the real-time speed values of all machines are not always available in practice due to insufficient measurement. Consequently, this makes it challenging to obtain the f_{COI} frequency, and the estimation of ROCOF also becomes difficult to apply in large power systems since ROCOF values appear different for different locations [97].

4.3 The Estimations of Center of Inertia Frequency, ROCOF, and the Disturbance's Size (MW)

4.3.1 Center of Inertia Frequency ($\mathbf{f_{COI}}$)

The Center of Inertia Frequency (f_{COI}) can be taken as a global parameter for a region so that all synchronous generators can be aggregated into one equivalent unit [91]

which can be expressed as follows

$$f_{COI_k} = \frac{\sum_{i=1}^{N} H_i \cdot f_k}{\sum_{i=1}^{N} H_i} = \frac{1}{H_{sys}} \cdot \sum_{i=1}^{N} H_i \cdot f_k, \tag{4.3}$$

where H_i and f_k are the inertia time constant and the real-time speed of the i^{th} machine, being N the total number of synchronous generators, respectively. Consequently, H_{sys} is the total system inertia.

4.3.2 Rate of Change of Frequency (ROCOF)

In turn, the ROCOF is defined as the first-order derivative of the frequency. But for reliability regulation purposes, the calculation method of ROCOF proposed by North American Electric Reliability Corporation (NERC) considers the frequency change in the first 0.5 [s] after a frequency disturbance, yielding

$$ROCOF = \frac{df}{dt} = \frac{1}{2}(f_s - f_{0.5}), \tag{4.4}$$

f_s and $f_{0.5}$ are the synchronous frequencies at the event start time and half a second after the disturbance, respectively. The IEEE Std. C.37.118.1 specifies that PMUs must provide ROCOF data at a reporting rate of 10 data per second with the steady-state error limited to 0.01 [Hz/s] [100].

4.3.3 Disturbance's Size - ΔP_{dist} (MW)

As the inertia of each synchronous generator in operation is a known parameter besides its nominal capacity (S_{nom_i}), the system inertia as a whole is becoming an accessible and monitored index in control rooms of many power grids [101, 99]. The total inertia from synchronized generators can be calculated as

$$H_{sys} = \sum_{i=1}^{N} H_i \cdot S_{nom_i}. \tag{4.5}$$

Hence, using the ROCOF values and the system inertia information, disregarding the unknown sources of inertia on the demand side, the size of the power imbalance right after the first moments of the disturbance (t_{dist} - Point A in Figure 5) can be estimated, yielding

$$\Delta P_{dist}(t) = P_m(t) - P_e(t) = 2 \cdot H_{sys} \cdot \left(\frac{d(\Delta f_{COI}(t))}{dt} \right), \tag{4.6}$$

where P_m is the mechanical power and P_e is the electrical power at instant t after the disturbance start time (t_{dist}). Moreover, observe that the sign of ΔP_{dist} is positive in case of a disturbance that causes power deficiency (e.g., disconnection of a generation) and negative in case of a disturbance that causes power surplus (e.g., loss of a load).

Furthermore, note that in (4.6), the power changes due to frequency and voltage variation in the estimation are not included. Notice that the change in total load demand also occurs and is attributed to the voltage- and frequency-dependency of the loads. This dependency may also contain certain variations. If a power imbalance is considered, the frequency and the voltage change; hence, the frequency and voltage-dependent loads change their demand accordingly. This power change can be significant; hence, if it is not included in the estimation method, the method's accuracy declines. [89]. However, these issues are beyond the scope of the present work and will be considered in the forthcoming work.

Therefore, once the ROCOF has been estimated as in (4.4) and the system inertia information is known, the estimated event MW magnitude as calculated above in (4.6) can be obtained right after the event occurrence and used in a fast primary frequency control, thus avoiding the Nadir based frequency from being reached (see, Figure 5 - Point C) [66]. Moreover, once the MW loss is based on ROCOF, some feedforward frequency control strategies can be designed to leverage fast response, e.g., inverters aid in low-inertia power grids [86].

5 Numerical Results

This chapter presents the numerical results and their respective discussions, organized to evaluate the proposed complex-domain framework across different levels of complexity. Initially, the structure and modeling of a dynamic state estimator are detailed for a 3-bus test system, providing a fundamental proof-of-concept using the classical synchronous machine model. Subsequently, the analysis is extended to the New England system [102], with 39 buses, employing the detailed two-axis machine model equipped with IEEE DC1A and TGOV1 regulators. To assess scalability and robustness in large-scale scenarios, further evaluations are conducted on the IEEE 118-bus system [103] and a 340-bus equivalent of the Brazilian Interconnected Power System (SIN-340).

Based on the theory established in Chapter 3, the performance of the following estimators is evaluated: the traditional Augmented EKF (CV-EKF), the proposed Decoupled EKF (D-EKF), and the Unscented Kalman Filter (CV-UKF), along with their respective robust versions (CV-SHGM-EKF and CV-SHGM-UKF). The analysis covers three main fronts:

- **Estimation Accuracy:** State tracking and prediction capacity, specifically in the presence of gross errors, communication failures, and bad leverage points;
- **Operational Security:** Discussions regarding the estimation of the center of inertia frequency and its impacts on power system monitoring;
- **Computational Performance:** A comparative analysis between real-domain and complex-domain formulations, focusing on execution times, structural optimizations, and the scalability of the algorithms.

All simulations were carried out in MATLAB, with the algorithms implemented using sparsity exploitation and vectorization techniques to improve computational efficiency. The numerical experiments were conducted on a computer equipped with an Intel(R) Core(TM) i7-7700HQ CPU @ 2.80 GHz, 16 GB of RAM, and a 64-bit operating system.

The dynamic behavior of the test systems was validated using the ORGANON software [104]. In addition, the real-domain dynamic state estimators proposed in [47] and [48] were adopted as benchmark methods, with their results further validated using the PSS/E software [105].

5.1 3-bus Test System

This section considers a test system composed of two synchronous generators interconnected through a three-bus transmission network, as illustrated in Figure 7.

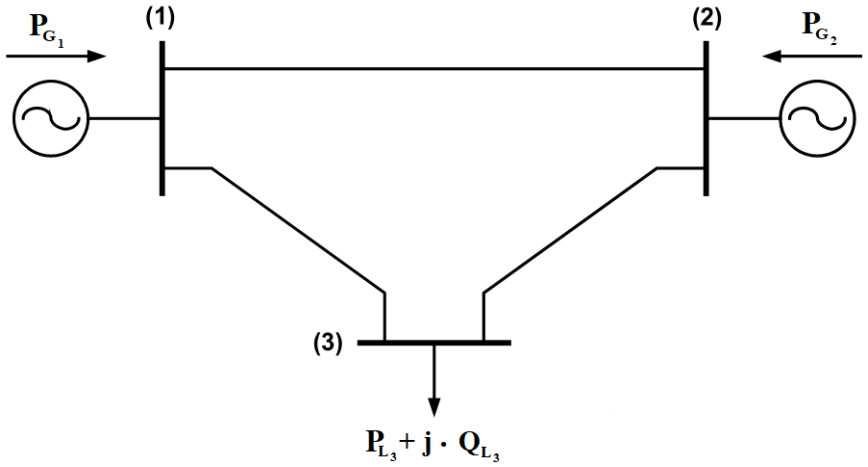


Figure 7 – 3-bus test system.

The electrical parameters of the network are summarized in Tables 6 and 7, which present the line and bus data, respectively.

Table 6 – Line data for 3-bus test system

Buses		R	X	B
From	To	[pu]	[pu]	[MVAr]
1	2	0.002	0.040	20
1	3	0.001	0.020	10
2	3	0.004	0.080	40

Table 7 – Bus data for 3-bus test system

Bus	V	P_G	Q_G	P_L	Q_L
	[pu]	[MW]	[MVAr]	[MW]	[MVAr]
1	1.03	–	–	–	–
2	1.05	600	–	–	–
3	–	–	–	1250	350

5.1.1 Preliminary Calculations

Initially, the Newton-Raphson [106] algorithm was used to obtain the power flow solution. A base power of 100 MVA was adopted, with a tolerance of 10^{-3} for the convergence criterion. Thus, the Tables 8 and 9 contain output reports relating to buses and branches, respectively.

Table 8 – Bus report for 3-bus test system

Bus	Voltage		Injected Power	
	V_i [pu]	θ_i [°]	P_i [pu]	Q_i [pu]
1	1.0300	0.000	6.6661	4.2604
2	1.0500	5.296	6.0000	1.8477
3	0.9460	-10.574	-12.5000	-3.5000

Table 9 – Branch report for 3-bus test system

Branch		Power Flow	
From	To	P_{ij} [pu]	Q_{ij} [pu]
1	2	-2.5093	-0.3802
2	1	2.5213	0.4041
1	3	9.1754	4.6406
3	1	-9.0753	-2.7359
2	3	3.4787	1.4436
3	2	-3.4247	-0.7641

To represent the electromechanical dynamics of the generators, Table 10 lists the parameters of each synchronous machine.

Table 10 – Machine data for 3-bus test system

SM	R_a [pu]	X'_d [pu]	H [MJ/MVA]	D_m [pu]	S_b [MVA]
1	0	0.25	5	1	1000
2	0	0.25	5	1	800

SM: Synchronous Machine.

The machine parameters are converted to the system base $S_b = 100$ [MVA] using the relations given in (5.1)–(5.3).

$$X'_{d_{new}} = X'_d \cdot \left(\frac{V}{V_{new}}\right)^2 \cdot \frac{S_{b_{new}}}{S_b}, \tag{5.1}$$

$$H_{new} = H \cdot \frac{S_b}{S_{b_{new}}}, \tag{5.2}$$

$$D_{new} = D \cdot \frac{\omega_{new}}{\omega} \cdot \frac{S_b}{S_{b_{new}}}. \tag{5.3}$$

Resulting in the parameters of Table 11:

Table 11 – Converted machine data for 3-bus test system

SM	R_a [pu]	X'_d [pu]	H [MJ/MVA]	D_m [pu]
1	0	0.0250	50	10
2	0	0.0312	40	8

SM: Synchronous Machine.

Based on the classical synchronous machine model, the initial operating conditions are computed using (2.4) and (2.5). Assuming steady-state operation, Table 12 summarizes the resulting initial conditions for each generator.

Table 12 – Initial operating conditions - 3-bus test system

SM	E [pu]	δ [°]	$\Delta\omega$ [pu]	P_e [pu]	P_M [pu]
1	1.1449	8.1243	0.0000	6.6661	6.6661
2	1.1193	14.4759	0.0000	6.0000	6.0000

SM: Synchronous Machine.

To emulate a network transient, a three-phase fault is applied near bus 2 at $t = 0.5$ [s], followed by the disconnection of the transmission line between buses 1 and 2. The loads are represented by constant impedances, and the passive buses are eliminated through Kron reduction [68]. The reduced admittance matrices before and after the event are given by

$$\bar{\boldsymbol{Y}}_{\boldsymbol{BF}}^{\text{red}} = \begin{bmatrix} 4.1719 - j \cdot 14.5720 & 2.0826 + j \cdot 10.2621 \\ 2.0826 + j \cdot 10.2621 & 1.5106 - j \cdot 12.5629 \end{bmatrix}, \tag{5.4}$$

$$\bar{\boldsymbol{Y}}_{\boldsymbol{AF}}^{\text{red}} = \begin{bmatrix} 5.0603 - j \cdot 9.9620 & 1.7854 + j \cdot 4.9932 \\ 1.7854 + j \cdot 4.9932 & 1.0227 - j \cdot 6.8365 \end{bmatrix}. \tag{5.5}$$

With the preliminary calculations completed, the Kalman filter-based algorithms are implemented for dynamic state estimation.

5.1.2 Construction of Kalman Filters

To initialize the filters, consider the state vector in complex-conjugate coordinates in (5.6), assuming $\bar{\alpha} = \delta + j\ \Delta\omega$. Since there is no initial variation in the angular velocity, the state vector is initially a vector with only real parts.

$$\hat{\bar{\boldsymbol{x}}}_{0|0} = \begin{bmatrix} \bar{\alpha}_1 \\ \bar{\alpha}_2 \\ \bar{\alpha}_1^* \\ \bar{\alpha}_2^* \end{bmatrix} = \begin{bmatrix} 0.1418 \\ 0.2527 \\ 0.1418 \\ 0.2527 \end{bmatrix}. \tag{5.6}$$

Assuming that the real and imaginary parts of the initial estimation errors are uncorrelated and share the same variance (10^{-4}), the augmented covariance matrix $\bar{\boldsymbol{P}}_{0|0}$ is initialized such that the diagonal elements of the conventional covariance block $\bar{\boldsymbol{P}}_{1_{0|0}}$ are equal to $2 \cdot 10^{-4}$. Under this circularity assumption, the pseudo-covariance block $\bar{\boldsymbol{P}}_{2_{0|0}}$ is initially set to zero. This initialization ensures that the total complex-domain uncertainty reflects the combined variance of the real and imaginary components. Furthermore, the process noise covariance matrix $\bar{\boldsymbol{Q}}$ and the measurement noise covariance matrix $\bar{\boldsymbol{R}}$ are diagonal matrices with variances of 10^{-4}, following the same statistical assumptions used for the state initialization.

The vectors of nonlinear functions that relate the differential equations $\left(\bar{\boldsymbol{f}}\left(\cdot\right)\right)$ and the measurements $\left(\bar{\boldsymbol{h}}\left(\cdot\right)\right)$ according to the state variables are presented in (5.8). PMU measurements are assumed to provide synchronized voltage and current phasors at the system buses with a sampling rate of 60 samples per second. These voltage and current measurements are subsequently used to construct the complex-power pseudo-measurements used in the estimation process. A full PMU metering scheme was adopted for all buses to provide a fully observable benchmark scenario for evaluating the proposed estimator. Although this assumption may not represent a practical large-scale deployment, it enables a clearer assessment of the numerical and statistical properties of the proposed methodology.

$$\bar{\boldsymbol{f}}_c = \begin{bmatrix} \bar{f}_{1_{(1)}} & \bar{f}_{1_{(2)}} \end{bmatrix}^T = \begin{bmatrix} \dfrac{d\bar{\alpha}_1}{dt} & \dfrac{d\bar{\alpha}_2}{dt} \end{bmatrix}^T, \qquad \bar{\boldsymbol{f}}(\bar{\boldsymbol{x}}) = \begin{bmatrix} \bar{\boldsymbol{f}}_c \\ \bar{\boldsymbol{f}}_c^* \end{bmatrix}, \tag{5.7}$$

$$\bar{\boldsymbol{h}}_c = \begin{bmatrix} \bar{V}_1 & \bar{V}_2 & \bar{V}_3 & \bar{S}_{e_1} & \bar{S}_{e_2} \end{bmatrix}^T, \qquad \bar{\boldsymbol{h}}(\bar{\boldsymbol{x}}) = \begin{bmatrix} \bar{\boldsymbol{h}}_c \\ \bar{\boldsymbol{h}}_c^* \end{bmatrix}. \tag{5.8}$$

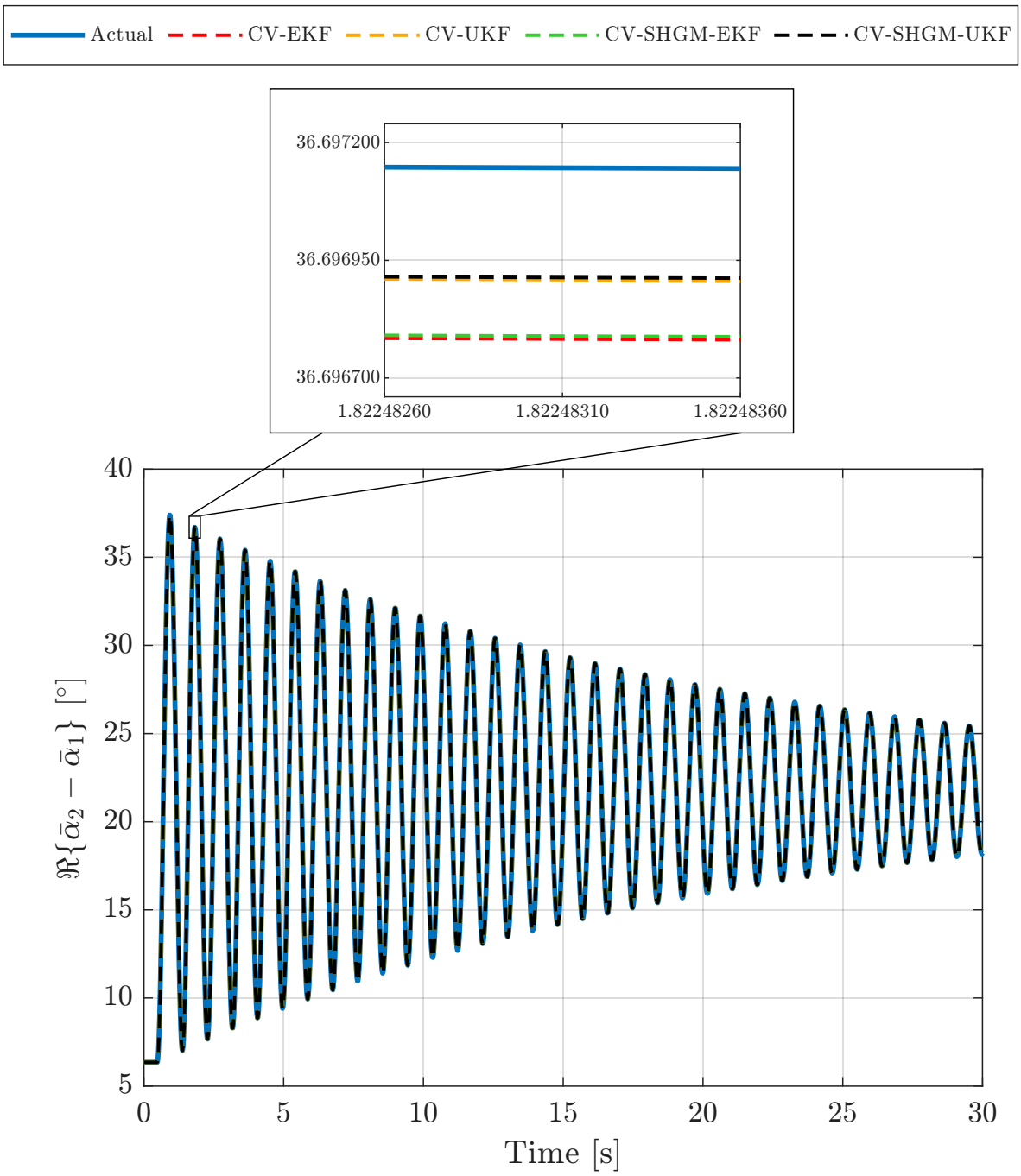
For the linearization-based algorithms, CV-EKF and CV-SHGM-EKF, the derivatives and Jacobian matrices are shown in the Appendix B. The tolerance for the IRLS algorithm in CV-SHGM-EKF and CV-SHGM-UKF is 10^{-3}.

5.1.3 Dynamic State Estimation - 3-bus Test System

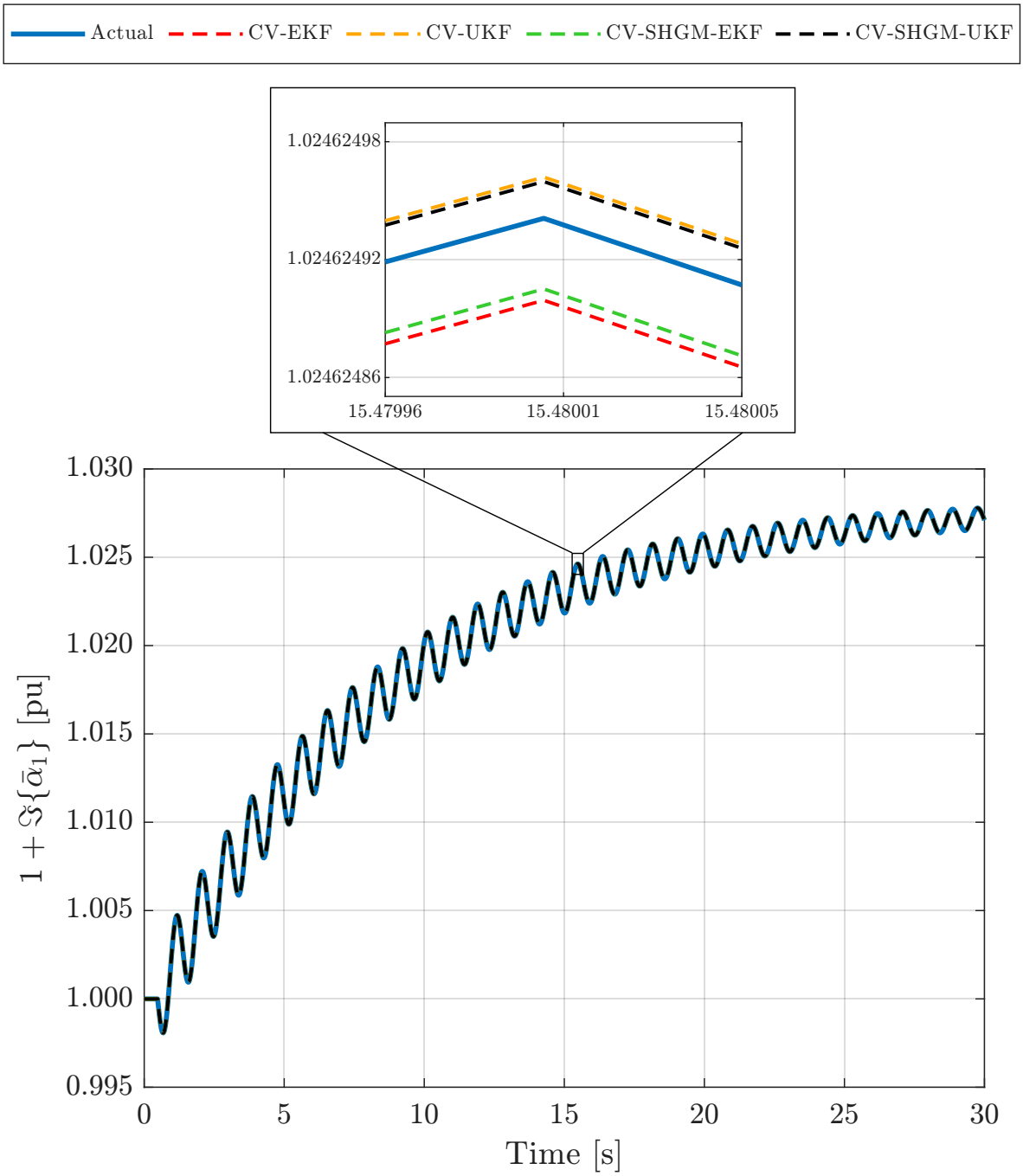
5.1.3.1 Scenario 1: Absence of Communication Failures and Gross Errors

Considering PMU measurements with standard deviation of the order of 1%, Figures 8a, 8b and 8c show the temporal estimation of the angular variable δ_{21} and the velocity variables ω_1 and ω_2, respectively, for the loss event of line 1-2 at time t = 0.5 [s]. All four algorithms evaluated in this first scenario demonstrate high efficiency in predict-

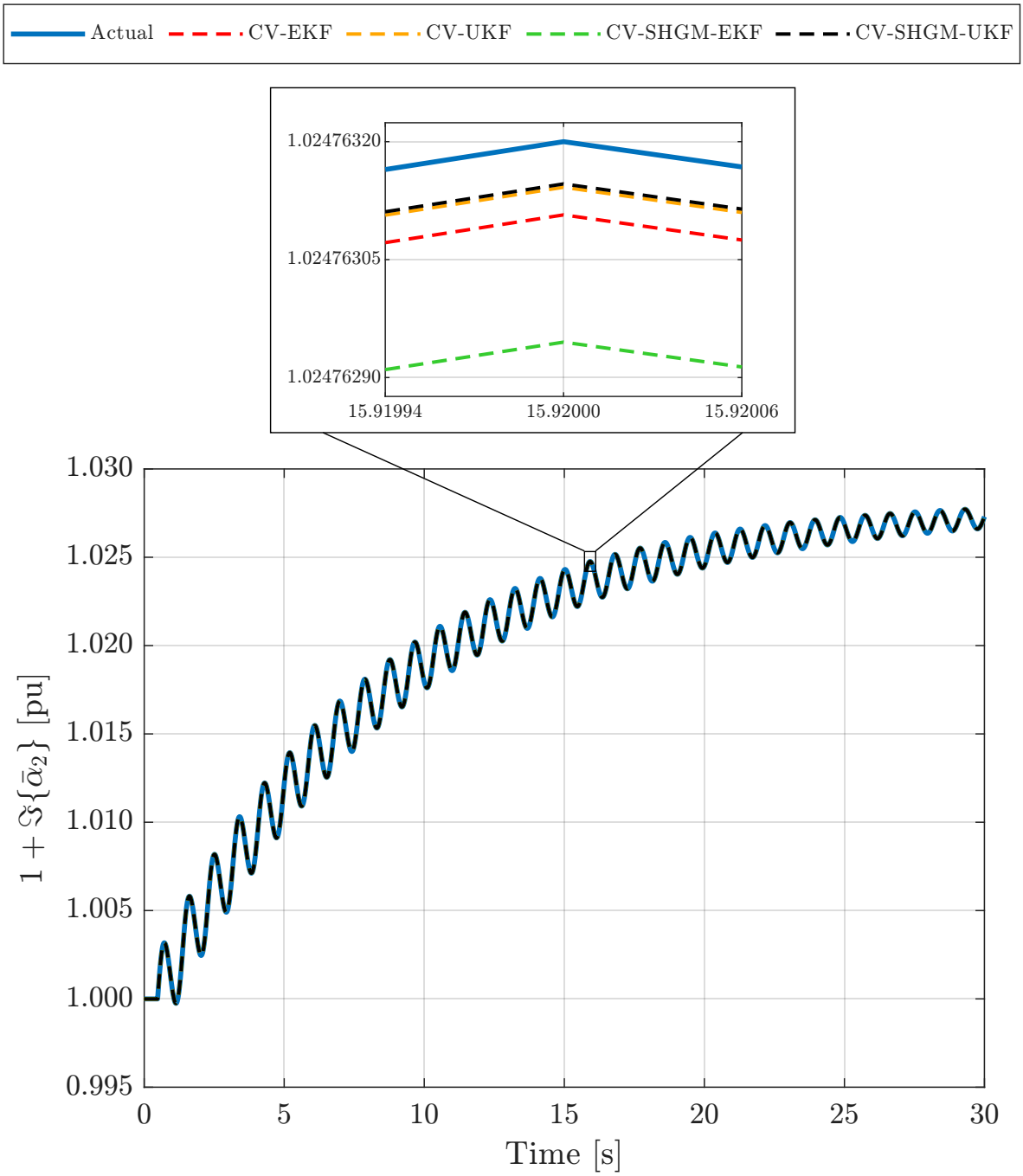
ing the network's transient effects, with prediction errors around 10^{-6}. The algorithms that do not rely on linearizations, CV-UKF and CV-SHGM-UKF, demonstrated slightly higher accuracy than their counterparts, CV-EKF and CV-SHGM-EKF. The graphs were enlarged in some areas to reduce overlap between curves.



(a) Angular difference between generators 2 and 1.



(b) Angular velocity of generator 1.



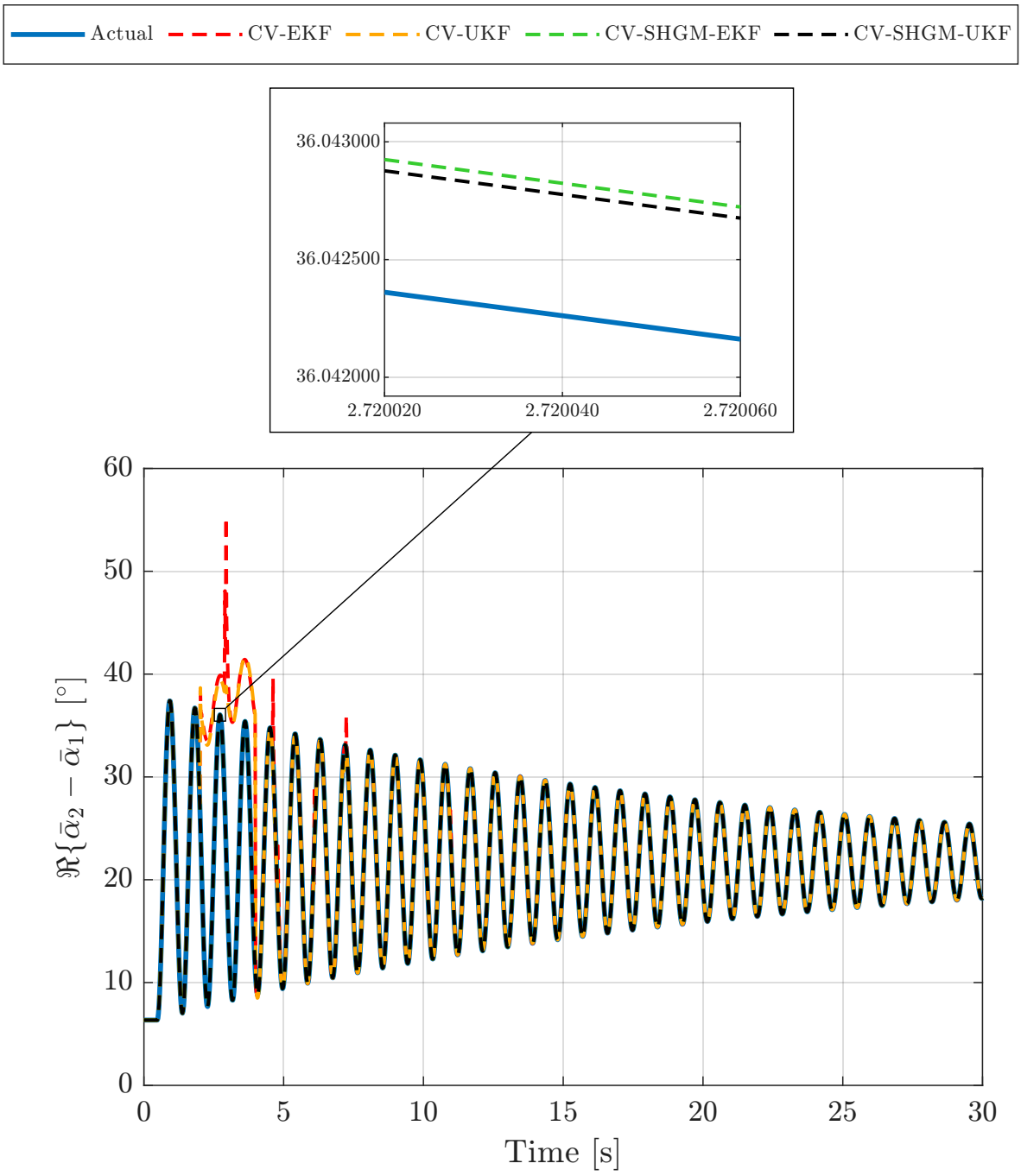
(c) Angular velocity of generator 2.

Figure 8 – Dynamic State Estimation: 3-bus system - Scenario 1.

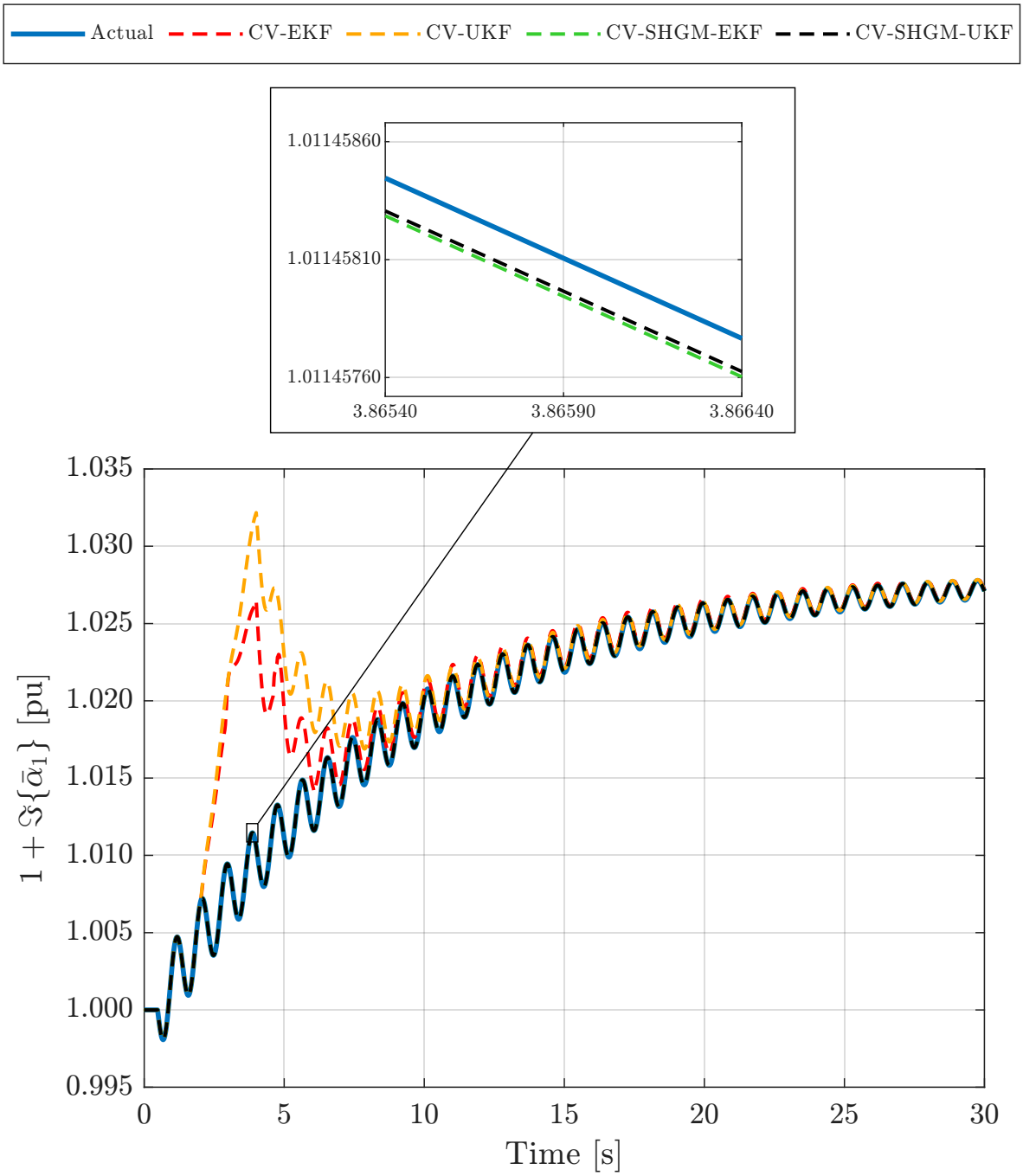
5.1.3.2 Scenario 2: Loss of Communication Link of the PMU of Bus 1

The PMUs can lose communication with the operational control centers due to several factors, such as equipment failures, cyberattacks, or interruptions to the communication system. Therefore, the second scenario simulates the loss of communication for the PMU allocated to bus one. For this, the respective measurements $\bar{V}_1$ and $\bar{S}_1$ become unavailable during the instants of t = 2 [s] and t = 4 [s]. Hence, the respective values became zero. It can be observed in Figures 9a, 9b, and 9c that the EKF and UKF algo-

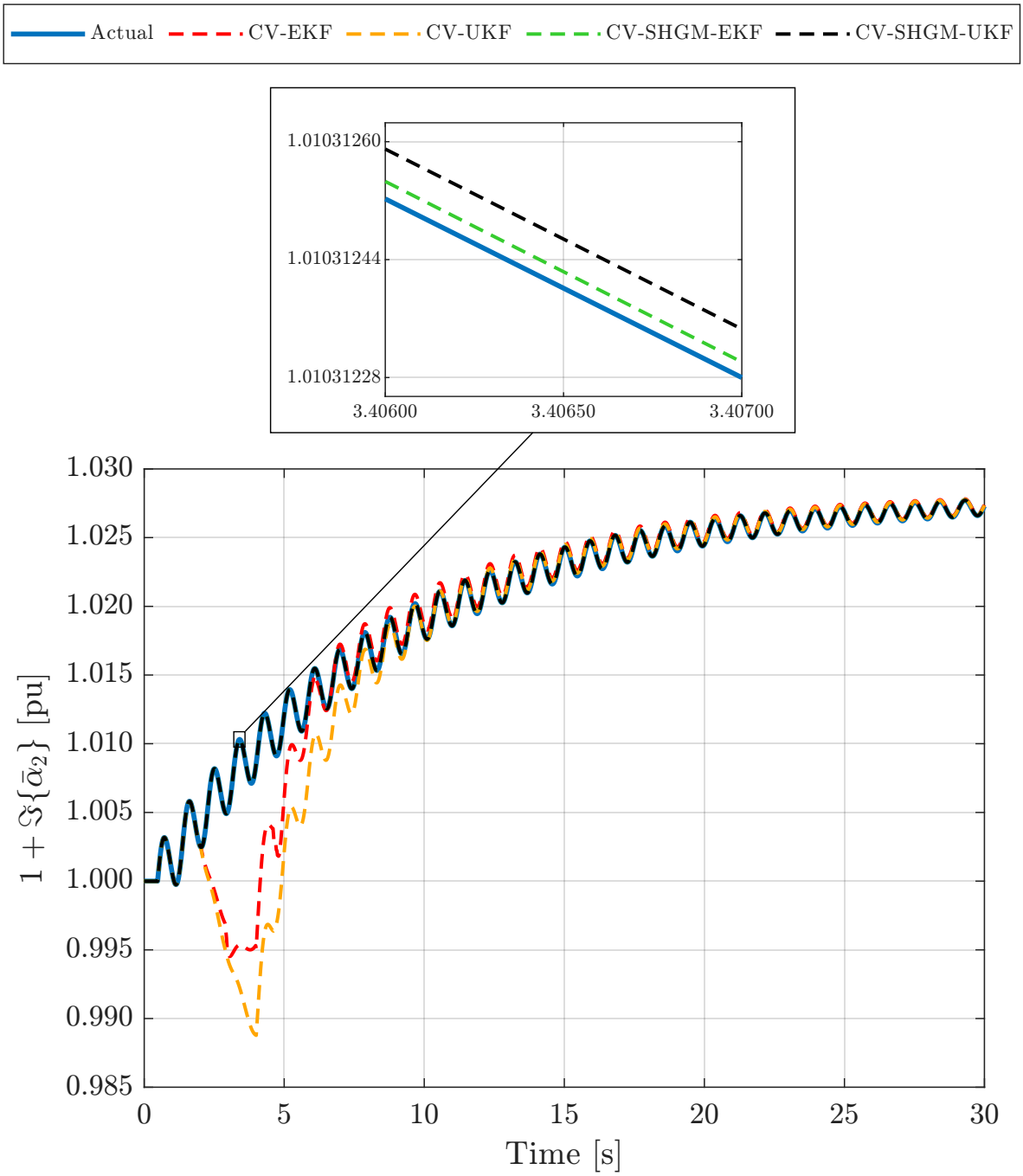
rithms exhibit transient peaks due to communication loss. In contrast, robust algorithms are efficient in the presence of failures. Some parts of the graphs were enlarged to highlight the results during communication loss.



(a) Angular difference between generators 2 and 1.



(b) Angular velocity of generator 1.



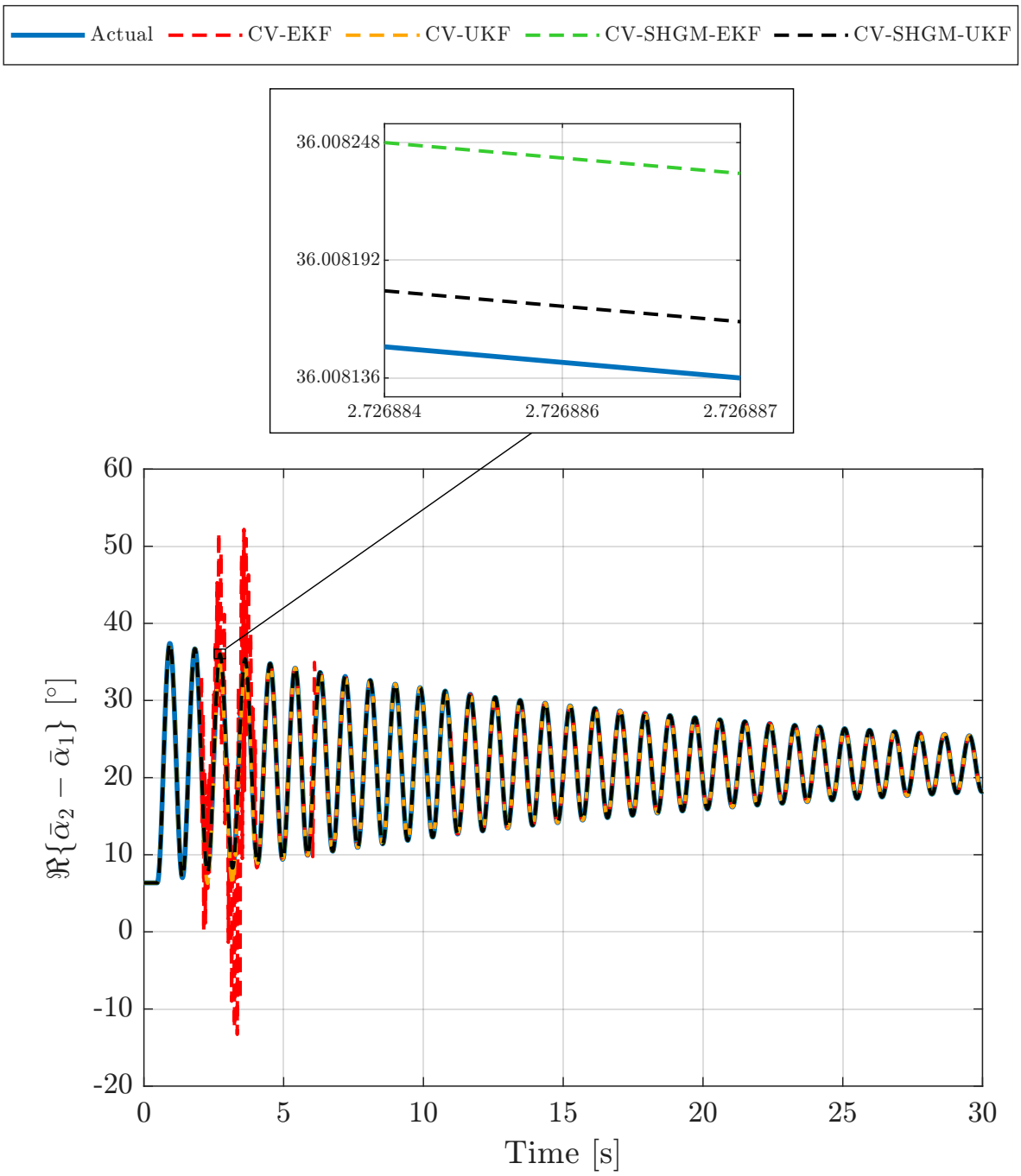
(c) Angular velocity of generator 2.

Figure 9 – Dynamic State Estimation: 3-bus system - Scenario 2.

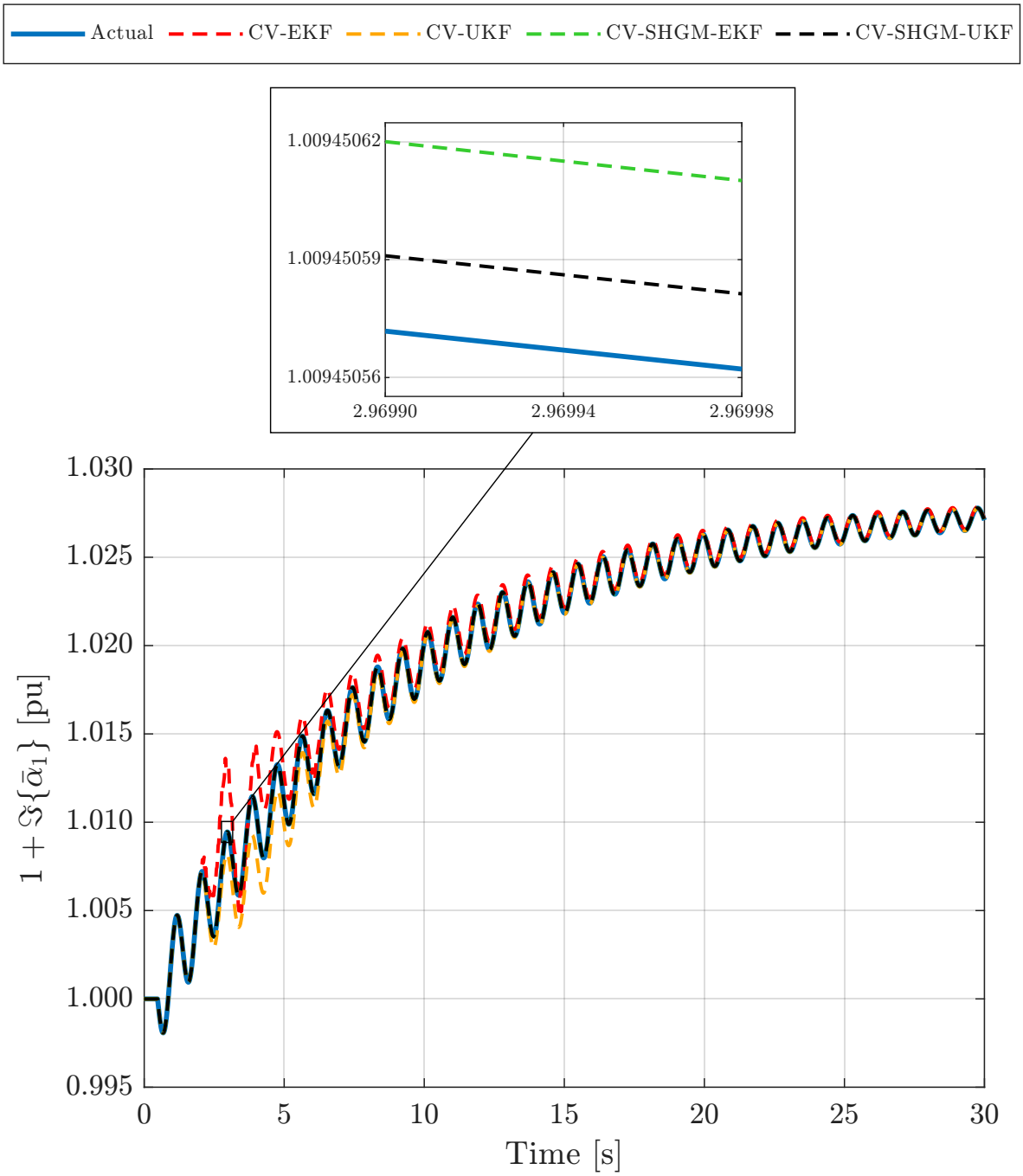
5.1.3.3 Scenario 3: Impulse in the $\bar{S}_2$

To emulate a severe failure in the observed data, the value of $\bar{S}_2$ obtained from the voltage and current phasor measurements at bus two was intentionally corrupted with a gross error of 6 [pu]. Although this disturbance magnitude is considerably larger than typical PMU measurement noise levels, it was deliberately adopted to emphasize the robustness differences between the conventional and SHGM-based estimators under extreme contamination conditions. Such defects may arise from impulsive communication

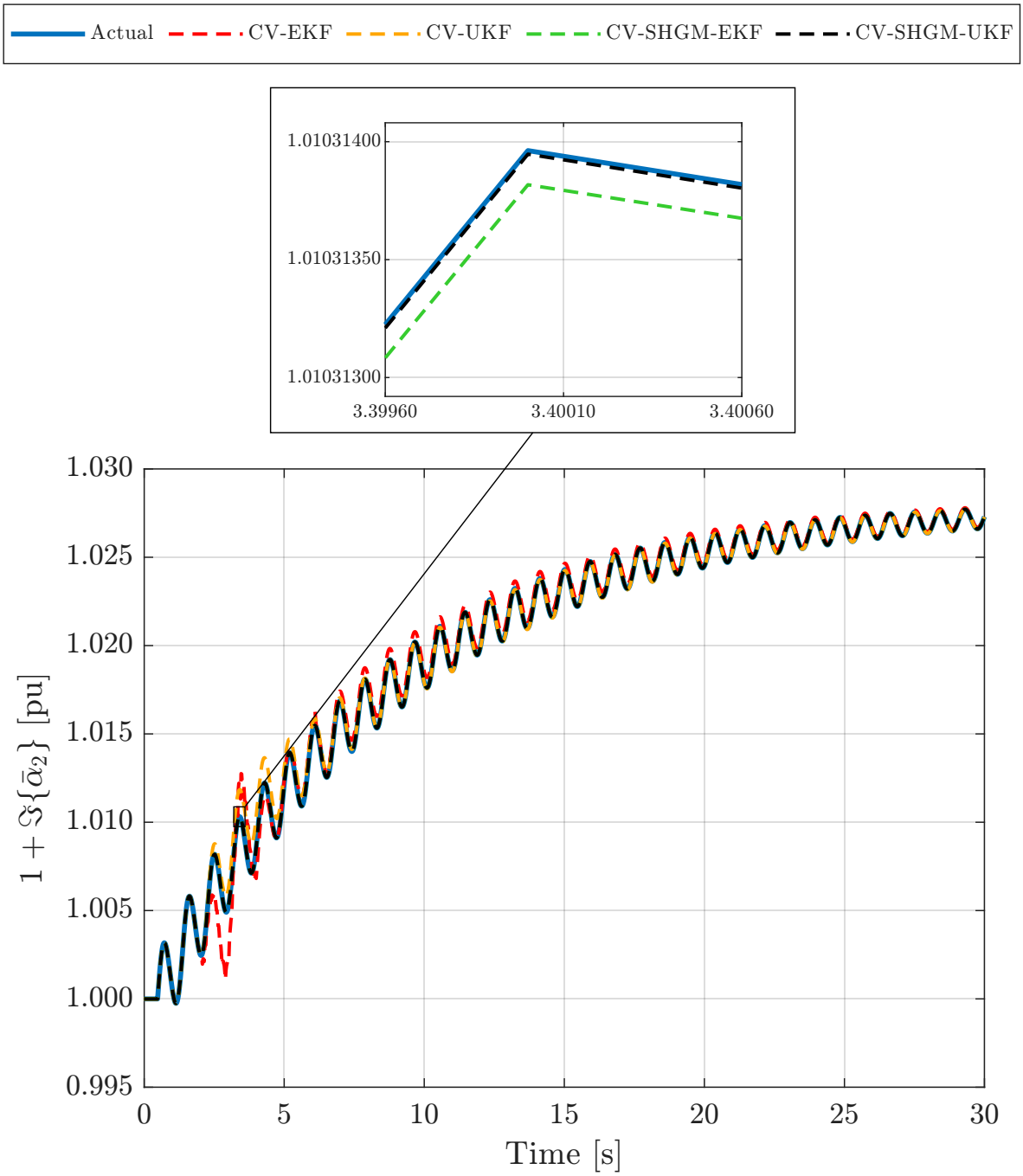
noise, synchronization inaccuracies, or severe data corruption events. The gross error persisted in the system between $t = 2$ s and $t = 4$ [s]. As shown in Figures 10a, 10b, and 10c, the CV-SHGM-EKF and CV-SHGM-UKF algorithms exhibited superior robustness when compared with their non-robust counterparts.



(a) Angular difference between generators 2 and 1.



(b) Angular velocity of generator 1.



(c) Angular velocity of generator 2.

Figure 10 – Dynamic State Estimation: 3-bus system - Scenario 3.

5.1.3.4 Scenario 4: Center of Inertia Frequency Estimation

Usually, control centers do not monitor power system inertia, a key attribute used to assess the impact of asynchronous machines on the power grid. Figure 11 presents the center-of-inertia frequency response for the 3-bus test system under normal operating conditions, i.e., in the absence of communication failures and gross measurement errors, obtained as a byproduct of the dynamic state estimator.

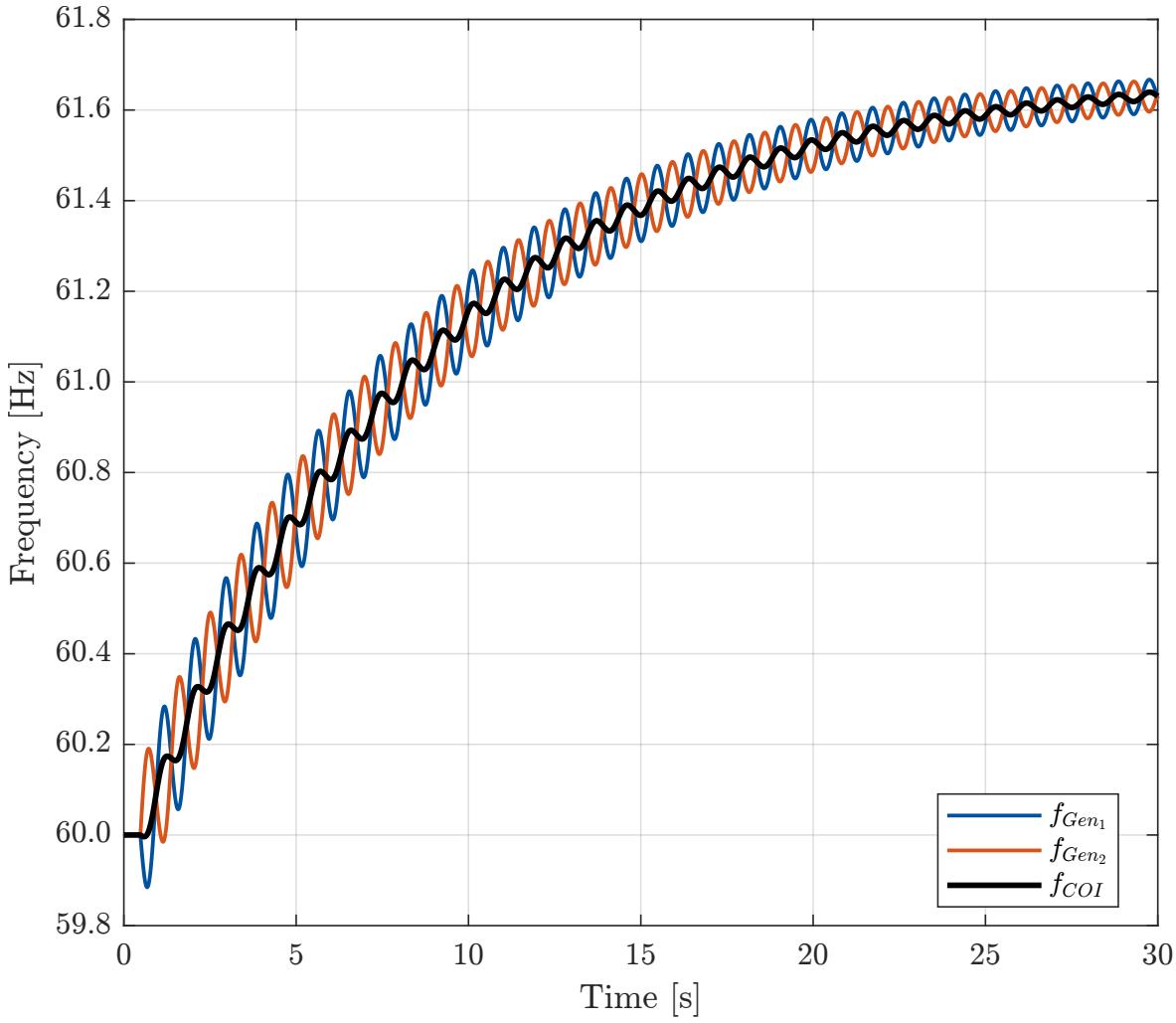


Figure 11 – Frequency of generators and center of inertia over time.

In the presence of errors and various types of failures, EKF and UKF algorithms do not impair the frequency estimation as shown in Figures 12 and 13, for the second and third scenarios, respectively. The robust counterparts perform well in estimating the system's center of inertia. Some areas of the graphs were highlighted to circumvent the effect of curve overlap.

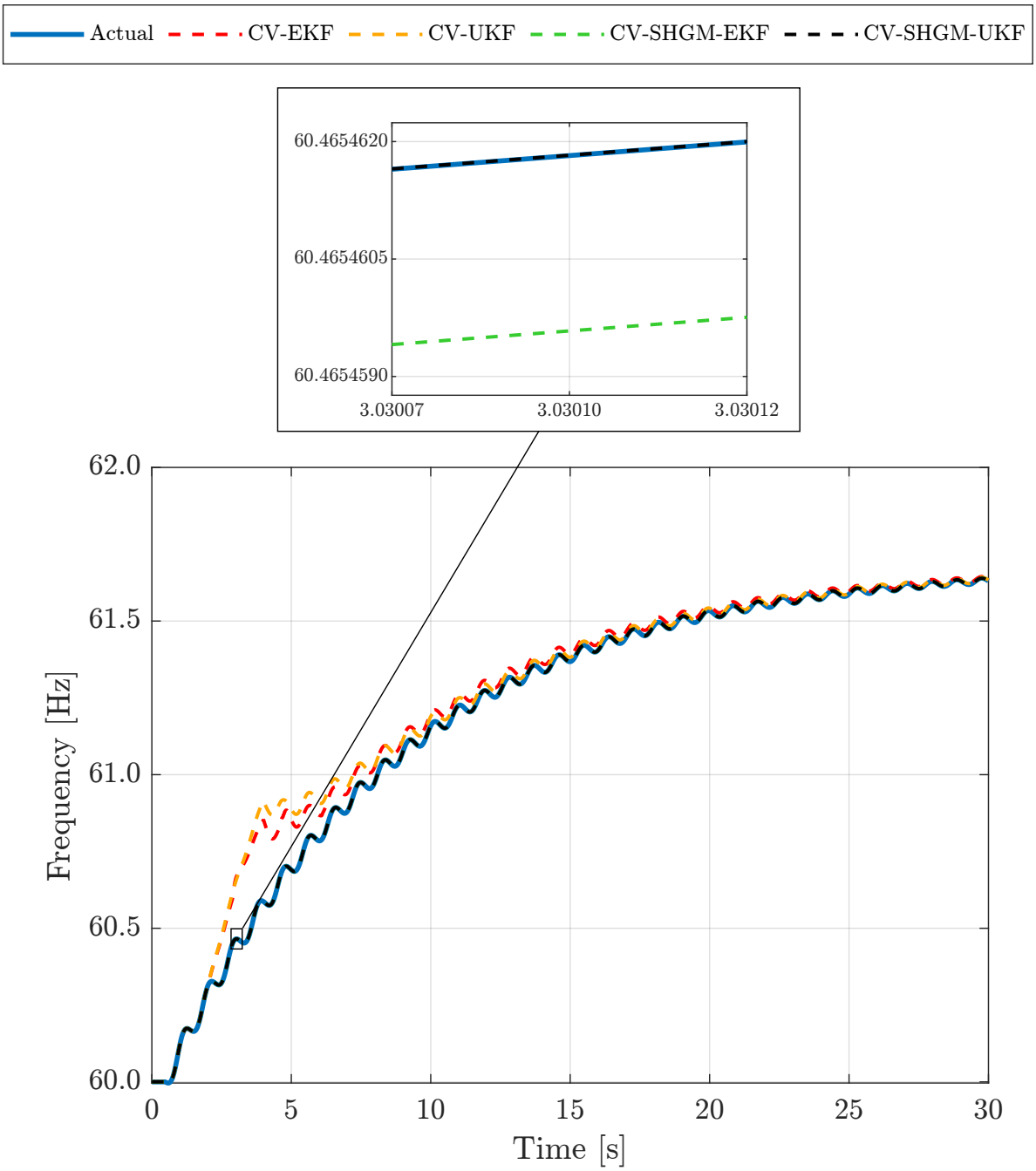


Figure 12 – Estimation of f_{COI} - Scenario 2.

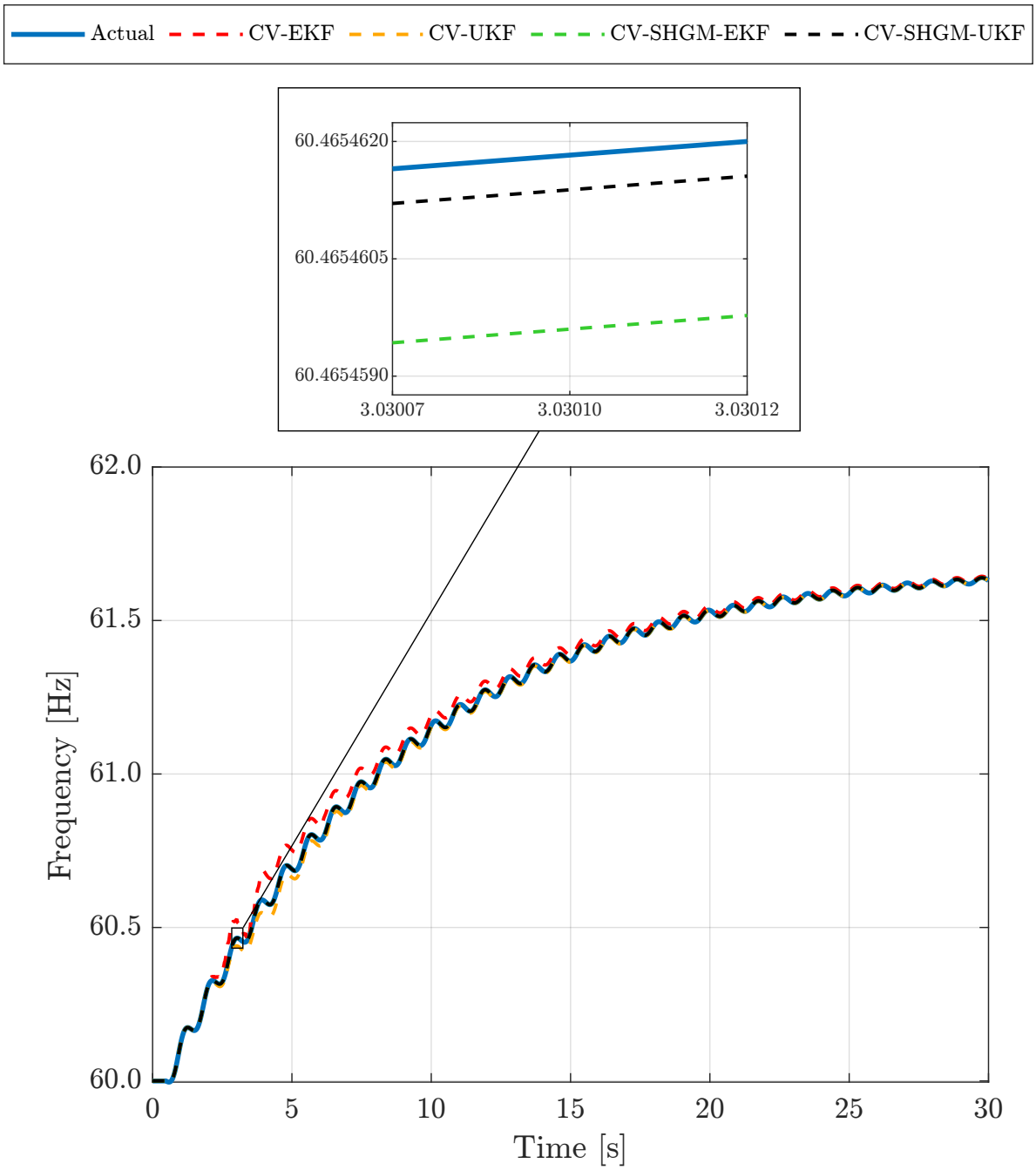


Figure 13 – Estimation of f_{COI} - Scenario 3.

5.2 IEEE 39-Bus Test System

This section presents the time-domain simulations performed on the IEEE 39-bus New England test system [102]. The system comprises 10 synchronous generators interconnected through 46 transmission branches. In this study, all synchronous generators are modeled using the detailed ninth-order two-axis representation, including the IEEE DC1A excitation system and the TGOV1 turbine governor, exactly as formulated and discussed in Chapter 2.

The initialization procedure of the dynamic state estimator, including the steady-state operating point calculation and the construction of the estimator structure, follows the same methodology adopted for the 3-bus system presented in the previous section and is therefore omitted here for brevity. As in the 3-bus case, the adopted measurement set consists of bus voltage phasors and pseudo-measurements of generated complex power, obtained from voltage and current phasor measurements provided by PMUs, with a reporting rate of 60 phasors per second. A full PMU metering scheme is adopted only as a benchmark assumption to ensure a fully observable and controlled simulation environment for comparing the proposed estimators, not as a practical deployment requirement. In practical applications, the same formulation can be applied to any PMU placement that provides sufficient observability and redundancy for the monitored system. For all simulations, the initial state-error covariance matrix $\bar{\boldsymbol{P}}$, as well as the process and measurement noise covariance matrices $\bar{\boldsymbol{Q}}$ and $\bar{\boldsymbol{R}}$, are assumed to be diagonal with entries equal to 10^{-6}.

To assess the estimator performance under a disturbance, a fault is applied near bus 4, followed by the disconnection of transmission line $[4;14]$ at $t = 1$ [s]. The corresponding dynamic state estimation results are depicted in Figure 14 for Generator 8, which is representative of the system response.

The estimated trajectories obtained by the different dynamic state estimation algorithms are nearly indistinguishable throughout the simulation horizon, indicating a high degree of consistency between the estimators, with no evident bias or divergence during either the transient or post-fault periods. Therefore, the results shown in Figure 14 indicate that all algorithms considered accurately track the complex-valued states.

The loss of communication is imposed on the PMU measurement associated with bus 17 because the voltage phasor $\bar{V}_{17}$ is identified by the projection statistics analysis as a leverage point. This choice allows the robustness of the proposed SHGM-based estimators to be evaluated under a severe condition in which a leverage-point measurement becomes corrupted. Specifically, the communication loss is modeled by forcing $\bar{V}_{17}$ to zero during the interval $t = 7$ [s] to $t = 9$ [s], introducing a measurement inconsistent with the network equations. In the SHGM framework, this measurement is handled through the IRLS weighting scheme and is assigned a reduced weight $\varpi_i = 9.108 \cdot 10^{-2}$.

Figure 15 shows that the non-robust estimators (CV-EKF and CV-UKF) are significantly affected during the outage interval, whereas the robust estimators (CV-SHGM-EKF and CV-SHGM-UKF) maintain close agreement with the actual response. As a result, the robust methods preserve stable tracking of the complex-valued states and avoid bias accumulation even under the severe measurement inconsistency imposed on $\bar{V}_{17}$.

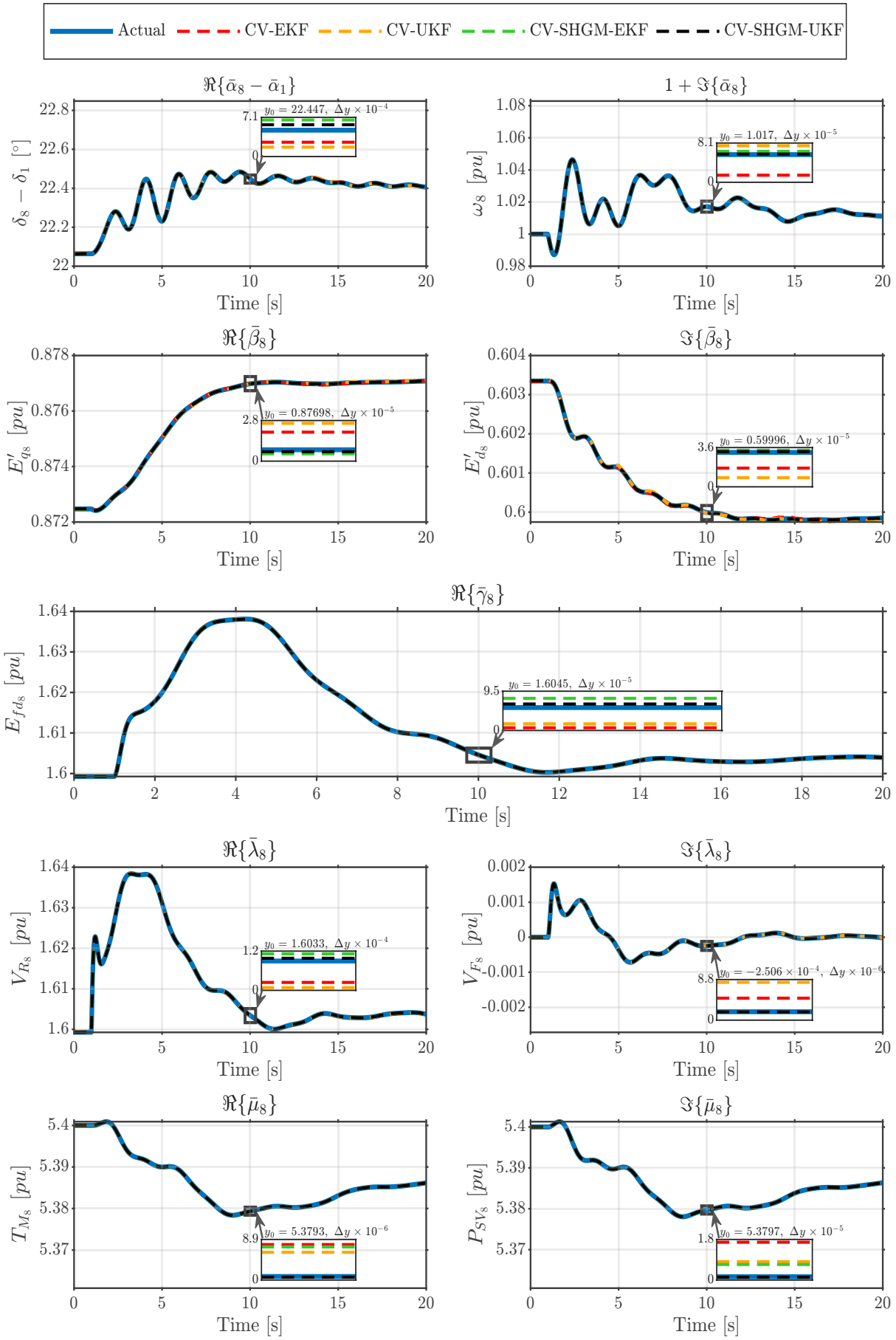


Figure 14 – Dynamic State Estimation for 39-bus system - Generator 8.

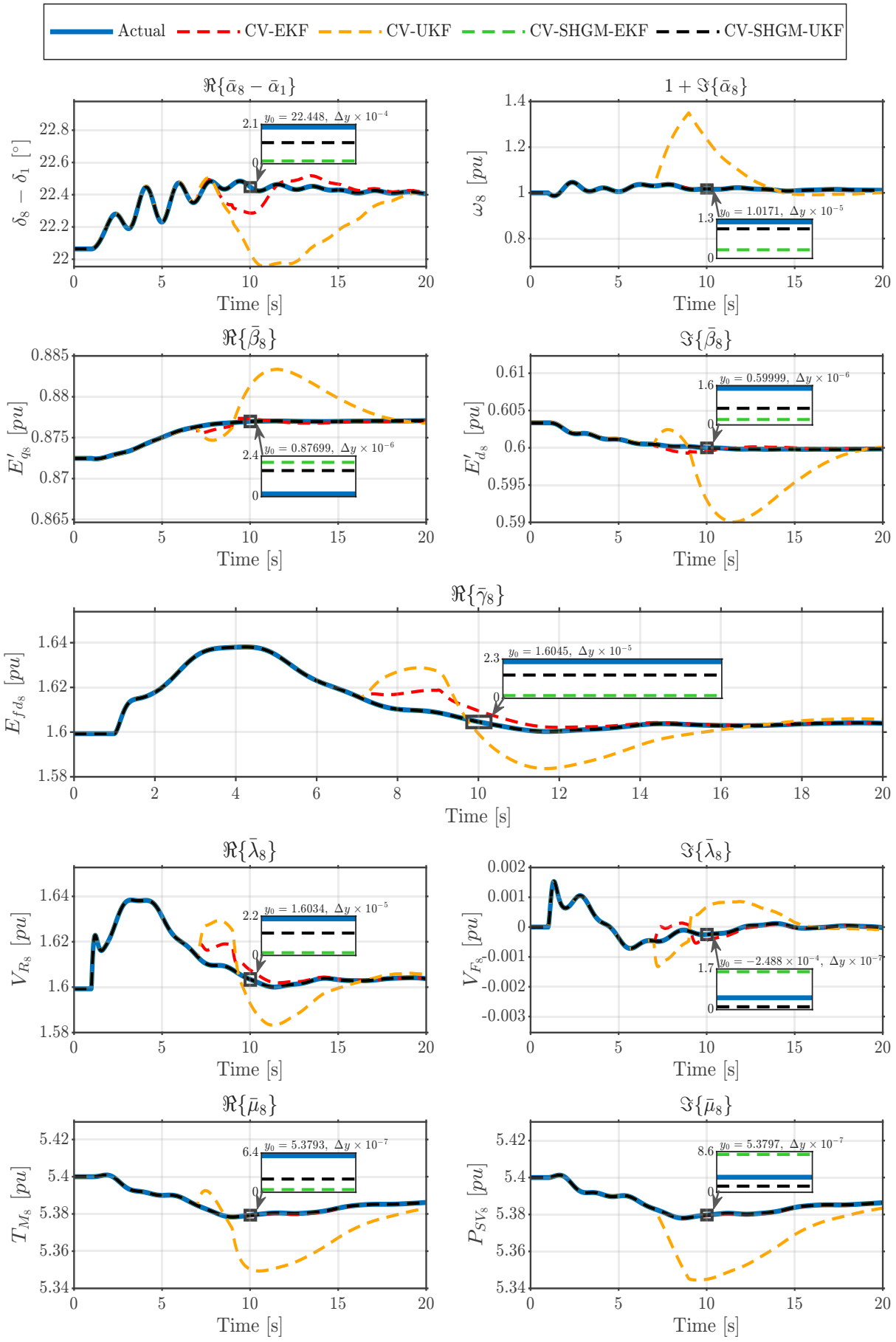
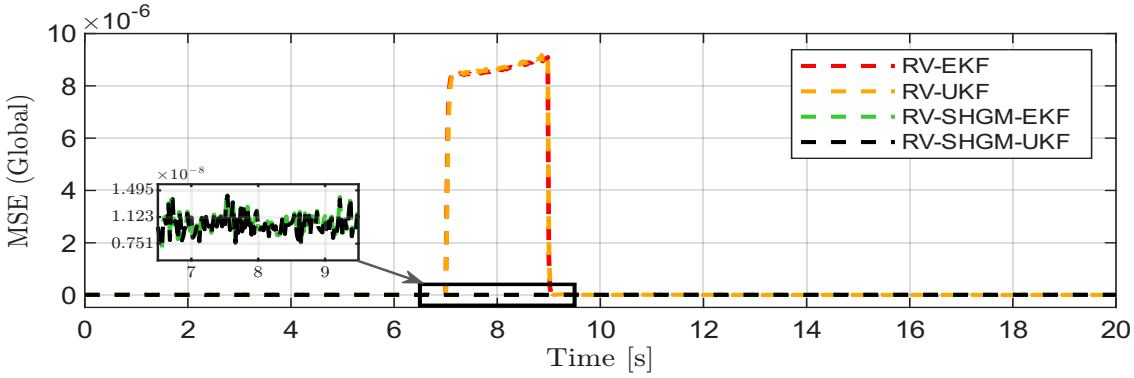


Figure 15 – Dynamic State Estimation for 39-bus system - Generator 8 - Loss of communication at bus 17.

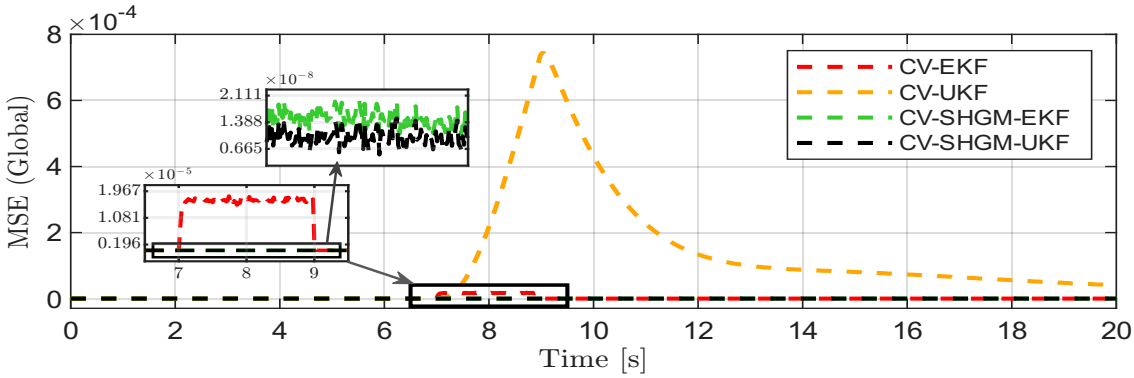
Figure 16 shows the global mean square error (MSE) computed over all estimated measurements during the PMU communication outage at bus 17, within the interval $t \in [7, 9]$ [s]. For comparative purposes, the same communication failure is evaluated in both the real-valued (RV) and complex-valued (CV) numerical domains. The EKF-based estimators exhibit very similar MSE profiles in both domains, indicating comparable sensitivity to communication failure. In both numerical domains, the robust filters maintain the MSE on the order of 10^{-8} throughout the outage window.

In contrast, the complex-valued UKF (CV-UKF) exhibits a higher MSE during the outage than its real-valued counterpart. As discussed in Section 3.2, this behavior is associated with the reduced number of measurements in the complex-domain formulation, which increases the sensitivity of the unscented transformation to measurement loss. It is worth noting that, in scenarios without measurement failures, the estimation accuracy of all filters remains of the same order in both numerical domains.

In addition to the global analysis, Figures 17 and 18 present the mean square error (MSE) calculated individually for each state variable of the IEEE 39-bus system, considering the real-valued and complex-valued formulations. For reference, the maximum MSE value attained in each case is explicitly indicated in the corresponding plots.



(a) Real domain



(b) Complex domain

Figure 16 – MSE for all estimated measurements - Communication loss at bus 17.

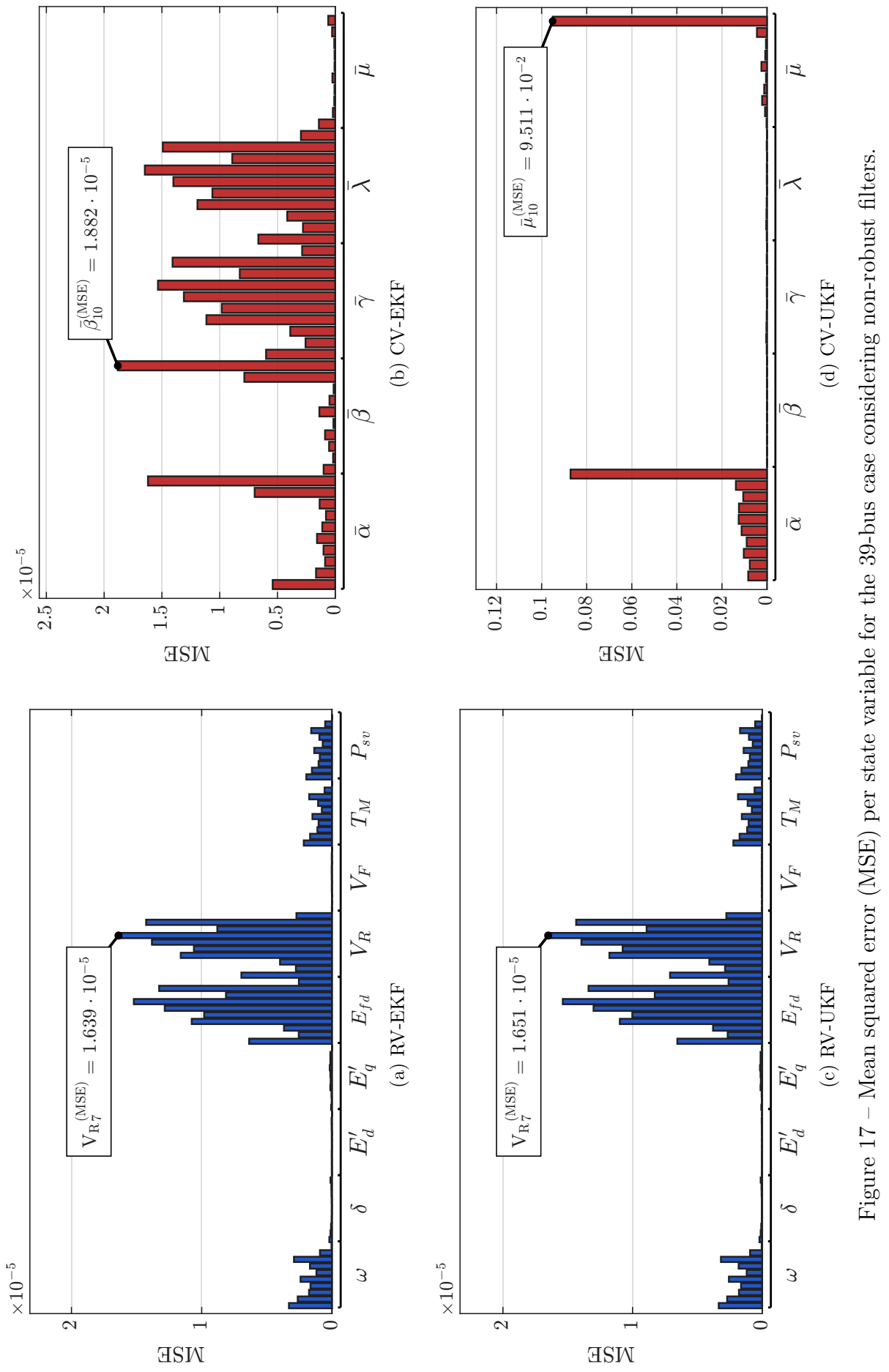


Figure 17 – Mean squared error (MSE) per state variable for the 39-bus case considering non-robust filters.

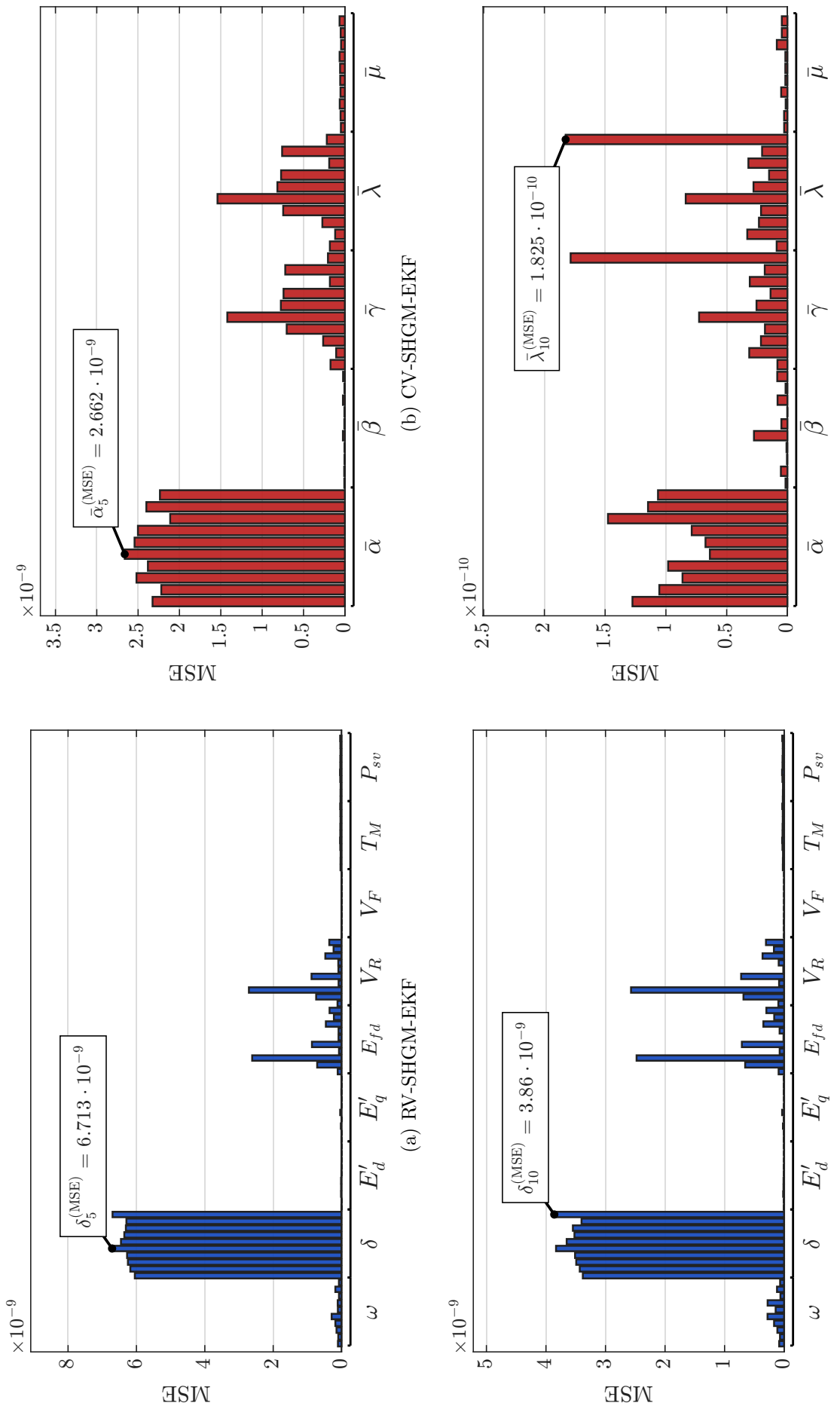


Figure 18 – Mean squared error (MSE) per state variable for the 39-bus case considering robust filters.

At the state-variable level, Figure 17 shows that the non-robust EKF estimators present similar sensitivity behavior in both the real-valued and complex-valued formulations, indicating that the impact of the considered measurement failure is comparable regardless of the numerical representation adopted, as also observed in Figure 16. In contrast, the complex-valued UKF shows higher sensitivity at the state-variable level. This behavior is mainly associated with the reduced non-augmented measurement set adopted in the complex-domain formulation, which is enabled by the proper/circular signal assumption and contains approximately half of the measurements used in the equivalent real-valued representation. Consequently, the CV-UKF becomes more susceptible to information loss during disturbances.

In contrast, when robust filtering strategies are employed, the MSE remains consistently low across all state variables, even in the presence of different types of measurement failures, including communication losses, impulsive noise, and bad leverage points. Notably, although the complex-valued UKF operates with a reduced measurement set, its robust variant preserves estimation accuracy at the state-variable level. This result indicates that the SHGM-based weighting mechanism effectively compensates for reduced measurement redundancy by limiting the influence of adverse measurements, thereby ensuring reliable dynamic state estimation.

Following the state-variable error assessment, the frequency response of the IEEE 39-bus system is analyzed with emphasis on the center-of-inertia (COI) frequency. Figure 19 depicts the individual generator frequencies along with the COI trajectory for the base scenario, i.e., in the absence of communication failures and impulsive noise. The results show that, despite the presence of machine-level oscillations, the COI provides a coherent representation of the global electromechanical behavior. As illustrated in Figure 20, non-robust estimators—most notably the CV-UKF—exhibit noticeable deviations due to the loss of PMU communication at bus 17, which are consistent with the reduced measurement set adopted in the complex-domain formulation and the higher sensitivity of unscented transformations to measurement inconsistencies, as previously observed in the state-wise MSE results.

On the other hand, the robust estimators maintain accurate tracking of the COI frequency throughout the simulation horizon, effectively preventing transient distortions and preventing bias propagation under adverse measurement conditions. From a practical perspective, this behavior is particularly relevant for protection and control applications, such as under-frequency load shedding (UFLS) and wide-area monitoring schemes, where reliable frequency estimates are critical. Although this work focuses on frequency estimation, more comprehensive assessments should also incorporate complementary indicators, including the Rate of Change of Frequency (ROCOF) and disturbance power metrics P_{dist}, as discussed in Chapter 4.

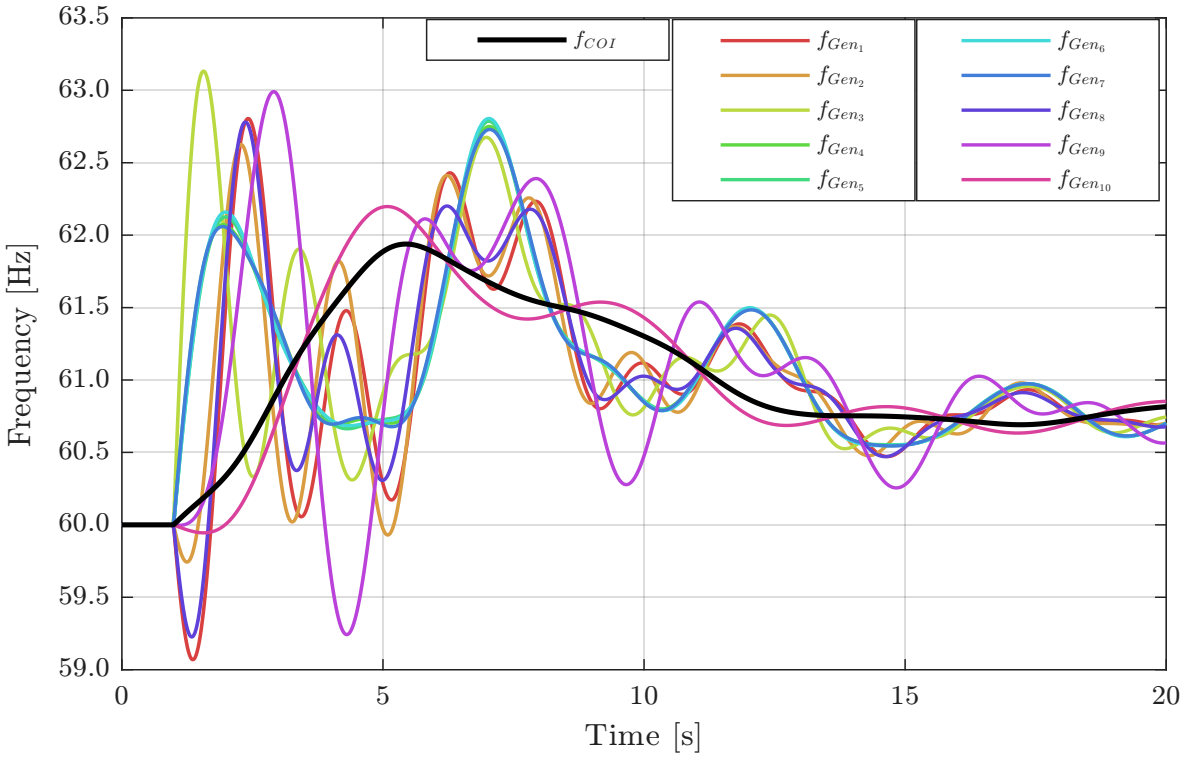


Figure 19 – Frequency of generators and center of inertia over time - IEEE - 39 bus.

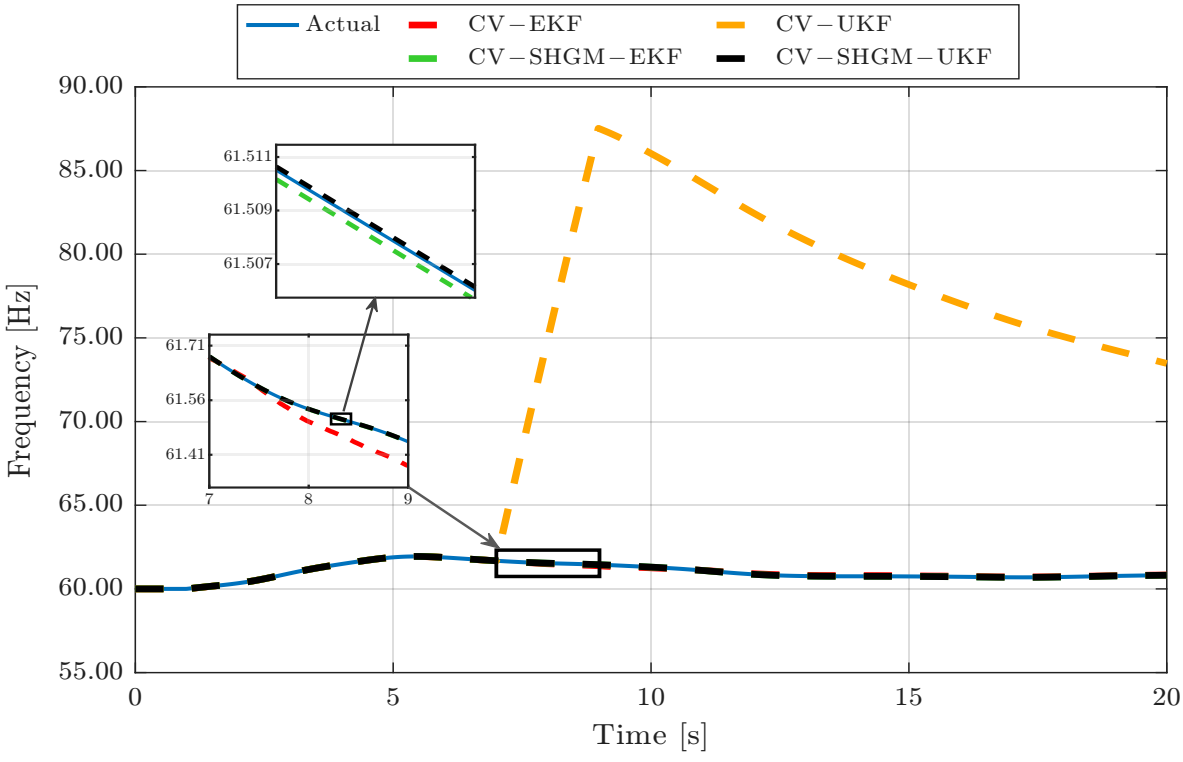


Figure 20 – Estimation of f_{COI} - Communication loss at bus 17.

5.3 Computational Performance Analysis

This section presents a comparative evaluation of the computational performance of the proposed estimators in both real-valued and complex-valued numerical domains. To guarantee a fair comparison, all estimators were implemented using the same computational framework. The algorithmic structure, numerical routines, and optimization strategies remain unchanged across numerical domains. In particular, identical code organization, vectorization strategies, sparse-matrix manipulations, and numerical linear algebra procedures were adopted in both real-valued and complex-valued formulations. Consequently, any observed difference in computational performance can be attributed solely to the numerical representation itself.

The simulations were carried out using three test systems of increasing size: the IEEE 39-bus system, the IEEE 118-bus system, and a 340-bus equivalent of the Brazilian Interconnected System (SIN). In all cases, synchronous generators were modeled using the ninth-order two-axis model, including the DC1A excitation system and the TGOV1 (GOV1) turbine speed regulator, as described in Chapter 2.

The measurement configuration consists of bus-voltage phasors at all buses and generator-power pseudo-measurements derived from synchronized voltage and current phasor data from PMUs. Furthermore, the initial covariance matrices adopted in the estimation process — namely the state covariance matrix $\bar{\boldsymbol{P}}$, the process noise covariance $\bar{\boldsymbol{Q}}$, and the measurement noise covariance $\bar{\boldsymbol{R}}$ — were assumed as diagonal matrices with elements equal to 10^{-6}, establishing uniform initial uncertainty levels in all simulations.

Table 13 summarizes the computational performance obtained for all evaluated algorithms and test systems, where the reported values correspond to the average results from 30 independent simulations considering dynamic operation windows of 10 seconds. The measurement values used in these simulations were determined from 50 Monte Carlo runs, ensuring statistically representative operating conditions. In all cases, identical fault scenarios were applied in both real-valued and complex-valued numerical domains, and no additional disturbances, such as communication losses, impulsive measurement noise, or modeling errors due to parameter uncertainties, were considered. For the complex-valued EKF formulation, the performance of the decoupled algorithm (D-EKF) and its robust counterpart (SHGM-D-EKF) is also presented, enabling a direct comparison between coupled and decoupled implementations. For each algorithm and system, the table reports the number of state variables (n_s), measurements (n_m), average computational time per iteration, the complex-to-real time ratio (C/R), and the maximum mean squared error among all estimated state variables, providing a consistent comparison of computational cost and estimation accuracy across formulations and system sizes.

Table 13 – Computational performance comparison (two-axis model).

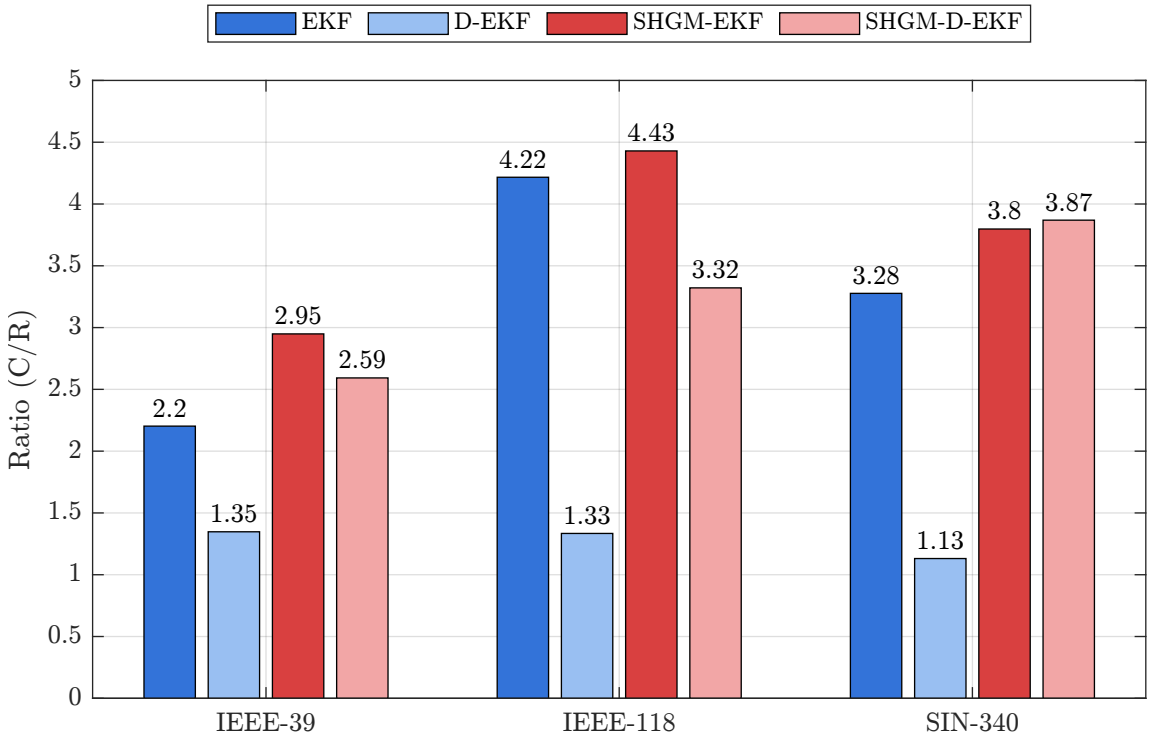
System	n_g	Algorithm	n_s		n_m		Time/iteration [ms]		Ratio (C/R)	max(MSE)	
			R	C	R	C	R	C		R	C
IEEE-39	10	EKF	90	100	98	98	2.0219	4.4533	2.2025	$4.147 \cdot 10^{-11}$	$3.599 \cdot 10^{-9}$
		D-EKF	90	50	98	49	2.0219	2.7245	1.3475	$4.147 \cdot 10^{-11}$	$3.086 \cdot 10^{-11}$
		UKF	90	50	98	64	4.8672	4.7524	0.9764	$5.028 \cdot 10^{-8}$	$5.582 \cdot 10^{-8}$
		SHGM-EKF	90	100	98	98	4.4687	13.1771	2.9488	$9.067 \cdot 10^{-12}$	$7.718 \cdot 10^{-13}$
		SHGM-D-EKF	90	50	98	49	4.4687	11.5856	2.5926	$9.067 \cdot 10^{-12}$	$1.777 \cdot 10^{-12}$
		SHGM-UKF	90	50	98	64	9.3260	9.2567	0.9925	$1.596 \cdot 10^{-11}$	$2.528 \cdot 10^{-10}$
IEEE-118	54	EKF	486	540	344	344	46.6991	196.9075	4.2165	$3.259 \cdot 10^{-12}$	$8.846 \cdot 10^{-11}$
		D-EKF	486	270	344	172	46.6991	62.2994	1.3341	$3.259 \cdot 10^{-12}$	$2.848 \cdot 10^{-9}$
		UKF	486	270	344	224	88.3947	70.1526	0.7936	$1.084 \cdot 10^{-9}$	$4.876 \cdot 10^{-9}$
		SHGM-EKF	486	540	344	344	138.9148	615.3346	4.4295	$2.668 \cdot 10^{-11}$	$1.843 \cdot 10^{-12}$
		SHGM-D-EKF	486	270	344	172	138.9148	461.3886	3.3213	$2.668 \cdot 10^{-11}$	$4.603 \cdot 10^{-12}$
		SHGM-UKF	486	270	344	224	183.6840	156.5304	0.8522	$2.269 \cdot 10^{-9}$	$6.454 \cdot 10^{-9}$
SIN-340	53	EKF	477	530	786	786	106.2393	348.1432	3.2769	$3.947 \cdot 10^{-11}$	$3.399 \cdot 10^{-8}$
		D-EKF	477	265	786	393	106.2393	120.1566	1.1310	$3.947 \cdot 10^{-11}$	$3.653 \cdot 10^{-9}$
		UKF	477	265	786	452	202.1445	143.4706	0.7097	$2.855 \cdot 10^{-9}$	$4.459 \cdot 10^{-8}$
		SHGM-EKF	477	530	786	786	237.2864	901.1181	3.7976	$2.594 \cdot 10^{-11}$	$4.881 \cdot 10^{-12}$
		SHGM-D-EKF	477	265	786	393	237.2864	918.1121	3.8692	$2.594 \cdot 10^{-11}$	$3.271 \cdot 10^{-12}$
		SHGM-UKF	477	265	786	452	430.1667	310.9686	0.7229	$3.764 \cdot 10^{-9}$	$4.276 \cdot 10^{-8}$

Notes: n_g denotes the number of synchronous generators. n_s and n_m denote the number of states and measurements, respectively. Time/iteration is averaged over the full simulation horizon. Ratio (C/R) is computed using only the time per iteration. max(MSE) corresponds to the worst estimated state variable over the simulation horizon.

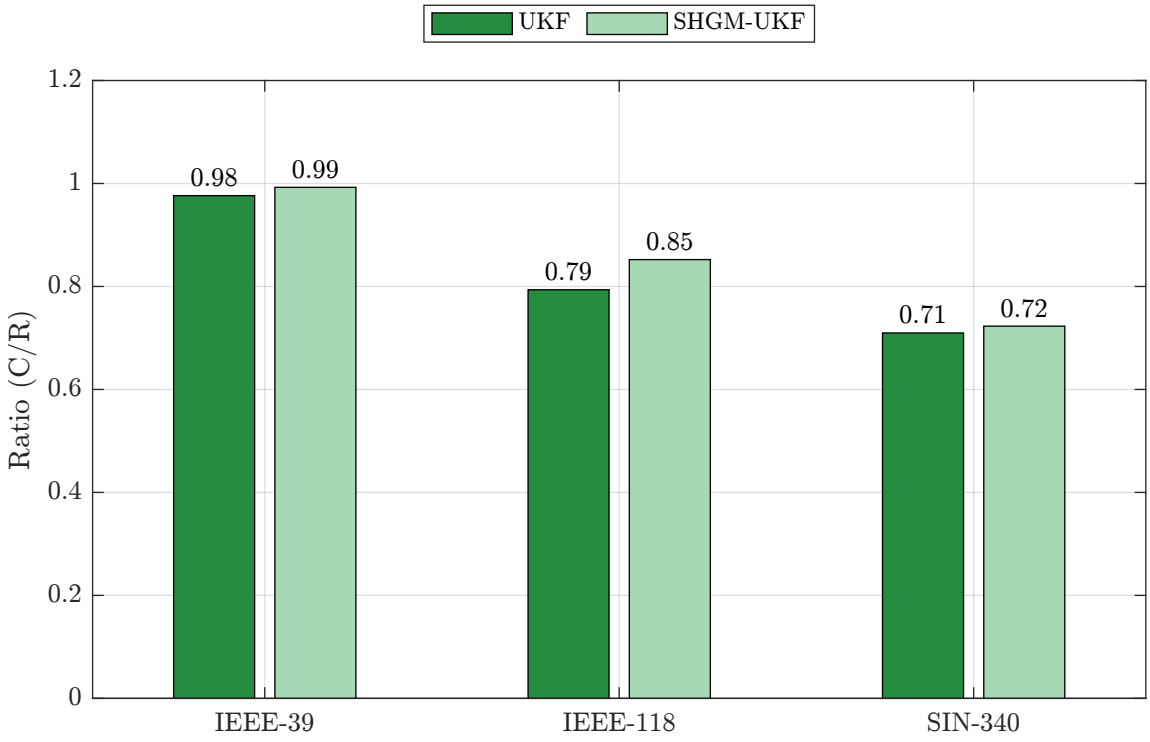
The computational results summarized in Table 13 show that the effect of the numerical domain on execution time is estimator-dependent rather than uniform across all algorithms. To identify the source of this behavior, profiling results for the standard augmented CV-EKF reveal that the computational burden is unevenly distributed among the estimation stages. In particular, although evaluating Jacobian matrices and the measurement update remain efficient, the covariance prediction step dominates the overall computational cost. In this step, computing $\bar{\boldsymbol{P}}_{k|k-1}$ requires dense matrix multiplications whose cost scales cubically with the state dimension. This operation is inherently more demanding when performed with complex-valued arithmetic. In large-scale networks such as the IEEE-118 and SIN-340 systems, this bottleneck causes the total execution time to be more than three times higher than in the real domain, as illustrated by the ratio analysis in Figure 21a.

To address this challenge, the proposed *Decoupled EKF* (D-EKF) introduces a structural optimization to mitigate the computational cost of the augmented formulation. By exploiting the mirror symmetry inherent to complex-conjugate coordinates, the D-EKF bypasses redundant operations during the covariance update without introducing numerical approximations. Consequently, the D-EKF significantly reduces complex-domain execution times—achieving reductions of approximately 68% in the IEEE-118 system and 65% in the SIN-340 system compared to the full augmented CV-EKF. Although the inherent complexity of complex-valued matrix multiplication prevents the D-EKF from matching the absolute speed of real-domain implementations, these results demonstrate that structural optimizations effectively narrow the performance gap, making the complex-domain modeling a manageable and viable alternative for large-scale systems.

A pivotal finding summarized in Table 13 is the *computational cross-over* observed in sigma-point-based estimators. For the UKF and SHGM-UKF, the complex-domain formulation achieves true computational superiority as the system scale increases, with execution times approximately 29% lower than their real-domain counterparts in the SIN-340 system. This occurs because the 50% dimensional reduction in the complex domain (n_s) directly reduces the number of propagated sigma points ($2n_s + 1$) and the associated nonlinear function evaluations. Therefore, for derivative-free estimators, the benefits of dimensional reduction outweigh the costs of complex arithmetic, making the complex-domain UKF highly scalable for high-dimensional monitoring tasks. However, as shown in the bad-data scenarios, the non-robust UKF is more sensitive to measurement inconsistencies, so robustification through the SHGM framework is essential to preserve estimation reliability under adverse conditions.



(a) EKF-based estimators.



(b) UKF-based estimators.

Figure 21 – Computational time ratio between complex-domain and real-domain formulations.

Regarding the robust formulations, the results in Table 13 indicate that the execution times for both SHGM-EKF and SHGM-D-EKF are significantly higher and more closely aligned than those of their non-robust counterparts. This behavior stems from the

fact that, for these linearized algorithms, the robust framework inherently requires manipulating augmented matrices to account for complex-conjugate state correlations via Wirtinger calculus during the iterative weighting process. Consequently, the computational burden is dominated by the calculation of projection statistics and the evaluation of influence functions. This intensive computational effort in the robustification routines effectively masks the gains from decoupled covariance propagation, explaining the narrower performance gap observed in large-scale systems like the SIN-340.

Furthermore, it is important to note that for the largest systems analyzed (IEEE-118 and SIN-340), the execution times per iteration currently exceed the standard PMU reporting interval (e.g., 16.67 ms). However, these results must be interpreted as a proof-of-concept regarding algorithmic scalability. Since the reported times are based on a high-level prototyping environment, the significant computational savings provided by the decoupled and sigma-point-reduced formulations indicate a clear path toward real-time viability. The modular structure of the proposed estimators is highly suitable for parallel processing and the application of sparse-matrix techniques, thereby further minimizing latency on industrial-grade hardware for large-scale interconnected networks.

Overall, the results demonstrate that computational scalability in dynamic state estimation depends on both the estimator structure and the numerical representation. While complex-domain modeling naturally aligns with phasor-based measurements, structural optimizations such as decoupled formulations and sigma-point reduction are essential to maintain computational feasibility. Therefore, the combination of complex-domain modeling with structurally optimized estimators emerges as a promising solution for real-time monitoring of large-scale power systems.

6 General Conclusions

This thesis establishes a comprehensive framework for Dynamic State Estimation (DSE) in power systems using complex-conjugate coordinates, proving that the transition to complex-valued modeling provides a more direct and physically consistent approach for modern grids. The research demonstrates that while the complex domain naturally aligns with the phasor-based nature of electrical quantities, its practical application requires a careful balance between modeling elegance and computational overhead.

A central contribution of this work is the development of the *Decoupled Complex-Valued EKF* (CV-D-EKF). The research reveals that while standard augmented formulations incur heavy computational penalties, the proposed CV-D-EKF mitigates this burden by exploiting mirror symmetry and eliminating redundant operations. Although it does not yet outperform real-valued implementations in absolute speed for the EKF case, the CV-D-EKF reduces execution time by up to 68%, rendering complex-domain linearization-based filters *computationally viable* for large-scale systems such as the SIN-340 bus network.

In contrast, the most striking finding of this research is the *computational crossover* observed in sigma-point-based estimators. For the UKF and SHGM-UKF algorithms, the 50% reduction in state dimension afforded by the complex domain yields a clear computational advantage as the system size scales. In the SIN-340 system, the complex-domain UKF was approximately 29% faster than its real-domain counterpart, effectively overcoming the overhead of complex algebra through the reduced number of propagated sigma points. These results indicate that the complex-domain UKF is highly scalable for high-dimensional monitoring tasks, where dimensional reduction outweighs algebraic complexity. However, since the non-robust UKF is more sensitive to bad data and measurement inconsistencies, the SHGM-UKF represents the preferred alternative when both computational efficiency and robustness are required.

The robustness of the proposed framework was also extensively validated, with the complex-valued SHGM-EKF and SHGM-UKF demonstrating superior capability in suppressing gross errors. It is important to note, however, that for the linearized estimators, the robust formulation requires augmented matrices to handle complex-conjugate correlations. As a result, the computational effort is primarily spent on computing projection statistics rather than on the prediction steps. This also explains why the relative speedup from decoupling is less pronounced in robust filters. Despite this overhead, the CV-SHGM-UKF emerged as the most reliable solution for scenarios involving severe anomalies, ensuring precise tracking of the system's dynamic state.

The frequency-estimation results further reinforce the practical relevance of the proposed DSE framework. By estimating the dynamic states of the generators, the proposed formulation enables the center-of-inertia frequency, ROCOF, and disturbance power indicators to be obtained as byproducts of the estimation process, without requiring an additional dedicated frequency-estimation module. The numerical results show that the COI frequency provides a coherent representation of the system's global electromechanical behavior, even in the presence of individual machine oscillations. Moreover, under adverse measurement conditions, the robust SHGM-based estimators preserve accurate frequency tracking, preventing corrupted PMU data from propagating into frequency-security indicators. This capability is particularly relevant for modern low-inertia systems, where reliable estimates of frequency, ROCOF, and disturbance size are essential for wide-area monitoring, under-frequency load shedding, and fast corrective control actions.

In conclusion, this work demonstrates that the choice of numerical domain must be paired with the appropriate estimator structure. While the EKF requires structural decoupling to achieve a manageable performance gap, the UKF naturally thrives in a complex domain, delivering on the promise of computational efficiency through dimensionality reduction. Together, these formulations offer a mathematically rigorous and scalable path for the real-time dynamic monitoring of modern, low-inertia power systems.

6.1 Future Works

The framework established in this thesis opens several promising avenues for further investigation into the application of complex-conjugate coordinates in power system dynamics. Beyond the models and algorithms validated in this work, the following topics represent the next frontier for this research:

- **Generalization for Non-Circular Signals:** A relevant future extension is to generalize the proposed dynamic state estimator to improper or non-circular complex signals. In this thesis, PMU phasors are assumed to be approximately proper/circular, as supported by the second-order statistical analysis reported in [74]. Physically, this means that the real and imaginary components of the phasor errors have similar variances and weak correlation, resulting in negligible pseudo-covariance. However, under severe unbalanced conditions, asymmetric faults, transformer saturation, or correlated measurement errors, this assumption may no longer hold. In such cases, as discussed by Mandic and Goh [72], pseudo-covariance matrices must be included to capture the correlation between the signal and its complex conjugate.

- **Exploitation of Matrix Sparsity and Topology:** Building on the successful implementation of the decoupled EKF, future work should explore the intrinsic

sparsity of power system matrices within the Wirtinger calculus framework. Since decoupling was achieved without mathematical approximations, investigating sparse matrix techniques and topology-based partitioning could further reduce execution times, potentially bridging the remaining gap between complex-domain EKF and real-time PMU sampling rates.

- **Extension to Advanced Filtering Techniques:** The concepts established in this work can be extended to other derivative-free algorithms. Evaluating the performance and dimensional reduction benefits in the Cubature Kalman Filter (CKF) [107], Ensemble Kalman Filter (EnKF) [108], and Particle Filter (PF) [109] would provide a broader understanding of how complex-domain modeling impacts different stochastic estimation paradigms.

- **Operator Training Simulators (OTS) and Real-Time Integration:** Finally, the integration of static and dynamic estimators in complex coordinates offers a unique opportunity to develop next-generation Operator Training Simulators [110]. By leveraging the flexibility of the proposed models, an OTS could be built to process real-time information on both steady-state and transient electromagnetic phenomena, providing a high-fidelity training environment for monitoring low-inertia modern power systems.

6.2 Publications

Published

1. E. M. Resende, R. Pires, and L. Mili, "Complex-Valued Projection Statistics for Hybrid Power System State Estimation," *IEEE Transactions on Power Systems*, vol. 39, no. 4, pp. 6052–6062, July 2024, DOI: 10.1109/TPWRS.2023.3349016.

2. E. Resende, R. Pires, and L. Mili, "New Topological Observability Algorithm for Hybrid Power System Static State Estimation," *Journal of Modern Power Systems and Clean Energy*, vol. 13, no. 6, pp. 1945-1954, November 2025, DOI: 10.35833/MPCE .2024.000951.

3. R. D. A. Ribeiro, E. M. Resende, R. Pires, and L. Mili, "Second Order Statistical Properties of PMU Data Aiming Power Systems Applications," in *2025 IEEE Kiel PowerTech*, Kiel, Germany, 2025, pp. 1–6, DOI: 10.1109/PowerTech59965.2025.11180407.

Submitted

1. E. Resende, F. Santos, R. Pires, and Z. Machado Junior, "A Complex-Domain Formulation of Synchronous Machine Dynamics with Integrated Control Systems," submitted to *IEEE Transactions on Power Systems*, 2026.

In preparation

1. E. Resende, R. Pires, and Z. Machado Junior, "Efficient Dynamic State Estimation via Structurally Decoupled Extended Kalman Filter in Complex-Conjugate Coordinates," 2026.
2. E. Resende, R. Pires, and Z. Machado Junior, "Overcoming the Computational Burden of Large-Scale DSE: The Dimensionality Advantage of Complex-Domain Unscented Kalman Filtering," 2026.

Bibliography

[1] J. Zhao, A. Gómez-Expósito, M. Netto, L. Mili, A. Abur, V. Terzija, I. Kamwa, B. Pal, A. K. Singh, J. Qi, Z. Huang, and A. P. S. Meliopoulos, "Power system dynamic state estimation: Motivations, definitions, methodologies, and future work," *IEEE Transactions on Power Systems*, vol. 34, no. 4, pp. 3188–3198, 2019. 14, 17, 18, 19

[2] Y. Liu, A. K. Singh, J. Zhao, A. P. S. Meliopoulos, B. Pal, M. A. b. M. Ariff, T. Van Cutsem, M. Glavic, Z. Huang, I. Kamwa, L. Mili, A. S. Mir, A. Taha, V. Terzija, and S. Yu, "Dynamic state estimation for power system control and protection," *IEEE Transactions on Power Systems*, vol. 36, no. 6, pp. 5909–5921, 2021. 14

[3] A. P. S. Meliopoulos, G. J. Cokkinides, P. Myrda, Y. Liu, R. Fan, L. Sun, R. Huang, and Z. Tan, "Dynamic state estimation-based protection: Status and promise," *IEEE Transactions on Power Delivery*, vol. 32, no. 1, pp. 320–330, 2017. 14, 18

[4] J. De La Ree, V. Centeno, J. S. Thorp, and A. G. Phadke, "Synchronized phasor measurement applications in power systems," *IEEE Transactions on Smart Grid*, vol. 1, no. 1, pp. 20–27, 2010. 14

[5] "IEEE standard for synchrophasor measurements for power systems," *IEEE Standard for Synchrophasor Measurements for Power Systems*. 14

[6] A. Phadke and J. Thorp, *Synchronized Phasor Measurements and Their Applications*. Springer Cham, 01 2017. 14

[7] A. Abur and A. Expósito, *Power System State Estimation: Theory and Implementation*. Power Engineering (Willis), CRC Press, 2004. 14

[8] F. C. Schweppe and D. B. Rom, "Power system static-state estimation, part II: Approximate model," *IEEE Transactions on Power Apparatus and Systems*, vol. PAS-89, no. 1, pp. 125–130, 1970. 14

[9] A. Monticelli, *State Estimation in Electric Power Systems: A Generalized Approach*. Springer, 1999. 14

[10] L. Wang and K. Morison, "Implementation of online security assessment," *IEEE Power and Energy Magazine*, vol. 4, no. 5, pp. 46–59, 2006. 15

[11] R. P. Haridas, "Synchrophasor measurement technology in electrical power system," *International journal of engineering research and technology*, 2013. 15

[12] B. A. Alcaide-Moreno, C. R. Fuerte-Esquivel, M. Glavic, and T. V. Cutsem, "Electric power network state tracking from multirate measurements," *IEEE Transactions on Instrumentation and Measurement*, 2017. 15

[13] G. Kusic and D. Garrison, "Measurement of transmission line parameters from SCADA data," in *IEEE PES Power Systems Conference and Exposition, 2004.*, pp. 440–445 vol.1, 2004. 15

[14] M. Ghosal and V. Rao, "Fusion of multirate measurements for nonlinear dynamic state estimation of the power systems," *IEEE Transactions on Smart Grid*, 2018. 15

[15] D. M. Bez and A. J. A. S. Costa, "Processamento de erros grosseiros para estimadores de estado híbrido SCADA-PMU," in *Proceedings of PMAPS (Power Modulation and Adaptive Protection Symposium)*, 2012. 15

[16] D. M. Bez, A. Simões Costa, L. B. Ascari, and E. Z. Junior, "A block version of orthogonal rotations for improving the accuracy of hybrid state estimators," *IEEE Transactions on Power Systems*, vol. 35, no. 6, pp. 4432–4444, 2020. 15

[17] M. Celik and A. Abur, "A robust WLAV state estimator using transformations," *IEEE Transactions on Power Systems*, vol. 7, no. 1, pp. 106–113, 1992. 15

[18] L. Mili, M. Cheniae, N. Vichare, and P. Rousseeuw, "Robust state estimation based on projection statistics [of power systems]," *IEEE Transactions on Power Systems*, vol. 11, pp. 1118–1127, 1996. 15, 19, 55, 57

[19] L. Mili, T. Cheniaux, M. B. Coutto Filho, and R. Roccasalva, "A robust optimal estimator for state estimation," *IEEE Transactions on Power Systems*, vol. 11, no. 1, pp. 257–263, 1996. 15

[20] W. Miller and J. Lewis, "Dynamic state estimation in power systems," *IEEE Transactions on Automatic Control*, vol. 16, no. 6, pp. 841–846, 1971. 16

[21] A. S. Debs and R. E. Larson, "A dynamic estimator for tracking the state of a power system," *IEEE Transactions on Power Apparatus and Systems*, vol. PAS-89, no. 7, pp. 1670–1678, 1970. 16

[22] J. Zhao, M. Netto, Z. Huang, S. Yu, A. Gomez-Exposito, S. Wang, I. Kamwa, S. Akhlaghi, L. Mili, V. Terzija, A. Meliopoulos, B. Pal, A. K. Singh, A. Abur, T. Bi, and A. Rouhani, "Roles of dynamic state estimation in power system modeling, monitoring and operation," *Power Systems, IEEE Transactions on*, vol. 38, pp. 2462 – 2472, 05 2021. 16

[23] P. Sauer, A. Pai, and J. Chow, *Power System Dynamics and Stability: With Synchrophasor Measurement and Power System Toolbox 2e: With Synchrophasor Measurement and Power System Toolbox*. 07 2017. 16

[24] S. Neumann, F. Wilhoit, M. Goodrich, and V. M. Balijepalli, "Everything's talking to each other: Smart meters generate big data for utilities and customers," *IEEE Power and Energy Magazine*, vol. 14, no. 1, pp. 40–47, 2016. 16

[25] A. von Meier, E. Stewart, A. McEachern, M. Andersen, and L. Mehrmanesh, "Precision micro-synchrophasors for distribution systems: A summary of applications," *IEEE Transactions on Smart Grid*, vol. 8, no. 6, pp. 2926–2936, 2017. 16

[26] A. M. Leite da Silva, M. B. Coutto Filho, and J. F. de Queiroz, "State forecasting in electric power systems," *IEE Proceedings C - Generation, Transmission and Distribution*, vol. 130, no. 5, pp. 237–244, 1983. 16

[27] M. B. Coutto Filho and J. C. S. de Souza, "Forecasting-aided state estimation: past, present and future," *IEEE Transactions on Power Systems*, vol. 24, no. 4, pp. 1646–1654, 2009. 16

[28] Z. Huang, P. Du, and D. Kosterev, "Dynamic state estimation of power systems using PMU measurements: A review," *IEEE Transactions on Power Systems*, vol. 33, no. 3, pp. 3279–3290, 2018. 17

[29] Y. Zhou, J. Zhao, and L. Mili, "Dynamic state estimation of power systems: A survey," *IEEE Transactions on Smart Grid*, vol. 11, no. 5, pp. 3956–3971, 2020. 17

[30] Q. Li, R. Li, K. Ji, and W. Dai, "Kalman filter and its application," in *2015 8th International Conference on Intelligent Networks and Intelligent Systems (ICINIS)*, pp. 74–77, 2015. 17, 43

[31] L. Fan and Y. Wehbe, "Extended Kalman filtering based real-time dynamic state and parameter estimation using PMU data," *Electric Power Systems Research*, vol. 103, pp. 168–177, 2013. 17

[32] H. Karimipour and V. Dinavahi, "Extended Kalman filter-based parallel dynamic state estimation," *IEEE Transactions on Smart Grid*, vol. 6, no. 3, pp. 1539–1549, 2015. 17

[33] S. Javadi and A. Hesami Naghshbandy, "Comparison of dynamic state estimation methods in the time domain," *International Journal of Industrial Electronics Control and Optimization*, pp. –, 2024. 17

[34] S. Julier and J. Uhlmann, "Unscented filtering and nonlinear estimation," *Proceedings of the IEEE*, vol. 92, no. 3, pp. 401–422, 2004. 17, 50

[35] J. Qi, K. Sun, J. Wang, and H. Liu, "Dynamic state estimation for multi-machine power system by unscented Kalman filter with enhanced numerical stability," *IEEE Transactions on Smart Grid*, vol. 9, no. 2, pp. 1184–1196, 2018. 17

[36] M. Huang, Z. Wei, G. Sun, Y. Sun, H. Zang, and K. W. Cheung, "A historical data-driven unscented Kalman filter for distribution system state estimation," in *2017 IEEE Power and Energy Society General Meeting*, pp. 1–5, 2017. 17

[37] E. Ghahremani and I. Kamwa, "Dynamic state estimation in power system by applying the extended Kalman filter with unknown inputs to phasor measurements," *IEEE Transactions on Power Systems*, vol. 26, no. 4, pp. 2556–2566, 2011. 18

[38] E. Ghahremani and I. Kamwa, "Online state estimation of a synchronous generator using unscented Kalman filter from phasor measurements units," *IEEE Transactions on Energy Conversion*, vol. 26, no. 4, pp. 1099–1108, 2011. 18

[39] A. Paul, I. Kamwa, and G. Joos, "Centralized dynamic state estimation using a federation of extended Kalman filters with intermittent PMU data from generator terminals," *IEEE Transactions on Power Systems*, vol. 2018, 05 2018. 18

[40] E. Ghahremani and I. Kamwa, "Local and wide-area PMU-based decentralized dynamic state estimation in multi-machine power systems," *IEEE Transactions on Power Systems*, vol. 31, no. 1, pp. 547–562, 2016. 18

[41] A. Srivastava, A. K. Singh, L. A. Tuan, D. Steen, and A. S. Mir, "Decentralized dynamic state estimation of transmission lines using local measurements," *IEEE Access*, vol. 11, pp. 78237–78250, 2023. 18

[42] S. Yu, T. Fernando, K. Emami, and H. H.-C. Iu, "Dynamic state estimation based control strategy for DFIG wind turbine connected to complex power systems," *IEEE Transactions on Power Systems*, vol. 32, no. 2, pp. 1272–1281, 2017. 18

[43] S. Yu, L. Zhang, H. H.-C. Lu, T. Fernando, and K. P. Wong, "A DSE-based power system frequency restoration strategy for PV-integrated power systems considering solar irradiance variations," *IEEE Transactions on Industrial Informatics*, vol. 13, no. 5, pp. 2511–2518, 2017. 18

[44] Y. Liu, A. Meliopoulos, Z. Tan, L. Sun, and R. Fan, "Dynamic state estimation based fault locating on transmission lines," *IET Generation, Transmission and Distribution*, vol. 11, 06 2017. 18

[45] B. Qu, Z. Wang, B. Shen, and H. Dong, "Decentralized dynamic state estimation for multi-machine power systems with non-gaussian noises: Outlier detection and localization," *Automatica*, vol. 153, p. 111010, 2023. 18

[46] A. M. L. da Silva, M. B. Coutto Filho, and J. M. C. Cantera, "An efficient dynamic state estimation algorithm including bad data processing," *IEEE Transactions on Power Systems*, vol. 2, no. 4, pp. 1050–1058, 1987. 18

[47] J. Zhao, M. Netto, and L. Mili, "A robust iterated extended Kalman filter for power system dynamic state estimation," *IEEE Transactions on Power Systems*, vol. 32, no. 4, pp. 3205–3216, 2017. 18, 39, 53, 54, 69

[48] J. Zhao and L. Mili, "A robust generalized-maximum likelihood unscented Kalman filter for power system dynamic state estimation," *IEEE Journal of Selected Topics in Signal Processing*, vol. 12, no. 4, pp. 578–592, 2018. 18, 39, 51, 53, 60, 69

[49] J. Zhao and L. Mili, "Robust unscented Kalman filter for power system dynamic state estimation with unknown noise statistics," *IEEE Transactions on Smart Grid*, vol. 10, no. 2, pp. 1215–1224, 2019. 18

[50] Z. Zheng, J. Zhao, L. Mili, and Z. Liu, "Robust unscented unbiased minimum-variance estimator for nonlinear system dynamic state estimation with unknown inputs," *IEEE Signal Processing Letters*, vol. 27, pp. 376–380, 2020. 18, 51, 60

[51] C. P. Steinmetz, "Complex quantities and their use in electrical engineering," *Proceedings of the International Electrical Congress*, pp. 33–74, 1893. 18

[52] R. Pires, L. Mili, and G. Chagas, "Robust complex-valued Levenberg-Marquardt algorithm as applied to power flow analysis," *International Journal of Electrical Power and Energy Systems*, vol. 113, no. May, pp. 383–392, 2019. 18, 117, 118

[53] R. Pires, G. Chagas, and L. Mili, "Enhanced power flow solution in complex plane," *International Journal of Electrical Power and Energy Systems*, vol. 135, p. 107501, 02 2022. 19

[54] G. Chagas and R. Pires, "The sequential power flow in complex plane for solving the VSC-MTDC hybrid AC/DC transmission grids," *International Journal of Electrical Power and Energy Systems*, vol. 148, p. 108900, 06 2023. 19

[55] K. Kreutz-Delgado, "The complex gradient operator and the cr-calculus," 2009. 19, 24, 40, 41, 115

[56] I. Dzafic, R. A. Jabr, and T. Hrnjic, "Hybrid State Estimation in Complex Variables," *IEEE Transactions on Power Systems*, vol. 33, no. 5, pp. 5288–5296, 2018. 19, 116

[57] I. Džafić and R. A. Jabr, "Real-time equality-constrained hybrid state estimation in complex variables," *International Journal of Electrical Power and Energy Systems*, vol. 117, p. 105634, 2020. 19

[58] I. Džafić, R. A. Jabr, and T. Hrnjić, "Complex variable multi-phase distribution system state estimation using vectorized code," *Journal of Modern Power Systems and Clean Energy*, vol. 8, no. 4, pp. 679–688, 2020. 19

[59] E. M. Resende, R. Pires, and L. Mili, "Complex-valued projection statistics for hybrid power system state estimation," *IEEE Transactions on Power Systems*, pp. 1–12, 2024. 19, 55

[60] R. C. Pires, "Complex-Valued Steady-State Models as Applied to Power Flow Analysis and Power System State Estimation," 2018. 19, 115

[61] D. H. Dini and D. P. Mandic, "Class of widely linear complex Kalman filters," *IEEE Transactions on Neural Networks and Learning Systems*, vol. 23, no. 5, pp. 775–786, 2012. 19

[62] S. L. Goh and D. Mandic, "An augmented extended Kalman filter algorithm for complex-valued recurrent neural networks," in *2006 IEEE International Conference on Acoustics Speech and Signal Processing Proceedings*, vol. 5, pp. V–V, 2006. 19

[63] X. Zhang, Y. Xia, C. Li, and L. Yang, "Unscented Kalman filter with general complex-valued signals," *IEEE Signal Processing Letters*, vol. 29, pp. 2023–2027, 2022. 19

[64] B. Picinbono, "On circularity," *IEEE Transactions on Signal Processing*, vol. 42, no. 12, pp. 3473–3482, 1994. 19

[65] B. Picinbono, "Second-order complex random vectors and normal distributions," *IEEE Transactions on Signal Processing*, vol. 44, no. 10, pp. 2637–2640, 1996. 19

[66] P. Kundur, *Power System Stability and Control*. McGraw-Hill Education, November 1993. 24, 39, 68

[67] W. Wirtinger, "Zur formalen Theorie der Funktionen von mehr komplexen Veranderlichen," *Mathematische Annalen*, vol. 97, pp. 357–375, dec 1927. 24, 116

[68] P. Anderson and A. Fouad, *Power System Control and Stability*. New York, NY: IEEE Press, 1994. 24, 25, 28, 73

[69] P. W. Sauer and M. A. Pai, *Power System Dynamics and Stability*. Upper Saddle River, NJ: Prentice Hall, 1998. 28, 29, 33, 34, 35

[70] "IEEE recommended practice for excitation system models for power system stability studies," *IEEE Std 421.5-2016 (Revision of IEEE Std 421.5-2005)*, pp. 1–207, 2016. 28

[71] PowerWorld, "Governor model: TGOV1 and TGOV1D," 2024. 28

[72] D. P. Mandic and V. S. L. Goh, *Complex Valued Nonlinear Adaptive Filters: Noncircularity, Widely Linear and Neural Models*. John Wiley and Sons, 2009. 39, 42, 43, 44, 51, 101

[73] M. Netto, *Robust identification, estimation, and control of power systems using the Koopman operator-theoretic framework*. PhD thesis, Virginia Polytechnic Institute and State University, 2018. 41

[74] R. D. A. Ribeiro, E. M. Resende, R. Pires, and L. Mili, "Second order statistical properties of PMU data aiming power systems applications," in *2025 IEEE Kiel PowerTech*, pp. 1–6, 2025. 43, 53, 101

[75] S. J. Julier and J. K. Uhlmann, "New extension of the Kalman filter to nonlinear systems," in *Signal Processing, Sensor Fusion, and Target Recognition VI* (I. Kadar, ed.), vol. 3068, pp. 182 – 193, International Society for Optics and Photonics, SPIE, 1997. 52

[76] M. A. Gandhi and L. Mili, "Robust Kalman filter based on a generalized maximum-likelihood-type estimator," *IEEE Transactions on Signal Processing*, vol. 58, no. 5, pp. 2509–2520, 2010. 53, 57

[77] L. Mili, V. Phaniraj, and P. Rousseeuw, "Least median of squares estimation in power systems," *IEEE Transactions on Power Systems*, vol. 6, no. 2, pp. 511–523, 1991. 53

[78] A. Simões Costa and A. Carvalho, "Robustez de estimadores de estados baseados no critério de máxima correntropia face à ocorrência de pontos de alavancamentos," *Anais do Simpósio Brasileiro de Sistemas Elétricos*, vol. 1, no. 1, 2020. 54

[79] W. A. Stahel, "Robuste schätzungen: infinitesimale optimalität und schätzungen von kovarianzmatrizen," 1981. 55

[80] D. L. Donoho, "Breakdown properties of multivariate location estimators," 1982. 55

[81] P. Rousseeuw and A. Leroy, *Robust Regression & Outlier Detection*. John Wiley and Sons, 09 1987. 55

[82] R. C. Pires, L. Mili, and F. A. B. Lemos, "Constrained Robust Estimation of Power System State Variables and Transformer Tap Positions Under Erroneous Zero-Injections," *IEEE Transactions on Power Systems*, vol. 29, pp. 1144–1152, 2014. 56

[83] MathWorks, "Minimum norm least-squares solution to linear equation," 2021. 58

[84] A. Awasthi, R. Guttal, N. Al-Dhahir, and P. T. Balsara, "Complex QR decomposition using fast plane rotations for mimo applications," *IEEE Communications Letters*, vol. 18, no. 10, pp. 1743–1746, 2014. 59

[85] T. Lefebvre, H. Bruyninckx, and J. De Schuller, "Comment on "a new method for the nonlinear transformation of means and covariances in filters and estimators" [with authors' reply]," *IEEE Transactions on Automatic Control*, vol. 47, no. 8, pp. 1406–1409, 2002. 60

[86] S. Xu, Y. Xue, and L. Chang, "Review of power system support functions for inverter-based distributed energy resources- standards, control algorithms, and trends," *IEEE Open Journal of Power Electronics*, vol. 2, pp. 88–105, 2021. 62, 68

[87] B. Tan, J. Zhao, M. Netto, V. Krishnan, V. Terzija, and Y. Zhang, "Power system inertia estimation: Review of methods and the impacts of converter-interfaced generations," *International Journal of Electrical Power and Energy Systems*, vol. 134, p. 107362, 2022. 62

[88] N. Hatziargyriou, J. Milanovic, C. Rahmann, V. Ajjarapu, C. Canizares, I. Erlich, D. Hill, I. Hiskens, I. Kamwa, B. Pal, P. Pourbeik, J. Sanchez-Gasca, A. Stankovic, T. Van Cutsem, V. Vittal, and C. Vournas, "Definition and classification of power system stability – revisited and extended," *IEEE Transactions on Power Systems*, vol. 36, no. 4, pp. 3271–3281, 2021. 62

[89] D. Zografos, *Power System Inertia Estimation and Frequency Response Assessment*. PhD thesis, KTH, School of Electrical Engineering and Computer Science, SE-100 44 Stockholm - Sweden, December 2019. 62, 63, 68

[90] S. You, H. Li, S. Liu, K. Sun, W. Wang, W. Qiu, and Y. Liu, "Calculate Center-of-Inertia Frequency and System RoCoF Using PMU Data," in *2021 IEEE Power and Energy Society General Meeting (PESGM)*, pp. 1–5, 2021. 62

[91] H. Yin, Y. Wu, W. Qiu, C. Zeng, S. You, J. Tan, A. Hoke, C. J. Kruse, B. W. Rockwell, K. A. Kawamura, and Y. Liu, "Precise ROCOF estimation algorithm for low inertia power grids," *Electric Power Systems Research*, vol. 209, p. 107968, 2022. 62, 66

[92] P. Banerjee, S. C. Srivastava, and A. K. Srivastava, "An improved method for estimating phasors and ROCOF suitable for M class PMUs," *IEEE Transactions on Instrumentation and Measurement*, pp. 1–1, 2023. 62

[93] Power System Operation Corporation (POSOCO), "Assessment of inertia in indian power system." https://posoco.in/wp-content/uploads/2022/01/Assessment-of-Inertia-in-Indian-Power-System.pdf, 2022. Accessed: 2024-02-24. 63

[94] P. Denholm, T. Mai, R. W. Kenyon, B. Kroposki, and M. O'Malley, "Inertia and the power grid: A guide without the spin," tech. rep., Golden, CO: National Renewable Energy Laboratory. NREL/TP-6120-73856, 2020. 63

[95] J. H. Eto, J. Undrill, P. Mackin, R. Daschmans, B. Williams, B. Haney, R. Hunt, J. Ellis, H. Illian, C. Martinez, M. OMalley, K. Coughlin, and K. H. LaCommare, "Use of frequency response metrics to assess the planning and operating requirements for reliable integration of variable renewable generation," tech. rep., Berkeley, California, 2010. 63, 64, 65, 66

[96] S. Azizi, M. Sun, G. Liu, and V. Terzija, "Local frequency-based estimation of the rate of change of frequency of the center of inertia," *IEEE Transactions on Power Systems*, vol. 35, no. 6, pp. 4948–4951, 2020. 63

[97] H. R. Chamorro, F. R. S. Sevilla, F. Gonzalez-Longatt, K. Rouzbehi, H. Chavez, and V. K. Sood, "Innovative primary frequency control in low-inertia power systems based on wide-area RoCoF sharing," *IET Energy Systems Integration*, vol. 2, no. 2, pp. 151–160, 2020. 63, 66

[98] A. Fernández-Guillamón, A. Vigueras-Rodríguez, and Molina-García, "Analysis of power system inertia estimation in high wind power plant integration scenarios," *IET Renewable Power Generation*, vol. 13, no. 15, pp. 2807–2816, 2019. 63

[99] P. Du and J. Matevosyan, "Forecast System Inertia Condition and Its Impact to Integrate More Renewables," *IEEE Transactions on Smart Grid*, vol. 9, no. 2, pp. 1531–1533, 2018. 66, 67

[100] G. Frigo, A. Derviškadić, Y. Zuo, and M. Paolone, "PMU-Based RoCoF Measurements: Uncertainty Limits and Metrological Significance in Power System Applications," *IEEE Transactions on Instrumentation and Measurement*, vol. 68, no. 10, pp. 3810–3822, 2019. 67

[101] L. Mehigan, D. Al Kez, S. Collins, A. Foley, B. Ó'Gallachóir, and P. Deane, "Renewables in the european power system and the impact on system rotational inertia," *Energy*, vol. 203, p. 117776, 2020. 67

[102] M. Pai, *Energy Function Analysis for Power System Stability*. Boston, MA: Springer US, 1989. 69, 86

[103] University of Washington, "Power Systems Test Case Archive - IEEE 118 Bus Power Flow Test Case," 1993. Accessed: 2024-05-20. 69

[104] J. L. d. A. Jardim, *ORGANON User Guide*. HPPA – High Performance Power System Applications, 2020. Power system analysis software documentation. 69

[105] Siemens Power Technologies International, *PSSE User Manual*. Siemens, Schenectady, NY, USA, 2018. Power system simulation software documentation. 69

[106] B. Stott and O. Alsac, "Fast decoupled load flow," *IEEE Transactions on Power Apparatus and Systems*, vol. PAS-93, no. 3, pp. 859–869, 1974. 71

[107] A. Sharma, S. C. Srivastava, and S. Chakrabarti, "A cubature Kalman filter based power system dynamic state estimator," *IEEE Transactions on Instrumentation and Measurement*, vol. 66, no. 8, pp. 2036–2045, 2017. 102

[108] C. Carquex, C. Rosenberg, and K. Bhattacharya, "State estimation in power distribution systems based on ensemble Kalman filtering," *IEEE Transactions on Power Systems*, vol. 33, no. 6, pp. 6600–6610, 2018. 102

[109] N. Zhou, D. Meng, and S. Lu, "Estimation of the dynamic states of synchronous machines using an extended particle filter," *IEEE Transactions on Power Systems*, vol. 28, no. 4, pp. 4152–4161, 2013. 102

[110] A. Bose, R. Podmore, and U. Spanel, "Challenges in operator training: Avoiding blackouts in the evolving power grid," *IEEE Power and Energy Magazine*, vol. 21, no. 3, pp. 61–69, 2023. 102

Appendix

APPENDIX A – Analysis of complex functions and variables

This appendix initially presents the basis for the differentiability of complex functions. Then it demonstrates the formulation of the Wirtinger Calculus, a handy tool for transforming non-analytic functions of complex variables into analytic functions in the complex-conjugate coordinate system.

A.1 Differentiability of Complex Functions

As described in [60], consider a complex variable $\bar{x} = a + j \cdot b$ and its respective function $\bar{f}(\bar{x})$ in (A.1). The terms $u(a, b)$ and $v(a, b)$ represent real functions, u and v: $\mathbb{R}^2 \to \mathbb{R}$.

$$\bar{f}(\bar{x}) = u(a, b) + j \cdot v(a, b) \tag{A.1}$$

Functions of this type (A.1) are generally complex but can be real in some cases, such as the cost function of optimization problems $\mathcal{J}(|e^2|)$. From the definition of differentiability of functions of complex variables, we have the limit with Δx tending to 0 in the complex plane, regardless of the direction, according to (A.2).

$$\bar{f}'(\bar{x}_0) = \lim_{\Delta\bar{x}\to 0} \frac{\bar{f}(\bar{x} + \Delta\bar{x}) - \bar{f}(\bar{x})}{\Delta\bar{x}} \tag{A.2}$$

The necessary and sufficient conditions to guarantee the differentiability of $f(x)$ are the Cauchy-Riemann equations, that is,

$$\frac{\partial u}{\partial a} = \frac{\partial v}{\partial b}, \qquad \frac{\partial v}{\partial a} = -\frac{\partial u}{\partial b}. \tag{A.3}$$

If the functions $u(a, b)$ and $v(a, b)$ are continuous throughout their domain, then the partial derivatives of these functions will also be continuous. If this is the case, it follows that $\bar{f}(\bar{x})$ is an analytic or holomorphic function [60, 55].

To illustrate these concepts, consider the following complex function, assuming $\bar{x} = a + jb$.

$$\bar{f}(\bar{x}) = \bar{x}^2 - 4 = \underbrace{a^2 - b^2 - 4}_{u} \; + \; j \cdot \underbrace{2ab}_{v} \tag{A.4}$$

Considering the Cauchy-Riemann assumptions for the differentiability of functions, it follows that

$$\frac{\partial u}{\partial a} = \frac{\partial v}{\partial b} = 2a, \qquad \frac{\partial v}{\partial a} = -\frac{\partial u}{\partial b} = 2b. \tag{A.5}$$

Thus, the satisfaction of the Cauchy-Riemann conditions characterizes $\bar{f}(\bar{x}) = \bar{x}^2 - 4$ as a holomorphic function.

A.2 Wirtinger Calculus or *CR-Calculus*

The device known as Wirtinger Calculus, or *CR-Calculus*, is used to establish the differentiability of non-analytic complex functions, as proposed by Wilhelm Wirtinger in 1927 [67]. Therefore, consider the function described in (A.1) and the relations described below:

$$a = \frac{(\bar{x} + \bar{x}^*)}{2}, \tag{A.6}$$

$$b = j\frac{(\bar{x}^* - \bar{x})}{2}, \tag{A.7}$$

where $\bar{x}$ and $\bar{x}^*$ represent a complex and complex-conjugate variable, respectively

Considering $\bar{x}_c$ as a complex variable, the key idea of Wirtinger Calculus is that if $\bar{f}(\bar{x}_c) = \bar{f}(a, b) = \bar{f}(\bar{x}, \bar{x}^*)$ is analytic in the space spanning a and b then it is also analytic with respect to $\bar{x}$ for constant $\bar{x}^*$, and analogously, it will be analytic for $\bar{x}^*$ considering constant $\bar{x}$ [56]. Furthermore, it is worth noting that such an artifice is applicable if functions like (A.1) are differentiable with respect to a and b. Thus, we have the equations

$$\frac{\partial \bar{f}(\bar{x}_c)}{\partial \bar{x}} = \left.\frac{\partial \bar{f}(\bar{x}, \bar{x}^*)}{\partial \bar{x}}\right|_{\bar{x}^*=Const} = \frac{\partial \bar{f}}{\partial a} \cdot \frac{\partial a}{\partial \bar{x}} + \frac{\partial \bar{f}}{\partial b} \cdot \frac{\partial b}{\partial \bar{x}} = \frac{1}{2}\left(\frac{\partial \bar{f}}{\partial a} - j\frac{\partial \bar{f}}{\partial b}\right), \tag{A.8}$$

$$\frac{\partial \bar{f}(\bar{x}_c)}{\partial \bar{x}^*} = \left.\frac{\partial \bar{f}(\bar{x}, \bar{x}^*)}{\partial \bar{x}^*}\right|_{x=Const} = \frac{\partial \bar{f}}{\partial a} \cdot \frac{\partial a}{\partial \bar{x}^*} + \frac{\partial \bar{f}}{\partial b} \cdot \frac{\partial b}{\partial \bar{x}^*} = \frac{1}{2}\left(\frac{\partial \bar{f}}{\partial a} + j\frac{\partial \bar{f}}{\partial b}\right). \tag{A.9}$$

Such a device would enable the expansion of initially non-holomorphic functions

in Taylor series. Thus, the first-order term of the Taylor series expansion will be

$$\begin{aligned} \bar{f}\left(\bar{x}+\Delta\bar{x},\bar{x}^{*}+\Delta\bar{x}^{*}\right) &\approx \bar{f}\left(\bar{x},\bar{x}^{*}\right)+\frac{\partial\bar{f}}{\partial\bar{x}}\cdot\Delta\bar{x}+\frac{\partial\bar{f}}{\partial\bar{x}^{*}}\cdot\Delta\bar{x}^{*} \\ &\approx \bar{f}\left(\bar{x},\bar{x}^{*}\right)+\begin{bmatrix}\frac{\partial\bar{f}}{\partial\bar{x}} & \frac{\partial\bar{f}}{\partial\bar{x}^{*}}\end{bmatrix}\cdot\begin{bmatrix}\Delta\bar{x}\\ \Delta\bar{x}^{*}\end{bmatrix}. \end{aligned} \tag{A.10}$$

According to [52], a good example is the real function referring to the square of the Euclidean distance from the origin expressed in the equation (A.11), considering the complex variable $\bar{x}=a+j\cdot b$.

$$\bar{f}\left(\bar{x}_{c}\right)=\bar{f}\left(\bar{x},\bar{x}^{*}\right)=\bar{x}^{*}\cdot\bar{x}=||\bar{x}||^{2}=\underbrace{a^{2}+b^{2}}_{u}\;+\;j\cdot\underbrace{(ab-ab)}_{v=0}. \tag{A.11}$$

Since $v=0$, the Cauchy-Riemann differentiability criteria (A.3) are not satisfied and, therefore, it is a non-analytic or non-holomorphic function.

To overcome this obstacle, the Wirtinger Calculus is applied through the equations (A.8) and (A.9), generating:

$$\frac{\partial\bar{f}(\bar{x}_{c})}{\partial\bar{x}}=\bar{x}^{*},\qquad\qquad\frac{\partial\bar{f}(\bar{x}_{c})}{\partial\bar{x}^{*}}=\bar{x}. \tag{A.12}$$

Therefore, the geometric interpretation of this fact is expressed in Fig. 22.

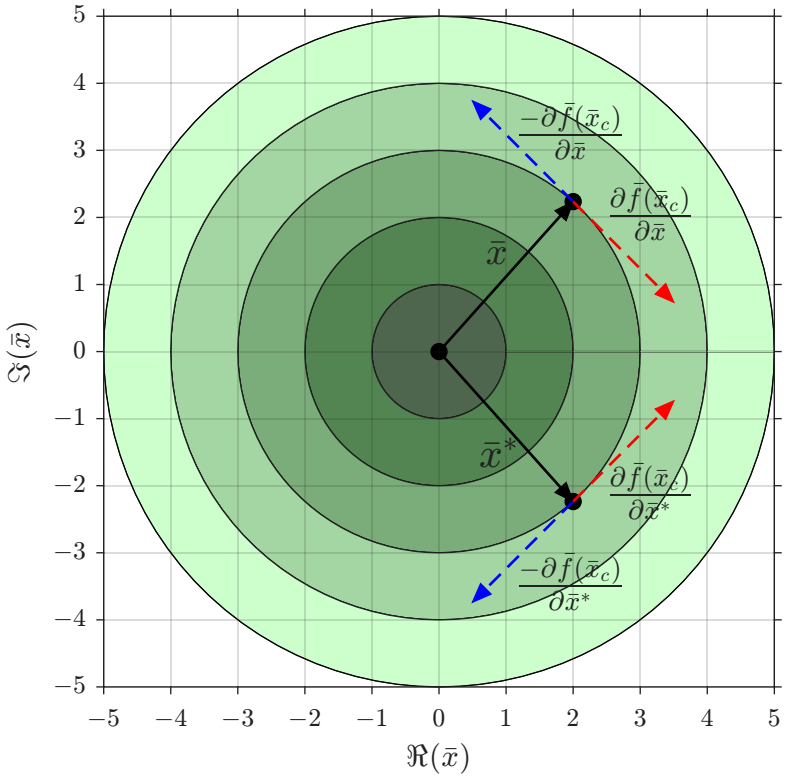


Figure 22 – Contour plot of scalar real function of complex variable [52].

The function corresponding to the square of the Euclidean distance from the origin expressed by $f(\bar{x}_c) = a^2 + b^2$ is equivalent to the equation of a circle centered at the origin of the complex plane, that is, the radius of each circle (contour) is equivalent to $\sqrt{f(x_c)}$. If there were a third axis perpendicular to the axes of the complex plane and fixed to the origin, the figure formed would be that of a paraboloid [52].

It is also important to note that the direction of the maximum rate of change is given by the conjugate gradient expressed in the equation (A.9). The dashed arrow (positive direction) points to the maximum of the function, while the opposite direction points to the minimum of the cost function, generally the minimization of errors [52].

Extending these concepts to the multi-variable scenario, the expressions (A.13-A.15) are valid.

$$\nabla_{\bar{\boldsymbol{x}}} \bar{\boldsymbol{f}} \left(\bar{\boldsymbol{x}}, \bar{\boldsymbol{x}}^* \right) = \begin{bmatrix} \dfrac{\partial \bar{f}}{\partial \bar{x}_1} \\ \vdots \\ \dfrac{\partial \bar{f}}{\partial \bar{x}_n} \end{bmatrix} = \begin{bmatrix} \dfrac{1}{2} \left(\dfrac{\partial \bar{f}}{\partial a_1} - j \cdot \dfrac{\partial \bar{f}}{\partial b_1} \right) \\ \vdots \\ \dfrac{1}{2} \left(\dfrac{\partial \bar{f}}{\partial a_n} - j \cdot \dfrac{\partial \bar{f}}{\partial b_n} \right) \end{bmatrix}, \tag{A.13}$$

$$\nabla_{\bar{\boldsymbol{x}}^*} \bar{\boldsymbol{f}} \left(\bar{\boldsymbol{x}}, \bar{\boldsymbol{x}}^* \right) = \begin{bmatrix} \dfrac{\partial \bar{f}}{\partial \bar{x}_1^*} \\ \vdots \\ \dfrac{\partial \bar{f}}{\partial \bar{x}_n^*} \end{bmatrix} = \begin{bmatrix} \dfrac{1}{2} \left(\dfrac{\partial \bar{f}}{\partial a_1} + j \cdot \dfrac{\partial \bar{f}}{\partial b_1} \right) \\ \vdots \\ \dfrac{1}{2} \left(\dfrac{\partial \bar{f}}{\partial a_n} + j \cdot \dfrac{\partial \bar{f}}{\partial b_n} \right) \end{bmatrix}, \tag{A.14}$$

$$\bar{\boldsymbol{f}} \left(\bar{\boldsymbol{x}} + \Delta \bar{\boldsymbol{x}}, \bar{\boldsymbol{x}}^* + \Delta \bar{\boldsymbol{x}}^* \right) \approx \bar{\boldsymbol{f}} \left(\bar{\boldsymbol{x}}, \bar{\boldsymbol{x}}^* \right) + \begin{bmatrix} \nabla_{\bar{\boldsymbol{x}}} \bar{\boldsymbol{f}}^T & \nabla_{\bar{\boldsymbol{x}}^*} \bar{\boldsymbol{f}}^T \end{bmatrix} \cdot \begin{bmatrix} \Delta \bar{\boldsymbol{x}} \\ \Delta \bar{\boldsymbol{x}}^* \end{bmatrix}. \tag{A.15}$$

APPENDIX B – Derivatives and Jacobian Matrices for the Dynamic State Estimator Formulated in the Complex Domain

B.1 Classical Model

The equations (B.1)-(B.4) show the derivatives that will be used in the linearization process of the classical model in the domain of complex and conjugate variables. The symbol $\bullet$ represents any state variable, that is, $\bar{\alpha}$ or $\bar{\alpha}^*$.

$$\bar{f}_1 = \frac{d\bar{\alpha}}{dt} = \bar{\mathcal{A}}_1 \cdot \bar{\alpha} - \bar{\mathcal{A}}_1 \cdot \bar{\alpha}^* - 0.5 \cdot \bar{\mathcal{A}}_2 \cdot \bar{S}_e - 0.5 \cdot \bar{\mathcal{A}}_2 \cdot \bar{S}_e^* + \bar{\mathcal{A}}_2 \cdot T_M.$$

$$\frac{\partial \bar{f}_1}{\partial \bar{\alpha}} = \bar{\mathcal{A}}_1 - 0.5 \cdot \bar{\mathcal{A}}_2 \cdot \frac{\partial \bar{S}_e}{\partial \bar{\alpha}} - 0.5 \cdot \bar{\mathcal{A}}_2 \cdot \frac{\partial \bar{S}_e^*}{\partial \bar{\alpha}}, \tag{B.1}$$

$$\frac{\partial \bar{f}_1}{\partial \bar{\alpha}^*} = -\bar{\mathcal{A}}_1 - 0.5 \cdot \bar{\mathcal{A}}_2 \cdot \frac{\partial \bar{S}_e}{\partial \bar{\alpha}^*} - 0.5 \cdot \bar{\mathcal{A}}_2 \cdot \frac{\partial \bar{S}_e^*}{\partial \bar{\alpha}^*}, \tag{B.2}$$

$$\frac{\partial \bar{S}_e}{\partial \bullet} = \frac{\partial \bar{E}}{\partial \bullet} \cdot \bar{I}^* + \frac{\partial \bar{I}^*}{\partial \bullet} \cdot \bar{E}, \tag{B.3}$$

$$\frac{\partial \bar{S}_e^*}{\partial \bullet} = \left(\frac{\partial \bar{S}_e}{\partial \bullet} \right)^*. \tag{B.4}$$

The Jacobian matrix of nonlinear functions representing the dynamics of machines in order to state variables will be of the form:

$$\bar{\boldsymbol{F}}_c(\bar{\boldsymbol{x}}) = \begin{bmatrix} \frac{\partial \bar{f}_{1_{(1)}}}{\partial \bar{\alpha}_1} & \cdots & \frac{\partial \bar{f}_{1_{(1)}}}{\partial \bar{\alpha}_n} & \frac{\partial \bar{f}_{1_{(1)}}}{\partial \bar{\alpha}_1^*} & \cdots & \frac{\partial \bar{f}_{1_{(1)}}}{\partial \bar{\alpha}_n^*} \\ \vdots & \ddots & \vdots & \vdots & \ddots & \vdots \\ \frac{\partial \bar{f}_{1_{(n)}}}{\partial \bar{\alpha}_1} & \cdots & \frac{\partial \bar{f}_{1_{(n)}}}{\partial \bar{\alpha}_n} & \frac{\partial \bar{f}_{1_{(n)}}}{\partial \bar{\alpha}_1^*} & \cdots & \frac{\partial \bar{f}_{1_{(n)}}}{\partial \bar{\alpha}_n^*} \end{bmatrix} \rightarrow \quad \bar{\boldsymbol{F}}(\bar{\boldsymbol{x}}) = \begin{bmatrix} \bar{\boldsymbol{F}}_c(\bar{\boldsymbol{x}}) \\ \bar{\boldsymbol{F}}_c^*(\bar{\boldsymbol{x}}) \cdot \boldsymbol{S_w} \end{bmatrix}, \tag{B.5}$$

where $\boldsymbol{S_w}$ is the *swap* operator, an orthogonal matrix defined as:

$$\boldsymbol{S_w} \triangleq \begin{bmatrix} \mathbf{0} & \boldsymbol{I} \\ \boldsymbol{I} & \mathbf{0} \end{bmatrix}, \tag{B.6}$$

where $\mathbf{0}$ and $\boldsymbol{I}$ are the null matrix and the identity matrix, respectively. Such an operator is responsible for permuting blocks of m rows or blocks of n columns, depending on whether $\boldsymbol{S_w}$ is pre- or post-multiplied to a matrix, respectively.

B.2 Two-Axis Model

For the two-axis model with IEEE DC1A voltage regulators and TGOV1 speed and turbine reported in Chapter 2, the derivatives of the following algebraic-differential equations are obtained:

- Differential Equations:
  - $\bar{f}_1 = \dfrac{d\bar{\alpha}}{dt} = \bar{\mathcal{A}}_1 \cdot \bar{\alpha} - \bar{\mathcal{A}}_1 \cdot \bar{\alpha}^* + \bar{\mathcal{A}}_2 \cdot \bar{\mu} + \bar{\mathcal{A}}_2 \cdot \bar{\mu}^* - \bar{\mathcal{A}}_2 \cdot \bar{S}_e - \bar{\mathcal{A}}_2 \cdot \bar{S}_e^*$

$$\frac{\partial \bar{f}_1}{\partial \bar{\alpha}} = \bar{\mathcal{A}}_1 - \bar{\mathcal{A}}_2 \cdot \frac{\partial \bar{S}_e}{\partial \bar{\alpha}} - \bar{\mathcal{A}}_2 \cdot \frac{\partial \bar{S}_e^*}{\partial \bar{\alpha}} \tag{B.7}$$

$$\frac{\partial \bar{f}_1}{\partial \bar{\alpha}^*} = -\bar{\mathcal{A}}_1 - \bar{\mathcal{A}}_2 \cdot \frac{\partial \bar{S}_e}{\partial \bar{\alpha}^*} - \bar{\mathcal{A}}_2 \cdot \frac{\partial \bar{S}_e^*}{\partial \bar{\alpha}^*} \tag{B.8}$$

$$\frac{\partial \bar{f}_1}{\partial \bar{\beta}} = -\bar{\mathcal{A}}_2 \cdot \frac{\partial \bar{S}_e}{\partial \bar{\beta}} - \bar{\mathcal{A}}_2 \cdot \frac{\partial \bar{S}_e^*}{\partial \bar{\beta}} \tag{B.9}$$

$$\frac{\partial \bar{f}_1}{\partial \bar{\beta}^*} = -\bar{\mathcal{A}}_2 \cdot \frac{\partial \bar{S}_e}{\partial \bar{\beta}^*} - \bar{\mathcal{A}}_2 \cdot \frac{\partial \bar{S}_e^*}{\partial \bar{\beta}^*} \tag{B.10}$$

$$\frac{\partial \bar{f}_1}{\partial \bar{\mu}} = \bar{\mathcal{A}}_2 \tag{B.11}$$

$$\frac{\partial \bar{f}_1}{\partial \bar{\mu}^*} = \frac{\partial \bar{f}_1}{\partial \bar{\mu}} \tag{B.12}$$

  - $\bar{f}_2 = \dfrac{d\bar{\beta}}{dt} = \bar{\mathcal{B}}_1 \cdot \bar{\beta} + \bar{\mathcal{B}}_2 \cdot \bar{\beta}^* + \bar{\mathcal{B}}_3 \cdot \bar{\gamma} + \bar{\mathcal{B}}_3 \cdot \bar{\gamma}^* + \bar{\mathcal{B}}_4 \cdot \bar{I}_{qd} + \bar{\mathcal{B}}_5 \cdot \bar{I}_{qd}^*$

$$\frac{\partial \bar{f}_2}{\partial \bar{\beta}} = \bar{\mathcal{B}}_1 + \bar{\mathcal{B}}_4 \cdot \frac{\partial \bar{I}_{qd}}{\partial \bar{\beta}} + \bar{\mathcal{B}}_5 \cdot \frac{\partial \bar{I}_{qd}^*}{\partial \bar{\beta}} \tag{B.13}$$

$$\frac{\partial \bar{f}_2}{\partial \bar{\beta}^*} = \bar{\mathcal{B}}_2 + \bar{\mathcal{B}}_4 \cdot \frac{\partial \bar{I}_{qd}}{\partial \bar{\beta}^*} + \bar{\mathcal{B}}_5 \cdot \frac{\partial \bar{I}^*_{qd}}{\partial \bar{\beta}^*} \tag{B.14}$$

$$\frac{\partial \bar{f}_2}{\partial \bar{\gamma}} = \bar{\mathcal{B}}_3 \tag{B.15}$$

$$\frac{\partial \bar{f}_2}{\partial \bar{\gamma}^*} = \frac{\partial \bar{f}_2}{\partial \bar{\gamma}} \tag{B.16}$$

- $\bar{f}_3 = \dfrac{d\bar{\gamma}}{dt} = \bar{\mathcal{C}}_1 \cdot \bar{\gamma} + \bar{\mathcal{C}}_1 \cdot \bar{\gamma}^* + \bar{\mathcal{C}}_2 \cdot U_x \cdot \bar{\gamma} + \bar{\mathcal{C}}_2 \cdot U_x \cdot \bar{\gamma}^* - \bar{\mathcal{C}}_2 \cdot \bar{\lambda} - \bar{\mathcal{C}}_2 \cdot \bar{\lambda}^*$

$$\frac{\partial \bar{f}_3}{\partial \bar{\gamma}} = \bar{\mathcal{C}}_1 + \bar{\mathcal{C}}_2 \cdot U_x \cdot (1 + 0.5 \cdot \bar{\gamma}) \tag{B.17}$$

$$\frac{\partial \bar{f}_3}{\partial \bar{\gamma}^*} = \bar{\mathcal{C}}_1 + \bar{\mathcal{C}}_2 \cdot U_x \cdot (1 + 0.5 \cdot \bar{\gamma}^*) \tag{B.18}$$

$$\frac{\partial \bar{f}_3}{\partial \bar{\lambda}} = -\bar{\mathcal{C}}_2 \tag{B.19}$$

$$\frac{\partial \bar{f}_3}{\partial \bar{\lambda}^*} = \frac{\partial \bar{f}_3}{\partial \bar{\lambda}} \tag{B.20}$$

- $\bar{f}_4 = \dfrac{d\bar{\lambda}}{dt} = \bar{\mathcal{D}}_1 \cdot \bar{\gamma} + \bar{\mathcal{D}}_1 \cdot \bar{\gamma}^* + \bar{\mathcal{D}}_2 \cdot U_x \cdot \bar{\gamma} + \bar{\mathcal{D}}_2 \cdot U_x \cdot \bar{\gamma}^* + \bar{\mathcal{D}}_3 \cdot \bar{\lambda} + \bar{\mathcal{D}}_4 \cdot \bar{\lambda}^* + \bar{\mathcal{D}}_5 \cdot V - \bar{\mathcal{D}}_5 \cdot V_{ref}$

$$\frac{\partial \bar{f}_4}{\partial \bar{\alpha}} = \bar{\mathcal{D}}_5 \cdot \frac{\partial V}{\partial \bar{\alpha}} \tag{B.21}$$

$$\frac{\partial \bar{f}_4}{\partial \bar{\alpha}^*} = \bar{\mathcal{D}}_5 \cdot \frac{\partial V}{\partial \bar{\alpha}^*} \tag{B.22}$$

$$\frac{\partial \bar{f}_4}{\partial \bar{\beta}} = \bar{\mathcal{D}}_5 \cdot \frac{\partial V}{\partial \bar{\beta}} \tag{B.23}$$

$$\frac{\partial \bar{f}_4}{\partial \bar{\beta}^*} = \bar{\mathcal{D}}_5 \cdot \frac{\partial V}{\partial \bar{\beta}^*} \tag{B.24}$$

$$\frac{\partial \bar{f}_4}{\partial \bar{\gamma}} = \bar{\mathcal{D}}_1 + \bar{\mathcal{D}}_2 \cdot U_x \cdot (1 + 0.5 \cdot \bar{\gamma}) \tag{B.25}$$

$$\frac{\partial \bar{f}_4}{\partial \bar{\gamma}^*} = \bar{\mathcal{D}}_1 + \bar{\mathcal{D}}_2 \cdot U_x \cdot (1 + 0.5 \cdot \bar{\gamma}^*) \tag{B.26}$$

$$\frac{\partial \bar{f}_4}{\partial \bar{\lambda}} = \bar{\mathcal{D}}_4 \tag{B.27}$$

$$\frac{\partial \bar{f}_4}{\partial \bar{\lambda}^*} = \frac{\partial \bar{f}_4}{\partial \bar{\lambda}} \tag{B.28}$$

- $\bar{f}_5 = \dfrac{d\bar{\mu}}{dt} = \bar{\mathcal{E}}_1 \cdot \bar{\alpha} - \bar{\mathcal{E}}_1 \cdot \bar{\alpha}^* + \bar{\mathcal{E}}_2 \cdot \bar{\mu} + \bar{\mathcal{E}}_3 \cdot \bar{\mu}^* + \bar{\mathcal{E}}_4 \cdot P_C$

$$\frac{\partial \bar{f}_5}{\partial \bar{\alpha}} = \bar{\mathcal{E}}_1 \tag{B.29}$$

$$\frac{\partial \bar{f}_5}{\partial \bar{\alpha}^*} = -\frac{\partial \bar{f}_5}{\partial \bar{\alpha}} \tag{B.30}$$

$$\frac{\partial \bar{f}_5}{\partial \bar{\mu}} = \bar{\mathcal{E}}_2 \tag{B.31}$$

$$\frac{\partial \bar{f}_5}{\partial \bar{\mu}^*} = \bar{\mathcal{E}}_3 \tag{B.32}$$

- Algebraic Equations:
  - $\bar{V}_{qd} = V \cdot e^{j\cdot(0.5\cdot(\bar{\alpha}+\bar{\alpha}^*)-\theta)}$

$$\frac{\partial \bar{V}_{qd}}{\partial \bar{\alpha}} = j \cdot 0.5 \cdot \bar{V}_{qd} \tag{B.33}$$

$$\frac{\partial \bar{V}_{qd}}{\partial \bar{\alpha}^*} = \frac{\partial \bar{V}_{qd}}{\partial \bar{\alpha}} \tag{B.34}$$

$$\frac{\partial \bar{V}_{qd}}{\partial \bar{\beta}} = -j \cdot \bar{V}_{qd} \cdot \frac{\partial \theta}{\partial \bar{\beta}} \tag{B.35}$$

$$\frac{\partial \bar{V}_{qd}}{\partial \bar{\beta}^*} = -j \cdot \bar{V}_{qd} \cdot \frac{\partial \theta}{\partial \bar{\beta}^*} \tag{B.36}$$

  - $\bar{V}^*_{qd} = V \cdot e^{-j\cdot(0.5\cdot(\bar{\alpha}+\bar{\alpha}^*)-\theta)}$

$$\frac{\partial \bar{V}^*_{qd}}{\partial \bar{\alpha}} = -j \cdot 0.5 \cdot \bar{V}^*_{qd} \tag{B.37}$$

$$\frac{\partial \bar{V}^*_{qd}}{\partial \bar{\alpha}^*} = \frac{\partial \bar{V}^*_{qd}}{\partial \bar{\alpha}} \tag{B.38}$$

$$\frac{\partial \bar{V}^*_{qd}}{\partial \bar{\beta}} = j \cdot \bar{V}^*_{qd} \cdot \frac{\partial \theta}{\partial \bar{\beta}} \tag{B.39}$$

$$\frac{\partial \bar{V}^*_{qd}}{\partial \bar{\beta}^*} = j \cdot \bar{V}^*_{qd} \cdot \frac{\partial \theta}{\partial \bar{\beta}^*} \tag{B.40}$$

  - $\bar{I}_{qd} = \bar{\mathcal{K}}_1 \cdot \bar{\beta} + \bar{\mathcal{K}}_2 \cdot \bar{\beta}^* - \bar{\mathcal{K}}_1 \cdot \bar{V}_{qd} - \bar{\mathcal{K}}_2 \cdot \bar{V}^*_{qd}$

$$\frac{\partial \bar{I}_{qd}}{\partial \bar{\alpha}} = -\bar{\mathcal{K}}_1 \cdot \frac{\partial \bar{V}_{qd}}{\partial \bar{\alpha}} - \bar{\mathcal{K}}_2 \cdot \frac{\partial \bar{V}^*_{qd}}{\partial \bar{\alpha}} \tag{B.41}$$

$$\frac{\partial \bar{I}_{qd}}{\partial \bar{\alpha}^*} = -\bar{\mathcal{K}}_1 \cdot \frac{\partial \bar{V}_{qd}}{\partial \bar{\alpha}^*} - \bar{\mathcal{K}}_2 \cdot \frac{\partial \bar{V}^*_{qd}}{\partial \bar{\alpha}^*} \tag{B.42}$$

$$\frac{\partial \bar{I}_{qd}}{\partial \bar{\beta}} = \bar{\mathcal{K}}_1 - \bar{\mathcal{K}}_1 \cdot \frac{\partial \bar{V}_{qd}}{\partial \bar{\beta}} - \bar{\mathcal{K}}_2 \cdot \frac{\partial \bar{V}^*_{qd}}{\partial \bar{\beta}} \tag{B.43}$$

$$\frac{\partial \bar{I}_{qd}}{\partial \bar{\beta}^*} = \bar{\mathcal{K}}_2 - \bar{\mathcal{K}}_1 \cdot \frac{\partial \bar{V}_{qd}}{\partial \bar{\beta}^*} - \bar{\mathcal{K}}_2 \cdot \frac{\partial \bar{V}^*_{qd}}{\partial \bar{\beta}^*} \tag{B.44}$$

- $\bar{I}^*_{qd} = -\bar{\mathcal{K}}_2 \cdot \bar{\beta} - \bar{\mathcal{K}}_1 \cdot \bar{\beta}^* + \bar{\mathcal{K}}_2 \cdot \bar{V}_{qd} + \bar{\mathcal{K}}_1 \cdot \bar{V}^*_{qd}$

$$\frac{\partial \bar{I}^*_{qd}}{\partial \bar{\alpha}} = \bar{\mathcal{K}}_2 \cdot \frac{\partial \bar{V}_{qd}}{\partial \bar{\alpha}} + \bar{\mathcal{K}}_1 \cdot \frac{\partial \bar{V}^*_{qd}}{\partial \bar{\alpha}} \tag{B.45}$$

$$\frac{\partial \bar{I}^*_{qd}}{\partial \bar{\alpha}^*} = \bar{\mathcal{K}}_2 \cdot \frac{\partial \bar{V}_{qd}}{\partial \bar{\alpha}^*} + \bar{\mathcal{K}}_1 \cdot \frac{\partial \bar{V}^*_{qd}}{\partial \bar{\alpha}^*} \tag{B.46}$$

$$\frac{\partial \bar{I}^*_{qd}}{\partial \bar{\beta}} = -\bar{\mathcal{K}}_2 + \bar{\mathcal{K}}_2 \cdot \frac{\partial \bar{V}_{qd}}{\partial \bar{\beta}} + \bar{\mathcal{K}}_1 \cdot \frac{\partial \bar{V}^*_{qd}}{\partial \bar{\beta}} \tag{B.47}$$

$$\frac{\partial \bar{I}^*_{qd}}{\partial \bar{\beta}^*} = -\bar{\mathcal{K}}_1 + \bar{\mathcal{K}}_2 \cdot \frac{\partial \bar{V}_{qd}}{\partial \bar{\beta}^*} + \bar{\mathcal{K}}_1 \cdot \frac{\partial \bar{V}^*_{qd}}{\partial \bar{\beta}^*} \tag{B.48}$$

- $\bar{S}_e = \bar{V}^*_{qd} \cdot \bar{I}_{qd}$

$$\frac{\partial \bar{S}_e}{\partial \bar{\alpha}} = \frac{\partial \bar{V}^*_{qd}}{\partial \bar{\alpha}} \cdot \bar{I}_{qd} + \bar{V}^*_{qd} \cdot \frac{\partial \bar{I}_{qd}}{\partial \bar{\alpha}} \tag{B.49}$$

$$\frac{\partial \bar{S}_e}{\partial \bar{\alpha}^*} = \frac{\partial \bar{V}^*_{qd}}{\partial \bar{\alpha}^*} \cdot \bar{I}_{qd} + \bar{V}^*_{qd} \cdot \frac{\partial \bar{I}_{qd}}{\partial \bar{\alpha}^*} \tag{B.50}$$

$$\frac{\partial \bar{S}_e}{\partial \bar{\beta}} = \frac{\partial \bar{V}^*_{qd}}{\partial \bar{\beta}} \cdot \bar{I}_{qd} + \bar{V}^*_{qd} \cdot \frac{\partial \bar{I}_{qd}}{\partial \bar{\beta}} \tag{B.51}$$

$$\frac{\partial \bar{S}_e}{\partial \bar{\beta}^*} = \frac{\partial \bar{V}^*_{qd}}{\partial \bar{\beta}^*} \cdot \bar{I}_{qd} + \bar{V}^*_{qd} \cdot \frac{\partial \bar{I}_{qd}}{\partial \bar{\beta}^*} \tag{B.52}$$

- $\bar{S}^*_e = \bar{V}_{qd} \cdot \bar{I}^*_{qd}$

$$\frac{\partial \bar{S}^*_e}{\partial \bar{\alpha}} = \frac{\partial \bar{V}_{qd}}{\partial \bar{\alpha}} \cdot \bar{I}^*_{qd} + \bar{V}_{qd} \cdot \frac{\partial \bar{I}^*_{qd}}{\partial \bar{\alpha}} \tag{B.53}$$

$$\frac{\partial \bar{S}^*_e}{\partial \bar{\alpha}^*} = \frac{\partial \bar{V}_{qd}}{\partial \bar{\alpha}^*} \cdot \bar{I}^*_{qd} + \bar{V}_{qd} \cdot \frac{\partial \bar{I}^*_{qd}}{\partial \bar{\alpha}^*} \tag{B.54}$$

$$\frac{\partial \bar{S}^*_e}{\partial \bar{\beta}} = \frac{\partial \bar{V}_{qd}}{\partial \bar{\beta}} \cdot \bar{I}^*_{qd} + \bar{V}_{qd} \cdot \frac{\partial \bar{I}^*_{qd}}{\partial \bar{\beta}} \tag{B.55}$$

$$\frac{\partial \bar{S}_e^*}{\partial \bar{\beta}^*} = \frac{\partial \bar{V}_{qd}}{\partial \bar{\beta}^*} \cdot \bar{I}_{qd}^* + \bar{V}_{qd} \cdot \frac{\partial \bar{I}_{qd}^*}{\partial \bar{\beta}^*} \tag{B.56}$$

The Jacobian matrix that relates the differential equations for the two-axis model to the complex-conjugate state variables will be of the form

$$\bar{\boldsymbol{F}}_c(\bar{\boldsymbol{x}}) = \begin{bmatrix} \frac{\partial \bar{f}_1}{\partial \bar{\alpha}} & \frac{\partial \bar{f}_1}{\partial \bar{\beta}} & 0 & 0 & \frac{\partial \bar{f}_1}{\partial \bar{\mu}} & \frac{\partial \bar{f}_1}{\partial \bar{\alpha}^*} & \frac{\partial \bar{f}_1}{\partial \bar{\beta}^*} & 0 & 0 & \frac{\partial \bar{f}_1}{\partial \bar{\mu}^*} \\ 0 & \frac{\partial \bar{f}_2}{\partial \bar{\beta}} & \frac{\partial \bar{f}_2}{\partial \bar{\gamma}} & 0 & 0 & 0 & \frac{\partial \bar{f}_2}{\partial \bar{\beta}^*} & \frac{\partial \bar{f}_2}{\partial \bar{\gamma}^*} & 0 & 0 \\ 0 & 0 & \frac{\partial \bar{f}_3}{\partial \bar{\gamma}} & \frac{\partial \bar{f}_3}{\partial \bar{\lambda}} & 0 & 0 & 0 & \frac{\partial \bar{f}_3}{\partial \bar{\gamma}^*} & \frac{\partial \bar{f}_3}{\partial \bar{\lambda}^*} & 0 \\ \frac{\partial \bar{f}_4}{\partial \bar{\alpha}} & \frac{\partial \bar{f}_4}{\partial \bar{\beta}} & \frac{\partial \bar{f}_4}{\partial \bar{\gamma}} & \frac{\partial \bar{f}_4}{\partial \bar{\lambda}} & 0 & \frac{\partial \bar{f}_4}{\partial \bar{\alpha}^*} & \frac{\partial \bar{f}_4}{\partial \bar{\beta}^*} & \frac{\partial \bar{f}_4}{\partial \bar{\gamma}^*} & \frac{\partial \bar{f}_4}{\partial \bar{\lambda}^*} & 0 \\ \frac{\partial \bar{f}_5}{\partial \bar{\alpha}} & 0 & 0 & 0 & \frac{\partial \bar{f}_5}{\partial \bar{\mu}} & \frac{\partial \bar{f}_5}{\partial \bar{\alpha}^*} & 0 & 0 & 0 & \frac{\partial \bar{f}_5}{\partial \bar{\mu}^*} \end{bmatrix} \tag{B.57}$$

The post-multiplication of the *swap* operator (B.6) on (B.57) produces the augmented Jacobian matrix, resulting in (B.5). In this way, the functions of complex variables satisfy holomorphicity.

Attachment

Complex-Valued Projection Statistics for Hybrid Power System State Estimation

Eduardo M. Resende, *Student Member, IEEE*, Robson Pires, *Senior Member, IEEE*, and Lamine Mili, *Life Fellow, IEEE*

***Abstract*—This paper develops a complex-valued Schweppe-type GM-estimator with the Huber cost function (known as SHGM estimator) that processes both phasor measurement units (PMUs) and supervisory control and data acquisition (SCADA) measurements. It is based on the projection statistics (PS) implemented in the complex domain. It is shown that the PS algorithm applied to a real- or a complex-valued Jacobian matrix provides different numerical results and thereby, different set of leverage points. Consequently, both approaches lead to different state estimates. It is demonstrated through simulations carried out on various test systems that the proposed estimator is more reliable and robust than its real-valued counterpart.**

***Index Terms*—Wirtinger calculus, complex-valued projection statistics, Power system hybrid state estimation.**

I. Introduction

ENGINEERING and applied science rely heavily on complex-valued data signal processing to model and analyze physical phenomena and processes [1]. Researchers in the power area have long been developing methods and algorithms for system stability analysis, state estimation and control in the real domain. However, power system models involve voltage and currents phasors in the complex domain, which were introduced by Steinmetz [2].

In addition to the conventional SCADA measurements, a growing number of PMUs have been recently deployed in electrical power systems in the USA, Europe, and a number of other countries. Because PMUs measure voltage and current phasors, conventional real-valued state estimators may be extended to the complex domain using the Wirtinger calculus [3].

When incorporating PMU measurements into the state estimator, the different reporting rates of the conventional measurements and the synchronized system of phasor measurements based on PMU raise the question as to how to synchronize the measurements and when to use them. This issue is beyond of this work but in the literature there are relevant contributions aiming this goal. Among them, we highlighted the proposals addressed to solve this problem on static and dynamic hybrid state estimation as described in [4] and [5], [6], respectively.

Regarding the complex-valued weighted least square state estimator, it has been initiated by Pires [7] and Dzafic et al. [8], who showed that it is faster than the conventional real-valued state estimator and can handle in easier way zero power injections [9], [10]. Later, Dzafic et al. [11] extended the state estimator to a three-phase model for unbalanced power distribution system applications and applied the largest normalized residual approach for bad data analysis. Initiated by Mili et al. [12] to handle all types of outliers, including vertical outliers and bad leverage points, using projection statistics (PS), others algorithms were also developed to mitigate the leverage points effect [13]. Nonetheless, the real-valued robust SHGM power system state estimator is solved using algorithms that have been further enhanced in [10], [14], [15], among others.

In this paper, the SHGM state estimator is developed in complex domain for solving the well known algorithm named iteratively re-weighted least-squares (IRLS) [16] by using Huber cost function [17]. Two approaches for calculating the PS, namely a real-valued and a complex-valued approach, are compared and their performances analyzed through simulations carried out on various IEEE test systems. For doing that, a suited nonlinear model for complex-valued measures is used which makes the bad data processing successful, regardless it is either leverage point or not. It is shown that the developed robust estimator outperforms its real-valued counterpart and the implementation of the algorithms is straightforward and it is much easier to encode them in the complex plane than in the real domain.

This paper is organized as follows. Section II derives the SHGM estimator in the complex domain. Section III presents and analyzes some simulation results performed on various test systems of different sizes. Section IV concludes the paper and provides some future work.

II. Robust Complex-Valued Schweppe-Type GM-Estimator

A. Circular and Proper Statistical Signals Properties

In hybrid monitoring systems, statistical and temporal analysis are performed by processing integrated and synchronized PMUs and SCADA measurements. From the PMUs,

Manuscript received 1 August 2023; revised 21 November 2023; accepted 17 December 2023. Date of publication 4 January 2024; date of current version 20 June 2024. This work was supported in part by CAPES and in part by UNIFEI for providing academic and laboratory support. Paper no. TPWRS-01196-2023. *(Corresponding author: Eduardo M. Resende.)*

Eduardo M. Resende and Robson Pires are with the Institute of Electric Systems, Energy - ISEE Federal University of Itajubá, 37 500-903 Itajubá, Brazil (e-mail: edumarresende@unifei.edu.br; rpires@unifei.edu.br).

Lamine Mili is with the Department of Electrical, Computer Engineering Virginia Tech National Capital Region Falls Church, Falls Church, VA 22043 USA (e-mail: lmili@vt.edu).

Color versions of one or more figures in this article are available at https://doi.org/10.1109/TPWRS.2023.3349016.

Digital Object Identifier 10.1109/TPWRS.2023.3349016

0885-8950 © 2024 IEEE. Personal use is permitted, but republication/redistribution requires IEEE permission.
See https://www.ieee.org/publications/rights/index.html for more information.

Authorized licensed use limited to: Centro Universitário Fei. Downloaded on October 31,2024 at 18:04:55 UTC from IEEE Xplore. Restrictions apply.

we typically obtain 30-240 synchronized phasor samplings per second [18] while from the SCADA, we obtain a set of measurements every 5 seconds, and in some cases a new batch of measurements becomes available every 3 seconds. At a control center, the run cycle of a state estimator depends on the need of power system analysis, which is typically executed every 5 minutes and, in some cases, every 30 seconds. Consequently, a large amount of measurements are available to build a reliable database for operators to make control decisions. Following the state-of-the-art literature on complex-valued signals [19], [20], [21], to cite a few, voltage and current phasors provided by PMUs are assumed proper and circular, which implies that their complementary (or pseudo-) correlations need to be estimated [22], [23], [24], [25], [26]. Now, let us recall a few definitions related to complex-valued variables.

A complex-valued random variable, $z = z_{Re} + jz_{Im}$, is proper if it is uncorrelated with its complex conjugate, and is circular if it has a probability density function (*pdf*) such that for any θ, z has an invariant *pdf* to rotation, i.e., $p(z) = p(z\, e^{j\theta})$ for $\forall\, \theta \in [0, 2\pi]$, and is zero-mean [22]. In addition, its covariance matrix is given by

$$\mathbf{C}_c = E\left[zz^H\right] = E[z_{Re}^2] + E[z_{Im}^2] = \sigma_{Re}^2 + \sigma_{Im}^2, \tag{1}$$

where the superscript $(\cdot)^H$ stands for Hermitian, which is the transpose complex conjugate operator. It is also necessary to include the so-called pseudo-covariance matrix [26], which is expressed as

$$\begin{aligned}\mathbf{P}_c &= E[zz^T],\\ &= E[{z_{Re}}^2] - E[{z_{Im}}^2] + 2j\, E[z_{Re}z_{Im}],\\ &= \sigma_{Re}^2 - \sigma_{Im}^2 + 2j\sigma_{Re,Im},\end{aligned} \tag{2}$$

where σ^2 is a variance and $\sigma_{Re,Im}$ is a covariance. Since, the pseudo-covariance matrix vanishes for uncorrelated real and imaginary parts of equal variances, a complex Gaussian random signal is called second-order *circular if* it has zero-mean and is *proper*, and its variance is twice the variances of the real and imaginary parts, that is, $\sigma^2 = 2 \times \sigma_{Re}^2 = 2 \times \sigma_{Im}^2$. However, among many other practical reasons, the most common being short observation windows, the pseudo-covariance matrix, $\mathbf{P}_c \neq 0$, should be taken into account. Thus, to account for noncircularity, the literature in signal processing [23], [24], [25] have recommended to use a signal model based on the matrix form of the complex-valued variable, that is,

$$z = \mathbf{M}\begin{bmatrix} z_{Re} \\ z_{Im} \end{bmatrix} = \begin{bmatrix} z \\ z^* \end{bmatrix}, \tag{3}$$

where the matrix $\mathbf{M} \in \mathbb{C}^{2\times 2}$ is defined as

$$\mathbf{M} = \begin{pmatrix} 1 & j \\ 1 & -j \end{pmatrix}, \tag{4}$$

and where $j = \sqrt{-1}$.

In what follows, it is important to note that

$$\mathbf{M}^{-1} = \frac{1}{2}\mathbf{M}^H. \tag{5}$$

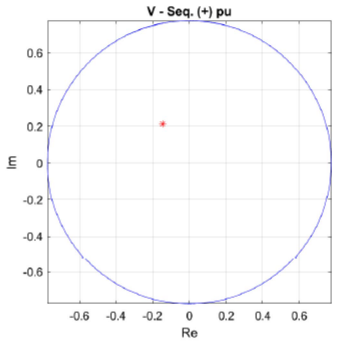


Fig. 1. Real and imaginary voltage measurements provided by a PMU.

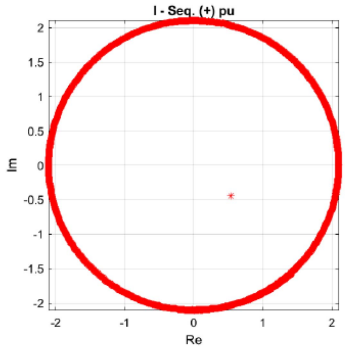


Fig. 2. Real and imaginary current measurements provided by a PMU.

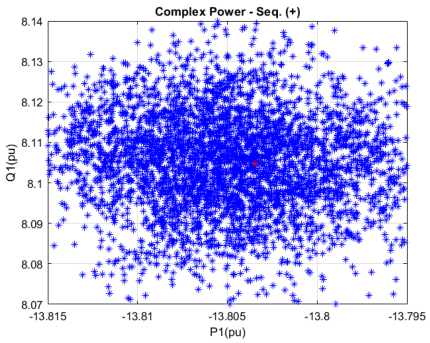


Fig. 3. Real and reactive power measurements provided by a PMU.

Thus, the augmented covariance matrix [26] is defined as

$$\mathbf{\Omega}_{\underline{c}} = E\left[\underline{\mathbf{z}} \cdot \underline{\mathbf{z}}^H\right] = \begin{bmatrix} \mathbf{C}_c & \mathbf{P}_c \\ \mathbf{P}_c^* & \mathbf{C_c}^* \end{bmatrix}. \tag{6}$$

Therefore, both second-order circular and noncircular signals can be modeled for general complex processes. Note that $\mathbf{\Omega}_c$ given by (6) has real-valued diagonal elements and complex-valued off-diagonal elements. Furthermore, z as defined in (3) is second-order *circular* and *proper* while the variances of z_{Re} and z_{Im} are the same and z_{Re} and z_{Im} are uncorrelated. Figs. 1 and 2 depicts the scatter plot of the positive sequence of voltage and current measurements in rectangular coordinates, respectively. Additionally, Fig. 3 depicts the corresponding complex power

Authorized licensed use limited to: Centro Universitário Fei. Downloaded on October 31,2024 at 18:04:55 UTC from IEEE Xplore. Restrictions apply.

that is calculated, which is given by

$$S = VI^* = P + jQ = (V_r I_r + V_i I_i) + j\,(V_i I_r - V_r I_i). \tag{7}$$

Because the PMUs only provide real and imaginary voltage and current measurements for each phase [27] and because the PMU output measurements follow the circular and proper properties, the augmented covariance matrix becomes a real-valued matrix if $\underline{\mathbf{\Omega}}_c = \mathbf{C}_c = diag\{\sigma_1^2; \sigma_2^2; \ldots; \sigma_{2m}^2\}$ and $\mathbf{P_c} = 0$, where $\sigma_i^2 = 2 \times \sigma_{Re_i}^2 = 2 \times \sigma_{Im_i}^2$.

B. Complex-Valued Nonlinear Measurement Model

As proposed by Van Den Bos [28], a conventional nonlinear measurement model is assumed to include additive errors that follow a complex-valued multivariate Gaussian distribution. More details can be found in [29], [30] and [31]. Moreover, assuming that $\underline{\mathbf{z}}_c$ denotes a measurement vector of complex-valued random variables defined by the Wirtinger calculus as

$$\underline{\mathbf{z}}_c = (z_1 \cdots z_m, z_1^* \cdots z_m^*)^T, \qquad \underline{\mathbf{z}}_c \in \mathbb{C}^{2m\times 1} \tag{8}$$

where

$$z_i = z_{Re_i} + j\, z_{Im_i} \quad \text{and} \quad z_i^* = z_{Re_i} - j\, z_{Im_i}, \tag{9}$$

and z_{Re_i}, $z_{Im_i} \in \mathbb{R}$. Additionally, the real variables z_{Re_i} and z_{Im_i}, for $i = 1, \ldots, m$, are normally distributed. Thus, the complex-valued nonlinear state estimation model of a power system is expressed as

$$\underline{\mathbf{z}}_c = \underline{\mathbf{h}}\,(\underline{\mathbf{x}}_c) + \underline{\omega}_c, \tag{10}$$

where

$$E(\underline{\omega}_c) = 0, \qquad E(\underline{\omega}_c\, \underline{\omega}_c^H) = \mathbf{\Omega}_c. \tag{11}$$

Here, $\underline{\mathbf{z}}_c = (\mathbf{z}, \mathbf{z}^*)$ is a vector of measurements of dimension $(2m \times 1)$; $\underline{\mathbf{x}}_c = (\mathbf{x}, \mathbf{x}^*)$ is a vector of true state variables of dimension $(2n \times 1)$; $\underline{\mathbf{h}}(\underline{\mathbf{x}}_c)$ is a vector of nonlinear functions of dimension $(2m \times 1)$; $\underline{\omega}_c$ is a vector of random measurement errors of dimension $(2m \times 1)$ while $\mathbf{\Omega}_c$ is a Hermitian positive-definite covariance matrix of $\underline{\omega}_c$ of dimension $(2\,m \times 2\,m)$.

C. Complex-Valued SHGM Estimator

The vector $\underline{\mathbf{x}}_c = (\mathbf{x}, \mathbf{x}^*)$ given by (10) is estimated by using the complex-valued SHGM estimator that minimizes an objective function expressed as

$$J(\underline{\mathbf{x}}_c) = \sum_{i=1}^{m} \omega_i^2 \rho(r_{s_i}), \tag{12}$$

Here, $\rho(r_{s_i})$ is the Huber function defined as

$$\rho(r_{s_i}) = \begin{cases} r_{s_i}^2/2 & \text{for } |r_{s_i}| \le \beta \\ \beta\,|r_{s_i}| - \frac{\beta^2}{2} & \text{for } |r_{s_i}| > \beta \end{cases} \tag{13}$$

and its first derivative with respect to r_{s_i}, $\psi(r_{s_i})$, is expressed as

$$\psi(r_{s_i}) = \begin{cases} r_{s_i} & \text{for } |r_{s_i}| \le \beta \\ \beta sign(r_{s_i}) & \text{for } |r_{s_i}| > \beta \end{cases} \tag{14}$$

In the above equations, β is made equal to 1.345 to achieve a statistical efficiency of 95% [17], and r_{s_i} is a standardized residual defined as $r_{s_i} = r_i/(\sigma_i \omega_i)$, where r_i is the ith entry of the residual vector, $\underline{\mathbf{r}}_c = \underline{\mathbf{z}}_c - \underline{\mathbf{h}}(\underline{\hat{\mathbf{x}}}_c)$, and ω_i is a weight that is either equal to one up to a given threshold, c_i, or to a decreasing function of the squared projection statistic, PS_i, associated with the ith-measurement. The reader is referred to [12] for a description of an efficient procedure for calculating the PS. Note that it is the $\omega_i' s$ that make the SHGM robust against bad leverage points, which are calculated off-line from the Jacobian matrix assessed at the flat voltage profile. They need to be updated only if the measurement configuration changes or the topology is modified. In this paper, the Jacobian matrix is built in the complex plane, which is further investigated next.

D. Leverage Points Calculation in the Complex Domain

Recall that a leverage point is a measurement whose associated row vector is an outlier in the Jacobian matrix. This latter is accessed at flat start condition and the whole procedure hereafter can be done *off-line* [12]. Instead, remark that the power of modern processors that posses single instruction multiple data (SIMD) extensions can be applied [11], [32]. In the complex plane, such row vector can be considered as a vector of complex numbers or two-dimensional real vectors, whose dot products are scalars that are function of their magnitudes and the angle between them.

As proposed by [12] in the real case, let us assume that the row vectors, $\mathbf{h}_i^T$, of the Jacobian matrix, $\mathbf{H}(\mathbf{x})$, in the complex domain follow a multivariate normal distribution, $N\,(\overline{\mathbf{h}}, \overline{\mathbf{C}}_c)$, whose mean vector, $\overline{\mathbf{h}}$, and covariance matrix, $\overline{\mathbf{C}}_c$, are respectively given by

$$\overline{h} = \frac{1}{m} \sum_{i=1}^{m} (H_i), \tag{15}$$

$$\overline{\mathbf{C}}_c = \frac{1}{m-1} \sum_{i=1}^{m} (H_i - \overline{h})(H_i - \overline{h})^H, \tag{16}$$

Under the above assumptions, the projection statistics are defined as in the real domain [12], except by complex number arithmetic, which yields

$$PS_i = \max_{H_k} \frac{|{H_i}^H . H_k|}{\overline{\beta}}, \tag{17}$$

where for any specific row i, the subscript k varies from 1 to m, e.g., $k = 1, 2, \ldots, m$.

In the foregoing equation, the highly robust scale estimator, $\overline{\beta}$, is given by

$$\overline{\beta} = \gamma \cdot lomed_i \left\{ lomed_{j \ne i} \left\{ |H_i^H H_k + H_j^H H_k| \right\} \right\}, \tag{18}$$

Authorized licensed use limited to: Centro Universitário Fei. Downloaded on October 31,2024 at 18:04:55 UTC from IEEE Xplore. Restrictions apply.

where *lomed* stands for low median of the m scalar numbers and $\gamma = 1.1926$ is needed to make this an approximately unbiased estimate of scale when the error model is Gaussian [12], [33]. Therefore, a measurement is flagged as leverage point if the following inequality is satisfied:

$$PS_i > c_i = \chi^2_{\nu;97.5\%}, \tag{19}$$

where ν is the number of non-zero entries in the corresponding row of the Jacobian matrix. Now, the weights, ω_i, used to standardize the residuals in (12) are defined as

$$\omega_i = \min\left(1, \left(\frac{c_i}{PS_i}\right)^2\right), \tag{20}$$

where c_i is the cutoff value given by (19).

E. The IRLS Algorithm in the Complex Domain

The necessary condition of optimatility derived from (12), $\nabla J(\underline{\mathbf{x}}_c) = \underline{0}$, is expressed as

$$\sum_{i=1}^{m} \omega_i^2 \left(\frac{\partial r_{s_i}}{\partial \widehat{x}_i}\right)^H \psi(r_{s_i}) = \underline{0}, \tag{21}$$

The foregoing equation is solved using the IRLS algorithm implemented in the complex domain. This algorithm is derived by dividing and multiplying $\psi(r_{s_i})$ by r_{s_i} in (21) and using the definition of r_{s_i}, yields

$$\sum_{i=1}^{m} \omega_i^2 \left(\frac{1}{\sigma_i \omega_i}\frac{\partial r_i}{\partial \widehat{x}_i}\right)^H \left(\frac{\psi(r_{s_i})}{\frac{r_i}{\sigma_i\omega_i}}\right)\left(\frac{r_i}{\sigma_i\omega_i}\right) = \underline{0}, \tag{22}$$

which, after algebraic simplifications, becomes

$$\sum_{i=1}^{m} \left(\frac{\partial r_i}{\partial \widehat{x}_i}\right)^H q\left(r_{s_i}\right)\left(\frac{r_i}{\sigma_i^2}\right) = \underline{0}. \tag{23}$$

If (23) is put in a matrix form, we get

$$\mathbf{H}_c^H \mathbf{Q}_c \mathbf{\Omega}_c^{-1}\left(\underline{\mathbf{z}}_c - \underline{\mathbf{h}}(\widehat{\underline{\mathbf{x}}}_c)\right) = \underline{0}, \tag{24}$$

where

$$\mathbf{Q}_c = diag(q(r_{s_i})). \tag{25}$$

Now replacing $\underline{\mathbf{h}}(\underline{\mathbf{x}}_c)$ in (24) by its first Taylor series expansion about $\underline{\mathbf{x}}_c^k$, yields

$$\underline{\mathbf{h}}(\underline{\mathbf{x}}_c) \cong \underline{\mathbf{h}}(\widehat{\underline{\mathbf{x}}}_c^k) + \mathbf{H}_c \Delta\widehat{\underline{\mathbf{x}}}_c^k, \tag{26}$$

which gives

$$\mathbf{H}_c^H \mathbf{Q}_c \mathbf{\Omega}_c^{-1}\left(\Delta\underline{\mathbf{z}}_c^k - \mathbf{H}_c \Delta\widehat{\underline{\mathbf{x}}}_c^k\right) = \underline{0}, \tag{27}$$

or

$$\mathbf{H}_c^H \mathbf{Q}_c \mathbf{\Omega}_c^{-1} \mathbf{H}_c \Delta\widehat{\underline{\mathbf{x}}}_c^k = \mathbf{H}_c^H \mathbf{Q}_c \mathbf{\Omega}_c^{-1} \Delta\underline{\mathbf{z}}_c^k, \tag{28}$$

where $\Delta\underline{\mathbf{z}}_c^k = \underline{\mathbf{z}}_c - \underline{\mathbf{h}}(\widehat{\underline{\mathbf{x}}}_c^k)$. The foregoing equation is equivalent to obtaining the solution to the redundant linear system of equations defined as

$$\Delta\widehat{\underline{\mathbf{x}}}_c^k = \widetilde{\mathbf{H}}_c^{\dagger}\,\widetilde{\underline{\mathbf{z}}}_c, \tag{29}$$

where the superscript $(\cdot)^{\dagger}$ stands for the Moore-Penrose pseudo inverse, and

$$\widetilde{\mathbf{H}}_{\mathbf{c}} = \mathbf{Q}_c^{1/2} \mathbf{\Omega}_c^{-1/2} \mathbf{H}_c, \tag{30}$$

and

$$\widetilde{\underline{\mathbf{z}}}_c = \mathbf{Q}_c^{1/2} \mathbf{\Omega}_c^{-1/2} \Delta\underline{\mathbf{z}}_c^k. \tag{31}$$

Notice that in (30) and (31) the weight matrix $\mathbf{Q}_c$ changes at each iteration. Consequently, the price to be paid for suppressing outliers during the updates of $\widehat{\underline{\mathbf{x}}}_c$ is the need to factorize the matrix $\widetilde{\mathbf{H}}_c$ in (29). Fortunately, the fast plane rotation can be applied efficiently by using square root- and division-free Givens rotations [34]. Finally, the state variables in Cartesian coordinates are updated via

$$\widehat{\underline{\mathbf{x}}}_c^{k+1} = \widehat{\underline{\mathbf{x}}}_c^k + \Delta\widehat{\underline{\mathbf{x}}}_c^k, \tag{32}$$

while the iterations are stopped when

$$\left|\left|\Delta\widehat{\underline{\mathbf{x}}}_c^k\right|\right|_{\infty} \leq tol, \text{e.g.}, 10^{-3}, \tag{33}$$

where $\|\Delta\widehat{\underline{\mathbf{x}}}_c^k\|_{\infty}$ is the infinity norm.

F. The Jacobian Matrix Framework for Hybrid PSSE

Note that in (24), $\mathbf{H}_c(\underline{\mathbf{x}}_c)$ is the Jacobian matrix of dimension $(2\,m \times 2n)$ defined in the complex domain as

$$\mathbf{H}_c(\underline{\mathbf{x}}_c) \triangleq \frac{\partial \underline{h}(\underline{\mathbf{x}}_c)}{\partial \underline{\mathbf{x}}_c} \triangleq \begin{pmatrix} \frac{\partial \underline{\mathbf{h}}(\underline{\mathbf{x}}_c)}{\partial \underline{\mathbf{x}}} & \frac{\partial \underline{h}(\underline{\mathbf{x}}_c)}{\partial \underline{\mathbf{x}}^*} \\ \\ \frac{\partial \underline{h}^*(\underline{\mathbf{x}}_c)}{\partial \underline{\mathbf{x}}} & \frac{\partial \underline{h}^*(\underline{\mathbf{x}}_c)}{\partial \underline{\mathbf{x}}^*} \end{pmatrix}. \tag{34}$$

Let $\mathbf{J_h} = \frac{\partial \underline{h}(\underline{\mathbf{x}}_c)}{\partial}\underline{\mathbf{x}}$ and $\mathbf{J_h^d} = \frac{\partial \underline{h}(\underline{\mathbf{x}}_c)}{\partial \underline{\mathbf{x}}^*}$ be Jacobian submatrices of dimension $(m \times n)$. They are obtained through the Wirtinger partial derivatives with respect to the complex and the complex conjugate state vector, respectively. Thus, the upper part of the Jacobian matrix expressed in (34) can be defined as

$$\mathbf{J}_c(\underline{x}_c) = (\mathbf{J_h}\ \mathbf{J_h^d}). \tag{35}$$

In the important special case given by (12) where $J(\underline{x}_c)$ is a real-valued function of complex variables, the following property holds:

$$J(\underline{\mathbf{x}}_c) \in \mathbb{R} \Rightarrow \frac{\partial \underline{h}^*(\underline{\mathbf{x}}_c)}{\partial \underline{\mathbf{x}}} = \left(\frac{\partial \underline{h}(\underline{\mathbf{x}}_c)}{\partial \underline{\mathbf{x}}^*}\right)^* = \left(\mathbf{J_h^d}\right)^*. \tag{36}$$

Therefore, taking into account the complex differentiability *chain* rule extended to multivariate case and the property stated in (36), (34) becomes

$$\mathbf{H}(\underline{x}_c) = \begin{pmatrix} \mathbf{J_h} & \mathbf{J_h^d} \\ (\mathbf{J_h^d})^* & (\mathbf{J_h})^* \end{pmatrix} = \begin{pmatrix} \mathbf{J}_c(\underline{x}_c) \\ \mathbf{J}_c^*(\underline{x}_c)\,\mathbf{S} \end{pmatrix}, \tag{37}$$

where $\mathbf{S}$ is a *swap operator* defined as

$$\mathbf{S} \triangleq \begin{bmatrix} 0 & I_n \\ I_n & 0 \end{bmatrix}, \tag{38}$$

and I_n is the identity matrix of dimension $n \times n$. Whereas $\mathbf{S}$ permutes blocks of m rows or blocks of n columns depending upon whether it pre-multiples or post-multiples a matrix, respectively. In the other hand, it is timely to recall that the

Authorized licensed use limited to: Centro Universitário Fei. Downloaded on October 31,2024 at 18:04:55 UTC from IEEE Xplore. Restrictions apply.

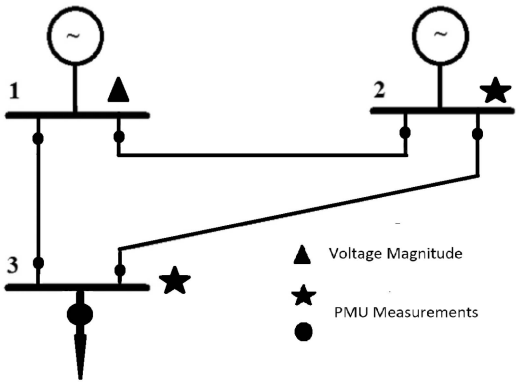


Fig. 4. Hybrid measurement placement.

measurements provided by the SCADA are all real values. Thus, they can be disregarded in the botom part of the Jacobian matrix stated in (37). Consequently, the number of rows in the Jacobian matrix is defined by the number of measurements provided by the SCADA and two times the number of measurements feeded by the synchronized phasors system based on PMU.

III. Numerical Results

This section first presents for a 3-bus system the projections statistics calculation based on the Jacobian matrix developed in the real and complex domain. The main point is the identification of the leverage points based on their PS and the weights assigned to them. Then, the performance of the complex- and real-valued robust SHGM estimators is compared in larger power systems.

The simulations are carried out in MATLAB using sparsity techniques. Numerical results are performed on an Intel(R) Core(TM) i7-10510U CPU @ 1.80 GHz 2.30 GHz, 16 GB RAM and 64-bit operating system. We use the flat start profile to initialize all state variables and the tolerance for the convergence is 10^{-4}. Notice the first iteration is performed using the WLS estimator in order to provide a better starting approximation toward the solution. This strategy avoids the loss of numerical observability due to downweighting of measurements performed by the robust estimator [10].

A. Small Example: 3-Bus System

Consider the 3-bus test system depicted in Fig. 4. Notice that the only measurement provided by the SCADA is the voltage magnitude at Bus #1, which is taken as the reference to calculate the measurement phases. The branch parameters data in *pu*, calculated on the base values of $V_{base} = 230$ kV and $S_{base} = 100$ MVA are provided in Table I while the set of measurements are shown in Table II. In this latter table, the set of measurements identified as true values are provided by the power flow solution while the measured quantities have been determined by adding white Gaussian noises to the true values.

Table III presents the identification of leverage points (LP) based on the Jacobian matrix developed in the real and complex domain, respectively. Three scenarios are considered as follows:

TABLE I
Branches Data

Branch	Serie		Shunt	
$k \rightarrow m$	R	X	Charging	Y/2
	pu	pu	MVAr	pu
1-2	0.0012	0.0021		
1-3	0.0150	0.0400		
2-3	0.3000	1.6000	39.2	0.196

TABLE II
Monitored Quantities in Pu

		True Values		Measured Values	
#	*Id.*	Real	Imaginary	Real	Imaginary
1	$\|V_1\|$	1.0000	-	0.9989	-
2	V_2	1.0000	0.0020	0.9989	0.0020
3	V_3	0.8755	-0.0820	0.8744	-0.0820
4	S_{12}	-0.7185	0.2155	-0.7196	0.2156
5	S_{21}	0.7193	-0.6061	0.7182	-0.6061
6	S_{13}	2.8205	2.0550	2.8195	2.0550
7	S_{31}	-2.6379	-1.5678	-2.6390	-1.5678
8	S_{23}	0.0647	0.0658	0.0636	0.0658
9	S_{32}	-0.0621	-0.0522	-0.0632	-0.0521
10	S_3	-2.7000	-1.6200	-2.7011	-1.6200

- √ **Scenario A**: Only real measurements are considered once they are all provided by the SCADA.
- √ **Scenario B**: All measurements are provided by the PMU except the voltage magnitude at bus #1
  .
- √ **Scenario C**: That is the same as **Scenario B** except the power injections at bus #3 (active and reactive) that are provided by the SCADA.

In most of the scenarios, the set of measurements flagged as leverage points are identical for the real and complex domain. However, in some few scenarios, they may be slightly different. This is expected since the factor-space associated with the Jacobian matrices in the real and complex domain are different. For instance, in Table III all measurements identified as leverage points are highlighted in light orange color whereas those with much larger weights are highlighted in dark orange. Further, we observe that the number of LP in the real domain under **Scenario A** is drastically reduced as compared to the complex domain. In **Scenarios B and C** in the real domain, the active and reactive power injection measurements at Bus #3 are flagged as LPs whereas in the complex domain they are not. On the other hand, the opposite happens with the voltage phasors at Bus #2 and #3 that show up as LPs in the complex domain whereas in the real domain, they are not. Furthermore, the magnitude of the weights assigned to the measurements identified as LPs may have a wide range of values. For instance, compare the magnitudes of the projection statistics and weight for the power flow measurements at the beginning and at the end of the branch that connects Bus #1 to Bus #2 in the **Scenario A** in the real and complex domain.

On the other hand, Table IV shows the estimates provided by the complex-valued robust SHGM estimator. They are those of the last iteration for all scenarios but upon the presence of different bad data (including bad leverage points) which is highlighted

Authorized licensed use limited to: Centro Universitário Fei. Downloaded on October 31,2024 at 18:04:55 UTC from IEEE Xplore. Restrictions apply.

TABLE III
PROJECTION STATISTICS DEVELOPED WITH ARITHMETICS OF REAL AND COMPLEX NUMBERS

Real Numbers

Scenario A: 100% **SCADA**				**Scenario B:** 90% **PMU**				**Scenario C: Hybrid**			
Id.	σ_i^2	**PS**	ω_i	**Id.**	σ_i^2	**PS**	ω_i	**Id.**	σ_i^2	**PS**	ω_i
$\lvert V_1\rvert$	10^{-6}	0.1161	1.0000	$\lvert V_1\rvert$	10^{-6}	0.0517	1.0000	$\lvert V_1\rvert$	10^{-6}	0.1161	1.0000
$\lvert V_2\rvert$	10^{-6}	0.8385	1.0000	V_2	10^{-8}	0.8385	1.0000	V_2	10^{-8}	0.8385	1.0000
$\lvert V_3\rvert$	10^{-6}	0.8385	1.0000	V_3	10^{-8}	0.8385	1.0000	V_3	10^{-8}	0.8385	1.0000
t_{12}	10^{-4}	172.0008	2.9540×10^{-3}								
u_{12}	10^{-4}	301.0015	9.6458×10^{-4}	S_{12}	10^{-4}	346.6788	7.2714×10^{-4}	S_{12}	10^{-4}	346.6788	7.2714×10^{-4}
t_{13}	10^{-4}	6.8918	1.0000								
u_{13}	10^{-4}	18.3782	0.2587	S_{13}	10^{-4}	19.6279	0.2268	S_{13}	10^{-4}	19.6279	0.2268
t_{21}	10^{-4}	172.0008	2.9540×10^{-3}								
u_{21}	10^{-4}	300.6728	9.6669×10^{-4}	S_{21}	10^{-4}	346.5361	7.2774×10^{-4}	S_{21}	10^{-4}	346.5361	7.2774×10^{-4}
t_{23}	10^{-4}	0.1956	1.0000								
u_{23}	10^{-4}	0.5063	1.0000	S_{23}	10^{-4}	0.8385	1.0000	S_{23}	10^{-4}	0.8385	1.0000
t_{31}	10^{-4}	6.8918	1.0000								
u_{31}	10^{-4}	18.3782	0.2587	S_{31}	10^{-4}	19.6279	0.2268	S_{31}	10^{-4}	19.6279	0.2268
t_{32}	10^{-4}	0.1956	1.0000								
u_{32}	10^{-4}	0.5063	1.0000	S_{32}	10^{-4}	0.8385	1.0000	S_{32}	10^{-4}	0.8385	1.0000
P_3	10^{-4}	6.9867	1.0000					P_3	10^{-4}	14.2379	0.8123
Q_3	10^{-4}	18.8844	0.4618	S_3	10^{-4}	20.1355	0.4062	Q_3	10^{-4}	14.2379	0.8123

Complex Numbers

Scenario A: 100% **SCADA**				**Scenario B:** 90% **PMU**				**Scenario C: Hybrid**			
Id.	σ_i^2	**PS**	ω_i	**Id.**	σ_i^2	**PS**	ω_i	**Id.**	σ_i^2	**PS**	ω_i
$\lvert V_1\rvert$	10^{-6}	0.8385	1.0000	$\lvert V_1\rvert$	10^{-6}	0.5672	1.0000	$\lvert V_1\rvert$	10^{-6}	0.8385	1.0000
$\lvert V_2\rvert$	10^{-6}	2.5048	1.0000	V_2	10^{-8}	54.5994	3.3866×10^{-2}	V_2	10^{-8}	54.5994	3.3866×10^{-2}
$\lvert V_3\rvert$	10^{-6}	2.5048	1.0000	V_3	10^{-8}	54.5994	3.3866×10^{-2}	V_3	10^{-8}	54.5994	3.3866×10^{-2}
t_{12}	10^{-4}	17.2001	1.0000								
u_{12}	10^{-4}	30.0673	0.5494	S_{12}	10^{-4}	282.1761	4.3903×10^{-3}	S_{12}	10^{-4}	282.1761	4.3903×10^{-3}
t_{13}	10^{-4}	0.8385	1.0000								
u_{13}	10^{-4}	1.8378	1.0000	S_{13}	10^{-4}	15.9760	0.8531	S_{13}	10^{-4}	15.9760	0.8531
t_{21}	10^{-4}	17.2001	1.0000								
u_{21}	10^{-4}	30.1001	0.5482	S_{21}	10^{-4}	282.0599	4.3939×10^{-3}	S_{21}	10^{-4}	282.0599	4.3939×10^{-3}
t_{23}	10^{-4}	0.0435	1.0000								
u_{23}	10^{-4}	0.0435	1.0000	S_{23}	10^{-4}	0.8385	1.0000	S_{23}	10^{-4}	0.8385	1.0000
t_{31}	10^{-4}	0.8385	1.0000								
u_{31}	10^{-4}	1.8378	1.0000	S_{31}	10^{-4}	15.9760	0.8531	S_{31}	10^{-4}	15.9760	0.8531
t_{32}	10^{-4}	0.0435	1.0000								
u_{32}	10^{-4}	0.0435	1.0000	S_{32}	10^{-4}	0.8385	1.0000	S_{32}	10^{-4}	0.8385	1.0000
P_3	10^{-4}	0.8603	1.0000					P_3	10^{-4}	9.5049	1.0000
Q_3	10^{-4}	1.8378	1.0000	S_3	10^{-4}	16.8025	1.0000	Q_3	10^{-4}	9.5049	1.0000

PS - Projection Statistics

in red color. This estimator provides good estimates in all cases by suppressing all the outliers, including bad leverage points.

B. Real- and Complex-Valued Robust Estimators

Before we carry out the simulations, we first ensure that there are no critical measurements or critical pairs in the measurement set of the power system under study. Recall that a critical measurement is one whose removal leads to the loss of observability of the system; a critical pair is a set of measurements for which the deletion of one of them leads to the appearance of at least one critical measurement in the remaining set. Then, to set up the number of measurements that contribute to each estimated state variable, we use an algorithm based on the Crainic's proposal [35] and on the local maximum fraction of measurement contaminated with gross errors. The latter is the number of bad data allowed in the local set of measurements used to estimate each state variable in order to avoid the local breakdown of the state estimator [36]. Note that this problem is beyond the scope of this work and will be addressed in a forthcoming paper.

Table V indicates the number of leverage points identified in the real and complex domain for large-scale test systems. As for Tables VI and VII, they provide the performance comparison between the real- and complex-valued IRLS algorithms. In the first table the estimates are obtained in the absence of *oltc* tap position modeled as state variable, i.e., all off-nominal tap transformers are taken as parameters. Regarding Table VII, all off-nominal tap transformers are taken as *oltc* so they are state variables. Such results refer to the mean among 100 simulations, adding white noise with Gaussian distribution with zero mean and covariance as depicted in Table III. The performances of the algorithms are compared on the IEEE-14, -30, -57 and -118 bus system along with the equivalents of the Brazilian system termed as SIN-340, -730 and -1916 bus system.

The algebric/topological observability of the power test systems is ensured via an adaptation of the methodology stated in [35]. Thus, we ensure the absence of critical measurements and critical sets of measurements. Furthermore, in all scenarios a good local redundancy [36] is ensured aiming to better estimate

Authorized licensed use limited to: Centro Universitário Fei. Downloaded on October 31,2024 at 18:04:55 UTC from IEEE Xplore. Restrictions apply.

TABLE IV
PERFORMANCE OF THE ROBUST COMPLEX-VALUED SHGM ESTIMATOR

Scenario A.1: 100% SCADA - 5 iterations				Scenario A.2: 100% SCADA - 6 iterations			
Id.	z_i	$\widehat{z}_i$	$q(rs_i)$	**Id.**	z_i	$\widehat{z}_i$	$q(rs_i)$
$\|V_1\|$	1.0000	1.0000	1.0000	$\|V_1\|$	1.0000	1.0000	1.0000
$\|V_2\|$	1.0000	1.0000	1.0000	$\|V_2\|$	1.0000	1.0000	1.0000
$\|V_3\|$	0.8793	0.8793	1.0000	$\|V_3\|$	0.8793	0.8793	1.0000
t_{12}	-0.7185	-0.7185	1.0000	t_{12}	-0.7185	-0.7185	1.0000
u_{12}	0.2155	0.2143	0.16565	u_{12}	-0.2155	0.2155	1.5662×10^{-2}
t_{13}	2.8205	2.8206	1.0000	t_{13}	2.8205	2.8206	1.0000
u_{13}	2.0550	2.0550	1.0000	u_{13}	2.0550	2.0550	1.0000
t_{21}	0.7193	0.7193	1.0000	t_{21}	0.7193	0.7193	1.0000
u_{21}	0.6061	-0.6056	6.1670×10^{-3}	u_{21}	-0.6061	-0.5998	0.1286
t_{23}	0.0647	0.0647	1.0000	t_{23}	0.0647	0.0647	1.0000
u_{23}	0.0658	0.0658	1.0000	u_{23}	0.0658	0.0658	1.0000
t_{31}	-2.6379	-2.6379	1.0000	t_{31}	-2.6379	-2.6379	1.0000
u_{31}	-1.5678	-1.5678	1.0000	u_{31}	-1.5678	-1.5678	1.0000
t_{32}	-0.0621	-0.0621	1.0000	t_{32}	-0.0621	-0.0621	1.0000
u_{32}	-0.0522	-0.0522	1.0000	u_{32}	-0.0522	-0.0522	1.0000
P_3	-2.7000	-2.7000	1.0000	P_3	-2.7000	-2.7000	1.0000
Q_3	-1.6200	-1.6200	1.0000	Q_3	-1.6200	-1.6200	1.0000
Scenario B.1: 90% PMU - 10 iterations				Scenario B.2: 90% PMU - 4 iterations			
Id.	z_i	$\widehat{z}_i$	$q(rs_i)$	**Id.**	z_i	$\widehat{z}_i$	$q(rs_i)$
$\|V_1\|$	1.0000	1.0000	1.0000	$\|V_1\|$	1.0000	1.0000	1.0000
V_2	1.0000+0.0020i	1.0000+0.0020i	3.9944×10^{-1}	V_2	1.0000+0.0020i	1.0000+0.0020i	0.2193
V_3	-0.8755+0.0820i	0.8755-0.0820i	3.6629×10^{-6}	V_3	0.8755-0.0820i	0.8755-0.0820i	0.1701
S_{12}	-0.7185+0.2155i	-0.7183+0.2152i	9.6328×10^{-3}	S_{12}	-0.7185+0.2155i	-0.7213+0.2098i	5.3468×10^{-3}
S_{13}	2.8205+2.0550i	2.8205+2.0550i	1.0000	S_{13}	2.8205+2.0550i	2.8205+2.0550i	1.0000
S_{21}	0.7193-0.6061i	0.7191-0.6058i	9.6032×10^{-3}	S_{21}	0.7193-0.6061i	0.7222-0.6003i	5.3527×10^{-3}
S_{23}	0.0647+0.0658i	0.0647+0.0658i	1.0000	S_{23}	0.0647+0.0658i	0.0647+0.0658i	1.0000
S_{31}	-2.6379-1.5678i	-2.6379-1.5678i	1.0000	S_{31}	-2.6379-1.5678i	-2.6379-1.5678i	1.0000
S_{32}	-0.0621-0.0522i	-0.0621-0.0522i	1.0000	S_{32}	-0.0621-0.0522i	-0.0621-0.0522i	1.0000
S_3	-2.7000-1.6200i	-2.7000-1.6200i	1.0000	S_3	2.7000+1.6200i	-2.7000-1.6200i	2.4165×10^{-3}
Scenario C.1: Hybrid - 4 iterations				Scenario C.2: Hybrid - 11 iterations			
Id.	z_i	$\widehat{z}_i$	$q(rs_i)$	**Id.**	z_i	$\widehat{z}_i$	$q(rs_i)$
$\|V_1\|$	1.0000	1.0000	1.0000	$\|V_1\|$	1.0000	1.0000	1.0000
V_2	1.0000+0.0020i	1.0000+0.0020i	1.0000	V_2	1.0000+0.0020i	1.0000+0.0020i	1.0000
V_3	0.8755-0.0820i	0.8755-0.0820i	0.2617	V_3	-0.8755+0.0820i	0.8755-0.0820i	3.6629×10^{-6}
S_{12}	0.7185-0.2155i	-0.7220+0.2087i	4.4577×10^{-5}	S_{12}	-0.7185-0.2155i	-0.7185+0.2155i	1.5535×10^{-4}
S_{13}	2.8205+2.0550i	2.8205+2.0550i	1.0000	S_{13}	2.8205+2.0550i	2.8205+2.0550i	1.0000
S_{21}	-0.7193+0.6061i	0.7228-0.5992i	3.5574×10^{-5}	S_{21}	-0.7193-0.6061i	0.7192-0.6057i	4.6479×10^{-5}
S_{23}	0.0647+0.0658i	0.0647+0.0658i	1.0000	S_{23}	0.0647+0.0658i	0.0647+0.0658i	1.0000
S_{31}	-2.6379-1.5678i	-2.6379-1.5678i	1.0000	S_{31}	-2.6379-1.5678i	-2.6379-1.5678i	1.0000
S_{32}	-0.0621-0.0522i	-0.0621-0.0522i	1.0000	S_{32}	-0.0621-0.0522i	-0.0621-0.0522i	1.0000
P_3	-2.7000	-2.7000	1.0000	P_3	-2.7000	-2.7000	1.0000
Q_3	1.6200	-1.6200	4.1513×10^{-3}	Q_3	-1.6200	-1.6200	1.0000

z_i - measured quantity / $\widehat{z}_i$ - estimated quantity

the tap position of the OLTC transformers. For instance, in Tables VI and VII phasor voltage measurements are used to increase the local redundancy of the transformer branches for the SIN 340- and SIN-1916-bus system.

Notice that the last two columns of the referred tables are included to present the efficiency indicators of the estimates of the state variables and the transformer tap position, which are given by

$$\sigma_u^2 = \sum_{i=1}^{n} \left(\hat{u}_i - u_i\right)^2, \tag{39}$$

$$\sigma_{tap}^2 = \sum_{j=1}^{k} \left(\hat{tap}_j - tap_j\right)^2, \tag{40}$$

where $\hat{u}$ and $\hat{tap}$ represent the estimated quantities of the actual values of u and tap, respectively.

The complex-valued robust estimator outperforms its real-valued counterpart. Furthermore, its performance becomes even greater as the size of the system increases as observed in Figs. 5 and 6. Interestingly, the computational efficiency of both estimation algorithms is quite similar.

IV. CONCLUSION

In this work a robust complex-valued SHGM estimator which handles SCADA and PMU measurements properly is developed. For doing that, a suited nonlinear model for measures in complex domain is presented. The calculated projection statistics and

Authorized licensed use limited to: Centro Universitário Fei. Downloaded on October 31,2024 at 18:04:55 UTC from IEEE Xplore. Restrictions apply.

TABLE V
NUMBER OF LEVERAGE POINTS IN LARGER TEST SYSTEMS

Number of	**Real Numbers**					
bus / (iterations)	IEEE-14 / (6)	IEEE-30 / (8)	IEEE-118 / (32)	SIN-340 / (17)	SIN-730 / (34)	SIN-1916 / (60)
Generator bus	5	6	34	53	104	163
Load bus	9	24	84	287	626	1753
branches	22	41	179	550	1078	2766
real state variables (n)	30	63	244	761	1693	4480
OLTC as real state variables	3	4	9	82	234	649
voltage magnitude(V_i)	7	8	21	143	389	994
active power flow(t_{ij})	16	27	111	295	901	1692
reactive power flow(u_{ij})	16	27	111	295	901	1692
active power injection (p_i)	11	23	86	275	641	1699
reactive power injection (q_i)	11	23	86	275	641	1699
real measurements (m)	61	108	415	1283	3474	7776
real leverage points (lp)	**7**	**12**	**54**	**430**	**1371**	**2421**
real global redundancy: $\rho = \frac{m}{n}$	2.03	1.71	1.70	1.70	2.05	1.74
$J(\widehat{x})\ =$	$3.1409 \times 10^{+1}$	$4.0182 \times 10^{+1}$	$1.0450 \times 10^{+2}$	$1.0387 \times 10^{+3}$	$1.7769 \times 10^{+3}$	$2.7438 \times 10^{+3}$
Number of	**Complex Numbers**					
bus / (iterations)	IEEE-14 / (4)	IEEE-30 / (4)	IEEE-118 / (4)	SIN-340 / (8)	SIN-730 / (6)	SIN-1916 / (10)
complex state variables (n)	17	34	127	422	964	2565
OLTC as complex state variables	3	4	9	82	234	649
phasor voltage (V_i)	7	9	21	143	387	992
complex power flow(S_{ij})	16	29	96	266	880	2004
complex power injection (S_{ij})	10	25	91	281	648	1813
complex measurements (m)	33	63	208	690	1915	4809
complex leverage points (lp)	**4**	**6**	**56**	**474**	**1394**	**2320**
complex global redundancy: $\rho = \frac{m}{n}$	1.94	1.85	1.63	1.63	1.98	1.87
$J(\widehat{x})\ =$	8.4674×10^{-2}	4.3768×10^{-1}	1.1585×10^{-3}	$6.9469 \times 10^{+2}$	$1.2891 \times 10^{+3}$	$1.0702 \times 10^{+3}$

TABLE VI
PERFORMANCE OF ROBUST ESTIMATORS IN BOTH DOMAINS - FIXED TAP

System	Measures		Iterations		Time (s)		Ratio	σ_u^2	
	SCADA	PMU	$\mathbb{R}$	$\mathbb{C}$	$\mathbb{R}$	$\mathbb{C}$	$\mathbb{R}/\mathbb{C}$	$\mathbb{R}$	$\mathbb{C}$
	68	0	4	4	0.0116	0.0121	0.96	4.40E-05	4.45E-05
14	34	19	4	4	0.0131	0.0114	1.14	2.33E-05	2.57E-05
	0	38	3	3	0.0087	0.0082	1.06	1.05E-05	1.47E-05
	136	0	4	4	0.0130	0.0141	0.92	2.10E-04	2.10E-04
30	63	39	4	4	0.0173	0.0140	1.24	9.63E-05	1.02E-04
	0	73	4	3	0.0144	0.0104	1.39	5.40E-05	6.21E-05
	273	0	3	4	0.0153	0.0175	0.88	4.48E-04	4.52E-04
57	141	73	4	4	0.0263	0.0214	1.23	1.43E-04	1.50E-04
	0	151	4	3	0.0209	0.0129	1.62	9.23E-05	6.28E-05
	419	0	4	4	0.0266	0.0237	1.12	4.53E-04	4.54E-04
118	213	108	4	4	0.0374	0.0285	1.31	3.09E-04	3.33E-04
	0	220	4	4	0.0304	0.0227	1.34	1.49E-04	1.54E-04
	1423	0	6	6	0.1434	0.1061	1.35	4.22E-04	4.02E-04
340	722	386	6	7	0.1524	0.1100	1.39	2.75E-04	2.79E-04
	0	783	6	6	0.1332	0.0919	1.45	1.21E-04	1.23E-04
	9171	0	6	6	0.4669	0.3441	1.36	1.49E-02	1.38E-02
1916	4577	2545	6	6	0.6872	0.4758	1.44	4.47E-03	4.54E-03
	0	5082	7	6	0.5841	0.2934	1.99	1.83E-03	1.91E-03

leverage points identification in complex domain is slightly different when compared with their counterpart in the real domain. Even though, the simulations results show that this estimator successfully identifies the bad leverage points regardless the magnitude of the corresponding weights are quite different from those produced by its real-valued counterpart. Furthermore, it outperforms its real-valued counterpart, with an increasing performance as the size of the monitored power system increases. For future investigations, recall that the complex-valued SHGM power system state estimator is naturally formulated in rectangular coordinates. This feature allows us to solve the set of redundant equations as a set of quadratic algebraic equations. This means that the exact nonlinearity of the complex-valued SHGM state estimator equations is retained, i.e., the Taylor series expansion as outlined by Iwamoto & Tamura [37] is exact. Not approximated as in the Newton-Raphson method in power flow analysis (PFA) and in the Gauss-Newton method in power system state estimation. Therefore, one addressed efforts for developing the EXACT complex-valued SHGM estimator so like that developed to produce the enhanced power flow solution

Authorized licensed use limited to: Centro Universitário Fei. Downloaded on October 31,2024 at 18:04:55 UTC from IEEE Xplore. Restrictions apply.

TABLE VII
PERFORMANCE OF ROBUST ESTIMATORS IN BOTH DOMAINS - OLTC

System	Measures		Taps	Iterations		Time (s)		Ratio	σ_u^2		σ_{tap}^2	
	SCADA	PMU		$\mathbb{R}$	$\mathbb{C}$	$\mathbb{R}$	$\mathbb{C}$	$\mathbb{R}/\mathbb{C}$	$\mathbb{R}$	$\mathbb{C}$	$\mathbb{R}$	$\mathbb{C}$
14	68	0	3	4	4	0.0144	0.0157	0.91	4.60E-05	6.07E-05	1.84E-05	3.75E-05
	34	19		4	4	0.0142	0.0120	1.18	2.04E-05	2.27E-05	1.15E-05	1.68E-05
	0	38		4	3	0.0130	0.0105	1.24	1.27E-05	1.51E-05	1.63E-05	2.35E-05
30	136	0	4	4	4	0.0147	0.0149	0.98	2.13E-04	2.66E-04	2.63E-05	6.33E-05
	63	39		4	4	0.0182	0.0157	1.16	9.66E-05	9.86E-05	1.51E-05	2.04E-05
	0	73		4	4	0.0170	0.0136	1.25	5.30E-05	5.97E-05	2.03E-05	2.83E-05
57	273	0	15	3	5	0.0160	0.0196	0.82	4.50E-04	7.67E-04	2.52E-04	5.90E-04
	141	73		4	5	0.0285	0.0274	1.04	1.22E-04	1.68E-04	2.26E-04	4.07E-04
	0	151		5	5	0.0263	0.0221	1.19	6.24E-05	6.73E-05	1.51E-04	2.21E-04
118	419	0	9	4	4	0.0261	0.0240	1.09	5.46E-04	1.57E-03	1.46E-05	7.86E-05
	213	108		4	4	0.0369	0.0276	1.34	4.36E-04	4.75E-04	2.20E-05	4.75E-05
	0	220		4	4	0.0290	0.0239	1.21	5.42E-04	5.52E-04	2.25E-05	3.03E-05
340	1281	142	82	9	7	0.2228	0.1223	1.82	5.74E-04	5.75E-04	8.35E-04	2.26E-04
	649	458		9	6	0.1920	0.0990	1.94	5.14E-04	5.27E-04	5.30E-04	5.04E-04
	0	783		9	7	0.1979	0.1235	1.60	5.11E-04	4.43E-04	4.74E-04	4.51E-04
1916	8180	991	649	14	7	1.6514	0.6755	2.44	5.84E-03	5.26E-03	8.36E-03	6.01E-03
	4095	3034		14	9	2.0119	1.0502	1.92	4.83E-03	4.29E-03	8.89E-03	6.18E-03
	0	5082		15	11	1.8360	0.8946	2.05	3.45E-03	3.36E-03	8.09E-03	6.05E-03

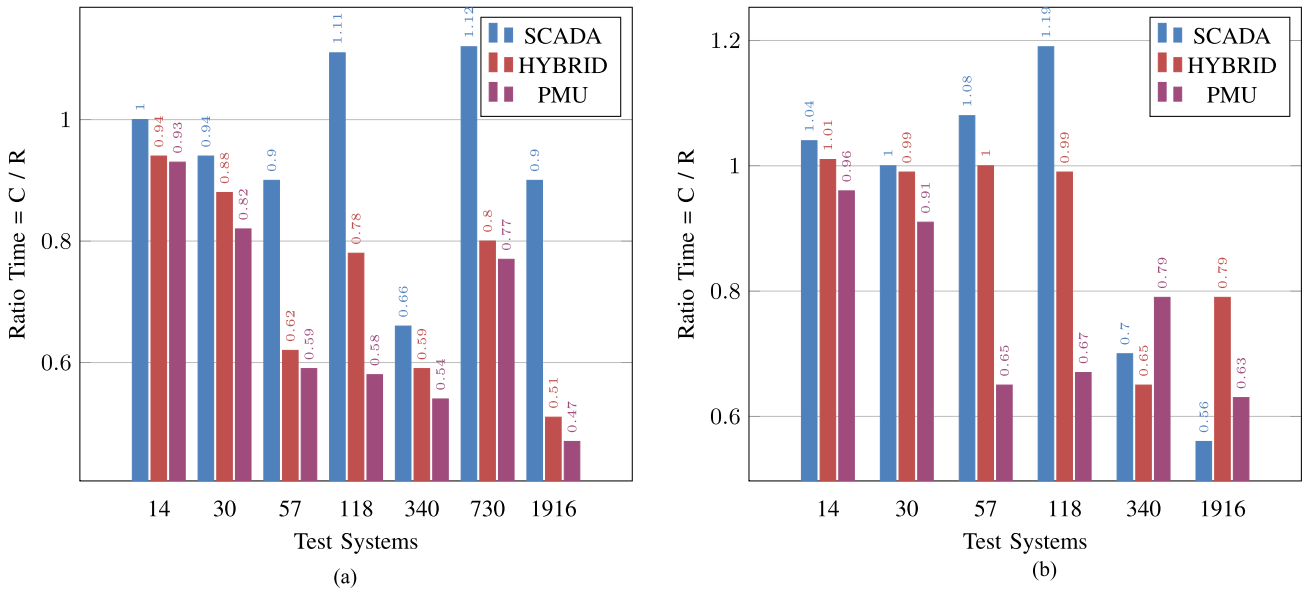


Fig. 5. (a) Ratio between the computational times of the ordinary WLS estimator formulated in the complex and real numbers - Fixed Tap. Fig. 5 (b) Ratio between the computational times of the ordinary WLS estimator formulated in the complex and real domain - OLTC.

in complex plane [38]. We also advocate the effort to build a complex-valued power system state estimation framework as the most suited tool to monitoring explicitly hybrid AC-DC systems that include a variety of FACTS devices x aimed at active smart grids [39].

APPENDIX
COMPLEX-VALUED MODELS OF SCADA/PMU MEASUREMENTS

1. *Reference Phase Angle as Pseudo Measurement:* Regardless the monitoring system, a reference angle is needed when the PSSE is developed in Cartesian coordinates. Hence, zeroing the imaginary part of the corresponding state variable, leads to

$$h_i(x_c) = \frac{i}{2}\left(x_i^\star - x_i\right) = 0, \tag{41}$$

where $x_c = (x_i, x_i^*)$, and the jacobian terms are

$$\left.\frac{\partial h_i}{\partial x_i}\right|_{x_i^\star = Const} = -0.5\,i, \tag{42}$$

$$\left.\frac{\partial h_i}{\partial x_i^\star}\right|_{x_i = Const} = +0.5\,i. \tag{43}$$

Notice the foregoing procedure can be adopted to model ordinary transformer with OLTC.

Authorized licensed use limited to: Centro Universitário Fei. Downloaded on October 31,2024 at 18:04:55 UTC from IEEE Xplore. Restrictions apply.

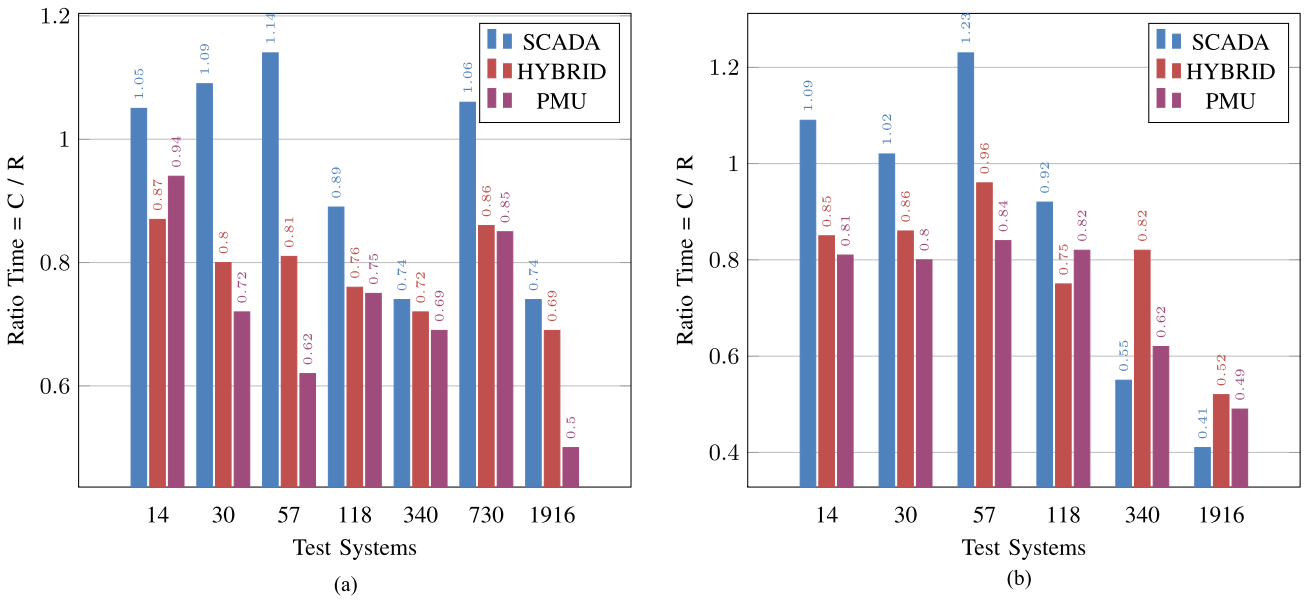


Fig. 6. (a) Ratio between the computational times of the robust SHGM estimator formulated in the complex and real numbers - Fixed Tap. (b) Ratio between the computational times of the robust SHGM estimator formulated in the complex and real domain - OLTC.

2. *Measurement of voltage or current magnitude:*

$$|h_i(x_c)| = \sqrt{x_i^\star\, x_i}. \tag{44}$$

Thus, the following entries are included in the Jacobian matrix

$$\left.\frac{\partial |h_i(x_c)|}{\partial x_i}\right|_{x_i^\star = Const} = 0.5\,\frac{x_i^\star}{\sqrt{x_i^\star\, x_i}}, \tag{45}$$

$$\left.\frac{\partial |h_i(x_c)|}{\partial x_i^\star}\right|_{x_i = Const} = 0.5\frac{x_i}{\sqrt{x_i^\star\, x_i}}. \tag{46}$$

3. *Active and Reactive Power flow Measurements:*

$$P_{km} = \frac{1}{2}\left(S_{km} + S_{km}^\star\right), \tag{47}$$

$$Q_{km} = \frac{i}{2}\left(S_{km}^\star - S_{km}\right). \tag{48}$$

Thereby, the corresponding derivatives regarding any state variable ($\bullet$) are given by

$$\frac{\partial P_{km}}{\partial \bullet} = \frac{1}{2}\left(\frac{\partial S_{km}}{\partial \bullet} + \frac{\partial S_{km}^\star}{\partial \bullet}\right), \tag{49}$$

$$\frac{\partial Q_{km}}{\partial \bullet} = \frac{i}{2}\left(\frac{\partial S_{km}^\star}{\partial \bullet} - \frac{\partial S_{km}}{\partial \bullet}\right). \tag{50}$$

4. *Active and Reactive Power Injection Measurements:*

$$S_k = S_{sh_k} + \sum_{m=1, m\neq k}^{n} S_{km} \tag{51}$$

where S_k^{sh} is

$$S_{sh_k} = i\, V_k\, V_k^\star\, B_{sh_k}. \tag{52}$$

Thereby, the Wirtinger calculus applied to the foregoing equation leads to

$$\frac{\partial S_k}{\partial \bullet} = \frac{\partial S_{sh_k}}{\partial \bullet} + \sum_{m=1, m\neq k}^{n} \frac{\partial S_{km}}{\partial \bullet}, \tag{53}$$

$$\frac{\partial Sk^\star}{\partial \bullet} = \frac{\partial (S_{sh_k})^\star}{\partial \bullet} + \sum_{m=1, m\neq k}^{n} \frac{\partial S_{km}^\star}{\partial \bullet}. \tag{54}$$

Now, the active and reactive power injections become known by using the following recursive equations, respectively.

$$P_k = \frac{1}{2}\left(S_k + S_k^\star\right), \tag{55}$$

$$Q_k = \frac{i}{2}\left(S_k^\star - S_k\right). \tag{56}$$

REFERENCES

[1] J. P. Schreier and L. L. Scharf, *Statistical Signal Processing of Complex-Valued Data: The Theory of Improper and Noncircular Signals.*, Cambridge, U.K.: Cambridge University Press, 2010.
[2] C. P. Steinmetz, "Complex quantities and their use in electrical engineering," in *Proc. Int. Elect. Congr.*, 1893, pp. 33–74.
[3] K. Kreutz-Delgado, "The complex gradient operator and the CR-calculus," 2009, *ArXIV e-print, arXIV:0906.4835v1 [math.OC]*.
[4] Q. Zhang, Y. Chakhchoukh, V. Vittal, G. T. Heydt, N. Logic, and S. Sturgill, "Impact of PMU measurement buffer length on state estimation and its optimization," *IEEE Trans. Power Syst.*, vol. 28, no. 2, pp. 1657–1665, May 2013.
[5] J. Zhao et al., "Power system real-time monitoring by using PMU-based robust state estimation method," *IEEE Trans. Smart Grid*, vol. 7, no. 1, pp. 300–309, Jan. 2016.
[6] P. Yang, Z. Tan, A. Wiesel, and A. Nehorai, "Power system state estimation using PMUs with imperfect synchronization," *IEEE Trans. Power Syst.*, vol. 28, no. 4, pp. 4162–4172, Nov. 2013.

Authorized licensed use limited to: Centro Universitário Fei. Downloaded on October 31,2024 at 18:04:55 UTC from IEEE Xplore. Restrictions apply.

[7] R. Pires, "Complex-valued steady-state models as applied to power flow analysis and power system state estimation," Ph.D. dissertation, Inst. Electr. Syst. Energy - ISEE Federal Univ. Itajubá, Itajubá, Brazil, Feb. 2018. [Online]. Available: https://repositorio.unifei.edu.br/xmlui/handle/123456789/5
[8] I. Džafić, A. R. Jabr, and T. Hrnjić, "Hybrid state estimation in complex variables," *IEEE Trans. Power Syst.*, vol. 33, no. 5, pp. 5288–5296, Sep. 2018.
[9] I. Džafić and R. A. Jabr, "Real-time equality-constrained hybrid state estimation in complex variables," *Int. J. Elect. Power Energy Syst.*, vol. 117, 2020, Art. no. 105634.
[10] R. C. Pires, L. Mili, and F. A. B. Lemos, "Constrained robust estimation of power system state variables and transformer tap positions under erroneous zero-injections," *IEEE Trans. Power Syst.*, vol. 29, no. 3, pp. 1144–1152, May 2014.
[11] I. Džafić, A. R. Jabr, and T. Hrnjić, "Complex variable multi-phase distribution system state estimation using vectorized code," *J. Modern Power Syst. Clean Energy*, vol. 8, no. 4, pp. 679–688, 2020.
[12] L. Mili, M. G. Cheniae, N. S. Vichare, and P. J. Rousseeuw, "Robust state estimation based on projection statistics," *IEEE Trans. Power Syst.*, vol. 11, no. 2, pp. 1118–1127, May 1996.
[13] Y. Chen, F. Liu, S. Mei, and J. Ma, "A robust WLAV state estimation using optimal transformations," *IEEE Trans. Power Syst.*, vol. 30, no. 4, pp. 2190–2191, Jul. 2015.
[14] J. Zhao, L. Mili, and R. Pires, "Statistical and numerical robust state estimator for heavily loaded power systems," *IEEE Trans. Power Syst.*, vol. 33, no. 6, pp. 6904–6914, Nov. 2018.
[15] J. Zhao, L. Mili, and M. L. Scala, "A robust hybrid power system state estimator with unknown measurement noise," in *Advances in Electric Power and Energy: Static State Estimation.* Hoboken, NJ, USA: Wiley, 2020, ch. 8, pp. 231–253.
[16] A. E. Beaton and J. W. Tukey, "The fitting of power series, meaning polynomials, illustrated on band-spectroscopic data," *Technometrics*, vol. 16, no. 2, pp. 147–185, 1974.
[17] P. W. Holland and R. E. Welsch, "Robust regression using iteratively reweighted least-squares," *Commun. Statist.*, vol. A 6, no. 9, pp. 813–827, 1977.
[18] Y. Zhang and N. Ansari, "Green data centers," in *Handbook of Green Information and Communication Systems*, Mohammad S. Obaidat, A. Anpalagan, and I. Woungang, Eds. Cambridge, MA, USA: Academic Press, 2013, ch. 12, pp. 331–352.
[19] B. Picinbono and P. Chevalier, "Widely linear estimation with complex data," *IEEE Trans. Signal Process.*, vol. 43, no. 8, pp. 2030–2033, Aug. 1995.
[20] V. Su and L. G. D. P. Mandic, "Augmented complex statistics," *Complex Valued Nonlinear Adaptive Filters*, pp. 151–168, 2009.
[21] T. Adali, P. J. Schreier, and L. L. Scharf, "Complex-valued signal processing: The proper way to deal with impropriety," *IEEE Trans. Signal Process.*, vol. 59, no. 11, pp. 5101–5125, Nov. 2011.
[22] B. Picinbono, "On circularity," *IEEE Trans. Signal Process.*, vol. 42, no. 12, pp. 3473–3482, Dec. 1994.
[23] B. Picinbono, "Second-order complex random vectors and normal distributions," *IEEE Trans. Signal Process.*, vol. 44, no. 10, pp. 2637–2640, Oct. 1996.
[24] P. J. Schreier and L. L. Scharf, "Second-order analysis of improper complex random vectors and processes," *IEEE Trans. Signal Process.*, vol. 51, no. 3, pp. 714–725, Mar. 2003.
[25] D. P. Mandic and S. L. Goh, *Complex Valued Nonlinear Adaptive Filters: Noncircularity, Widely Linear and Neural Models*. Hoboken, NJ, USA: Wiley, 2009.
[26] D. Looney and D. P. Mandic, "Augmented complex matrix factorisation," in *Proc. IEEE Int. Conf. Acoust. Speech Signal Process.*, 2011, pp. 4072–4075.
[27] D. Kalke and G. Gurrala, "IEC/IEEE 60255-118-1-2018 compliance testing of SRF, SOGI and park PLLS for synchrophasors," in *Proc. Int. Conf. Elect. Comput. Energy Technol.*, 2022, pp. 1–6.
[28] A. Bos and V. Den, "The multivariate complex normal distribution - A generalization," *IEEE Trans. Inf. Theory*, vol. 41, no. 2, pp. 537–539, Mar. 1995.
[29] T. Adalý and P. J. Schreier, "Optimization and estimation of complex-valued signals," *IEEE Signal Process. Mag.*, vol. 31, no. 5, pp. 112–128, Sep. 2014.
[30] T. Adalý and S. Haykin, *Adaptive Signal Processing: Next-Generation Solutions.* Hoboken, NJ, USA: Wiley, 2010.
[31] J. P. Schreier and L. L. Scharf, *Statistical Signal Processing of Complex-Valued Data - the Theory of Improper and Noncircular Signals.*, Cambridge, U.K.: Cambridge University Press, 2010.
[32] C. Hughes, "Single-instruction multiple-data execution," *Synth. Lectures Comput. Archit.*, vol. 10, pp. 1–121, 2015.
[33] P. J. Rousseeuw and A. M. Leroy, *Robust Regression and Outlier Detection.*, Hoboken, NJ, USA: Wiley, 1987.
[34] A. Awasthi, R. Guttal, N. Al-Dhahir, and P. T. Balsara, "Complex QR decomposition using fast plane rotations for MIMO applications," *IEEE Commun. Lett.*, vol. 18, no. 10, pp. 1743–1746, Oct. 2014.
[35] E. D. Crainic, X. D. Do, P. J. Lagacé, and D. Mukhedkar, "Power system observability: On-line measurement set contingency analysis," in *Proc. IFAC Symp. Power Syst. Modelling Control Appl.*, 1988, vol. 21, pp. 491–499.
[36] L. Mili, V. Phaniraj, and P. J. Rousseeuw, "High breakdown point estimation in electric power systems," in *Proc. IEEE Int. Symp. Circuits Syst.*, 1990, vol. 3, pp. 1843–1846.
[37] S. Iwamoto and Y. Tamura, "A fast load flow method retaining nonlinearity," *IEEE Trans. Power App. Syst.*, vol. PAS-97, no. 5, pp. 1586–1599, Sep. 1978.
[38] R. Pires, G. Chagas, and L. Mili, "Enhanced power flow solution in complex plane," *Int. J. Elect. Power Energy Syst.*, vol. 135, 2022, Art. no. 107501.
[39] G. Chagas and R. Pires, "The sequential power flow in complex plane for solving the VSC-MTDC hybrid AC/DC transmission grids," *Int. J. Elect. Power Energy Syst.*, vol. 148, 2023, Art. no. 108900.



Eduardo M. Resende (Graduate Student Member, IEEE) received the B.Sc. degree in electrical engineering in 2020, and the M.Sc. degree in electrical engineering from Federal University of Itajubá (UNIFEI) - MG, Brazil, in 2021. Since 2022, he has been working toward the Ph.D. degree with the Institute of Electric Systems and Energy (ISEE), UNIFEI. His research interests include computer methods as applied to power systems analysis, operation and control.



Robson Pires (Senior Member, IEEE) received the B.Sc., degree in electrical engineering from Fluminense Federal University, Brazil, in 1983, the M.Sc. degree in electrical engineering from the Federal University of Itajubá (UNIFEI), Itajuba, Brazil, in 1989, and the D.Sc. degree in electrical engineering from the Federal University of Santa Catarina, Florianópolis, Brazil, in 1998. In 1996, he did part of his Graduate Program at The Bradley Department of Electrical and Computer Engineering - VTech, Blacksburg, VA, USA. Since 1987, he has been with the Institute of Electric Systems and Energy, UNIFEI, where he is currently a Professor. His research interests include power system analysis and real-time control of wide area monitoring (WAM) and complex-valued network applications.



Lamine Mili (Life Fellow, IEEE) is currently a Professor and the Program Director of the Department of Electrical and Computer Engineering, Northern Virginia Center, Virginia Tech. He was a Visiting Professor with the Swiss Federal Institute of Technology Lausanne, Switzerland, the Grenoble Institute of Technology; École supérieure d'électricité, France, and École Polytechnique de Tunisie, Tunisia, and did consulting work for Hydro-Québec and French Power Transmission Company, RTE. He has authored or coauthored more than 150 hundred technical articles and edited two books. His research interests include robust estimation and control, robust Kalman filtering, copula indices, risk management of complex systems to catastrophic failures, non-linear dynamics, and bifurcation theory.

Authorized licensed use limited to: Centro Universitário Fei. Downloaded on October 31,2024 at 18:04:55 UTC from IEEE Xplore. Restrictions apply.

New Topological Observability Algorithm for Hybrid Power System Static State Estimation

Eduardo Resende, *Graduate Student*, Robson Pires, *Senior Member*, *IEEE*, and Lamine Mili, *Life Fellow*, *IEEE*

***Abstract*—This work presents a new topological observability algorithm to strengthen the performance of the hybrid power system static state estimation, assuming that the supervisory control and data acquisition (SCADA) and phasor measurement unit (PMU) measurements are recorded at the same time intervals. The observability of each estimated state variable is assessed by the value assigned to its least local redundancy index. The algorithm has been specifically developed to enhance the observability of an existing wide-area monitored system and exempts its expansion from critical sets and critical measurements. These objectives are achieved by building the incidence matrices of the measurements for the nodes and branches. The performance of the proposed algorithm is evaluated using the IEEE test systems and the SIN test systems of Brazilian equivalent systems.**

***Index Terms*—Power system, static state estimation, least local redundancy index, observability.**

I. Introduction

LOCAL observability assessment is important in building a reliable database. It involves determining the observability of individual buses in a power system, which is crucial to estimate the operating conditions of a power system accurately. As an open problem, many proposals on the observability problem that aim at several goals can be found in recent research works [1]-[6], to name a few. Although the proposals in [4] and [7] consider the local observability redundancy index, the latter is conceptually different from the definition presented in this work.

A hybrid observability analysis can be addressed in two ways. The first way concerns the applied algorithms, that is, topological, numerical, algebraic, or hybrid algorithms [8]-[11]. In contrast, the second way refers to its ability to deal with measurements provided by the supervisory control and data acquisition (SCADA) or information based on phasor measurement units (PMUs) fed by the wide-area measurement system (WAMS).

In this work, the proposed algorithm is hybrid in both ways, which is based on topological and algebraic algorithms. It also deals with measurements provided by SCADA and PMU, considering that both measurement channels are recorded at the same time intervals. Although the PMU placement is a critical issue demanded by several applications [2], [5], [7]-[10], [12], [13], in this work, the PMUs throughout the system have been placed anywhere, because at the state variable level, it does not matter which telemetry channels the measurements come from. Moreover, the algorithm can be used online to identify the observability status of each bus after a contingency from failures in one or both telemetry channels. The computational time for doing this task is consistent with real-time requirements.

In the literature, one can find several studies for analysis and restoration of algebraic observability that are based on both the gain matrix [14] and the Gram matrix [15]-[17]. The algebraic observability analysis algorithm used in this work is based on that in [18], whose motivation is ease of implementation and low computational cost because the incidence matrices are all unimodular. Let us recall that a unimodular matrix is a square integer matrix with determinant 1 or −1; it is invertible. The method proposed in [18] allows us to analyze the algebraic observability of a power system using a set of measurements following the occurrence of contingencies in the communication network that causes changes in the topology of the monitored power system. Note that if a monitored system is algebraically observable, it ensures that the system is topologically observable [19]; but the converse is not generally true. However, the new topological observability algorithm is based on the least local redundancy index, which mitigates the risk of algebraic observability loss. Thus, the necessary and sufficient condition for a monitoring system to be algebraically observable is the existence of an observable spanning tree (OST).

The main contribution of this paper lies in developing a new topological observability algorithm to evaluate the monitored power system based on an assigned local redundancy index for each state variable as defined in [20]. The methodology is to build a measurement digraph from the redundant measurement placement used to monitor the system. This task is performed using the complex number formulation of the state estimator because the sparsity pattern of the resul-

Manuscript received: August 28, 2024; revised: January 18, 2025; accepted: April 14, 2025. Date of CrossCheck: April 14, 2025. Date of online publication: April 25, 2025.

This work was supported in part by CAPES (Coordenação de Aperfeiçoamento de Pessoal de Nível Superior) aiming the scholarship and financial aid addressed to E. Resende.

This article is distributed under the terms of the Creative Commons Attribution 4.0 International License (http://creativecommons.org/licenses/by/4.0/).

E. Resende and R. Pires (corresponding author) are with the Institute of Electric Systems and Energy, Federal University of Itajubá, CEP 37500-903, Itajubá, Brazil (e-mail: edumarresende@unifei.edu.br; rpires@unifei.edu.br).

L. Mili is with the Electrical and Computer Engineering Department, Virginia Tech National Capital Region, Falls Church, USA (e-mail: lmili@vt.edu).

DOI: 10.35833/MPCE.2024.000951

tant incidence matrix, which is constructed by mirroring (duplicating) its columns, is equivalent to that of the Jacobian matrix in the complex domain [21].

Furthermore, the creation of the OST for power systems is built in two steps. The first step is to obtain a minimum spanning tree, considering the digraphs of measurements used for monitoring the systems. Two algorithms can be used: Prim [22] and Kruskal [23]. The standard method (dense) uses the Prim algorithm that starts from an initial vertex, traversing the adjacent vertices and choosing the vertex connected by the arc of the most negligible weight, thus generating a minimal spanning tree to the weights of each arc. On the other hand, the sparse method is based on the Kruskal algorithm, which performs an ascending sort of the weights of each arc, sequentially adding such arcs to the minimum spanning tree as long as they do not form a loop with the previous tree. In this way, a minimal spanning tree with N vertices and $N-1$ arcs is guaranteed. To this end, the single measurements for spanning tree (SMST) algorithm is developed and applied to choose different measurements stemming from each arc of the spanning tree, avoiding the repetition of existing measurements in the critical set.

To ensure the local observability regarding each state variable to be estimated, an assigned number of measurements in the fundamental set (columns of Jacobian matrix) is guaranteed through the assignment of weighted arcs concerning the following sequence of measurements: active power flow, active power injection, and voltage angle measurements for the P-δ spanning tree. Analogously, for the Q-V spanning tree, reactive power flow, reactive power injection, and voltage magnitude measurements are assigned to each fundamental set. In addition to being useful for evaluating local observability, the proposed methodology is helpful to study the expansion of monitoring systems free of critical sets of measurements.

This paper is organized as follows. Section II describes the core of the contribution proposed in this work: the new topological observability algorithm. Section III presents the numerical applications of IEEE test systems and the SIN test systems of of Brazilian equivalent systems. Section IV summarizes the main results and conclusions and outlines future investigations.

II. New Topological Observability Algorithm

In the literature, two classes of algorithms are aimed at analyzing the system observability. The first class is based on algebraic observability analysis; and the second uses graph theory and is called topological observability analysis. In this work, we develop a new topological observability algorithm based on an assigned local redundancy index of measurements around each state variable. Regardless of which telemetry channel provides the set of measurements, i.e., SCADA or WAMS, the topological observability analysis is performed considering an assigned value for the least local redundancy index.

The developed algorithm can be used to achieve two objectives. The first objective is to evaluate an existing set of measurements. All critical sets and measurements are found if they exist, including observable islands in the monitored system. The second objective is to obtain a new placement of measurements based on an assigned local redundancy index around each state variable [20]. To this end, the measurements used to monitor the system are split into the P-δ and Q-V sub-problems. In the sequel, the incidence matrices [18] for each sub-problem are built using the topology of a network system and its power flow solution. The proposed algorithm builds the set of P-δ and Q-V measurements exempted from the critical sets and critical measurements based on the full incidence matrices and the assigned local redundancy index.

A. Local Redundancy Index

Identifying weaknesses in the monitored system is carried out for each estimated state variable. This task is performed by analyzing the columns of the incidence matrix $\boldsymbol{W}_0$ for the P-δ and Q-V sub-problems $\boldsymbol{W}_{0P\text{-}\delta}$ and $\boldsymbol{W}_{0Q\text{-}V}$, respectively. The framework of these matrices is the same as the Jacobian matrix presented in [21]. The columns of the incidence matrices are referred to as the "fundamental set of measurements". These measurements play a crucial role in estimating the corresponding state variable. It is important to note that any measurement may be shared among fundamental sets, such as active and reactive power injection and voltage phase angle measurements.

The "fundamental set" concept was introduced in power system static state estimation by [24]. It is based on defining a maximum fraction of measurements contaminated by gross error. This concept ensures that the number of measurements with gross errors in each fundamental set does not violate the constraint given by:

$$f_{j,\max} \le \left\lceil \frac{m_j - 1}{2} \right\rceil \tag{1}$$

where m_j is the local redundancy index and is equal to the number of measurements of the j^{th} fundamental set Z_j; and the operator $\lceil \cdot \rceil$ denotes the integer part of its argument. Therefore, the state estimator can produce valid estimates if the constraint expressed in (1) is not violated. Consequently, let us consider that each state variable is estimated at least by an assigned minimum number of measurements, i.e., $m_j \ge \eta_{target}$. For instance, if $\eta_{target} = 3$ or 4, only one gross error in the fundamental set is possible. Otherwise, the corresponding estimated state and neighbor state variables might be unacceptable. Hence, η_{target} can now be defined as being the least local redundancy index, that is, the smallest number of measurements in any fundamental set that allows the state estimator to produce valid estimates since the constraint established in (1) is satisfied. Indeed, assigning sufficient measurements to each node in incidence matrices of P-δ and Q-V sub-problems $\boldsymbol{W}_{P\text{-}\delta}$ and $\boldsymbol{W}_{Q\text{-}V}$, which are used to construct the Jacobian matrix, ensures that the local measurement redundancy for estimating each state variable is adequate to allow an algorithm to effectively perform bad data detection and identification, i.e., detecting, identifying, down-weighting its impact on estimates, or even recovering it as a pseudo measurement.

In the sequel, Fig. 1 displays the flowchart, and Algorithm 1 shows the pseudo-code for new topological observability algorithm aimed at building a reliable database.

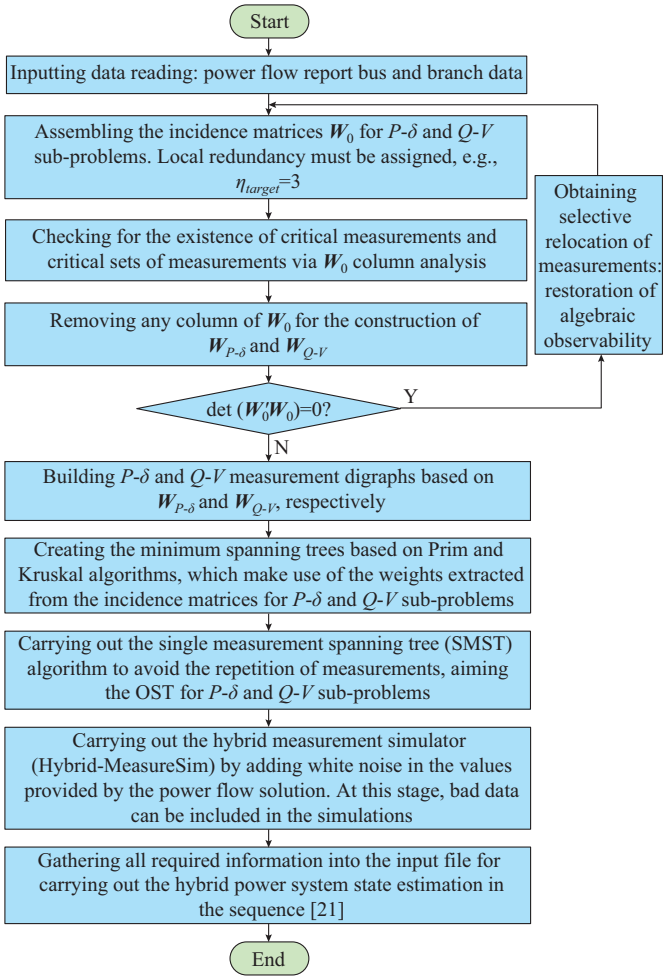


Fig. 1. Flowchart for real-time algorithm execution.

Algorithm 1: new topological observability algorithm

Input power flow data
Construct $W_{0P\text{-}\delta}$ and $W_{0Q\text{-}V}$
Set η_{target}
for $i=1,2,\ldots,n_{columns}$ of $W_{0P\text{-}\delta}$ and $W_{0Q\text{-}V}$ **do**
  Choose η_{target} measurements for each column of $W_{0P\text{-}\delta}$ and $W_{0Q\text{-}V}$ originating $W_{P\text{-}\delta}$ and $W_{Q\text{-}V}$
end for
for $i=1,2,\ldots,n_{columns}$ of $W_{P\text{-}\delta}$ and $W_{Q\text{-}V}$ **do**
  $W_{1P\text{-}\delta} \leftarrow$ remove the i^{th} column of $W_{P\text{-}\delta}$
  $W_{1Q\text{-}V} \leftarrow$ remove the i^{th} column of $W_{Q\text{-}V}$
  if $\det(W_{1P\text{-}\delta}W_{1P\text{-}\delta}^{T})=0$ or $\det(W_{1Q\text{-}V}W_{1Q\text{-}V})=0$ **then**
    System is not algebraically observable (relocation of measurements)
    Break
  else
    Continue
  end if
  For each i^{th} column of $W_{P\text{-}\delta}$ and $W_{Q\text{-}V}$, the local redundancy index and the existence of critical sets and measurements are verified
end for
Construct measurement digraphs based on $W_{P\text{-}\delta}$ and $W_{Q\text{-}V}$
Generate a minimum spanning tree applying Prim or Kruskal algorithms to measurement digraphs considering the weights extracted from incidence matrices
for $i=1,2,\ldots,n_{arcs}$ of each minimum spanning tree **do**
  Choose one measurement to represent the arc based on the weights of each possible measurement for that arc
  Exclude this measurement from all possible sets of measurements
end for

As an example of application, the performance of the proposed algorithm is used in the simulations carried out and presented in [21] to assess the performance of hybrid power system static state estimation.

B. Incidence Matrices for P - δ and Q - V Sub-problems

To show how the proposed algorithm works, let us first consider a small example system, as shown in Fig. 2, where t and u represent the active and reactive power flow measurements, respectively; P and Q are the active and reactive power injections, respectively; and $\dot{V}$ is the voltage phasor measurement. Hence, the full incidence matrices of measurements to nodes regarding the P - δ and Q - V sub-problems can be known, as shown in the sequence [18]. Notice that in the P - δ sub-problem (2), the voltage phase angle measurement follows the same rule of active power injection, while in the Q - V sub-problem (3), the node 0 refers to the ground potential.

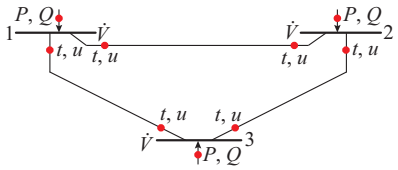


Fig. 2. Single-line diagram of 3-bus system.

$$W_{0P\text{-}\delta}=\overbrace{\begin{matrix}1&2&3\end{matrix}}^{\text{Nodes}}\left[\begin{matrix}1&-1&0\\-1&1&0\\1&0&-1\\-1&0&1\\0&1&-1\\0&-1&1\\2&-1&-1\\2&-1&-1\\-1&2&-1\\-1&2&-1\\-1&-1&2\\1&1&2\end{matrix}\right]\begin{matrix}t_{12}\\t_{21}\\t_{13}\\t_{31}\\t_{23}\\t_{32}\\\delta_1\\P_1\\\delta_2\\P_2\\\delta_3\\P_3\end{matrix}\Big\}\text{Measurements} \tag{2}$$

where t_{ij} ($i,j=1,2,3$ and $i\neq j$) denotes the active power flow measurement between nodes i and j; δ_i ($i=1,2,3$) denotes the voltage phase angle of node i; and P_i ($i=1,2,3$) denotes the active power of node i.

$$W_{0Q\text{-}V}=\overbrace{\begin{matrix}0&1&2&3\end{matrix}}^{\text{Nodes}}\left[\begin{matrix}-1&1&0&0\\-1&0&1&0\\-1&0&0&1\\0&1&-1&0\\0&-1&1&0\\0&1&0&-1\\0&-1&0&1\\0&0&1&-1\\0&0&-1&1\\0&2&-1&-1\\0&-1&2&-1\\0&-1&-1&2\end{matrix}\right]\begin{matrix}|V_1|\\|V_2|\\|V_3|\\u_{12}\\u_{21}\\u_{13}\\u_{31}\\u_{23}\\u_{32}\\Q_1\\Q_2\\Q_3\end{matrix}\Big\}\text{Measurements} \tag{3}$$

where $|V_i|$ ($i=1,2,3$) denotes the magnitude of the voltage at node i; u_{ij} ($i,j=1,2,3$ and $i\neq j$) denotes the reactive power flow measurement between nodes i and j; and Q_i (i=1, 2, 3) denotes the reactive power of node i.

Additionally, in the above incidence matrices, i.e., (2) and (3), the positive values represent the emission degrees of the corresponding vertex in the P-δ and Q-V plans of measurements to be built hereafter.

Note that in (2), each fundamental set of measurements is of the same size, i.e., $m_j=10$. Whereas in (3), except for the node representative of the ground potential where $m_j=3$, which is equal to η_{target}, the size of the remaining fundamental sets is $m_j=8$.

Note that the algebraic observability makes use of the property present in the Gram matrix, $G(\boldsymbol{W})=\det|\boldsymbol{W}^{\mathrm{T}}\boldsymbol{W}|$, as follows.

$$\begin{cases}\det|\boldsymbol{W}^{\mathrm{T}}\boldsymbol{W}|\neq 0 & \text{network is observable}\\ \text{otherwise} & \text{network is not observable}\end{cases} \tag{4}$$

Note that the incidence matrix $\boldsymbol{W}$ of measurements to the nodes is also a function of two other incidence matrices given by (5). $\boldsymbol{M}$ and $\boldsymbol{A}$ for the foregoing sub-problems are defined as [18]:

$$\boldsymbol{W}=\boldsymbol{M}\boldsymbol{A}^{\mathrm{T}} \tag{5}$$

1) $\boldsymbol{M}$: Incidence Matrix of Measurements to Network Branches

$$\boldsymbol{M}_{0P\text{-}\delta}=\begin{array}{c}\overbrace{\begin{array}{ccc}1\text{-}2 & 1\text{-}3 & 2\text{-}3\end{array}}^{\text{Branches}}\\ \left[\begin{array}{ccc}1 & 0 & 0\\ -1 & 0 & 0\\ 0 & 1 & 0\\ 0 & -1 & 0\\ 0 & 0 & 1\\ 0 & 0 & -1\\ 1 & 1 & 0\\ 1 & 1 & 0\\ -1 & 0 & 1\\ -1 & 0 & 1\\ 0 & -1 & -1\\ 0 & -1 & -1\end{array}\right.\end{array}\begin{array}{l}t_{12}\\ t_{21}\\ t_{13}\\ t_{31}\\ t_{23}\\ t_{32}\\ \delta_1\\ P_1\\ \delta_2\\ P_2\\ \delta_3\\ \left.P_3\right\}\end{array}\text{Measurements} \tag{6}$$

$$\boldsymbol{M}_{0Q-V}=\begin{array}{c}\overbrace{\begin{array}{cccccc}1\text{-}2 & 1\text{-}3 & 2\text{-}3 & 1\text{-}0 & 2\text{-}0 & 3\text{-}0\end{array}}^{\text{Branches}}\\ \left[\begin{array}{cccccc}0 & 0 & 0 & 1 & 0 & 0\\ 0 & 0 & 0 & 0 & 1 & 0\\ 0 & 0 & 0 & 0 & 0 & 1\\ 1 & 0 & 0 & 0 & 0 & 0\\ -1 & 0 & 0 & 0 & 0 & 0\\ 0 & 1 & 0 & 0 & 0 & 0\\ 0 & -1 & 0 & 0 & 0 & 0\\ 0 & 0 & 1 & 0 & 0 & 0\\ 0 & 0 & -1 & 0 & 0 & 0\\ 1 & 1 & 0 & 0 & 0 & 0\\ -1 & 0 & 1 & 0 & 0 & 0\\ 0 & -1 & -1 & 0 & 0 & 0\end{array}\right.\end{array}\begin{array}{l}|V_1|\\ |V_2|\\ |V_3|\\ u_{12}\\ u_{21}\\ u_{13}\\ u_{31}\\ u_{23}\\ u_{32}\\ Q_1\\ Q_2\\ \left.Q_3\right\}\end{array}\text{Measurements} \tag{7}$$

2) $\boldsymbol{A}$: Incidence Matrix of Nodes to Network Branches

$$\boldsymbol{A}_{0P\text{-}\delta}=\begin{array}{c}\overbrace{\begin{array}{ccc}1\text{-}2 & 1\text{-}3 & 2\text{-}3\end{array}}^{\text{Branches}}\\ \left[\begin{array}{ccc}1 & 1 & 0\\ -1 & 0 & 1\\ 0 & -1 & -1\end{array}\right.\end{array}\begin{array}{l}1\\ 2\\ \left.3\right\}\end{array}\text{Nodes} \tag{8}$$

$$\boldsymbol{A}_{0Q\text{-}V}=\begin{array}{c}\overbrace{\begin{array}{cccccc}1\text{-}2 & 1\text{-}3 & 2\text{-}3 & 1\text{-}0 & 2\text{-}0 & 3\text{-}0\end{array}}^{\text{Branches}}\\ \left[\begin{array}{cccccc}0 & 0 & 0 & -1 & -1 & -1\\ 1 & 1 & 0 & 1 & 0 & 0\\ -1 & 0 & 1 & 0 & 1 & 0\\ 0 & -1 & -1 & 0 & 0 & 1\end{array}\right.\end{array}\begin{array}{l}0\\ 1\\ 2\\ \left.3\right\}\end{array}\text{Nodes} \tag{9}$$

The primary motivation for using the above incidence matrices is that both of them are unimodular arrays. They are matrices made up of integers or multiples equal to 1, −1, and 0. In addition, they are sparse matrices that are easy to build and do not suffer from numerical instability.

Now, let us find the set of measurements for the P-δ and Q-V sub-problems exempt from critical sets and critical measurements, including an assigned local redundancy index. The criterion for choosing the local redundancy index is explained next.

C. Building Full Measurement Plans for P-δ and Q-V

Obtaining the P-δ and Q-V sets of measurements is done independently. In this sense, the starting node (fundamental set) may be random, including choosing η_{target} measurements among $m_j=10$ measurements available in the P-δ incidence matrix. The same reasoning may be applied to the Q-V incidence matrix, where $m_j=8$.

After the first one has been analyzed, the processing of each fundamental set of measurements must obey the following necessary rule: whatever the η_{target} measurements are chosen in the first fundamental set, if any other fundamental set either totally or partially shares them, they have to be taken into account with respect to the assigned least local redundancy index, e.g., $\eta_{target}=3$.

Before continuing, it is worth remembering that in graph theory, a graph is termed a digraph when the edges are directed, which in turn is termed as arc [25]. This representation allows us to identify the emitter and receiver vertices, which are directly in line with the measurement placement of power flow, injected power, voltage phase angle, and voltage magnitude. Based on that, the digraph generated for each measurement placement can be obtained from the analysis of the matrices defined in (2) and (3). For this, consider a graph $\boldsymbol{G}_r=[\underline{\boldsymbol{a}},\underline{\boldsymbol{b}}]$, where $\underline{\boldsymbol{a}}$ and $\underline{\boldsymbol{b}}$ are the vectors with the emitter and receiver vertices that form the arcs of the digraph, respectively. The logic elaborated for the creation of the digraphs from the incidence matrices $\boldsymbol{W}_0$ obeys the assembly rules of the vectors as follows.

1) Each bus in the electrical network corresponds to a vertex in the digraph of measurements.

2) For power flow measurements from buses k to m, the sender vertex is k and the receiver vertex is m. For the reverse power flow measurements, the sender vertex is m, and the receiver vertex is k.

3) For power injection measurements on the k^{th} bus, the positive value of the row relative to that measurement indicates the number of repetitions of the emitter vertex k, and the columns of the other non-zero elements of that row indicate the respective receiver vertices.

4) For the angular state measurements, the rule is the same as applied for power injection measurements.

5) For voltage magnitude measurements on the k^{th} bus, the emitter vertex is k, and the receiver vertex is 0.

Consequently, the full digraphs for $P\text{-}\delta$ and $Q\text{-}V$ sub-problems can be obtained, yielding:

$$\boldsymbol{G}_{rP\text{-}\delta}=\begin{bmatrix}1&2\\1&3\\2&1\\2&3\\3&1\\3&2\\1&2\\1&3\\2&1\\2&3\\3&1\\3&2\\1&2\\1&3\\2&1\\2&3\\3&1\\3&2\end{bmatrix}\begin{matrix}\rightarrow t_{12}\\\rightarrow t_{13}\\\rightarrow t_{21}\\\rightarrow t_{23}\\\rightarrow t_{31}\\\rightarrow t_{32}\\\rightarrow P_1\\\rightarrow P_1\\\rightarrow P_2\\\rightarrow P_2\\\rightarrow P_3\\\rightarrow P_3\\\rightarrow \delta_1\\\rightarrow \delta_1\\\rightarrow \delta_2\\\rightarrow \delta_2\\\rightarrow \delta_3\\\rightarrow \delta_3\end{matrix} \tag{10a}$$

$$\boldsymbol{G}_{rQ\text{-}V}=\begin{bmatrix}1&0\\2&0\\3&0\\1&2\\1&3\\2&1\\2&3\\3&1\\3&2\\1&2\\1&3\\2&1\\2&3\\3&1\\3&2\end{bmatrix}\begin{matrix}\rightarrow |V_1|\\\rightarrow |V_2|\\\rightarrow |V_3|\\\rightarrow u_{12}\\\rightarrow u_{13}\\\rightarrow u_{21}\\\rightarrow u_{23}\\\rightarrow u_{31}\\\rightarrow u_{32}\\\rightarrow Q_1\\\rightarrow Q_1\\\rightarrow Q_2\\\rightarrow Q_2\\\rightarrow Q_3\\\rightarrow Q_3\end{matrix} \tag{10b}$$

In the above equation, we recall the positive impact of measurements of the angular state in the $P\text{-}\delta$ sub-problem. In the $Q\text{-}V$ sub-problem, the number of voltage magnitude measurements ensures the vertex representative of the ground potential observability. Figures 3 and 4 show the full measurement plans for the $P\text{-}\delta$ and $Q\text{-}V$ sub-problems, respectively. However, the corresponding measurement digraphs of $P\text{-}\delta$ and $Q\text{-}V$ sub-problems, considering $\eta_{target}=3$, are shown in Figs. 5 and 6, respectively. It can be observed that for each vertex in Figs. 5 and 6, there are at least $\eta_{target}=3$ different measurements.

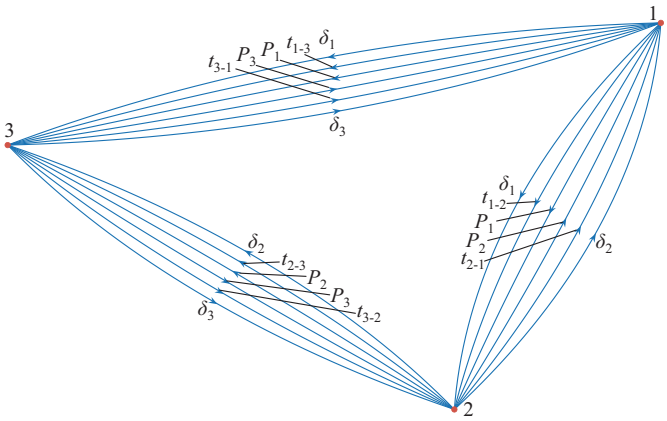


Fig. 3. Full measurement plan for $P\text{-}\delta$ sub-problem.

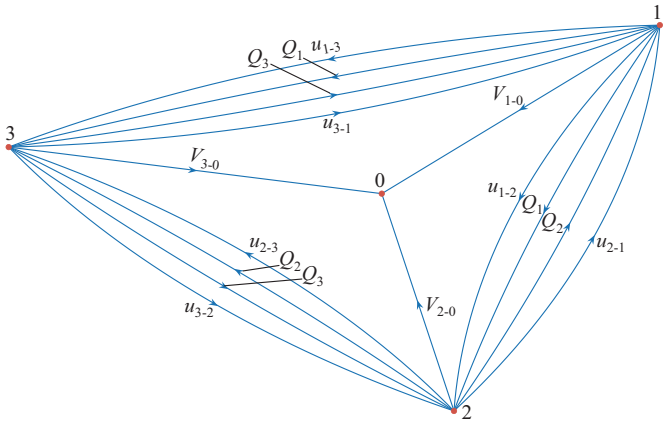


Fig. 4. Full measurement plan for $Q\text{-}V$ sub-problem.

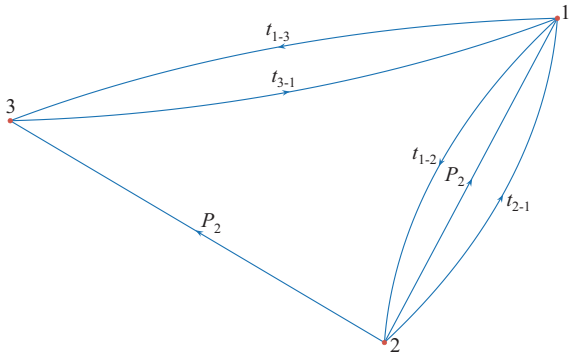


Fig. 5. Measurement digraphs of $P\text{-}\delta$ sub-problem considering $\eta_{target}=3$.

D. OST for P-δ and Q-V Sub-problems

The search for an OST for the $P\text{-}\delta$ and $Q\text{-}V$ sub-problems is done by making use of three algorithms, i.e., Prim [22], Kruskal [23], and SMST. The Prim and Kruskal algorithms search for the minimum spanning tree, whereas the SMST algorithm finds the OST for the $P\text{-}\delta$ and $Q\text{-}V$ sub-problems.

Prim algorithm (dense) starts from a random initial vertex connected by the arc of the most negligible weight, thus generating a minimal spanning tree about the weights of each

arc. Recall that the positive value at each row in the incidence matrices of the measurements for the network nodes in (2) and (3) represents the number of arcs emitted from the node (emission degree) due to the corresponding measurement, hence, each emission degree in (2) and (3) is used as the weight assigned to the arcs referred to each measurement in the spanning tree. For instance, the weight assigned to each power flow measurement is 1. In contrast, the weight is usually 2 or more for power injection, depending on the number of incident branches converging toward the node where the power injection is measured. Furthermore, since the measurement of the angular state follows the same rule as applied to power injection, a first consideration in the construction of the spanning tree, since it is a measurement of the variable state, is to take its weight as a fraction of the actual weight, e. g., 90%. This strategy reduces its weight to less than the weight of the power injection measurement.

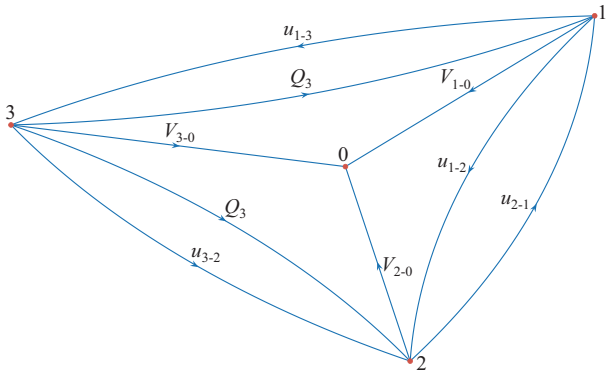


Fig. 6. Measurement digraphs of Q-V sub-problem considering $\eta_{target}=3$.

On the other hand, the sparse method is based on Kruskal algorithm, which performs an ascending sort of weights for each arc, sequentially adding such arcs to the minimum spanning tree as long as they do not form a loop with the previous tree.

At this stage, the SMST is carried out to obtain the OST once it avoids the loop formation and ensures different measurements in the minimum spanning tree. For example, Tables I and II present the OST obtained for the P-δ and Q-V sub-problems based on the Prim and Kruskal algorithms [22], [23] under the supervision of SMST algorithm, respectively. Note that the weight for each measurement is indicated by appending (1) and (2) to the arc specification.

TABLE I
OST OBTAINED FOR P-δ SUB-PROBLEM

Spanning tree arc	Set of measurement	Randomly chosen measurement
1-2	$t_{1\text{-}2}$ (1), $t_{2\text{-}1}$ (1), P_2 (2)	$t_{1\text{-}2}$
1-3	$t_{1\text{-}3}$ (1), $t_{3\text{-}1}$ (1)	$t_{1\text{-}3}$

Recall that the chosen measurements for the composition of OST are selected following the ascending order of the weight assigned to each type of measurement under the supervision of SMST algorithm. For instance, for the P-δ sub-problem, the order is power flow → angular state measurements →power injection measurements. In contrast, for the Q-V sub-problem, the order is voltage magnitude measurement → power flow → power injection measurements.

TABLE II
OST OBTAINED FOR Q-V SUB-PROBLEM

Spanning tree arc	Set of measurement	Randomly chosen measurement
1-2	$u_{1\text{-}2}$ (1) $u_{2\text{-}1}$ (1)	$u_{1\text{-}2}$
1-3	$u_{1\text{-}3}$ (1) Q_3 (2)	$u_{1\text{-}3}$
1-0	$V_{1\text{-}0}$ (1)	
2-0	$V_{2\text{-}0}$ (1)	$V_{2\text{-}0}$
3-0	$V_{3\text{-}0}$ (1)	

Note that in Figs. 7 and 8, all vertices are connected to each other. Otherwise, the corresponding measurement placement is not topologically observable.

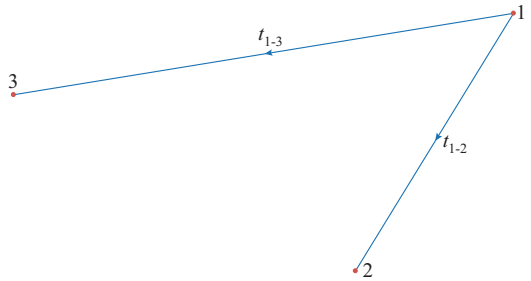


Fig. 7. OST for P-δ sub-problem.

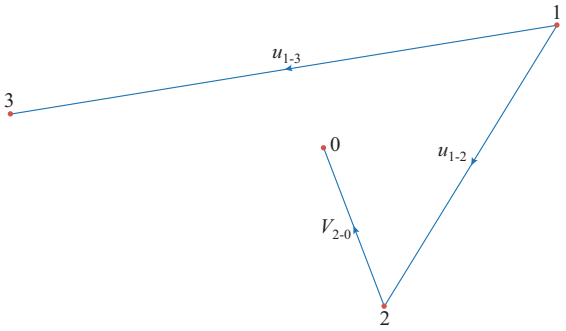


Fig. 8. OST for Q-V sub-problem.

III. NUMERICAL APPLICATIONS

This section presents the main network features and the monitored quantities for the larger-scale systems used in the simulations. The SMST algorithm was developed in MATLAB using sparsity techniques and performed on an Intel(R) Core(TM) i7-10510U CPU (@ 1.80 GHz, up to 2.30 GHz), 16 GB RAM, and 64-bit operating system. Table III depicts the power flow parameters for IEEE and SIN test systems, where N_{PV} is the number of P-V buses; N_{PQ} is the number of P-Q buses; $\boldsymbol{CV}_r$ is the complex-valued Jacobian matrix

in rectangular coordinates and its dimension $n=2(N_{PV}+N_{PQ})$; and $\boldsymbol{RV}_p$ is the real-valued Jacobian matrix in polar coordinates and its dimension $n=N_{PV}+2N_{PQ}$. In contrast, Table IV presents the SMST performance considering several scenarios of measurements provided by the SCADA and PMUs.

TABLE III
POWER FLOW PARAMETERS FOR IEEE AND SIN TEST SYSTEMS

Test system	N_{PV}	N_{PQ}	No. of transformer	No. of transmission line and shunt device	n for $\boldsymbol{RV}_p$	n for $\boldsymbol{CV}_r$
IEEE 57-bus	6	50	15	83	106	112
SIN-340	53	287	82	550	627	680
SIN-730	104	626	234	1078	1356	1460
SIN-1916	163	1753	835	3197	3669	3832

TABLE IV
SMST PERFORMANCE CONSIDERING $\eta_{target}=3$

Test system	SCADA		PMU		A (s)	B (s)	
	N_m	R (%)	N_m	R (%)		P-δ	Q-V
IEEE 57-bus	239	100	-	0	0.0453	0.0132	0.0126
	185	75	27	25	0.0484	0.0136	0.0141
	120	50	60	50	0.0584	0.0129	0.0114
	59	25	91	75	0.0559	0.0122	0.0126
	-	0	121	100	0.0504	0.0131	0.0121
SIN-340	1427	100	-	0	0.2822	0.1052	0.1025
	1067	75	180	25	0.3521	0.1797	0.2564
	710	50	359	50	0.3355	0.1048	0.0972
	367	25	531	75	0.3645	0.1648	0.1877
	-	0	715	100	0.3955	0.1664	0.1838
SIN-730	3417	100	-	0	0.6898	0.6125	0.4253
	2559	75	429	25	0.6822	0.3612	0.3469
	1720	50	849	50	0.7878	0.6269	0.4538
	859	25	1280	75	0.7727	0.5036	0.4727
	-	0	1710	100	0.7675	0.4844	0.4517
SIN-1916	8453	100	-	0	2.4401	1.9982	1.8671
	6287	75	1083	25	1.8205	1.7203	1.7626
	4220	50	2117	50	1.9887	2.1164	1.9822
	2095	25	3180	75	1.9419	2.0569	1.9009
	-	0	4228	100	1.7991	1.7334	1.7511

Note: A denotes the total time for searching the critical sets and critical measurements; B denotes the time for obtaining an OST; N_m denotes the number of measurements; and R denotes the percentage of the number of measurements by the measurement devices in the total number of measurements.

When measurement noise is present in SCADA or PMUs, the impact of SMST performance is described in [21], in which results are obtained under various scenarios, assuming $\eta_{target}=3$. Furthermore, Figs. 9-12 show the comparative performance of the SMST algorithm for the most representative test systems considering different least local redundancy indices of measurements, e.g., $\eta_{target}=3$ and $\eta_{target}=5$, in P-δ and Q-V sub-problems. The least local redundancy index of the measurements has a low impact on SMST performance. Still, it positively impacts the robustness of a highly robust state estimator, as it can handle two bad data if $\eta_{target}=5$ is assigned to each fundamental set.

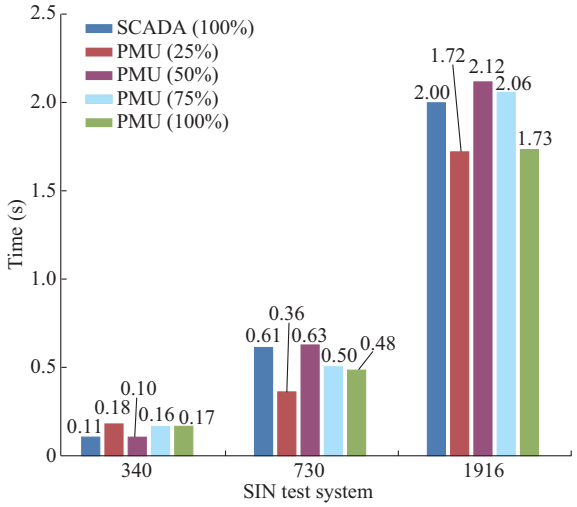


Fig. 9. P-δ sub-problem considering $\eta_{target}=3$ under SIN test systems.

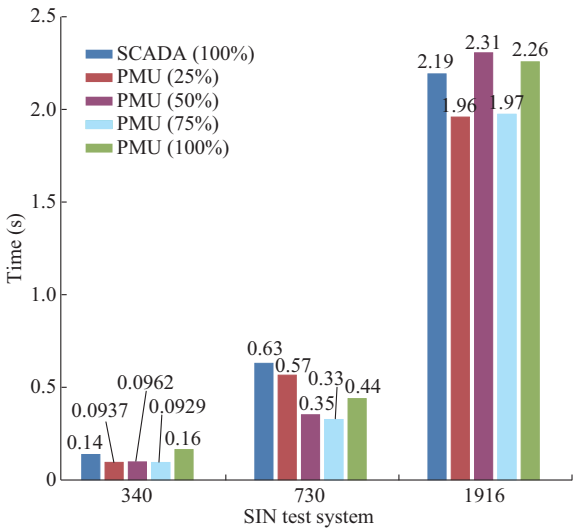


Fig. 10. P-δ sub-problem considering $\eta_{target}=5$ under SIN test systems.

On the other hand, the measurement digraphs and OSTs for the P-δ and Q-V sub-problems for larger-scale systems, considering $\eta_{target}=3$, are shown in Supplementary Material A Figs. SA1 and SA2 and in Figs. 13 and 14, respectively. Note that in both digraphs of measurements, the vertices show up with at least three ($\eta_{target}=3$) arcs converging to them, e.g., vertices #33 and #35, among others. Furthermore, for much larger-scale systems, the following functionality is useful to see the overall local redundancy for the P-δ and Q-V sub-problems, as shown in Figs. 15 and 16, respectively. Note that the IEEE 57-bus test system is chosen for illustration since much larger-scale systems cause visual pollution in the pictures due to the density of digraph connections.

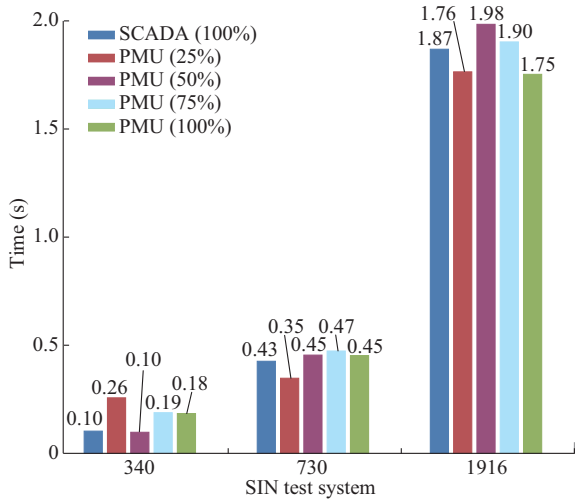


Fig. 11. Q-V sub-problem considering $\eta_{target}=3$ under SIN test systems.

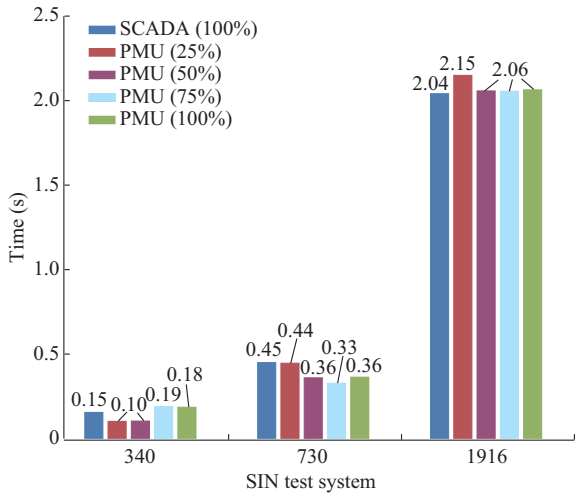


Fig. 12. Q-V sub-problem considering $\eta_{target}=5$ under SIN test systems.

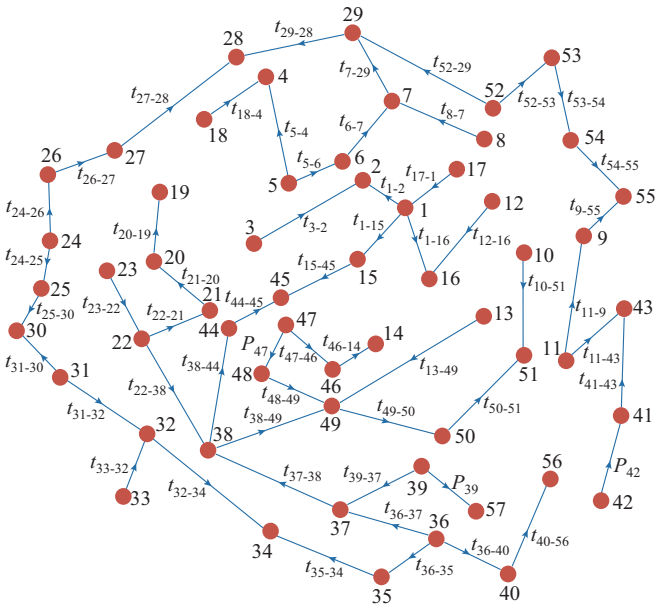


Fig. 13. OST for P-δ sub-problem applied to IEEE 57-bus test system.

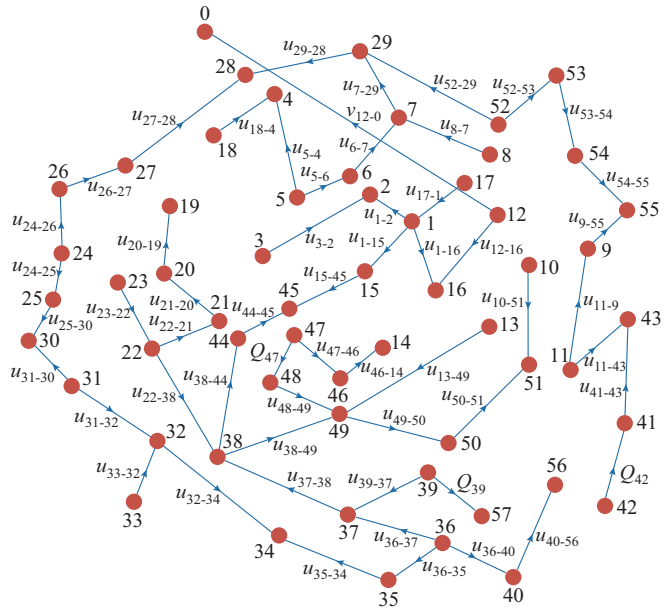


Fig. 14. OST for Q-V sub-problem applied to IEEE 57-bus test system.

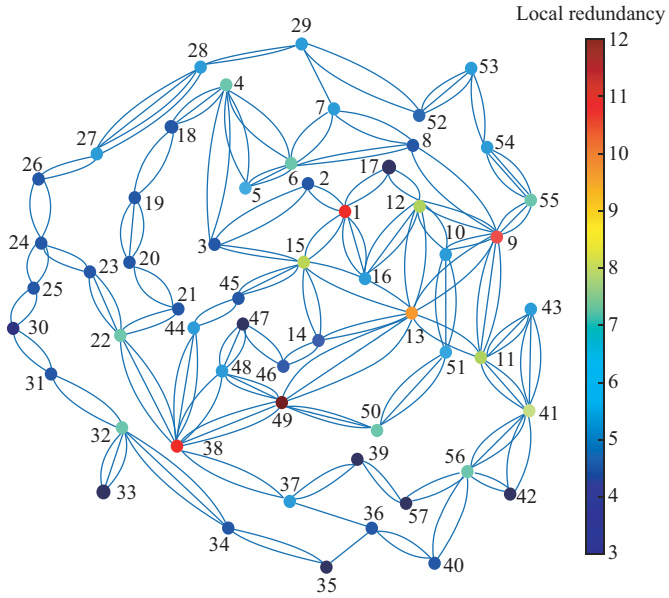


Fig. 15. Local redundancy for P-δ sub-problem under IEEE 57-bus test system.

IV. Conclusion and Future Investigation

This paper presents an algorithm of low computational cost for analyzing topological observability based on an assigned local redundancy index. Such features result from unimodular matrices obtained by the topological analysis of the network and the established real-time monitoring plan. These, known as incidence matrices, are sparse and easy to build, and do not have the risk of numerical instability. Furthermore, these matrices can be easily converted to computational applications based on graph theory, encouraging the elaboration of measurement digraphs for P-δ and Q-V sub-problems.

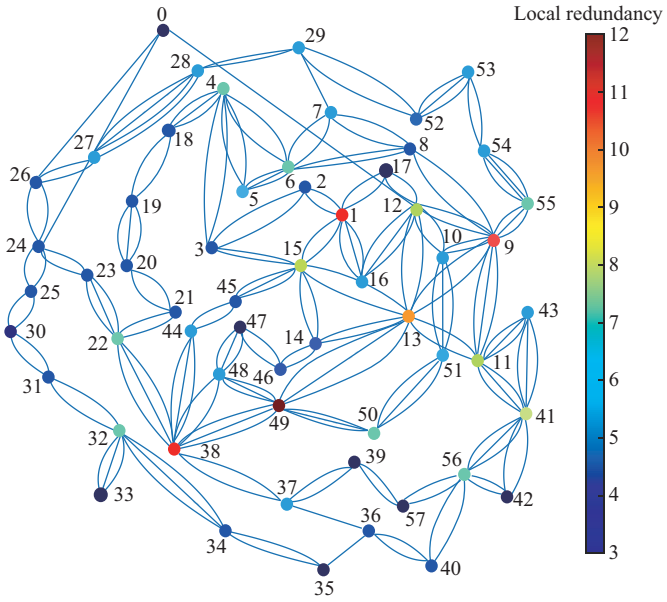


Fig. 16. Local redundancy for Q-V sub-problem under IEEE 57-bus test system.

Moreover, such applications are the basis for searching for OSTs, which is a necessary and sufficient condition to ensure topological observability. The Prim and Kruskal algorithms create spanning trees based on a given measurement digraph. A new algorithm is developed to avoid duplicity of measurement and loop formation when constructing the spanning tree. Therefore, this algorithm allows the creation of OSTs for the P-δ and Q-V sub-problems, avoiding a high computational effort since it belongs to a combinatorial problem.

Future investigations could involve developing an algorithm to create a monitoring plan that considers local redundancy depending on operational requirements. This can be done by assigning larger weights to power injection measurements, e.g., zero injection buses, since this strategy provides more arcs in the measurement digraph, ensuring algebraic observability.

REFERENCES

[1] M. Z. Islam, Y. Lin, V. M. Vokkarane *et al*., "Observability-aware resilient PMU networking," *IEEE Transactions on Power Systems*, vol. 40, no. 1, pp. 218-230, Jan. 2025.

[2] N. P. Theodorakatos, R. Babu, and A. P. Moschoudis, "The branch-and-bound algorithm in optimizing mathematical programming models to achieve power grid observability," *Axioms*, vol. 12, no. 11, p. 1040, Nov. 2023.

[3] C. Ren, X. Wang, C. Cao *et al*., "Power systems observability analysis based on parallel Gaussian belief propagation," in *Proceedings of 2022 IEEE 10th International Conference on Computer Science and Network Technology*, Dalian, China, Oct. 2022, pp. 19-23.

[4] E. O. Okendo, C. W. Wekesa, and M. J. Saulo, "Optimal placement of phasor measurement unit considering system observability redundancy index: case study of the Kenya power transmission network," *Heliyon*, vol. 7, no. 7, p. e07670, Jul. 2021.

[5] G. N. Korres, "An integer-arithmetic algorithm for observability analysis of systems with SCADA and PMU measurements," *Electric Power Systems Research*, vol. 81, no. 7, pp. 1388-1402, Jul. 2011.

[6] M. Shahraeini and M. H. Javidi, "A survey on topological observability of power systems," in *Proceedings of 2011 IEEE Power Engineering and Automation Conference*, Wuhan, China, Sept. 2011, pp. 373-376.

[7] D. Dua, S. Dambhare, R. K. Gajbhiye *et al*., "Optimal multistage scheduling of PMU placement: an ILP approach," *IEEE Transactions on Power Delivery*, vol. 23, no. 4, pp. 1812-1820, Oct. 2008.

[8] N. P. Theodorakatos, R. Babu, C. A. Theodoridis *et al*., "Mathematical models for the single-channel and multi-channel PMU allocation problem and their solution algorithms," *Algorithms*, vol. 17, no. 5, p. 191, May 2024.

[9] M. Korkali, *Robust Wide-area Fault Visibility and Structural Observability in Power Systems with Synchronized Measurement Units*. New York: IEEE Press, 2020.

[10] G. N. Korres, N. M. Manousakis, T. C. Xygkis *et al*., "Optimal phasor measurement unit placement for numerical observability in the presence of conventional measurements using semi-definite programming," *IET Generation, Transmission & Distribution*, vol. 9, no. 15, pp. 2427-2436, Dec. 2015.

[11] H. Zhang and K. Han, "A hybrid observability analysis method for power system state estimation," *IEEE Access*, vol. 8, pp. 73388-73397, Apr. 2020.

[12] T. L. Baldwin, L. Mili, M. B. Boisen *et al*., "Power system observability with minimal phasor measurement placement," *IEEE Transactions on Power Systems*, vol. 8, no. 2, pp. 707-715, May 1993.

[13] L. Mili, T. Baldwin, and R. Adapa, "Phasor measurement placement for voltage stability analysis of power systems," in *Proceedings of 29th IEEE Conference on Decision and Control*, Honolulu, USA, Dec. 1990, pp. 3033-3038.

[14] A. Monticelli and F. F. Wu, "Network observability: identification of observable islands and measurement placement," *IEEE Transactions on Power Apparatus and Systems*, vol. 104, no. 5, pp. 1035-1041, May 1985.

[15] M. C. Almeida, E. N. Asada, and A. V. Garcia, "A numerical method for finding spanning trees in power system state estimation," in *Proceedings of 2006 International Conference on Power System Technology*, Chongqing, China, Oct. 2006, pp. 1-6.

[16] M. C. de Almeida, E. N. Asada, and A. V. Garcia, "On the use of gram matrix in observability analysis," *IEEE Transactions on Power Systems*, vol. 23, no. 1, pp. 249-251, Feb. 2008.

[17] G. N. Korres, "A gram matrix-based method for observability restoration," *IEEE Transactions on Power Systems*, vol. 26, no. 4, pp. 2569-2571, Nov. 2011.

[18] E. D. Crainic, X. D. Do, P. J. Lagacé *et al*., "Power system observability: on-line measurement set contingency analysis," *IFAC Proceedings Volumes*, vol. 21, no. 11, pp. 491-499, Sept. 1988.

[19] G. R. Krumpholz, K. A. Clements, and P. W. Davis, "Power system observability: a practical algorithm using network topology," *IEEE Transactions on Power Apparatus and Systems*, vol. 99, no. 4, pp. 1534-1542, Jul. 1980.

[20] L. Mili, V. Phaniraj, and P. J. Rousseeuw, "Least Median of squares estimation in power systems," *IEEE Transactions on Power Systems*, vol. 6, no. 2, pp. 511-523, May 1991.

[21] E. M. Resende, R. Pires, and L. Mili, "Complex-valued projection statistics for hybrid power system state estimation," *IEEE Transactions on Power Systems*, vol. 39, no. 4, pp. 6052-6062, Jul. 2024.

[22] GeekforGeeks. (2021, Jan.). Prim's minimum spanning tree (MST)-greedy algo-5. [Online]. Available: https://www. geeksforgeeks. org/ prims-minimum-spanning-tree-mst-greedy-algo-5

[23] GeekforGeeks. (2021, Jan.). Kruskal's minimum spanning tree algorithm-greedy algo-2. [Online]. Available: https://www. geeksforgeeks. org/ kruskals-minimum-spanning-tree-algorithm-greedy-algo-2/

[24] L. Mili, V. Phaniraj, and P. J. Rousseeuw, "High breakdown point estimation in electric power systems," in *Proceedings of IEEE International Symposium on Circuits and Systems*, New Orleans, USA, May 1990, pp. 1843-1846.

[25] R. Diestel, *Graph Theory*. Heidelberg: Springer-Verlag, 2017, pp. 59-172.

Eduardo Resende received the B.Sc. degree and the M.Sc. degree in electrical engineering from Federal University of Itajuba (UNIFEI), Itajuba, Brazil, in 2020 and 2021, respectively. Since 2022, he has been working to pursue the Ph.D. degree at the Institute of Electric Systems and Energy (ISEE) at UNIFEI. His research interests include computer technologies applied to power system analysis, operation, and control.

Robson Pires received the B.Sc, M.Sc., and D.Sc. degrees in electrical engineering from Fluminense Federal University (UFF), Niterói, Brazil, Federal University of Itajuba (UNIFEI), Itajuba, Brazil, and Federal University of

Santa Catarina (UFSC), Florianópolis, Brazil, respectively. In Jan.-Jul. 1996, he did part of his graduate program at "The Bradley Department of Electrical and Computer Engineering" of Virginia Tech, Blacksburg, USA. Since 1987, he has been with the Institute of Electric Systems and Energy at UNIFEI, where he is currently a Professor. His research interests include power system analysis, real-time wide-area measurement system (WAMS) control, and complex-valued network application.

Lamine Mili is currently a Professor and the Program Director of the Department of Electrical and Computer Engineering, Northern Virginia Center, Virginia Tech, Blacksburg, USA. He was a Visiting Professor with the Swiss Federal Institute of Technology Lausanne, Lausanne, Switzerland; the Grenoble Institute of Technology, Grenoble, France, École supérieure d'électricité, Parice, France, and École Polytechnique de Tunisie, La Marsa, Tunisia. His research interests include robust estimation and control, robust Kalman filtering, copula index, risk management of complex system under catastrophic failure, non-linear dynamics, and bifurcation theory.

Second Order Statistical Properties of PMU Data Aiming Power Systems Applications

1st Renata de Almeida Ribeiro
Institute of Electric Systems and Energy - ISEE
Federal University of Itajubá, UNIFEI
Itajubá, Brazil
renata0527@unifei.edu.br

2nd Eduardo Marcel Resende
Institute of Electric Systems and Energy - ISEE
Federal University of Itajubá, UNIFEI
Itajubá, Brazil
https://orcid.org/0009-0008-6270-2725

3rd Robson Pires
Institute of Electric Systems and Energy - ISEE
Federal University of Itajubá, UNIFEI
Itajubá, Brazil
https://orcid.org/0000-0003-1943-6691

4th Lamine Mili
Department of Electrical and Computer Engineering
Virginia Tech National Capital Region
Falls Church, VA 22043 - USA
https://orcid.org/0000-0001-6134-3945

2025 IEEE Kiel PowerTech | 979-8-3315-4397-6/25/$31.00 ©2025 IEEE | DOI: 10.1109/PowerTech59965.2025.11180407

***Abstract*—The increasing deployment of Phasor Measurement Units (PMUs) has introduced complex-valued measurements into system monitoring and control frameworks. This work applies the second-order statistical properties of complex signals to PMU data, aiming at power systems applications in the complex domain. Two sets of actual data are used to this end. The first uses data from PMU installed in the National Interconnected Brazilian power grid, which is termed (SIN). The second uses data from the phasor measurement unit (PMU) installed in low-voltage distribution systems, notably PMUs installed on university campuses across Brazil and funded by the MedFasee project. Results demonstrate that PMU signals predominantly show proper and circular characteristics, hence guaranteeing the reduction to real-valued covariance matrices in actual systems.**

***Index Terms*—Second order statistical properties of PMU signals; Power systems applications in the complex domain.**

I. Introduction

Complex-valued signals have been applied to a great number of research areas, such as communications, radar, echocardiogram images, features for face recognition, geophysics, optics, and electromagnetics, to name a few [1]. Recently, electric power companies worldwide have deployed many Phasor Measurement Units - PMUs aimed to enhance the monitoring of the operation security of power transmission systems under either steady state or dynamic conditions. The signals provided by the PMUs represent a particular case of complex-valued random vectors. Hence, these signals should be suitably embedded into the non-linear measurement model for hybrid power system state estimation developed in the complex domain [2]–[5]. Notice the findings described in this work are already applied in [2].

In this paper, the different reporting rates of the conventional measurements and the synchronized system of phasor measurements based on PMU are assumed to be perfectly synchronized. This issue is beyond this work, but in the literature, relevant contributions aim at this goal. Among them, we highlighted the proposals addressed to solve this problem on static and dynamic hybrid state estimation as described in [6] and [7], [8], respectively.

The performance of bad-data processing algorithms formulated in the complex domain should rely on the methodology recommended by the technical literature in signal processing once this issue is a novelty for the power system community [2]. For instance, Picinbono [9], [10] showed that the covariance matrix usually used to describe complex-valued random vectors is insufficient for a complete description of second-order statistics, and an additional matrix named *relation or pseudo covariance matrix* is necessary. Some of its properties should be analyzed and used to express the probability density function of normal complex-valued vectors. On the other hand, in [11], the main focus relies on the case where the *pseudo covariance* matrix does not vanish, i.e., the complex-valued random vectors are *improper*. Whereas in [12], the analysis follows the case of *non-circular* complex-valued random vectors.

The reasons above are the true motivation for the proposed work presented in this paper. To this end, two sets of PMU actual data are analyzed to identify the statistical properties of the complex-valued recorded metered signals. In the first set of data, the signals come from the PMUs installed in an extra-high voltage transmission system, which is operated by Companhia de Transmissão de Energia Elétrica Paulista (CTEEP), a vital transmission system operator in Brazil. The real and imaginary parts of the voltages and currents are the positive sequences (+) obtained from the transformation of the symmetrical components. In contrast, the complex powers expressed in the rectangular coordinates are obtained through the element-wise products of $\underline{V} \odot \underline{I}^*$, where $\odot$ is the Hadamard product. In the second set of data, only the positive sequences of voltages are available because the PMUs are installed in the low-voltage at the consumer level, which are PMUs installed at University campuses across Brazil and funded by the MedFasee project [13]. Both sets of PMU data were obtained at 60 phasors per second reporting rate.

The key contribution of this paper is the statistical confirmation that PMU complex-valued signals predominantly show circular and proper characteristics. This observation warrants simplifying their statistical modeling, allowing for the application of real-valued covariance matrices without accuracy loss, lessening computational complexity for real-time applications in the complex domain.

Authorized licensed use limited to: Eduardo Resende. Downloaded on December 25,2025 at 14:27:32 UTC from IEEE Xplore. Restrictions apply.

This paper is organized as follows: Section II presents the theoretical foundation of complex-valued random signal processing and the multivariate generalized Gaussian distribution (CV-GGD). Section III provides some numerical results based on the second-order statistical properties recommended by the signal processing community. Finally, Section IV concludes the paper.

II. Theoretical Foundation

A. Complex-Valued Random Variables

The covariance function generally characterizes the second-order statistical properties of complex-valued signals. However, this is not enough for a complete second-order statistics description, and another statistic called *pseudo-covariance* or *complementary covariance* needs to be taken into account [9]. Its properties, especially the conditions that must be satisfied, lead to a new perspective on complex-valued white noise and modeling any signal as the output of a linear system added to white noise. Therefore, considering a complex-valued random variable, $z_i = z_{re} + j z_{im}$, where $j = \sqrt{-1}$ and z_{re} and z_{im} stand for the real and imaginary parts of z_i, the second-order statistic [14] for the multi variables case is expressed as

$$\mathbf{C} = E[\underline{z}\ \underline{z}^H] = E[\underline{z}_{re}^2] + E[\underline{z}_{im}^2] = \underline{\sigma}_{re}^2 + \underline{\sigma}_{im}^2, \qquad (1)$$

where $\mathbf{C}$ is the covariance matrix and $\underline{(\cdot)}$ denotes a vector, and $(\cdot)^H$ denotes the transposition and complex conjugation, i.e., the Hermitian transpose, and $E[\cdot]$ denotes the statistical expectation operator. In addition, it is necessary to define the so-called pseudo-covariance matrix, $\mathbf{P}$, which in turn is expressed as

$$\begin{aligned} \mathbf{P} &= E[\underline{z}\ \underline{z}^T], \\ &= E[{\underline{z}_{re}}^2] - E[{\underline{z}_{im}}^2] + 2j\ E[\underline{z}_{re}\ \underline{z}_{im}], \\ &= \underline{\sigma}_{re}^2 - \underline{\sigma}_{im}^2 + j\ 2 \times \underline{\sigma}_{re\ im}, \end{aligned} \qquad (2)$$

where $(\cdot)^T$ denotes transposition, σ^2 is the variance, $j = \sqrt{-1}$, and $2 \times \sigma_{re\ im}$ is the correlation. Note that $\mathbf{P}$ is a complex and symmetric matrix and therefore satisfies $\mathbf{P}^* = \mathbf{P}^H$, where $(\cdot)^H$ denotes the complex conjugate. The pseudo-covariance matrix is rarely introduced in the signal processing literature because it is explicitly or implicitly assumed to be zero. Observe that $\mathbf{P}$ vanishes for uncorrelated real and imaginary parts of equal variances. Moreover, under such condition, a complex-valued Gaussian random signal is said to be *circular* if for a given complex-valued random variable, $z_i \in \mathbb{C}$, with *probability density function (pdf)* is *invariant to rotation in* $\mathbb{C}$, i.e., $p(z_i) = p(z_i\ e^{j\theta})$ for $\forall\ \theta \in [0, 2\pi]$ and has zero mean. Additionally, it is *proper* if its variance is twice the variances of its real and imaginary parts, i.e., $\sigma_i^2 = 2\,\sigma_{i_{re}}^2 = 2\,\sigma_{i_{im}}^2$. Otherwise, the complex-valued Gaussian random signal is *non-circular* and *improper*. However, among many other practical reasons, the most common being short observation windows, the pseudo-covariance should be considered, i.e., $\mathbf{P} \neq 0$. Thus, to deal with non-circularity, the literature in signals processing [9], [11], [15] have recommended the signal model based on the augmented form of the complex variable, i.e.

$$\underline{z}_c = \mathbf{M} \begin{bmatrix} z_{re} \\ z_{im} \end{bmatrix} = \begin{bmatrix} z \\ z^* \end{bmatrix}, \qquad (3)$$

where the matrix $\mathbf{M} \in \mathbb{C}^{2\times 2}$ is defined as

$$\mathbf{M} = \begin{pmatrix} 1 & j \\ 1 & -j \end{pmatrix}, \qquad (4)$$

and for what follows it is important to note that

$$\mathbf{M}^{-1} = \frac{1}{2}\,\mathbf{M}^H. \qquad (5)$$

Thus, the following augmented covariance matrix [16] can be derived as

$$\mathbf{\Omega_c} = E[\underline{z}_c\ \underline{z}_c^H] = \begin{bmatrix} \mathbf{C} & \mathbf{P} \\ \mathbf{P}^* & \mathbf{C}^* \end{bmatrix}. \qquad (6)$$

Note that $\mathbf{\Omega}_c$ in (6) models both second-order circular and noncircular properties of signals for general complex processes. Moreover, $\mathbf{\Omega}_c$ will have real-valued diagonal elements, whereas the off-diagonal elements are complex values. The latter are the correlation coefficients between the real and imaginary parts of the complex-valued random variable, which allow us to quantify the degree of impropriety of complex signals. For instance, the *complex correlation coefficient* between z_i and z_i^* for the multivariable case is defined as [17]

$$|\rho| \quad = \frac{E[\underline{z}\ \underline{z}^T]}{E[\underline{z}\ \underline{z}^H]}, \qquad (7)$$

with bounds $0 \leq |\rho| \leq 1$. However, since the pseudo-covariance is a complex number, ρ can also be expressed in polar coordinates, such as

$$\rho = |\rho|\ e^{j\theta}, \qquad (8)$$

Thus, the ratio coefficient between the real and imaginary parts of the signal is calculated as follows:

$$\rho_{z_{re}, z_{im}} = \frac{\rho_{im}}{\sqrt{1 - {\rho_{re}}^2}}. \qquad (9)$$

Therefore, when $|\rho| = 0$, it can be inferred that the complex-valued signal is *proper*. To sum up, note that circularity implies zero mean and propriety, but not vice versa, whereas impropriety implies noncircularity, but not vice versa.

B. CV-Multivariate Generalized Gaussian Distribution

As aforementioned, complex statistics are not straightforward extensions of real-value statistics. For instance, consider the distribution of samples from a complex process in which the real and imaginary parts are Gaussian distributed. The key concept herein is to derive a compact form of the density function, which can be written directly as a function of a complex argument rather than its real and imaginary parts. In this sense, a collection of m complex numbers is simply a collection of $2 \times m$ real numbers. Thus, a collection of m complex-valued random variables is just a collection of $2 \times m$ real-valued random variables with some joint probability distribution of its real and imaginary parts in $\mathbb{R}^{2m}$. Firstly, consider a Gaussian random error vector $\underline{\eta} \in \mathbb{R}^{2m\times 1}$ in the *real domain*, i.e.,

$$\underline{\eta} = \left(\eta_{re_1}, \eta_{im_1}, \cdots, \eta_{re_m}, \eta_{im_m}\right)^T, \qquad (10)$$

Authorized licensed use limited to: Eduardo Resende. Downloaded on December 25,2025 at 14:27:32 UTC from IEEE Xplore. Restrictions apply.

and $E\left[\eta_{re_i}\right] = E\left[\eta_{im_i}\right] = 0$ for all i, which are samples of a circular and proper complex stochastic process. Then, the covariance matrix of $\underline{\eta}$ is defined as

$$\mathbf{R} = E\left[\ \underline{\eta}\ \underline{\eta}^T\right]. \tag{11}$$

The distribution function of η_{re_i} and η_{im_i} is given by

$$f(\underline{\eta}) = \frac{1}{(2\pi)^m \left(\det \mathbf{R}\right)^{1/2}}\ e^{(-\frac{1}{2}\ \underline{\eta}^T\ \mathbf{R}^{-1}\ \underline{\eta})}. \tag{12}$$

On the other hand, based on (3) and (12), follows

$$\begin{pmatrix} \varpi_i \\ \varpi_i^* \end{pmatrix} = \mathbf{M} \begin{pmatrix} \eta_{re_i} \\ \eta_{im_i} \end{pmatrix}, \tag{13}$$

where $\varpi_i = (\eta_{re_i} + j\ \eta_{im_i})$ and $\mathbf{M}$ is defined as in (4). Now, defining $\underline{\varpi_c} \in \mathbb{C}^{2m\times 1}$ as the augmented random error of measurements in the complex domain. Formally, we have

$$\underline{\varpi_c} = \left(\varpi_1, \varpi_1^*, \cdots \varpi_m, \varpi_m^*\right)^T. \tag{14}$$

Then, by (13) it yields

$$\underline{\varpi_c} = \mathbf{A}\ \underline{\eta}, \tag{15}$$

where the block-diagonal matrix $\mathbf{A} \in \mathbb{C}^{2m\times 2m}$ is defined as

$$\mathbf{A} = diag\left(\mathbf{M}, \mathbf{M}, \cdots, \mathbf{M}\right). \tag{16}$$

Hence, according to (15) and (5) we get

$$\underline{\eta} = \mathbf{A}^{-1}\ \underline{\varpi_c} = \frac{1}{2}\ \mathbf{A}^H\ \underline{\varpi_c}, \tag{17}$$

and since $\underline{\eta}$ is a real vector, thus

$$\underline{\eta} = \frac{1}{2}\ \mathbf{A}^T\ \underline{\varpi_c}^*. \tag{18}$$

The augmented covariance matrix $\mathbf{\Omega}_c \in \mathbb{C}^{2m\times 2m}$ of $\underline{\varpi_c}$ given by (15) becomes

$$\mathbf{\Omega}_c = \mathbf{A}\ \mathbf{R}\ \mathbf{A}^H. \tag{19}$$

Now, following [18], consider the quadratic form in (12) given by

$$\underline{\eta}^T\ \mathbf{R}^{-1}\ \underline{\eta}. \tag{20}$$

According to (17), (18) and (19), this form can be written as

$$\begin{aligned} \underline{\varpi_c}^H\ (\tfrac{1}{2}\mathbf{A})\ \mathbf{R}^{-1}\ (\tfrac{1}{2}\mathbf{A}^H)\ \underline{\varpi_c} &= \underline{\varpi_c}^H\ \left(\mathbf{A}\ \mathbf{R}\ \mathbf{A}^H\right)^{-1}\ \underline{\varpi_c}, \\ &= \underline{\varpi_c}^H\ \mathbf{\Omega_c^{-1}}\ \underline{\varpi_c}. \end{aligned} \tag{21}$$

Moreover, the determinant given by (12) is written as

$$\begin{aligned} \det \mathbf{R} &= \det(\tfrac{1}{2}\mathbf{A}^H\ \mathbf{\Omega_c}\ \tfrac{1}{2}\mathbf{A}), \\ &= \left(\tfrac{1}{2}\right)^{2m}\ \left(\det \mathbf{M}^H\right)^m\ \det \mathbf{\Omega}\left(\tfrac{1}{2}\right)^{2m}\ \left(\det \mathbf{M}\right)^m, \\ &= \left(\tfrac{1}{2}\right)^{4m}\ (2j)^m\ (-2j)^m\ \det \mathbf{\Omega_c}, \\ &= \left(\tfrac{1}{2}\right)^{2m}\ \det \mathbf{\Omega_c}. \end{aligned} \tag{22}$$

Substituting (21) and (22) in (12) allows us to obtain the *complex-valued multivariate generalized Gaussian distribution*, that is,

$$f(\underline{\varpi_c}) = \frac{1}{\pi^m(\det \mathbf{\Omega_c})}\ e^{(-\underline{\varpi_c}^H\ \mathbf{\Omega_c}^{-1}\ \underline{\varpi_c})}. \tag{23}$$

with $\underline{\varpi_c}$ defined by (14). Moreover, note that the *pdf* depends algebraically on $\underline{\varpi_c}$, i.e., ϖ_i and ${\varpi_i}^*$, but is interpreted as the joint *pdf* of η_{R_i} and η_{I_i}, and can be used for proper and improper ϖ_i. Introducing a non-zero mean μ is straightforward, which is the complex vector isomorphic to the mean of its real counterpart. The resulting *pdf* is

$$f(\underline{\varpi_c}) = \frac{1}{\pi^m(\det \mathbf{\Omega_c})}\ e^{-(\underline{\varpi_c}-\mu)^H\ \mathbf{\Omega_c}^{-1}\ (\underline{\varpi_c}-\mu)}. \tag{24}$$

Finally, according to the definition and the format usually assumed, $\underline{\varpi_c}$ can be rearranged as follows:

$$\underline{\omega_c} = \mathbf{S_w}\ \underline{\varpi_c} = \left(\varpi_1 \cdots \varpi_m, \varpi_1^* \cdots \varpi_m^*\right)^T, \tag{25}$$

where $\mathbf{S_w} \in \mathbb{R}^{2m\times 2m}$ is a *swap operator* defined as

$$\mathbf{S_w} \triangleq \begin{bmatrix} 0 & I_n \\ I_n & 0 \end{bmatrix}, \tag{26}$$

and I_n is the identity matrix of dimension $n \times n$. That matrix has the following property: ${\mathbf{S_w}}^T = {\mathbf{S_w}}^{-1}$ and $|\det \mathbf{S_w}| = 1$, i.e., $\mathbf{S_w}$ is an orthogonal matrix [19]. Notice that $\mathbf{S_w}$ permutes blocks of m rows or blocks of n columns depending upon whether $\mathbf{S_w}$ pre-multiples or post-multiples a matrix, respectively.

III. Numerical Results

This section presents the statistical properties of the voltage, current, and complex power measurements provided by the PMUs. To validate the methodology across different voltage levels and operational conditions, the authors use PMU measurements installed in an extra-high voltage transmission system, specifically the network operated by Companhia de Transmissão de Energia Elétrica Paulista (CTEEP). Additionally, the analysis using PMU measurements installed in the low-voltage distribution systems is equally addressed. These latter are PMUs installed on University campuses across Brazil funded by the MedFasee project [13].

A. Statistical Signal Properties of PMU Data

The deployment of many PMUs to monitor power transmission systems worldwide is widely known [20]. Today, a hybrid monitoring system is used in many countries' utilities. As can be seen in Fig. 1, a logical diagram for the conventional PMU according to IEC/IEEE 60255-118-1:2018 is presented

Authorized licensed use limited to: Eduardo Resende. Downloaded on December 25,2025 at 14:27:32 UTC from IEEE Xplore. Restrictions apply.

[21], only the phase components of voltage, i.e., V_{ag}, V_{bg}, V_{cg} where the subscript g means the ground potential, and current I_a, I_b, I_c synchrophasors are available at the PMU output in rectangular coordinates. Thus, each measured quantity is accessed through two real values. Hence, the user has to apply the symmetrical component transformation to the synchrophasors of voltage and current once the standard studies are conducted on the positive sequence $(+)$ emerged from the transformation of the symmetrical components. Moreover, the complex power signal is not measured but calculated, so it plays the role of a pseudo measurement. Unlike what happens with the locus of the voltage $(V_r + j\ V_i)$ (see Fig. 2a) and current $(I_r + j\ I_i)$ (see Fig. 2b) phasors, the locus of the complex power signal, i.e., active and reactive power (see Fig. 2c) is expressively correlated to the real and imaginary parts of the voltage and current signals. The real and imaginary parts of the complex power are functions of the real and imaginary parts of the voltage and current signals, as shown below:

$$S = V I^* = P + j\ Q = (V_r I_r + V_i I_i) + j\ (V_i I_r - V_r I_i). \quad (27)$$

Remark that the thickness of the red line in Fig. 2b represents the current variation throughout the accessed data window.

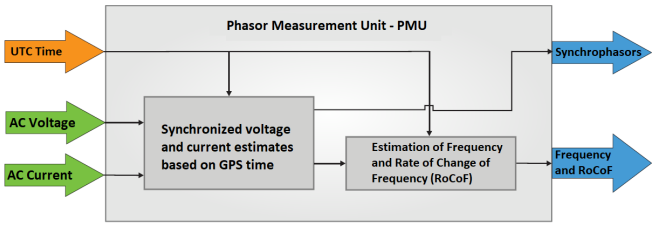
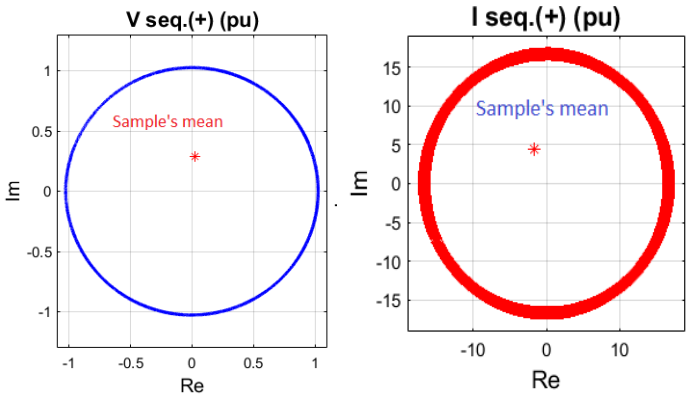


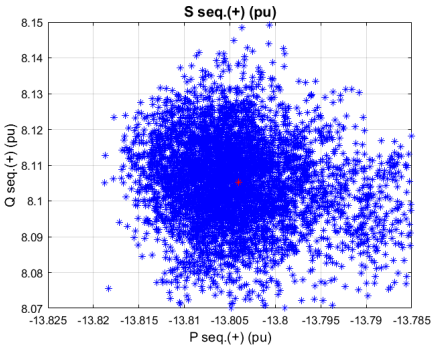
Figure 1: Logical diagram for the conventional PMU.

In the CTEEP data set, the analysis takes place on voltage, current, and complex power signals. In the MedFasee data set, only the voltage signal performed at the consumer voltage level is available. The data set provided by the CTEEP company is equivalent to approximately 15 minutes of acquisition of signals obtained from 3 PMU that monitor part of the National Interconnected System (SIN) at a reporting rate of 60 phasors/s. The measurement points are at the Araraquara, Baixada Santista, and Porto Velho substations. These measurements contain voltage and current information, with 54,060 records for each measured quantity. The three data sets are obtained at the same day and time interval. However, accordingly, with the statistical premise stated by the *Central Limit Theorem* [22], it is sufficient to use a smaller sample size of data. All installations assume the signals in a steady state regime ($= 60 \pm 0.05$ Hz). Due to the space limitation, in the sequel, only the scatter plots of signals at the Araraquara substation are shown in Fig. 2. The sample mean for each quantity is displayed via the star (*) symbol in these plots.

On the other hand, among 28 University campuses, only the scatter plot for the *probability density function* at UFMG campus is displayed in Fig. 3. In contrast, the corresponding variance (blue) and pseudo-variance (red) are shown in Fig. 4, which were calculated by using the Matlab code available in [23].



(a) Voltage (b) Current



(c) Complex Power

Figure 2: Scatter plots for voltage, current, and complex power at Araraquara substation (CTEEP).

In turn, Table I presents the values of the mean (μ), covariance ($\mathbf{C}$), pseudo-covariance ($\mathbf{P}$), and the complex correlation coefficients (ρ) for the CTEEP PMU data. The $|\rho|$ values may attest to the properties of circularity of the voltage, current, and complex power signals once their magnitude, in the worst case, is less than 5%. Furthermore, similar results are shown for the voltage signals for four University campuses as depicted in Table II.

Similarly, from the pictures shown in Figs. 5, one can infer that the complex correlation coefficient (ρ) is close to zero, characterizing a weak correlation between the real part and the imaginary part of the measurements at the Araraquara substation. In addition, note that the pseudo-covariance values are much smaller than the covariance magnitude. Therefore, the analysis leads to the conclusion that a pseudo-covariance normalized by a fixed time interval of the considered time series (*LAG - "lead and lag effect"*) is much lower than the covariance. This fact makes it negligible in applications of the second-order covariance matrix defined in (6). The data set analysis referred to the remaining substations that exhibited the same standard.

Also, strictly speaking, when the data are proper and circular, the problem of the complex-valued nonlinear model can be solved similarly to its real-valued counterpart. The covariance matrix becomes a real-valued diagonal matrix as stated in (1), i.e., $\mathbf{\Omega_c} = \mathbf{C}$. Otherwise, i.e., when the

Authorized licensed use limited to: Eduardo Resende. Downloaded on December 25,2025 at 14:27:32 UTC from IEEE Xplore. Restrictions apply.

Table I: Statistical Signal Properties of PMU's Data at CTEEP.

Sample	Araraquara	Baixada Santista	Porto Velho
Voltage: $V_{seq.}(+)$			
μ_{re}	-0.12000	-0.71000	0.02700
μ_{im}	0.51000	-0.03500	0.29000
σ_{re}	0.61000	0.55000	0.71000
σ_{im}	0.71000	0.51000	0.69000
σ	0.92736	0.75498	0.97980
C	0.86600	0.56200	0.97000
P	-0.133+0.299i	0.051-0.026i	0.025+0.199i
ρ	$0.0213 \times e^{j136.15}$	$0.030 \times e^{-j8.25}$	$0.0102 \times e^{j75.76}$
Current: $I_{seq.}(+)$			
μ_{re}	-2.21000	3.07000	-1.62000
μ_{im}	-6.96000	1.09000	4.43000
σ_{re}	9.56000	2.54000	10.99000
σ_{im}	9.05000	2.35000	11.68000
σ	13.15751	3.45832	16.03652
C	173.12100	257.156	257.17000
P	9.308+0.416i	0.949+0.080i	-15.642+0.165i
ρ	$0.0214 \times e^{j75.48}$	$0.039 \times e^{j26.63}$	$0.0102 \times e^{j126.49}$
Complex Power: $S_{seq.}(+)$			
μ_{re}	-13.81000	-4.69000	15.46000
μ_{im}	8.11000	-1.42000	7.41000
σ_{re}	0.00600	0.01400	0.01900
σ_{im}	0.01200	0.01700	0.02600
σ	0.01378	0.02145	0.03271
C	0.001	0.001	0.002
P	-0.001+0.345i	-0.001-1.712i	-0.001-0.313i
ρ	$0.0293 \times e^{-j166.3}$	$0.0162 \times e^{103.6}$	$0.0310 \times e^{151.0}$

Table II: Statistical Signal Properties of PMU's Data provided by MedFasee.

Sample	UFBA	UFMG	UFRR	UTFPR
μ	-0.107+0.010i	-0.045-0.099i	0.008-0.005i	-0.086-0.07i
$\lvert\mu\rvert$	1.002	1.012	0.998	1.023
σ_{re}	0.698	0.709	0.708	0.706
σ_{im}	0.712	0.715	0.704	0.733
C	0.993	1.012	0.996	1.035
P	-0.021+0.074i	-0.009-0.083i	0.006-0.01i	-0.04-0.038i
ρ	$0.042 \times e^{j119.75}$	$0.042 \times e^{-j101.25}$	$0.007 \times e^{-j40.74}$	$0.042 \times e^{-j154.13}$

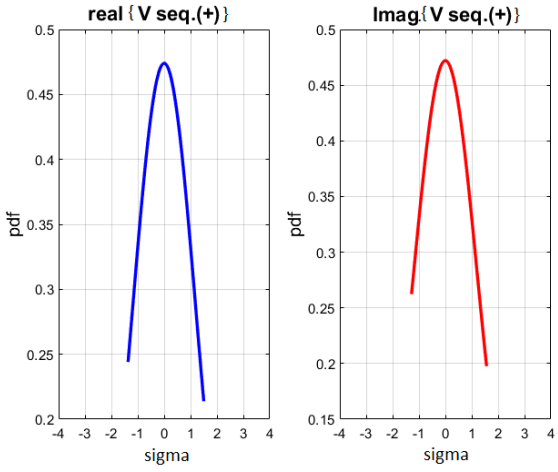


Figure 3: Scatter plot for the *pdf* at UFMG campus: real (blue) and imaginary (red) parts of $V_{seq.}(+)$.

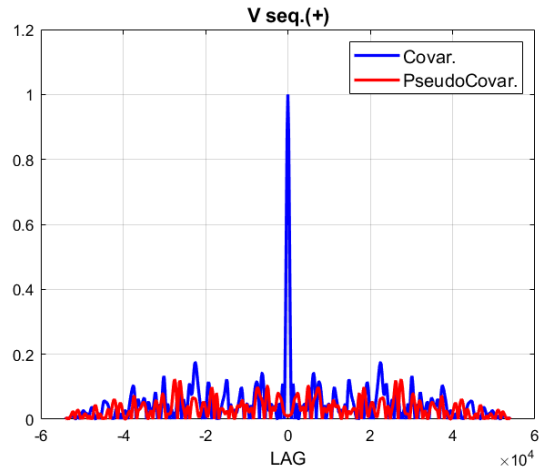
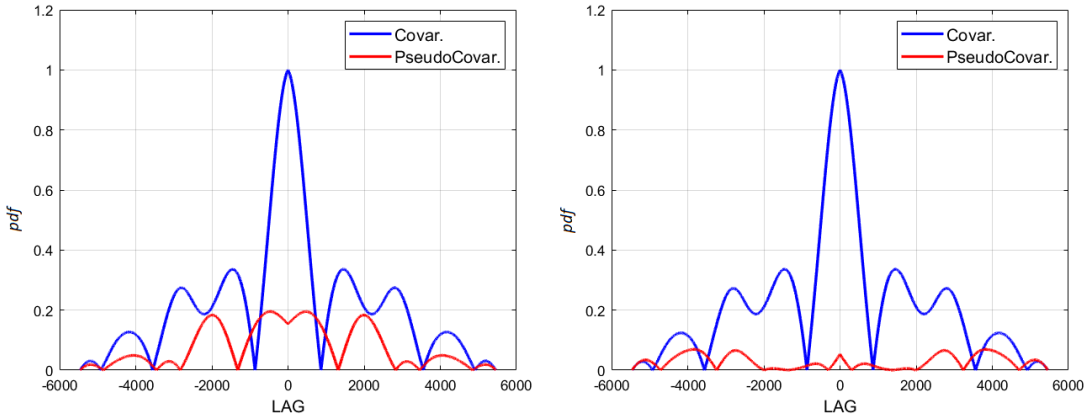


Figure 4: Scatter plot for the *Covariance* (blue) and *Pseudo-covariance* (red) low-voltage at UFMG cumpus.

pseudo-covariance matrix cannot be neglected ($\mathbf{P} \neq 0$), the above formulation must be employed, and the computational overhead has to be circumvented, e.g., by applying augmented matrix factorization techniques [14]. Opportunely, this issue will be investigated, and the results will be presented in the forthcoming paper.

Therefore, the overall analysis of voltage, current, and complex power signals allows us to assume the second-order circular property in all cases once the complex correlation coefficients are small enough to neglect the pseudo-covariance

Authorized licensed use limited to: Eduardo Resende. Downloaded on December 25,2025 at 14:27:32 UTC from IEEE Xplore. Restrictions apply.



(a) Voltage - $V_{seq.}(+)$ (b) Current - $I_{seq.}(+)$

Figure 5: Araraquara substation (CTEEP) - Covariance (blue) and Pseudo-covariance (red).

matrix, $\mathbf{P}$, in (6).

IV. Conclusions and Future Investigation

This paper applies the second-order statistical properties of complex signals to actual PMU data. This approach allows one to deal with complex random variables, i.e., whether proper or improper, circular or non-circular. It is shown that the PMU signals of voltage, current, and complex power can be assumed based on the statistical properties of circularity and propriety. Consequently, the magnitude of measurement error assigned to each complex-valued measure equals $2 \times \sigma$. Otherwise, for instance, the state estimator collapses, e.g., see [2]. The statistical properties of non-circularity and impropriety of voltage, current, and complex power signals will be the target of investigation in the forthcoming paper.

Acknowledgment

Prof. Robson Pires is thankfull to CTEEP - Companhia de Transmissão de Energia Elétrica Paulista for sharing the data provided from PMU. Eduardo Resende would like to thank CAPES for its financial support and UNIFEI for delivering academic and laboratory support.

References

[1] T. Adalý and P. J. Schreier, "Optimization and estimation of complex-valued signals," *IEEE Signal Processing Magazine*, pp. 112–128, September 2014.

[2] E. M. Resende, R. Pires, and L. Mili, "Complex-valued projection statistics for hybrid power system state estimation," *IEEE Transactions on Power Systems*, vol. 39, no. 4, pp. 6052–6062, 2024.

[3] R. Pires, "Complex-valued steady-state models as applied to power flow analysis and power system state estimation," Ph.D. dissertation, Institute of Electric Systems and Energy - ISEE, https://repositorio.unifei.edu.br/xmlui/handle/123456789/5, February 2018.

[4] I. Džafić, R. A. Jabr, and T. Hrnjić, "Complex variable multi-phase distribution system state estimation using vectorized code," *Journal of Modern Power Systems and Clean Energy*, vol. 8, no. 4, pp. 679–688, 2020.

[5] ——, "Hybrid state estimation in complex variables," *IEEE Transactions on Power Systems*, vol. 33, no. 5, pp. 5288–5296, 2018.

[6] Q. Zhang, Y. Chakhchoukh, V. Vittal, G. T. Heydt, N. Logic, and S. Sturgill, "Impact of PMU Measurement Buffer Length on State Estimation and its Optimization," *IEEE Transactions on Power Systems*, vol. 28, no. 2, pp. 1657–1665, 2013.

[7] J. Zhao, G. Zhang, K. Das, G. N. Korres, N. M. Manousakis, A. K. Sinha, and Z. He, "Power system real-time monitoring by using PMU-Based robust state estimation method," *IEEE Transactions on Smart Grid*, vol. 7, no. 1, pp. 300–309, 2016.

[8] P. Yang, Z. Tan, A. Wiesel, and A. Nehorai, "Power system state estimation using PMUs with imperfect synchronization," *IEEE Transactions on Power Systems*, vol. 28, no. 4, pp. 4162–4172, 2013.

[9] B. Picinbono, "Second-order complex random vectors and normal distributions," *IEEE Transactions on Signal Processing*, vol. 44, no. 10, pp. 2637–2640, Oct 1996.

[10] ——, "On circularity," *IEEE Transactions on Signal Processing*, vol. 42, no. 12, pp. 3473–3482, Dec 1994.

[11] P. J. Schreier and L. L. Scharf, "Second-order analysis of improper complex random vectors and processes," *IEEE Transactions on Signal Processing*, vol. 51, no. 3, pp. 714–725, March 2003.

[12] D. Mandic and S. Goh, *Complex Valued Nonlinear Adaptive Filters: Noncircularity, Widely Linear and Neural Models*. Wiley, 2009.

[13] http://www.medfasee.ufsc.br/brasil/, accessed: 2024-03-06.

[14] D. Looney and D. P. Mandic, "Augmented complex matrix factorisation," in *2011 IEEE International Conference on Acoustics, Speech and Signal Processing (ICASSP)*, 2011, pp. 4072–4075.

[15] B. Picinbono and P. Chevalier, "Widely linear estimation with complex data," *IEEE Transactions on Signal Processing*, vol. 43, no. 8, pp. 2030–2033, Aug 1995.

[16] D. Looney and D. P. Mandic, "Augmented complex matrix factorisation," in *2011 IEEE International Conference on Acoustics, Speech and Signal Processing (ICASSP)*, May 2011, pp. 4072–4075.

[17] T. Adali, P. J. Schreier, and L. L. Scharf, "Complex-valued signal processing: The proper way to deal with impropriety," *IEEE Transactions on Signal Processing*, vol. 59, no. 11, pp. 5101–5125, 2011.

[18] B. A. Van Den, "The multivariate complex normal distribution - A Generalization," *Information Theory, IEEE Transactions on*, vol. 41, no. 2, pp. 537–539, Mar 1995.

[19] H. Li and T. Adalý, "Optimization in the complex domain for nonlinear adaptive filtering," in *Signals, Systems and Computers, 2006. ACSSC '06. Fortieth Asilomar Conference on*, Oct 2006, pp. 263–267.

[20] R. B. Bobba, J. Dagle, E. Heine, H. Khurana, W. H. Sanders, P. Sauer, and T. Yardley, "Enhancing Grid Measurements: Wide Area Measurement Systems, NASPInet, and Security," *IEEE Power and Energy Magazine*, vol. 10, no. 1, pp. 67–73, 2012.

[21] D. Kalke and G. Gurrala, "IEC/IEEE 60255-118-1-2018 compliance testing of srf, sogi and park plls for synchrophasors," in *2022 International Conference on Electrical, Computer and Energy Technologies (ICECET)*, 2022, pp. 1–6.

[22] G. Polya, "Uber den zentralen grenzwertsatz der wahrscheinlichkeit-srechnung und das momentenproblem," *Mathematische Zeitschrift*, vol. 8, pp. 171–181, 1920.

[23] http://mlsp.umbc.edu/resources.html, accessed: 2024-03-06.

Authorized licensed use limited to: Eduardo Resende. Downloaded on December 25,2025 at 14:27:32 UTC from IEEE Xplore. Restrictions apply.